ADVANCEMENT OF PERFORMANCE TEST METHODS OF BITUMINOUS MIXTURES

FOR PRACTICAL IMPLEMENTATION AND FUNDAMENTAL UNDERSTANDING OF

DEFORMATION AND FRACTURE

A Dissertation

by

GABRIEL NSENGIYUMVA

Submitted to the Office of Graduate and Professional Studies of
Texas A&M University
in partial fulfillment of the requirements for the degree of

DOCTOR OF PHILOSOPHY

Chair of Committee,	Yong-Rak Kim
Committee Members,	Dallas N. Little
	Amy Epps Martin
	David H. Allen
Head of Department,	Robin Autenrieth

December 2020

Major Subject: Civil Engineering

ABSTRACT

Design and material selection of bituminous mixtures (asphalt concrete) have a decisive role in mixture and pavement performance. Traditionally, the design of the mixtures has focused on the volumetric fractions of components. However, recently there have been an increase in the use of additives and recycled asphalt pavement (RAP) materials that can significantly affect the characteristics of a bituminous mixture with minimal changes to the volumetric fraction. As a result, performance-based mixture design whose key components are performance tests and performance criteria has been proposed for designing mixtures for performance rather than volumetrics. There are numerous performance test methods whose overabundance and complexity lead to results that often contradict each other. To tackle the challenge, this study first examined two test methods, the semicircular bending and gyratory stability tests for the primary distresses of fracture and permanent deformation, respectively. The experimental-statistical approach was used to determine the recommended values for critical testing variables that are repeatable and practical. The two performance tests were then used to successfully perform performance-based mixture design on high-RAP mixtures with different types of rejuvenators and dosages. Secondly, to enhance the understanding of inelastic deformation and fracture in mixtures, this study proposed an inverse method based on optimizing local displacements from digital image correlation (DIC) and finite element method (FEM) simulation. The inverse method was utilized to determine constitutive and fracture properties of example materials that are elastic (polyetheretherketone, PEEK) and viscoelastic (fine aggregate matrix, FAM). A three-point bending configuration was selected for testing coupled with the DIC. MATLAB module was used to calculate the objective function of displacement difference from both experimental and numerical results. The objective function was then minimized using

derivative-free non-linear optimization. The DIC-FEM inverse method produced reasonable elastic modulus of PEEK, viscoelastic relaxation modulus of FAM, and cohesive zone fracture characteristics of FAM, while fracture toughness of PEEK requires further examination as PEEK showed a brittle fracture and was not fully characterized by the DIC in this study. Further studies that employ the developed DIC-FEM inverse method for heterogeneous materials such as asphalt concrete mixtures are recommended as the method can capture important local phenomena within the mixture. This enhanced understanding can help develop the mixture performance tests in a more accurate and efficient manner.

DEDICATION

To my mother.

ACKNOWLEDGMENTS

I would like to take this opportunity to convey my gratitude to all the people that supported me throughout my graduate school life. Without these people, my successful completion of the program would have been more challenging to impossible. I want to let them know that I will forever be grateful for their support, academically, socially, and emotionally about my successful completion of this Ph.D.

First and foremost, I extremely grateful for the advisory, financial support, academic mentoring, life advice by Professor Yong-Rak Kim. I met Dr. Kim in my undergraduate at Kyung Hee University, South Korea as I took his courses. After I joined his research group at the University of Nebraska-Lincoln, I admired his dedication to my learning and academic growth. He gave me much advice that fundamentally improved my life and my way of looking at academic and life challenges. I especially enjoyed the individual weekly meetings I had with him to talk about research progress, challenges, and plans. The talks with him and his dedication to top-notch research kept me motivated throughout my graduate school life. For all the above, thank you Dr. Kim.

Secondly, I would like to extend my gratitude to my dissertation committee members: Professor Dallas N. Little, Professor Amy Epps Martin, and Professor Allen H. David. They have truly been outstanding in improving my dissertation work. Special thanks to Professor Amy Epps Martin whose incredible feedback has helped me to substantially enhance the writing and organization of both my proposal and dissertation. Discussions with Dr. Epps Martin about performance-based mixture design, recycled asphalt concrete mixtures with rejuvenators, asphalt concrete testing methods, writing, organization of the dissertation, have truly been instrumental in this dissertation. I thank Dr. Little for the talks about soil stabilization, performance-based

mixture testing, and rate-dependent micromechanical models. Dr. Little has been very charismatic, supportive, and eager to help me improve my work at Texas A&M University. I thank Dr. Allen for sharing with me his deep knowledge of fracture mechanics. Talks with Dr. Allen always challenged and inspired me to consider mechanical-based approaches to all my research problems. It is without a doubt that my future research endeavors will be influenced by the discussions I had with Dr. Allen.

At the University of Nebraska-Lincoln (UNL), I would like to thank my former professors, Professor Mehrdad Negahban, Professor Florin Bobaru, and Professor Ruqiang Feng they have been instrumental to my knowledge in mechanics, non-linear optimization, and experimental stress analysis that were the basis of this dissertation.

I would like to thank all former colleagues, Mr. Santosh Reddy Kommidi, Dr. Hamzeh Fatmehsari Haghshenas, Dr. Soroosh Amelian, Dr. Mahdieh Khedmati, Mr. Shayan Gholami, Dr. Keyvan Zare Rami, for their friendship and professionalism towards me throughout the years. Special thanks to Dr. Wenlong Li for all mentorship, friendship, and teaching several things.

I would like to thank my friends and family for being incredibly supportive and encouraging during my studies, Mr. Christian Bora, Dr. Loic Constantin, Dr. Celestin Nkundineza, Mr. Johnathan Bucyana, Ms. Jessie Peter, and Ms. Noelle Atieno Mware.

Finally, I am deeply grateful for my family's support, my mother Patricie, my sisters Annuarite and Jeanne D'Arc, and my brother Jean-Aimé. You are the fuel that keeps me going.

CONTRIBUTORS AND FUNDING SOURCES

Contributors

This work was supervised by a dissertation committee consisting of Professor Yong-Rak Kim, Professor Dallas N. Little and Amy Epps Martin of the Department of Civil and Environmental Engineering, and Professor David H. Allen of the Department of Ocean Engineering.

All work conducted for the dissertation was completed by the student independently.

Funding Sources

NOMENCLATURE

AC	Asphalt Concrete
PMD	Performance-based Mixture Design
BMD	Balanced Mixture Design
SCB	Semi-Circular Bending
FN	Flow Number
G_f	Fracture Energy
FI	Flexibility Index
W	Work of Fracture
CRI	Coefficient of Cracking Index
n	Number of Replicates
t	Thickness
nl	Notch Length
lr	Loading Rate
T	Temperature
P_{max}	Maximum Load
m_1	Pre-peak Slope
m_2	Post-peak Slope
LPD	Load-Point Displacement
COV	Coefficient of Variation
SGC	Superpave Gyratory Compactor
PSD	Performance Space Diagram

G-Stability   Gyratory Stability

PG   Performance Grade

FEM   Finite Element Modeling

FAM   Fine Aggregate Matrix

PEEK   Polyetheretherketone

DIC   Digital Image Correlation

CZM   Cohesive Zone Model

OT   Overlay Tester

χ A vector of size N material properties

$\Psi_u(\chi)$ Objective Function

$\mathbf{u}_{FEM}(\chi)$ Computational Displacement from FEM at χ

$\mathbf{u}_{DIC}$ Experimental Displacement from DIC

v Poisson's Ratio

E   Young's Modulus

E(t)   Time-dependent Relaxation Modulus

D(t)   Time-dependent Creep Compliance

$T_{critical}$ Cohesive Critical Traction

$\delta_{critical}$ Cohesive Crack Opening Displacement

$\left\lVert \bullet \right\rVert_2$ Euclidean norm

TABLE OF CONTENTS

LIST OF FIGURES

xiv

LIST OF TABLES

CHAPTER I

INTRODUCTION

The design of bituminous mixtures and pavement structure ultimately depends on the properties

of mixture components and their interactions between one another because they collectively

contribute to the overall performance of a mixture by resisting applied traffic and environment-

induced loads. Understanding the properties of mixture components and their interactions still

present important challenges despite recent advancements in the performance-based mixture

design (or balanced mixture design, BMD) method, which can better address mechanistic

responses of mixtures than the traditional Superpave volumetric-based approach.

Implementation of performance-based mixture design by SHAs (State highway agencies)

has been slow with individual SHAs developing and adopting different performance tests. The

overabundance of information has caused so much complexity such that performance tests often

contradict each other. The fact that there are so many tests, complicate the selection of BMD

tests by SHAs for practical implementation. A need, therefore, arises to investigate primary

performance test methods and improve them for efficiency and increased implementation-

friendliness. The newly improved test methods subsequently help accelerate the performance-

based mixture design approach as a potential mixture design method to replace (or significantly

supplement) the current volumetric-based the Superpave mixture design method.

As more alternative material sources such as RAP (recycled asphalt pavement), warm

mix additives, and rejuvenators are increasingly being used in bituminous mixtures, there is a

growing need to fundamentally understand the properties of the components and their

interactions with each other for more accurate design of mixtures and ultimately pavement structures.

Methods to better understand inelastic deformation and fracture in highly heterogeneous bituminous mixtures are necessary to achieve the performance-based mixture design by accurately selecting mixture components towards the structural design of pavements. The goal of this study is to improve performance test methods of bituminous mixtures for their practical implementation and to develop test methods for a fundamental understanding of inelastic deformation and fracture.

1.1. **Background**

Asphalt concrete (AC) is a heterogeneous composite of air, asphalt (bitumen), and aggregates proportioned to resist both traffic and environmental loads. Rigid aggregates in AC provide stiffness to the mixture by interlocking to resist deformation, while the asphalt binds all the aggregates together and provides cohesion. The air contained in AC controls the rigidity, dampening, and deformation behavior of the mixture.

Conceptually, AC is composed of coarse aggregates with a surrounding mastic known as the fine aggregates matrix (FAM) (Im, Ban et al. 2014). The coarse aggregates are generally considered elastic with a typical Young's modulus of 63 GPa (Ban, Karki et al. 2014, Allen, Little et al. 2017), while the remaining FAM is considered highly viscoelastic (Im, Ban et al. 2014). Collectively, the properties of components and their interactions govern the overall behavior and performance of the mixture. AC mixture design consists of proportioning all the constituents to meet desired volumetric or performance criteria. The Hveem and Marshall methods are legacy standards for AC mixture design which both used a form of stability testing to determine optimum binder content (Roberts, Kandhal et al. 1991). The main weaknesses of

Hveem and Marshall methods were lack of consideration of varied climates, traffic, and materials. As a result, the Superpave design method was introduced by SHRP to accommodate variable materials sources in AC mixture design and address the unique demands of traffic, environment, structure, and reliability of the pavement (Cominsky, Huber et al. 1994). The Superpave uses volumetric indicators such as optimum binder content, VMA (voids in mineral aggregates), and air voids to achieve satisfactory performance characteristics while allowing enough workability during construction. The second phase of the Superpave design method involved mixture testing to ensure sufficient performance. However, except for the moisture susceptibility test (AASHTO T283), performance tests proposed by the Superpave were not adopted by most SHAs (state highway agencies) due to their excessive complexity. As a result, the Superpave method was limited to only considering the volumetric fractions mixture components during mixture design. Solely relying on volumetrics can greatly result in inaccurate mixture performance prediction as the same mixtures with the same volumetrics can produce significantly different mixtures depending on the properties of components and their interactions.

The Superpave mixture design method is inadequate to properly design modern mixtures based solely on volumetrics, especially, with the increasing use of RAP (recycled asphalt pavement) (Daniel and Lachance 2005, Al-Qadi, Ozer et al. 2015, Nsengiyumva 2015, Haghshenas, Nabizadeh et al. 2016) and other additives such as antistripping and rejuvenating agents (Haghshenas, Nabizadeh et al. 2016), antioxidants (Apeagyei 2011), polymers (Goodrich 1988) and fibers (Nsengiyumva, Santosh et al. 2018). To address this issue, a new type of mixture design method called performance-based mixture design (or balanced mixture design, BMD) was introduced and incorporates primary damage-related mixture performance such as

permanent deformation (i.e., rutting) and fracture (i.e., cracking) into the design process (Zhou, Hu et al. 2006).

Although the performance-based mixture design concept was introduced in 2007 by Zhou, Hu et al. (2006), its implementation by SHAs (State highway agencies) has been slow due to the overabundance of information that caused so much complexity such that performance tests often contradict each-others. The fact that there are so many tests, complicate the selection of performance tests by SHAs for practical implementation. The tests include fracture tests such as the DCT (disk-shaped compact test) (Buttlar), the SENB (single-edge notched beam) (Wagoner, Buttlar et al. 2005), the IDEAL-CT (indirect tensile asphalt-cracking test) (Zhou 2019), and the OT (overlay tester) (Walubita, Faruk et al. 2012), and rutting tests such as the IDEAL-RT (indirect tensile asphalt-rutting test) (Fujie Zhou and Sun 2020), the Hamburg (Aschenbrener 1995, Walubita, Faruk et al. 2012, Newcomb and Zhou 2018) and the Flow Number (Haghshenas, Nsengiyumva et al. 2019). Henceforth, the first part of this study developed a single performance test per distress (i.e., cracking and rutting) to simplify and improve performance testing towards reducing the mixture testing burden and improving the practicality of the tests.

Although being an improvement from the volumetrics-based approach, the performance-based method overlooks the properties of components (i.e., FAM and large aggregates) and how they interact to collectively contribute to the overall performance of mixtures. As a result, recursive mixture testing in the form of trial and error is often required to improve the AC mixture design. The process is both cumbersome and inefficient. To alleviate this problem, there is a need for an efficient and appropriate selection of materials based on fundamental materials properties of mixture components and their interactions. Objective selection of materials can

improve design concepts, increase the accuracy of performance models, reduce the life cycle cost of asphalt mixtures, and result in more resilient pavements structures. Furthermore, knowledge of the fundamental properties can facilitate the rigorous design of mixtures using advanced techniques such as virtual mixture testing through computation micromechanics. Incorporating computation techniques during mixture design significantly reduces the cumbersome experimental testing while also allowing easy integration with pavement structure modeling and design.

Previous studies have attempted to characterize material properties belonging to the conceptual AC components of FAM (fine aggregate matrix) and aggregates (Lutif, Souza et al. 2010, Allen, Little et al. 2017). Also, the interactions between the components that control cohesion and adhesion properties were investigated (Rami, Kim et al. 2018). Nonetheless, understanding the mechanical behavior of mixtures has remained challenging due to inherent complexities associated with AC such as complex heterogeneity, anisotropy, nonlinear inelasticity, and damage growth in multiple forms (Lutif, Souza et al. 2010). A method to reduce the complexities of modeling AC is to simply characterize FAM as the main media where significant deformation and damage occur (Kim, Allen et al. 2005, Kim and Aragão 2013, Osmari, da Costa et al. 2020). However, there are several unknowns about FAM design to ensure an accurate representation of the actual FAM in the AC mixture. In addition, the FAM design is especially challenging in the presence of RAP (Little, Allen et al. , Amelian, Kim et al. 2019, Osmari, da Costa et al. 2020) and other additives such as anti-stripping agents and rejuvenators. Furthermore, although useful, using FAM to infer AC mixture-level properties is limited as the FAM-aggregate interaction is ignored. Therefore, accurate characterization of AC components and their interactions need to be conducted on AC mixture.

Several studies have attempted to computationally model AC mixtures (Dai and You 2007, Liu, Wang et al. 2018, Shanbara, Ruddock et al. 2018, Kollmann, Liu et al. 2019). The accuracy of the computational models critically depended on material property inputs from experimental testing. The properties described deformation and fracture behaviors which ultimately control AC mixture responses.

Recently, development in full-field displacement techniques such as DIC (digital image correlation) (Sutton, Orteu et al. 2009) have been attractive to characterize materials properties of heterogeneous materials undergoing deformation and fracture (Hill, Giraldo-Londoño et al. 2017, Mokhtari, Hayatdavoudi et al. 2017). Unlike other traditional methods such as strain gauges, DIC is capable of measuring non-uniform deformations on the surface of heterogeneous materials under deformation (Choi and Shah 1997) and fracture (Doll, Ozer et al. 2017). To obtain materials properties from pure kinematics measurements of DIC involves solving an inverse problem from a known material response (i.e., displacement field from DIC) to material properties. Optimization is used to solve the inverse problem by minimizing the error between displacement fields from DIC and those from numerical computation, such as FEM (finite element modeling) and DEM (discrete element modeling)(Shen and Paulino 2011, He, Makeev et al. 2012, Passieux, Bugarin et al. 2015). The inverse problem approach to DIC results has been applied to a wide range of materials to determine elastic properties (Young's modulus and Poisson's ratio), cohesive fracture properties(Shen and Paulino 2011), and nonlinear shear properties (He, Makeev et al. 2012).

Recently, Hill, Giraldo-Londoño et al. (2017) used DIC-DEM inverse method to estimate cohesive contact properties in AC mixtures. DIC tracked a grid of 16 points close to the crack-tip during the experiment. Another grid of points was also tracked from the DEM results to

correspond to the location of the DIC results. Since the study applied DIC-FEM only to determine fracture properties, constitutive properties were obtained using the traditional IDT (indirect tension) creep test. The creep test was conducted at the temperature of -12°C for 1000 seconds to obtain LVE (linear viscoelastic) properties of the AC mixture. Subsequently, fracture tests in the form of DCT and SENB were carried in the presence of DIC. Since constitutive properties were experimentally determined the DIC-FEM inverse problem was only used to determine fracture properties. A predetermined grid of possible solutions was used to minimize the possibility of the multiple solutions associated with inverse problems (McDonald, Grantham et al. 2007, Boulkeraa, Ghenaiet et al. 2014). The main limitation of Hill, Giraldo-Londoño et al. (2017) study is the use of low testing temperature, which minimized significant viscoelastic behaviors that are dominant during the typical life cycle of AC mixtures. The lack of viscoelastic effect in the results was manifested in global experimental results (i.e., force vs. displacement) which behaved more elastic than viscoelastic on the same microstructure. Furthermore, the study was limited by using separate test methods to obtain constitutive (i.e., LVE) and fracture properties of AC which reduced the efficiency of the DIC-DEM method.

1.2. **Problem Statement**

The effectiveness of performance-based mixture design relies on the performance test methods for cracking- and rutting-related properties. With this in mind, individual SHAs have developed and adopted numerous and different performance tests. However, there is an overabundance of information that has caused so much complexity such that performance tests often contradict each other. The fact that there are so many tests, complicate the selection of performance tests by SHAs for practical implementation. This might be a reason for the current status: almost half of SHAs still use the volumetric-based approach to design mixtures (West, Rodezno et al. 2018). It

is thus necessary to take a closer look at several primary performance test methods and improve them for efficiency and increased implementation-friendliness. The newly improved test methods subsequently help accelerate the performance-based AC mixture design method that can replace (or significantly supplement) the current volumetric-based Superpave approach.

Even with improved performance tests, identification of mixture components, and their interactions that collectively contribute to mixture-level performance is still limited. As a result, the performance-based mixture design is accomplished through recursive mixture testing in the form of trial-and-error. This is both cumbersome and inefficient. To alleviate this, a linkage between components properties and mixture performance via computational micromechanics modeling is advantageous. However, directly obtaining component-level properties from AC mixture testing presents challenges from heterogeneity, anisotropy, nonlinear inelasticity, and damage growth in multiple forms. With advances in digital image correlation (DIC) and computation modeling, it is possible to experimentally measure and numerically model complex failure and deformation phenomena in heterogeneous materials. Subsequently, optimization of the results from numerical modeling (e.g., FEM) and DIC is used to inversely solve for unknown material properties. The inverse method is attractive to identify complex material properties in both homogenous as well as in heterogeneous materials since it inherits the advantages of both computation modeling and DIC. However, in AC mixtures, the DIC-computation method has been limited to mainly the elastic-dominant regime (i.e., low temperatures) even though significant inelastic deformation and fatigue cracking occur at intermediate temperatures during the AC pavement lifecycle. Therefore, there is a lack of a robust DIC-computation inverse method capable of characterizing properties of bituminous mixture components and their interactions in the presence of significant viscoelastic effects, inelastic deformation, and fracture.

The inverse method can significantly save time and cost related to obtaining necessary properties of materials and mixtures that are one of the core inputs that pavement design engineers need to know.

1.3. **Research Objectives**

The goal of this study is to advance performance test methods of bituminous mixtures for practical implementation and fundamental understanding of inelastic deformation and fracture. To meet the goal, this study used experimental approaches aided by statistical methods and computational modeling with the following two specific objectives:

(1) To develop practical and repeatable primary (i.e., cracking and rutting) performance test methods using experimental-statistical approach;

    (i) The semicircular bending (SCB) fracture test method was advanced by conducting tests aided by statistical analyses to identify several important testing variables such as the number of replicates, specimen geometry, testing conditions (e.g., boundary conditions, loading rate, and testing temperature).

    (ii) The gyratory stability (G-stability) rutting test method was developed by conducting tests and statistical analyses to identify the number of replicates, specimen geometry, loading rate, and testing temperature.

(2) To develop a method for fundamental understanding of inelastic deformation and fracture of materials based on an integrated FEM and full-field DIC results.

    (i) Establishing a linkage between DIC and FEM results via MATLAB and Python tools for the optimization of properties.

(ii) Testing of two example materials (PEEK as an elastic material and fine aggregate bituminous mixture as a viscoelastic material) using DIC and its finite element modeling.

(iii) Identification of constitutive properties and fracture characteristics of the two example materials using the developed DIC-FEM inverse method.

The originality of this study lays at improving the current performance testing practices through simpler, practice-friendly, and reliable performance tests methods, specifically, semi-circular bending (SCB) and G-Stability tests for fracture and rutting test of mixtures, respectively. Furthermore, this study pursues an understanding of the mixture properties in the presence of inelastic deformation and fracture solely through the full-field DIC-FEM displacement optimization approach.

This study advanced the current practical mixture performance tests and provide technology to more accurately characterize inelastic deformation and fracture of bituminous mixtures subjected to complex deformation and damage. The outcomes of this study can advance the performance-based design of mixtures and benefit the next-generation mechanistic design of bituminous mixtures and pavement structures. Ultimately, this study can lead to saving of life cycle costs, preservation of natural resources, and reduction of carbon-dioxide emissions.

1.4. **Research Methodology**

To achieve the objectives, a research methodology shown in Figure 1 was adopted. In the figure, the scope of this study is highlighted in a grey box. Two mixture performance test methods for fracture and rutting were examined followed by the exploration of the DIC-FEM inverse method. The mixture test methods are the SCB (semi-circular bending) and G-Stability for fracture and rutting performance, respectively. The SCB geometry was selected for fracture testing based on

several reasons including simplicity and repeatability. The SCB test method was examined in two successive stages using an experimental-statistical approach. The first stage involves the determination of critical testing variables such as the recommended minimum number of replicates, thickness of specimens, notch length, and testing temperature. Values for SCB testing variables were determined within a reasonable range investigated to maximize repeatability and practicality. The second phase investigated the effects of testing fixtures (i.e., boundary conditions) on test results and their repeatability. In total, predominant six SCB test fixtures were investigated.
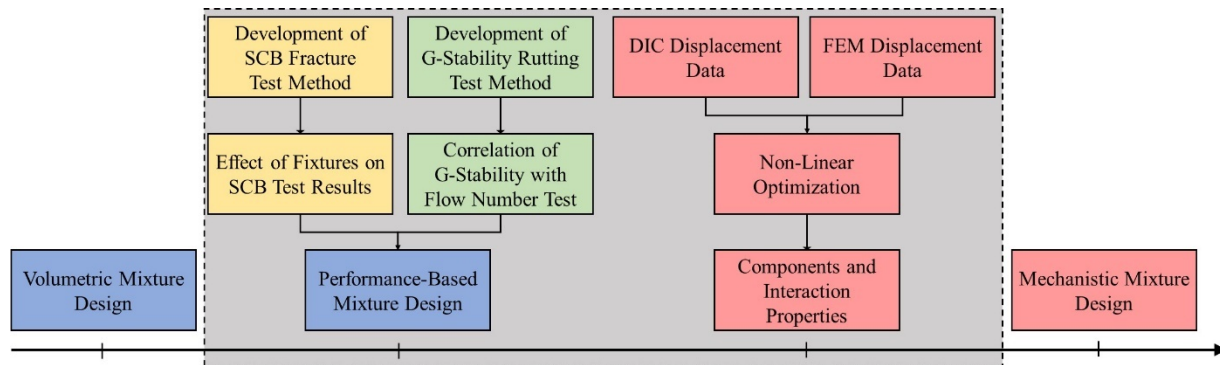
Figure 1 Proposed research methodology.

Subsequently, the performance test method for rutting was explored by investigating critical testing variables such as specimen geometry, loading rate, testing temperature, and recommended minimum number of replicates. The rutting test method was named G-Stability after the SGC (Superpave gyratory compactor), which was used to prepare compacted samples. It is noteworthy that the exploration of the G-Stability test also employed an experimental-statistical approach to determine critical testing variables. For simplicity, the testing temperature for the G-Stability was selected to match that of a well-known rutting test, FN (flow number) testing. The same temperature can facilitate to correlate results from the newly-explored G-

Stability and the established but complicated FN test. Ultimately, both performance test methods were applied to a performance-based mixture design on high-RAP mixtures treated with rejuvenating agents.

To advance a fundamental understanding of deformation and fracture, a DIC-FEM inverse method was explored. The inverse method can identify the properties of materials by minimizing the displacement difference between experimental DIC and computational FEM results. The inverse method calculates and optimizes the objective function formulated from the error between both sets of data (i.e., DIC measurements and FEM simulations). Due to the nature of the inverse problem a nonlinear optimization algorithm (implemented in MATLAB), specifically, the Needler-Mead algorithm was used to find optimal material properties (Shen 2009). A module was then implemented to ensure communication between FEA (finite element analysis) software (e.g., Abaqus™ in this case) with the optimizer. To formulate the objective function the communication module targets the exact node coordinates in a region of interest within the FEA that was matched with corresponding DIC grid nodes. The developed DIC-FEM method was used for two example materials: PEEK as an elastic material and FAM as a viscoelastic material with and without fracture.

1.5. **Organization of the Dissertation**

This dissertation is subdivided into 8 chapters. Immediately after this introduction, Chapter II presents the background of the performance-based mixture design and includes different types of performance tests and criteria. Next, Chapter III presents the effort to develop the SCB fracture test method for AC mixtures. Chapter IV discusses the development efforts for the G-Stability rutting performance test. In Chapter V, the two performance test methods developed were applied to a set of data of high-RAP mixtures with and without rejuvenating agents. More

specifically, Chapter V includes an investigation on the effects of rejuvenator dosages, types, and blending methods to the AC mixture performance. Chapter VI presents the underlying theory of the DIC method and subsequent optimization algorithm, efforts to develop the DIC-FEM inverse method that can be applied to general materials and mixtures including the two example materials of PEEK and FAM undergoing linear deformation (elastic for PEEK and viscoelastic for FAM), respectively. In Chapter VII, the inverse method was extended to include the characterization of fracture properties in both example materials. Finally, Chapter VIII summarizes the major findings and makes conclusions of this study.

CHAPTER II

PERFORMANCE TESTING OF ASPHALT MIXTURES

Performance testing is critical in characterizing the AC mixture's failure profile due to a variety

of loads (e.g., traffic and environmental) once implemented in the pavement structure. Typically,

distresses of interest in AC mixtures include fracture (i.e., cracking) and permanent deformation

(i.e., rutting) both of which have performance tests are conceived to characterize. The results

from the tests are used in combination with established performance criteria to determine the

admissibility of the mixture. This type of AC mixture design is called performance-based

mixture design in contrast to the volumetric mixture design (i.e., the Superpave) which uses

volumetric fractions of mixture constituents as the main design criteria. The advantage of the

performance-based mixture design is that contributions from additives such as polymers, warm-

mix additives, antistripping, can be reflected more accurately. Although additives can minimally

affect volumetric fractions of AC mixtures, they can have a significant impact on the mixture's

mechanical characteristics that are better reflected during performance testing.

Performance testing along with performance criteria are the key components of the

performance-based AC mixture design. Factors such as accessibility, repeatability, and

practicality play a crucial role in the selection of a performance test for the design process.

Researchers have proposed several performance tests each with different advantages and

limitations.

2.1. **Fracture Performance Tests**

2.1.1. SCB (Semi-Circular Bending)

The semi-circular bending test (Figure 2) was initially developed by Chong and Kuruppu (1984) aiming to simplify fracture testing in rock materials. Since then SCB test method has been widely adopted in the asphalt community due to its simplicity, repeatability, and practicality. The test involves and semi-circular specimen with a fracture notch in the bottom (i.e., flat side). The specimen is then loaded from the top (i.e., curved side) at a given loading rate until failure. The results are then interpreted by calculating a fracture-related indicator such as fracture energy, cracking resistance index, and flexibility index (Nsengiyumva and Kim 2019, Nsengiyumva, Haghshenas et al. 2020).
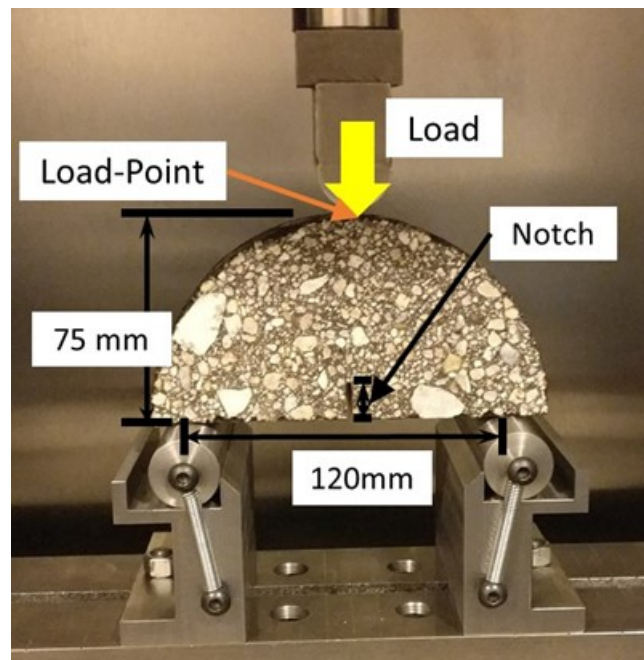
Figure 2. Semi-circular bending test set-up (Nsengiyumva and Kim 2019).

2.1.2. DCT (Disk-Shaped Compact Test)

DCT was adopted from ASTM E399 (standard test method for linear-elastic plane-strain fracture toughness K_{Ic} of metallic materials) to be used on AC mixture by Wagnoner, Buttlar et al. (2005). DCT specimens (Figure 3) are disk-shaped with an offset cut from one end, where a notch perpendicular to the cut is inserted. In addition, DCT specimens have two drilled loading holes located at each side of the notch to load the specimen during testing. DCT specimens have the advantage of having a considerably larger fracture ligament compared to specimens from other fracture test methods which can improve the repeatability of results. However, DCT specimens preparation is delicate and requires significant expertise to properly accomplish. Furthermore, there is a chance that the failure can occur at the loading holes in heterogeneous materials such as AC mixtures (Wagnoner, Buttlar et al. 2005). DCT test has been standardized for AC mixtures through the ASTM D7313 (standard test method for determining fracture energy of asphalt-aggregate mixtures using the disk-shaped compact tension geometry).

Figure 3. Disk-shaped compact test set-up (reprinted from Wagoner, Buttlar et al. (2005)).

2.1.3. OT (Overlay Tester)

The overlay tester (Figure 4) was developed by Zhou and Scullion (2005) as a method to evaluate the cracking resistance of AC mixtures overlays. The test simulates an existing crack at the bottom layer immediately underneath the overlays. The simulated crack then propagates upwards as during the testing as a result of slabs movements. This test involves an unconventional specimen which is a hybrid between a disk and a beam. The specimen is glued on the bottom support plates which are subsequently loaded cyclically at room temperature over 24 hours (Newcomb and Zhou 2018). Although this test can more realistically replicate overlay loading of AC mixtures, the specimen preparation (i.e., cutting and gluing) and the long testing time reduces the practicality of the test. Besides, there is a probability of debonding between the specimen and the bottom support fixture which can lead to failure of the test.
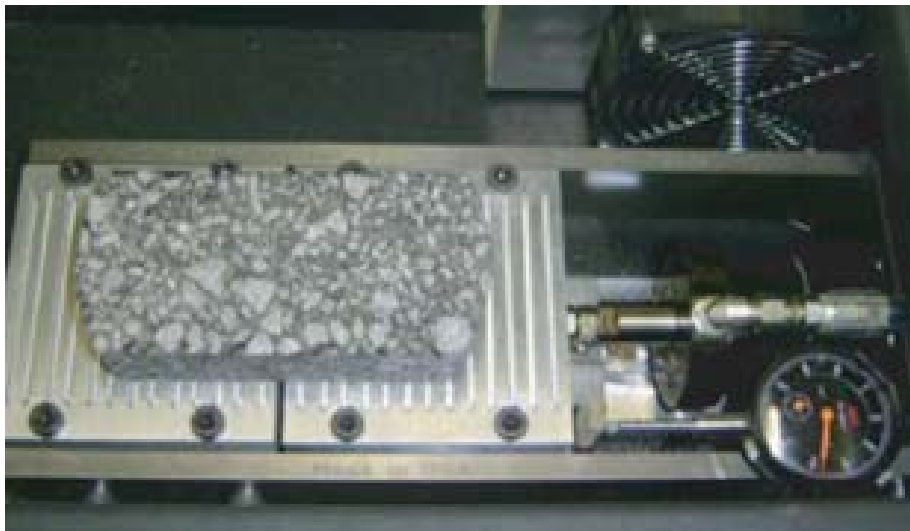
Figure 4. Overlay tester set-up (reprinted from Walubita, Faruk et al. (2012)).

2.1.4. IDEAL-CT (Indirect Tensile Asphalt Cracking Test)

The IDEAL-CT (Figure 5) was developed by in a bid to simplify fracture testing AC mixtures.

The test was meant as a practical and easy method to quickly evaluate the fracture resistance of

mixtures, especially during QA/QC phases. Specimens of 62 mm thickness are loaded with an

LPD (load-point displacement) rate of 50 mm/min to induce indirect tensile loads at room

temperature. Test results are then analyzed to infer fracture-related indicators (e.g., fracture

energy). Although this test is simple and practical, there is a possibility of significant stress

localization round LPD which can dilute the observed results. Also, the lack of a notch in the

specimen complicates the application of the theory of fracture mechanics (Anderson 2017),

therefore, limiting the interpretation of IDEAL-CT results for QA/QC-related purposes.

Figure 5. IDEAL-CT test set-up (reprinted from Zhou (2019)).

2.1.5. SNEB (Single Edge Notched Beam)

The SNEB (Figure 6) was developed by Wagoner, Buttlar et al. (2005) and used beam-shaped

specimens with a notch in the middle. Testing is conducted in the CMOD controlled mode and

the testing temperature is typically low (e.g., -10C). This test has the advantage of having

numerical and analytical solutions using classical fracture mechanics. However, SNEB is

disadvantaged by complicated sample preparation and testing set-up which reduces the

practicality of the test in AC where compacted samples and cores are typically cylindrical.

Figure 6. SENB test set-up (reprinted from Wagoner, Buttlar et al. (2005)).

2.2. **Rutting Performance Tests**

2.2.1. FN (Flow Number)

The flow number test (Figure 7) was recommended by the NCHRP Project 9-19 as part of the

SPT (simple performance test) program. The test consists of cyclically loading cylindrical AC

specimens, similar to those used for the DM, for 0.1 seconds with a rest period of 0.9 seconds.

The test continues until the flow is achieved or until 10,000 loading cycles are reached. The flow

is achieved when the rate of accumulated strain is minimal. The testing temperature and the deviatoric stress for FN are selected to achieve flow within the 10,000 cycles or 2.778 hours. The FN test has the advantage of being a fundamental test that simulates pavement loading conditions where a truck passes followed by a short rest period and at high temperature. The test has shown a good correlation with the field performance on AC mixtures (Rodezno, West et al. 2015). However, FN is disadvantaged by the complicated test set-up, which requires robust enough equipment that can accurately apply cyclic loading while maintaining temperature. Furthermore, data analysis of FN involves finding a derivative of the test results which require curve fitting and further inhibits the simplicity, application, and practicality of FN.

Figure 7. Flow number test.

2.2.2. IDEAL-RT (Indirect Tensile Asphalt Rutting Test)

The indirect tensile asphalt rutting test (Figure 8) was recently proposed test by Fujie Zhou and Sun (2020) to simplify rutting testing of AC mixtures during the design and QA/QC phases. The

IDEAL-RT is essentially IDEAL-CT with exception of increased testing temperature and different bottom fixtures (Figure 8). In the rutting test, a Marshall bottom fixture is used to induce shear failure in the specimen at a high temperature of 50ºC and the loading rate of 50 mm/min. The IDEAL-RT has correlated well with field performance observation of mixtures and showed good repeatability. The main disadvantage of this test is that it relies on shear deformation to predict rutting which is typically a normal deformation (i.e., top-down) phenomenon. Also, test specimens are loaded from the top using a narrow contact area which does not reflect field conditions where rutting distress is caused by large tires (i.e., large contact area) from heavy trucks.
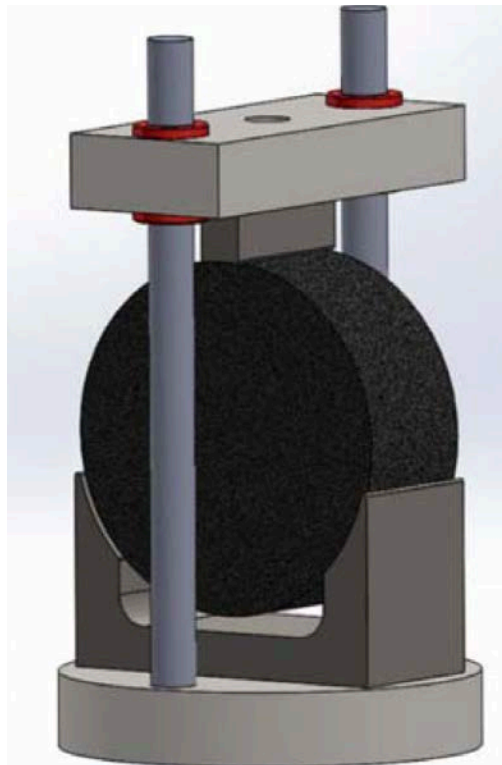
Figure 8. IDEAL-RT (reprinted from Fujie Zhou and Sun (2020)).

2.2.3. HWTT (Hamburg Wheel Track Tester)

The Hamburg wheel track tester was developed in Germany by Aschenbrener (1995) to evaluate the rutting of asphaltic mixtures. The HWTT is a torture test of mixtures where two disks specimens from SGC samples are repeatedly loaded using a steel track wheel until failure rutting depth (Figure 9). Moisture effect on the rutting performance of the mixture can also be evaluated using the HWTT by simply introducing water to the test chamber during testing. The test is conducted according to the AASHTO T324 (Standard Method of Test for Hamburg Wheel-Track Testing of Compacted Hot Mix Asphalt, HMA). The specimens are kept at the testing temperature of 40ºC while the wheel passes 52 times loaded with 705 N (Newcomb and Zhou 2018). Although HWTT results correlate well with field performance, the complexity of the test set-up and equipment costs limits its practicality and repeatability.

Figure 9. Hamburg test (reprinted from Newcomb and Zhou (2018)).

2.3. **Implementation of Performance Testing**

Several studies have explored using the aforementioned performance tests for conduct performance-based mixture designs. Cooper III, Mohammad et al. (2014) used the SCB test to evaluate the fracture resistance of Louisiana mixtures in the form of the critical strain energy release rate (J-integral). Although J-integral has the advantage of being based on principles of fracture mechanics, it requires multiple notch lengths (e.g., 25.4 mm, 31.8 mm, and 38 mm notch lengths) which may discourage its adoption for practical purposes. The J-integral performance criterion for fracture energy was selected to be 0.5 kJ/m^2 based on overall the average of test results from several Louisiana mixtures (Kim, Mohammad et al. 2012). Interestingly, the same performance criterion for fracture was applied to all mixtures without regard to the binder types even though modified binders which contributed to higher fracture resistance of mixtures. For the rutting resistance efforts conducted in the same study (Cooper III, Mohammad et al. 2014) the criteria were specific to binder types used in mixtures (e.g., modified or unmodified).

Bahia, Teymourpour et al. (2016) conducted a study about the feasibility of implementation of performance-based specifications for Wisconsin DoT (WisDOT). Two versions of SCB were used to evaluate fatigue (i.e., intermediate temperature) and thermal (i.e., low temperature) cracking of AC mixtures. For fatigue cracking the I-FIT (Illinois Flexibility Index Test) was adopted while the SCB test developed by Li and Marasteanu (2010) was adopted for thermal cracking. It is noteworthy that both versions of SCB tests utilized a single notch thus eliminating the multiple notches required in Cooper III, Mohammad et al. (2014). The difference between the two SCB tests lies in the loading rate: 50mm for I-FIT vs. 0.5 mm for SCB by Li and Marasteanu (2010) and the fracture-related indicator used are the Flexibility Index (FI) for I-FIT and the fracture energy (G_f) for SCB by Li and Marasteanu (2010). After

conducting the SCB tests of several mixtures with different volumetrics and composition, Bahia, Teymourpour et al. (2016) concluded that FI provided results with a wider range in which mixtures could be distinguished in contrast to the G_f results of the same mixtures. As result, FI was recommended to be included in the WisDOT performance-based mixture design for intermediate temperatures. However, G_f was recommended for the low temperatures SCB testing results due to the difficulty of calculating the post-peak slope required to obtain FI at the low temperatures where mixtures behave in brittle fashion.

Kim, Mohammad et al. (2015) conducted a study about performance-based mixture design in the State of Louisiana using the LWT (loaded wheel tracking) and SCB tests to measure rutting and fracture performances, respectively. The study compared fracture results (i.e., J_c, in kJ/m^2) and the rut dept from LWT (in millimeters) to actual field performance. This led to the determination of the performance criteria of mixtures. Fracture criterion was established to be 0.5 and 0.6 kJ/m^2 of J_c for low and high traffic roads, respectively. Similarly, the rutting criteria using LWT was determined as 10 mm and 6 mm for low and high traffic roads, respectively. The study then combined the test methods and the criteria to propose PBS (performance-based specifications) for Louisiana. It should be noted that the LWT test used in the study was the HWTT and was conducted per AASHTO T 324.

Buttlar, Hill et al. (2017) used HWTT rutting and DCT fracture test results to establish a PSD (performance space diagram) for Illinois AC mixtures (Figure 10). In their study, the HWTT rut dept was plotted on the y-axis in descending order from bottom to top, while DCT fracture energy was plotted on the x-axis in ascending order. The resulting plot designates regions to classify mixtures based on their rutting and cracking performance and expected traffic. It is noted that while all mixtures satisfied the same rutting requirement, the cracking was traffic-

dependent since roads with high traffic demanded higher fracture performance criteria. The study noted that polymer modification of binder and gravel aggregates contributed to improved fracture and rutting performances. The study also noted that SAM (stone matrix asphalt) mixture generally satisfied high traffic criteria. Another study that used HWTT-DCT PSD was conducted by Jahangiri, Majidifard et al. (2019) to investigate the effects of RAP and RAS (reclaimed asphalt shingles) on the performance of AC mixtures. Test results showed that RAP and RAS reduced fracture resistance of mixtures, which then failed to meet the DCT fracture energy performance criteria. This highlights the need for improving characteristics of RAP materials and mixtures when reusing them in new mixtures as done by Nsengiyumva, Haghshenas et al. (2020).
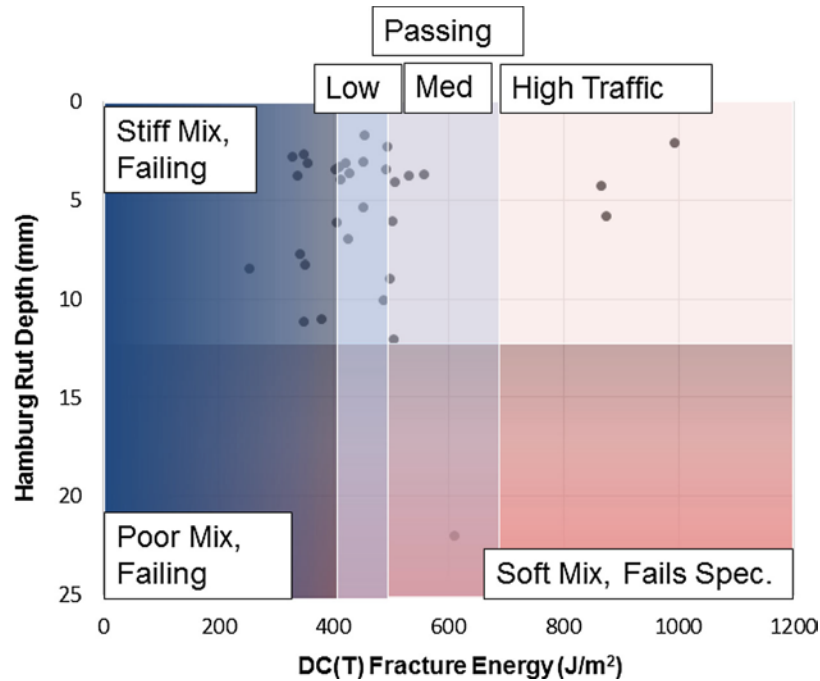
Figure 10. PSD from HWTT and DCT tests showing performance criteria for different mixtures (reprinted from Buttlar, Hill et al. (2017)).

A study by Barros, Garcia et al. (2019) at the University of Texas at El Paso investigated the effect of RAP content and origin on the performance of asphalt concrete mixtures. Toward that, the study adopted the tests, HWTT, OT, and IDT (indirect tension test) for rutting, fracture, and tensile performance, respectively. A three-dimensional performance interaction diagram (i.e., PSD) was used as a tool to evaluate the mechanical properties of mixtures. The PSD contained performance for fracture, permanent deformation, and tension as crack progression rate (Garcia, Miramontes et al. 2018), normalized rutting resistance index (Wu, Zhang et al. 2017), and tensile strength, respectively (Figure 11). The performance criteria for the PSD were 0.5 and 1 for CPR(following(Miramontes, Garibay et al. 2017)), NRRI (following (Garcia, Valenzuela et al. 2019)), respectively. The tensile criterion was 85 psi following TxDOT. The test results (shown in Figure 11) showed increasing RAP content increased the rutting resistance and reduced fracture resistance of mixtures (Figure 11(a)). In addition, the results showed a difference in performance characteristics of mixtures with RAP from different sources (Figure 11(b)).
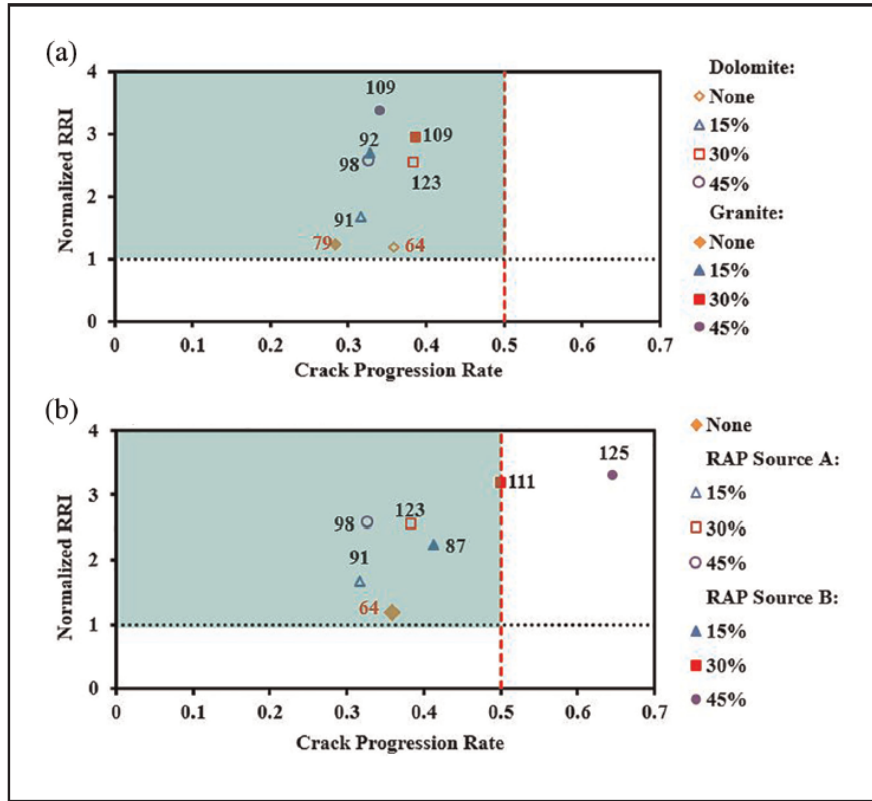
Figure 11. Performance interaction diagram showing: (a) influence of RAP content, and (b) influence of RAP source (reprinted from Barros, Garcia et al. (2019)). Note: the three-dimensionality is provided by data labels representing the tensile strength (in psi).

Around the US several states (e.g., Louisiana, New Mexico, Oklahoma, South Dakota, Wisconsin) are studying the feasibility of implementation of performance testing in the mixture design process to replace the Superpave volumetric design method. Other states (e.g., California, Florida, Georgia, Illinois, Texas, Utah) have to some degree already adopted performance testing along with criteria for their mixture design (West, Rodezno et al. 2018). States located in a cold climate (e.g., Minnesota) tend to focus on fracture/cracking while States from warmer climates (e.g., Georgia and Florida) emphasize more on rutting than cracking criteria. The most common fracture performance tests adopted or being considered by most states are the SCB, DCT, and OT, albeit with different standards and test conditions. For rutting, FN, HWTT, and APA at high

27

temperatures (typically > 40ºC) have been adopted or under consideration. Each state tends to

choose its performance criteria by correlating the test results and field performance. Most

fracture tests are conducted at room temperature on two hours oven aged (at 135ºC) mixtures.

The combination of tests developed by each state for fracture and rutting and the existence of

several testing methods can overwhelm AC mixture designers when selecting a performance test

to adopt. It is noteworthy that moisture susceptibility test is typically conducted on mixtures per

AASHTO T283: resistance of compacted hot mix asphalt (HMA) to moisture-induced damage.

Table 1 summarizes the current state of practice implementation of performance-based

mixture design by different states (West, Rodezno et al. 2018). As can be seen, only four states

(Illinois, New Jersey, Oklahoma, and Texas) have fully implemented the performance-based

mixture design. The remaining states are currently conducting research and field performance

monitoring to establish appropriate tests and criteria. The states without a finalized performance-

based mixture design method have adopted preliminary performance testing and criteria that are

summarized in Table 1. It should be noted that the different design traffic requires different

performance criteria with higher traffic requiring a higher performance limit (e.g., higher fracture

energy).

Table 1. Performance-Based Mixture Design by State (Summary from West, Rodezno et al. (2018) NCHRP 20-07/Task 406)

State	Approach	Distress	Test	Criterion
California		Rutting	HWTT at 50C	< 12.5 mm at 20,000 passes
		Cracking	AASHTO T 321	
Florida		Rutting	APA at 64C	< 4.5 mm at 8,000 cycles
		Cracking	—	—
Georgia		Rutting	HWTT at 50C	< 12.5 mm at 20,000 passes
		Cracking	—	—
Illinois	1	Rutting	HWTT at 50C	< 12.5 mm at 20,000 passes
		Cracking	I-FIT (AASHTO TP 124)	> 8
Iowa		Rutting	HWTT at 50C	< 8 mm at 8,000 passes
		Cracking	DCT (under consideration)	
Louisiana		Rutting	HWTT at 50C	< 10 mm at 20,000 passes
		Cracking	SCB-Jc at 25C	> 0.6 kJ/m2
Minnesota		Rutting	—	—
		Cracking	DCT-Gf (ASTM D7313)	> 690 J/m2
New Jersey	1	Rutting	APA at 64C	< 7 mm at 8,000 cycles
		Cracking	OT (NJDOT B-10) at 25C	> 700 cycles
Ohio		Rutting	APA at 54.4C	< 5 mm at 8,000 cycles
		Cracking	—	—
Oklahoma	2	Rutting	HWTT at 50C	< 12.5 mm at 20,000 passes
		Cracking	I-FIT (AASHTO TP 124)	—
South Dakota		Rutting	APA at 64C	< 8 mm at 8,000 cycles
		Cracking	—	—
Texas	1	Rutting	HWTT (Tex-242-F) at 50C	> 10,000 and > 20,000 passes at 12.5 mm rut depth
		Cracking	OT (Tex-248-F) at 25C	> 150 and >300 cycles
Utah		Rutting	HWTT at 46C - 50C	< 10 mm at 20,000 passes
		Cracking	—	—
Wisconsin		Rutting	HWTT (AASHTO T 324)	> 5,000 and > 10,000 passes at 12.5 mm rut depth
		Cracking*	DCT-Gf (ASTM D7313)	> 400 J/m2
		Cracking**	SCB-Jc (ASTM D8044) at 25C	> 0.4 kJ/m2

* Low-temperature test, and ** Intermediate temperature test

2.4. **Approaches of Performance-Based Mixture Design**

There are different approaches to conduct the performance-based mixture design depending on the weight placed on the volumetrics. Despite the differences, all performance-based mixture designs need to satisfy performance and moisture susceptibility criteria. Figure 12 by NCHRP 20-07(406) graphically shows flowcharts of three different approaches that can be used for AC mixtures.
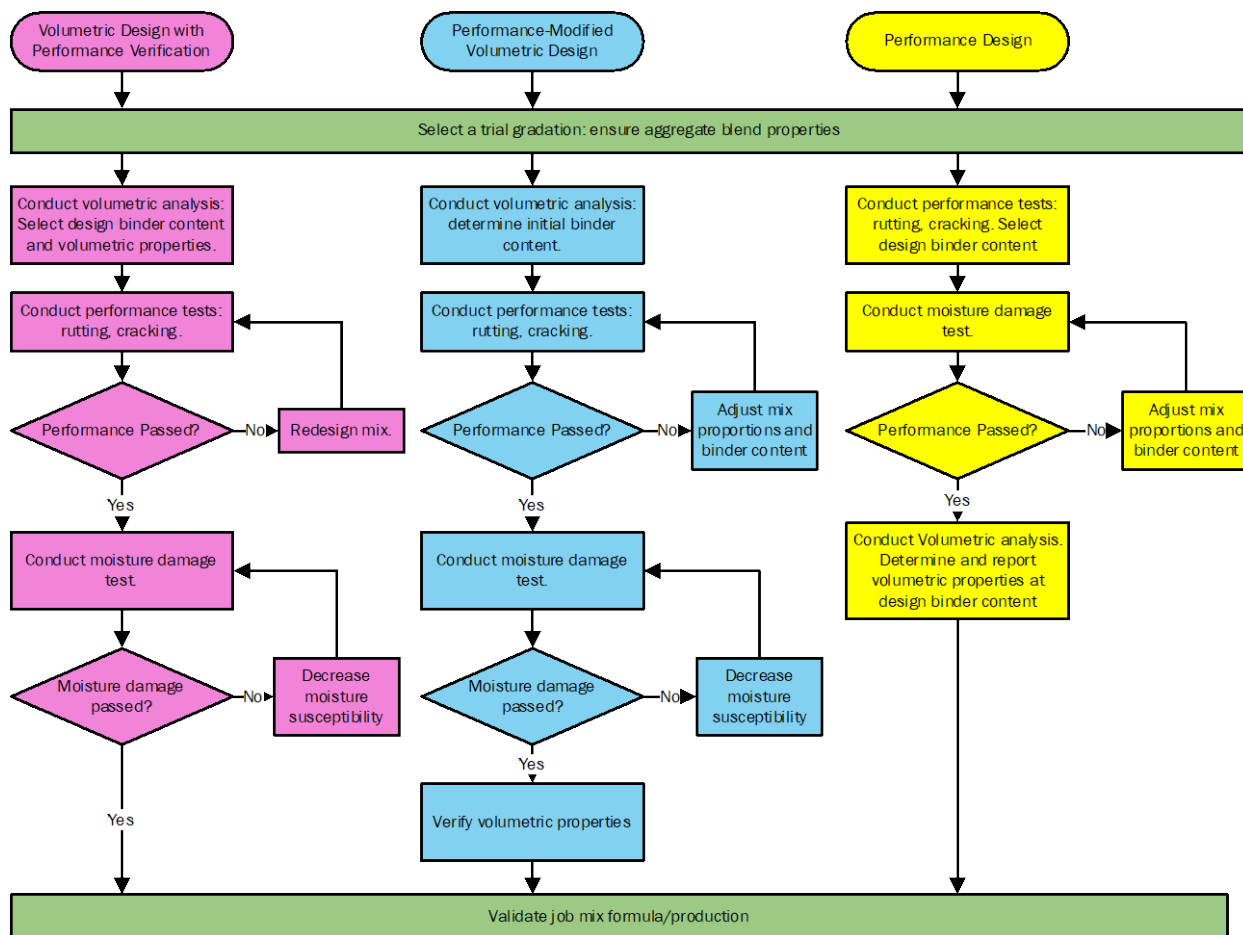
Figure 12. Schematic illustration of three approaches for performance-based mixture design of AC (adapted from NCHRP 20-07(406)).

2.4.1. Volumetric Design with Performance Verification

The volumetric design with performance verification (VDPV) is the application of performance-based mixture design in which both the volumetrics and performance criteria need to be satisfied before the design is considered complete (Figure 12). A mixture that fails the performance part can be improved by adjusting the source or gradation of aggregates or by changing the source or composition of the asphalt binder. VDPV is popular among state DoTs since it supplements the existing volumetrics-based methods. However, once a mixture fails the performance test, then the whole mixtures must be redesigned following the Superpave (i.e., AASHTO R 35). Even so, the redesigned mixture is not guaranteed to meet the performance criteria while still satisfying the Superpave design. As a result, VDPV can sometimes be cumbersome to implement by mixture designers given the constraints.

2.4.2. Performance-Modified Volumetric Design

To address the elaborated constraints issue of VDPV, performance-modified volumetric design (PMVD) was introduced (Figure 12). In this method, the AC mixture is first designed to meet volumetrics criteria per the Superpave method followed by performance criteria checking. Subsequently, if the mixture fails the performance criteria adjustment can be conducted on asphalt content, asphalt source, aggregate gradation, and aggregate source to meet the performance criteria without regard to the volumetric requirements. So, PMVD only relies on volumetrics as a basis to determine the initial asphalt-aggregate combination and then modify the mix to meet performance criteria. The PMVD approach is more flexible and offers a more performance-oriented and practice-friendly version than the VDPV. The most common practice to improve mixture performance with PMVD is to recursively vary the optimum binder content

by $\pm 0.5\%$ until the performance criteria are satisfied. It is noteworthy that, higher asphalt content typically improves fracture resistance and reduces the rutting resistance.

2.4.3. Performance Design

The final form of performance-based mixture design is the performance design (PD) method in which there is an absence or limited consideration of the volumetric requirements at any stage of mixture design. As a result, PD relies solely on performance testing to establish proportions of mixture components. To simplify the PD method, traditional volumetric properties such and V_{air}, VMA, minimum asphalt content, and aggregate gradation are used as recommendations rather than requirements. Before the mixture can be approved as a JMF (job-mix formula) a moisture sensitivity test is performed to ensure the durability of the mix. However, once a mixture design that meets performance and moisture damage criteria has been found, its volumetrics are recorded and used in subsequent projects. From there, if the design mixture needs to be adapted for a new project with a different performance requirement then the mixture serves as the starting point.

CHAPTER III

INVESTIGATION OF SEMICIRCULAR BENDING TEST VARIABLES*

This chapter presents the effort of examining the SCB (semicircular bending) test for assessing fracture performance of asphalt concrete mixtures. After a literature review, the SCB sample preparation, test set-up, and data analysis are presented. The advancement of the test method involved the determination of repeatable and practical testing variables followed by the investigation of SCB testing fixtures on the test results (Table 2).

Table 2. Phases of SCB Test Development with Parameters Investigated in this Chapter

Phase of SCB test development	Parameter investigated
SCB testing variables	Number of replicates
	Specimen thickness
	Notch length
	Loading rate
	Temperature
SCB testing fixtures	Rolling freedom
	The shape of the rolling surface
	Presence of a mid-span jig

3.1. **Introduction**

Among existing fracture tests, the SCB (semicircular bending) test has been attractive due to several reasons such as repeatability, practicality, and simplicity. Although the test has been around since Chong and Kurupu introduced it to simplify testing in rocks materials, it has not readily be implemented in AC mixtures to reliably improve testing parameters and reparability. Also, the effects of testing fixtures have not been investigated toward broader implementation of the test as a fracture performance test.

The semi-circular bending (SCB) test has been attractive in the flexible pavement community (Li and Marasteanu 2009, Shu, Huang et al. 2010, Liu 2011, Aragão and Kim 2012, Biligiri, Said et al. 2012, Zegeye, Le et al. 2012, Kim and Aragão 2013, Im, Ban et al. 2014, Saadeh, Hakimelahi et al. 2014) for its several advantages: (1) easiness and effectiveness in fabricating specimens, (2) suitability for field cores, and (3) repeatability in testing results (Wu, Mohammad et al. 2005, Li and Marasteanu 2009, Aragão and Kim 2012, Im, Kim et al. 2013, Im, Ban et al. 2014). Initially, the SCB test method was proposed by Chong and Kuruppu (1984) because other existing fracture tests based on linear elastic fracture mechanics (LEFM) were expensive and difficult to perform for rock materials. The SCB test has proven to be adequate to evaluate the fracture properties of both laboratories compacted samples and field cores due to simplified specimen preparation (Huang, Shu et al. 2013). Although a specimen for the SCB test has a lower potential fracture area compared to that for the DCT test, the semi-circular geometry enables to test twice as many specimens obtained from field cores or laboratory-compacted samples as compared to the DCT. In addition, the SCB has shown a great potential to characterize mixed-mode fracture behavior of asphalt mixtures by simply adjusting an

inclination angle of the notch and the space between two supports (Im, Ban et al. 2014, Im, Ban et al. 2014).

The SCB test results have shown sufficient testing sensitivities to testing variables such as loading rate, specimen thickness, and testing temperature (Allen, Lutif et al. 2009, Li and Marasteanu 2009, Im, Kim et al. 2013). Previous studies have used testing variables for SCB without a full investigation of their effects on testing results and repeatability (Li and Marasteanu 2009, Shu, Huang et al. 2010, Faruk, Hu et al. 2014) which leads to inconsistent and reduce repeatability of the test results. In addition, it is not clear how many SCB specimens should be tested to reasonably examine fracture behavior or an asphalt concrete mixture. It is necessary to explore the SCB test with testing variables that can improve the repeatability and reliability of the fracture test results.

3.2. **Objectives and Research Methodology**

3.2.1. Testing Variables

Existing SCB tests use testing variables selected subjectively without a full understanding of how the variables affect test results and their repeatability. The objective is to investigate the SCB testing variables for their repeatability and practicality. The variables are the minimum recommended number of replicates (n), the specimen thickness (t), notch length (nl), loading rate (lr), and the testing temperature (T).

To achieve the objective, the methodology shown in Figure 13 was implemented. An extensive literature review was conducted to serve as the starting point to the testing variables which were determined concurrently as follows: first, a reasonably large sample of SCB specimens (e.g., 18) was tested using testing variables from the literature review to determine the

recommended number of replicates for SCB. Second, using the determined number of replicates, SCB test specimens were tested at varying thicknesses (e.g., 25 – 60 mm) to select specimen thickness based on repeatability (i.e., coefficient of variation) and practicality. Third, the determined n and t, several specimens were prepared at different notch lengths (i.e., 0 – 40 mm) to select a nl based on observed repeatability and practicality. The loading rate was also investigated by considering the previously determined testing variables (i.e., n, t, nl) on SCB specimens at different loading rates. The lr was then selected considering practicality and repeatability. Finally, the testing temperature was investigated using pre-determined n, t, nl, and lr at different temperatures.
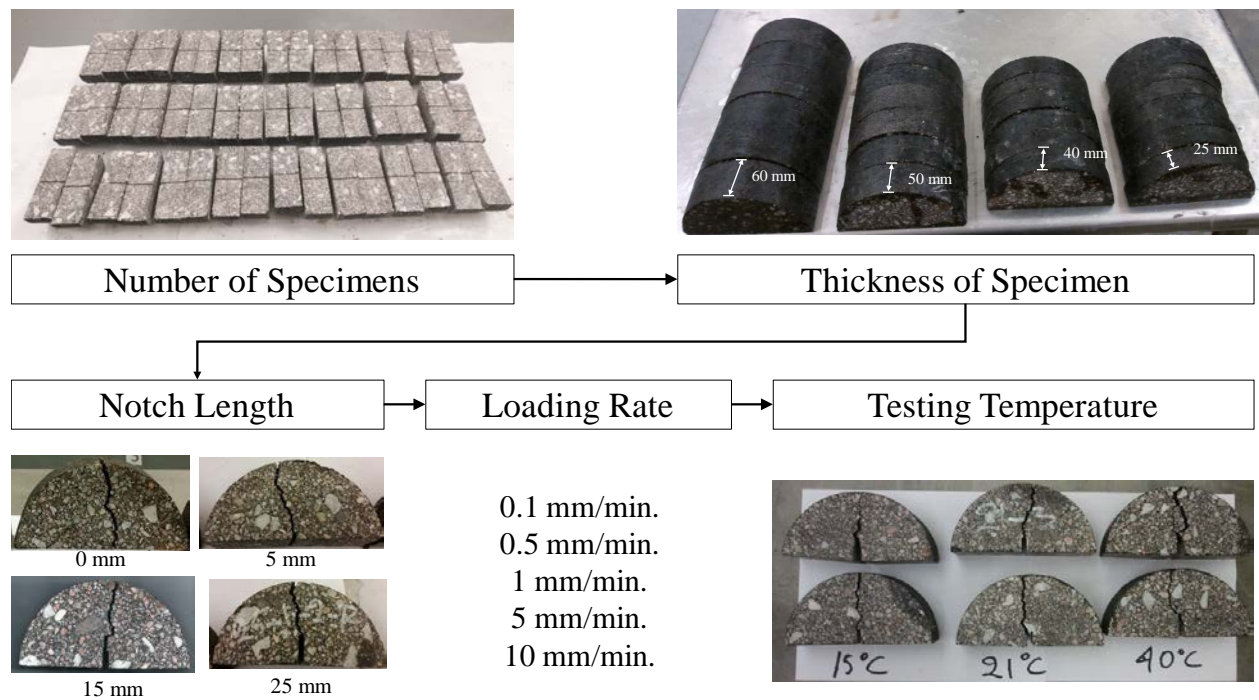
Figure 13 Research methodology for determining the SCB testing variables.

36

3.2.2. Testing Fixtures

Although SCB testing variables are critical in ensuring repeatability of the test results, equally important are the fixtures used in conducting the test. Understanding the effect of load-support fixtures on SCB test results is important towards the wide adoption of the SCB test method by state departments of transportation (DOTs) as a tool for QC/QA. This is because when SCB is widely adopted, it may be performed using readily available load-support fixtures, which may not be identical between laboratories. Consequently, due to the different fixtures, varying SCB results may be obtained despite similar testing variables (e.g., n, t, nl, lr, and T). In addition, repeatability (i.e., COV) of the test results could also be fixture dependent which, if not taken into consideration, may dilute the statistical significance of the results.

A possibility then arises that results from different DOTs or laboratories that used different load-support fixtures cannot be directly compared in a statistically meaningful manner. Thus, to ensure the quality of the results and towards the consistent implementation of the SCB test method, it is necessary to investigate how the different load-support fixtures frequently used for SCB testing influence test results and testing repeatability.

The objectives of the efforts on SCB testing fixtures are:

1) To investigate the effects of load-support fixtures on SCB test results and their repeatability and

2) To determine the effects of predominant SCB testing fixtures on test results (i.e., fracture energy, flexibility index, etc.)

To meet the objectives stated above, six different configurations of SCB load-support fixtures were identified and investigated. All fixtures were assigned to SCB specimens fabricated from the same AC mixture and tested under identical conditions. Consistent sample preparation

was achieved by dedicating a single working day to each sample preparation step (i.e., compaction, cutting, testing). The testing fixtures were selected to include the effects of key fixtures components on the test results. The components were the rolling freedom, the shape of rolling, and the presence of a mid-span jig on test results. Figure 14 presents the nomenclature used to describe each testing fixture.
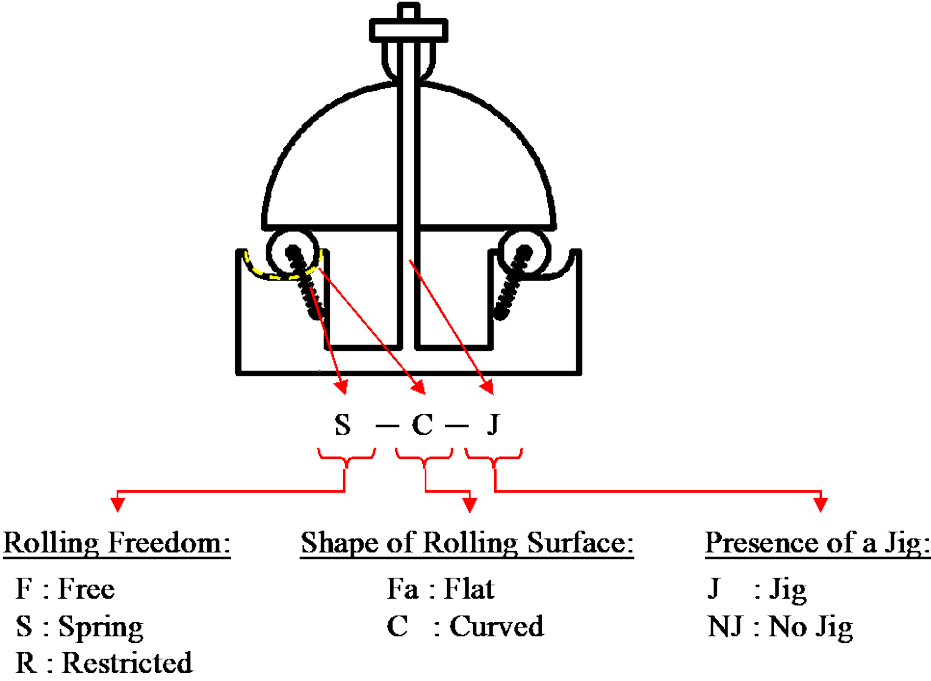
Figure 14. The nomenclature for SCB test fixtures.

3.2.2.1. Configurations of Test Fixtures

As shown in Figure 14, each fixture component is composed of specific descriptions. For example, the rolling freedom component has the following descriptions: free, spring, and restricted. When nothing is inhibiting free rolling the support rollers, the rolling freedom is free (Im, Ban et al. 2014, Nsengiyumva, You et al. 2017). In contrast, if the rollers cannot move

38

horizontally while rotating, the rolling freedom is restricted (Artamendi and Khalid 2006, Mahmoud, Saadeh et al. 2014, Fakhri and Ahmadi 2017). Finally, if a spring was used to retain the rollers from straying too far from initial positions then the rolling freedom is named spring. It is noteworthy that the roller springs had a typical spring constant of 0.12 N/mm used load-supporting fixtures for SCB (Nsengiyumva, Haghshenas et al. 2020).

The shape of the rolling surface haves two descriptions: flat or curved which, simply describes the shape on which the support rollers are placed and rolling. Both flat and curved shapes have been used by several studies without insight on how these surfaces affect the results. The last fixture component was the middle span jig and which have been implemented on commercial SCB testing load frames such as Auto_SCB™ that several SHAs have acquired. It is, therefore, necessary to understand the effects of the presence of the jig on test results before being deployed.
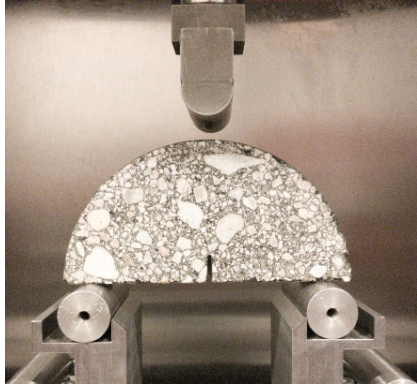
F-Fa-NJ (Im, Ban et al. 2014, Nsengiyumva,
You et al. 2017)
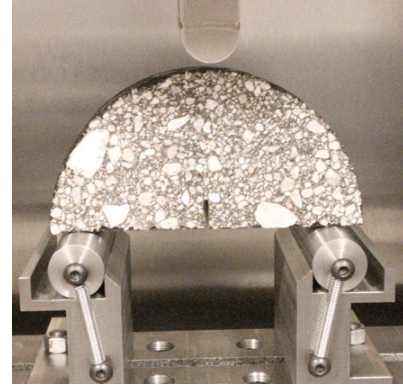
S-Fa-NJ

F-C-J
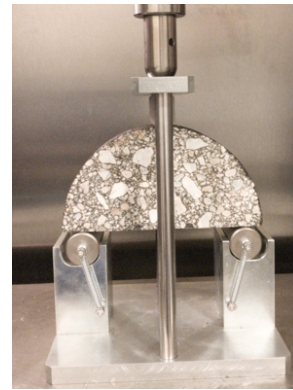
S-C-J

S-C-NJ
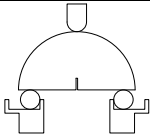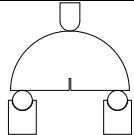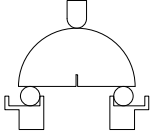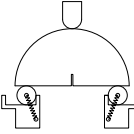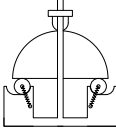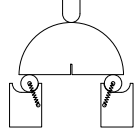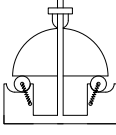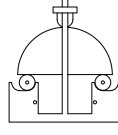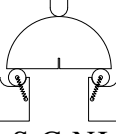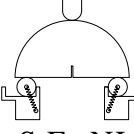
R-C-NJ (Artamendi and Khalid 2006,
Mahmoud, Saadeh et al. 2014, Fakhri and
Ahmadi 2017)

Figure 15. Configurations of investigated SCB load-support fixtures.

3.2.2.2. Pairwise Comparison of Fixtures

Six testing configurations selected for fixture study effort are shown in Figure 15. Fixtures were selected to provide helpful insight on how each component affects the SCB test results by using a simple comparison. For example, comparing F-C-J with S-C-J, one can deduce the effect of having a roller spring on a curved rolling surface. Similarly comparing results from S-Fa-NJ with F-Fa-NJ one can also infer the effect of roller springs on a flat rolling surface. A complete comparison process to extract the effect of each component is shown in Table 3.

Table 3. Comparison Process to Extract the Effect of Fixtures Components

Fixtures comparison			Comparison result
F-Fa-NJ	vs. R-C-NJ	→	Effect of free rolling at support
F-Fa-NJ	vs. S-Fa-NJ	→	Effect of roller springs on a flat rolling surface
S-C-J	vs. S-C-NJ	→	Effect of mid-span jig
S-C-J	vs. F-C-J	→	Effect of roller springs on a curved rolling surface
S-C-NJ	vs. S-Fa-NJ	→	Effect of rolling surface shape

All tests in Table 3 were performed using identical testing conditions. Data were analyzed to determine several fracture-related indicators, and the coefficient of variation (COV) values were calculated to examine testing repeatability. Results were interpreted to characterize the contribution of individual fixture components to the variability (or repeatability) of test results.

3.2.2.3. Assigning Specimen to Fixtures

The process of fabrication of SCB specimens involves compaction of a 170 mm tall and 150 mm diameter AC samples by the Superpave Gyratory Compactor (SGC). Previous studies (Chehab 2002, Ozer, Al-Qadi et al. 2017) have demonstrated the existence of non-uniform air void distribution within the SGC compacted tall samples with the relatively higher air void content located towards the outer surface of the sample. Thus, even though the bulk air voids of tall specimens were measured, different levels of air could be introduced into specific areas of each tall sample (Chehab 2002) which would contribute to sample-to-sample variability. To reduce the inevitable location-specific variability and improve the distribution of specimens, the scheme shown in Figure 16 was implemented when assigning specimens to the testing fixtures. In addition, higher air void containing top and bottom 10 mm disks were trimmed and discarded from tall SGC samples before proceeding with fabrication of SCB specimens.
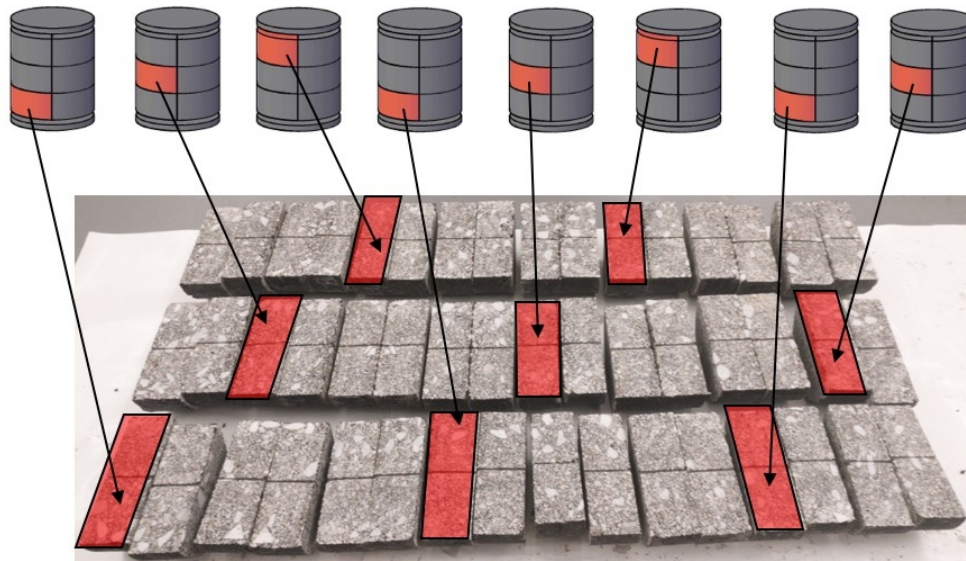
Figure 16. Scheme to reduce location-specific variability of SCB testing specimens.

3.3. **Materials**

A typical Nebraska mixture called SPH was selected for the SCB test method development. The mixture is mainly used on important roads (e.g., interstate) as it is of high quality with better grade binder and a better source of aggregates. This mixture is widely used in Nebraska highways with high traffic flow rate and consists of 32% recycled asphalt pavement (RAP) and PG 64-34 binder with a warm mix asphalt additive (i.e., Evotherm). The aggregate gradation of the mixture and the corresponding blending proportions are shown in Table 4. The total binder content, which includes recycled binder from RAP, was 5.20% of the total mixture weight, which included 0.7% of Evotherm by the weight of asphalt cement. The aggregates blend was of four different sources with the overall nominal maximum aggregate size of 12.5 mm.

Table 4. Aggregate Gradation and Properties

Aggregate	%	Aggregate Gradation (% Passing on Each Sieve)									Binder PG 64-34
		19mm	12.5mm	9.5mm	#4	#8	#16	#30	#50	#200	
¾" CHIPS	10	100	60	18	2.0	2.0	1.0	1.0	1.0	1.0	
CR. Gravel	53	100	100	100	92.7	73	45.2	29.1	16.2	6.3	
2A Gravel	5	100	95.4	90.9	68	27.3	8.6	3.5	1.1	0.2	5.2%
Millings	32	100	94	90	68	41	29	23	19	8	
Combined	100	100	93.9	88.1	74.5	53.4	33.8	23.1	14.8	6	

Aggregate Properties					
FAA	CAA	SE	F&E	D/B	G_{sb}
45	99/96	79	0.1	1.18	2.585

FAA: Fine aggregates angularity; CAA: Coarse aggregates angularity; SE: Sand equivalent
F&E: Flat and elongated particles; D/B: Dust to Binder Ratio; G_{sb}: Bulk specific gravity.

3.4. SCB Sample Fabrication

The mixture sample was collected just as the truck was leaving the plant heading to the paving area(Figure 17(a)) and transported to the testing laboratory in sealed containers to avoid undesired aging due to oxidation before sample fabrication (Figure 17(b)). To fabricate SCB specimens, the AC mixture was heated at the recommended compaction temperature of 150°C for two hours. The two hours of oven heating the collected AC mixtures served a dual purpose of increasing workability and allowing for short-time aging of the mixture. The short-term aging corresponds to the duration of mixture transportation from the plant to the construction field. During the oven short-term aging, the mixture is intermittently disturbed (e.g., every 30 minutes) using a spatula to ensure homogenous heating throughout. Besides compaction/mixing and aging, the oven heating serves to increase the workability of mixtures before compaction.

44

(a)   (b)

Figure 17. Mixture collection: (a) from a mixture delivery truck and (b) containers of mixtures.

The loose mixture was compacted into a cylindrical tall sample of 170 mm in height and 150 mm in diameter (Figure 18(a)) targeting air voids of $4 \pm 0.5\%$. Next, the compacted samples are sliced into discs with a given thickness after discarding the top and bottom 10 mm discs of the sample (Figure 18(b)). Subsequently, the discs are cut in half into semi-circulars (Figure 18(c)) onto which a notch is inserted (Figure 18(d)). Water was used during the fabrication process to cool down the specimens and help neutralize dust generated during the cutting/slicing. Finally, SCB specimens are left to dry at room temperature in front of a fan for 24 hours.

(a)   (b)   (c)   (d)
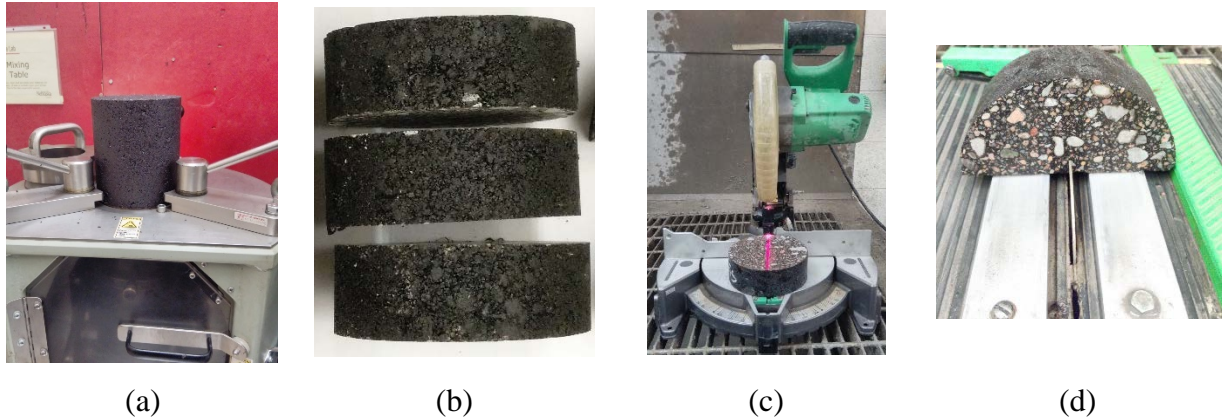
Figure 18. SCB sample preparation: (a) compaction by SGC, (b) slicing, (c) halving and (d) notching.

3.5. **SCB Test Set up and Data Analysis**

Figure 19(a) shows the set-up of the SCB test method, which is composed of the prepared specimen on a three-point bending fixture. The specimen is loaded monotonically from the top-center by controlling the LPD (load-point displacement). Throughout this study, the span length for all specimens was selected as 120 millimeters (i.e., 0.8 diameters). It is noteworthy that the purpose of the notch is to initiate fracture since the main objective of the SCB test is to characterize crack propagation rather than crack initiation. The post-test Figure 19(b) shows a full propagated fracture profile. The location and inclination of the notch, relative to the bottom of the specimen, dictate the mode of fracture experienced by the specimen. In this study, mode I was investigates in all cases thus the notch was centered in the middle of the specimen and perpendicular to the horizontal profile. Mode I fracture, which is the focus of this study, results in fracture profiles parallel to the notch Figure 19(b).

(a)   (b)
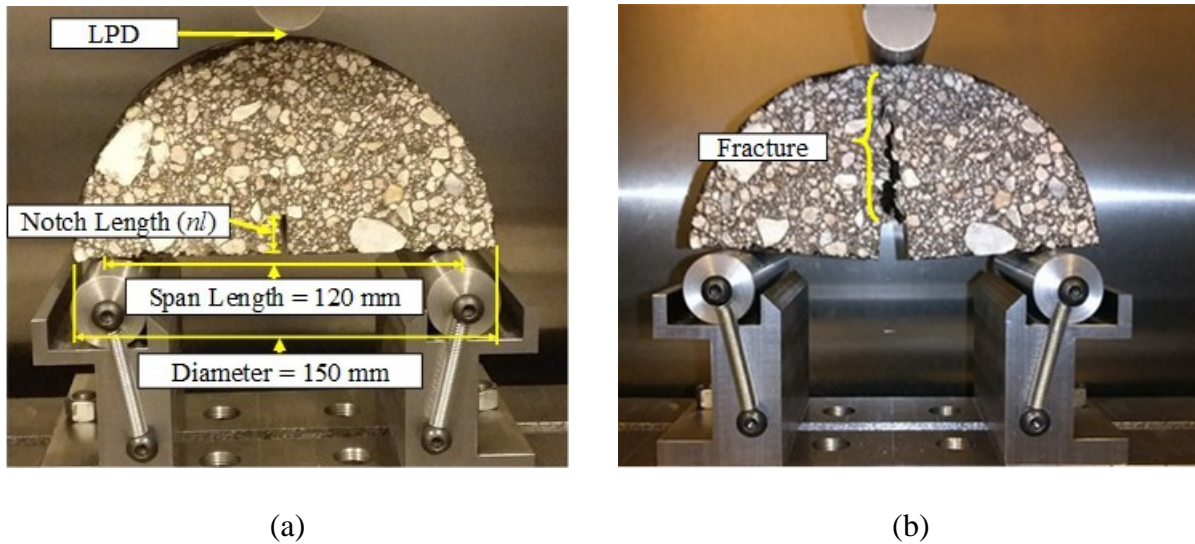
Figure 19. SCB fracture test: (a) test set-up and (b) fracture after SCB testing.

During the test, the load and the displacement at load-point (LPD) are measured and recorded by the data acquisition system. Specifically, this study used a UTM-25kN load machine fitted with a 25kN load cell, an environmental chamber capable of -16°C to 60°C and a computer-controlled CDAS (central data acquisition system).

Typical SCB test results are shown in Figure 20 with applied data analysis. Work (W) is defined as the area underneath the load-LPD curve calculated by numerically integrating a fitted function to the results (Figure 20). All SCB data fitted with eight Gaussian functions (Dowdy, Wearden et al. 2011), which allowed calculations of curve-derived variables such as the maximum load (i.e., peak load or P_{max}), pre-peak (m_1) and post-peak (m_2) slopes and critical displacement. It's noteworthy that the post-peak slope (m_2) is calculated at post-peak the inflection point of the fitted function which was numerically differentiated to find a curvature change point.
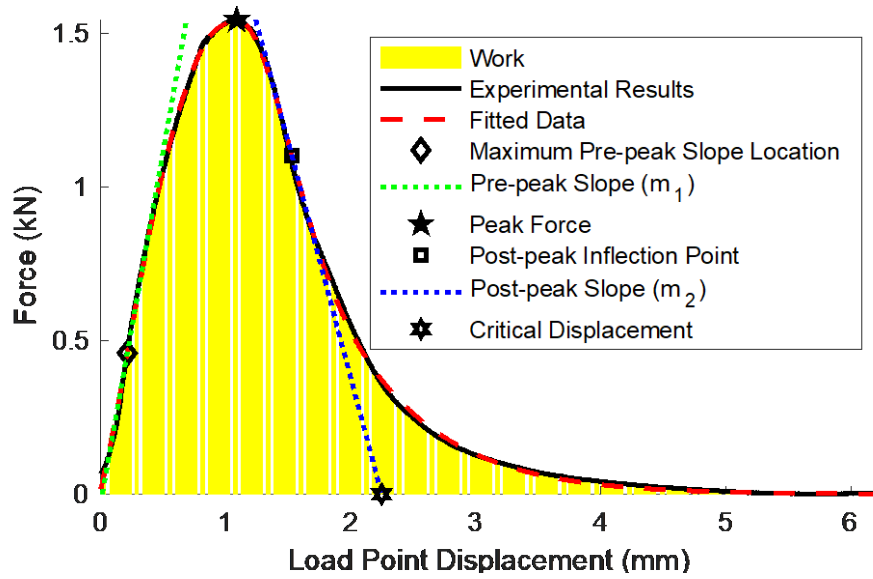
Figure 20. SCB test results and analysis.

From the test results in Figure 20, several fracture-related indicators such as Fracture

energy (G_f) is calculated per (3.1) by normalizing work (W) to the ligament area (A_{lig}).

$$G_f = \frac{W}{A_{lig}} \tag{3.1}$$

where $A_{lig} = t \times (R - nl)$ and t, R, and *nl* are the specimen thickness, radius, and the notch length.

The flexibility index developed by Ozer, Al-Qadi et al. (2017) can also be calculated

from the test results using the equation (3.2) as such:

$$FI = \frac{G_f}{|m_2|} \times 10 \tag{3.2}$$

where G_f is expressed in kJ/m^2 and the post-peak slope at the inflection point, m_2, is expressed in

kN/mm. As the above equation indicates, FI considers the speed at which damage occurs by

incorporating the post-peak (m_2) slope. It is noteworthy that during the SCB testing, damage due to cracking occurs immediately after the maximum load and is characterized by a continuous reduction of the load-bearing capacity of the specimen as the crack propagates until complete failure.

The cracking resistance index recently developed by Kaseer, Yin et al. (2018) as another fracture-related indicator can be calculated from SCB results per equation (3.3):

$$CRI = \frac{G_f}{P_{max}} \tag{3.3}$$

It is noteworthy that fracture energy is the basis of all fracture-related indicators, as such, its repeatability propagates the other indicators.

3.6. **Results and Discussions**

3.6.1. Testing Variables

3.6.1.1. Recommended Minimum Number of Replicates

Using the testing variables found in the literature, 18 specimens (Figure 21)were prepared and tested at $t = 50$ mm, $nl = 15$ mm, $lr = 1$ mm/min, and $T = 21°C$ (Duan, Hu et al. 2003, Li and Marasteanu 2009, European Committee for Standardization 2010, Biligiri, Said et al. 2012, Im, Kim et al. 2013). By testing a large enough sample size, the inference of the recommended minimum number of replicates could be made with reasonably good accuracy. Due to the heterogeneous nature of AC mixtures, the number of replicates is critical in ensuring the reliability of test results. As such, the first effort of the SCB test development effort was to find the necessary number of replicates within a statistical significance.
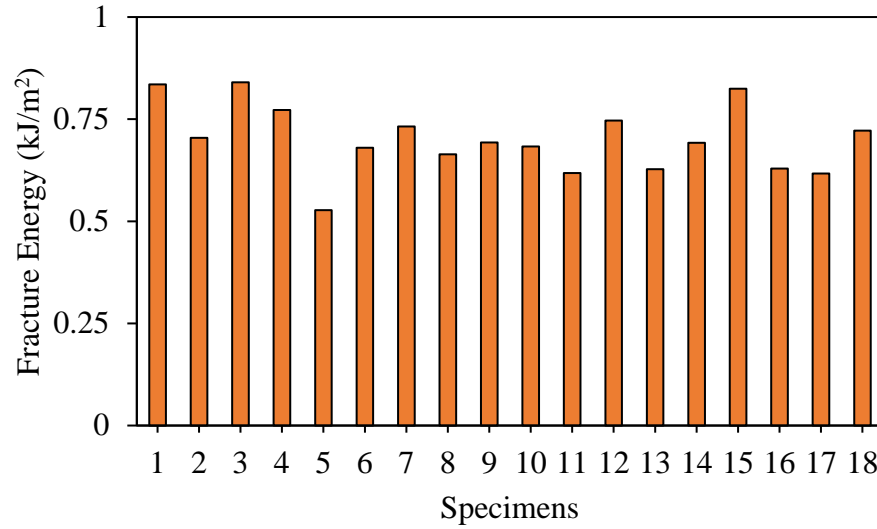
Figure 21 Test results for the sample used to determine the recommended minimum number of replicates.

The recommended minimum number of replicates was calculated using the equation (3.4) which assumes a normal distribution of the results (Dowdy, Wearden et al. 2011).

$$n = \left[\frac{Z_{\alpha/2} \times \sigma}{E} \right]^2 \tag{3.4}$$

where E is the margin of error, $Z_{\alpha/2}$ is the standard normal deviate at a given probability level α (e.g., 5% in this study), and σ is the sample standard deviation. The margin of error is simply the difference between the observed sample mean ($\bar{y}$) and the true value of the population mean (μ) and is calculated as $E = \bar{y} - \mu$.

Due to that equation (3.4) assumes a normal distribution of the sample data, a normality check of the G_f from the 18 specimens was conducted following (Razali and Wah 2011,

Machiwal and Jha 2012).The normality test is also commonly known as the Lilliefors test (Abdi and Molin 2007).
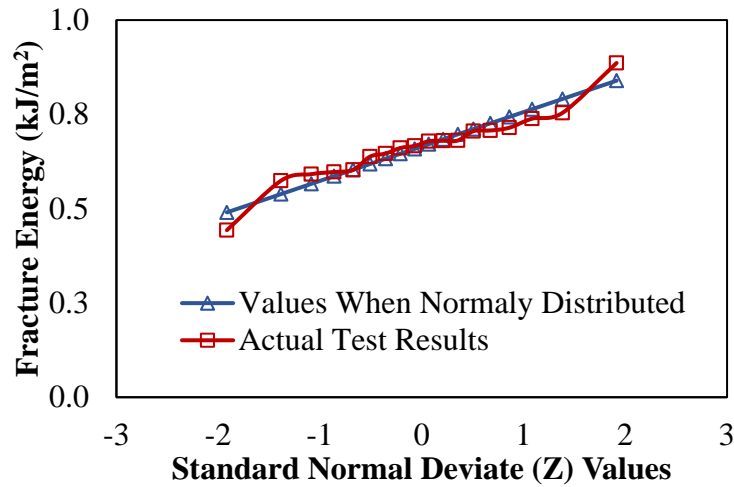
Figure 22. Normality check of the sample.

Figure 22 shows the test results as compared to results from a normal distribution of the same standard deviation and mean. It is noteworthy that the mean and the standard deviation are sufficient to describe a normal distribution. Both data sets, the actual and the normal values, were statistically compared using the Chi-square to check similarity within a 95% confidence level (i.e., α =5%). The analysis results showed that the data sets were not significantly different at α =5% (i.e., $0.016 \leq \chi^2 \leq 27.587$).
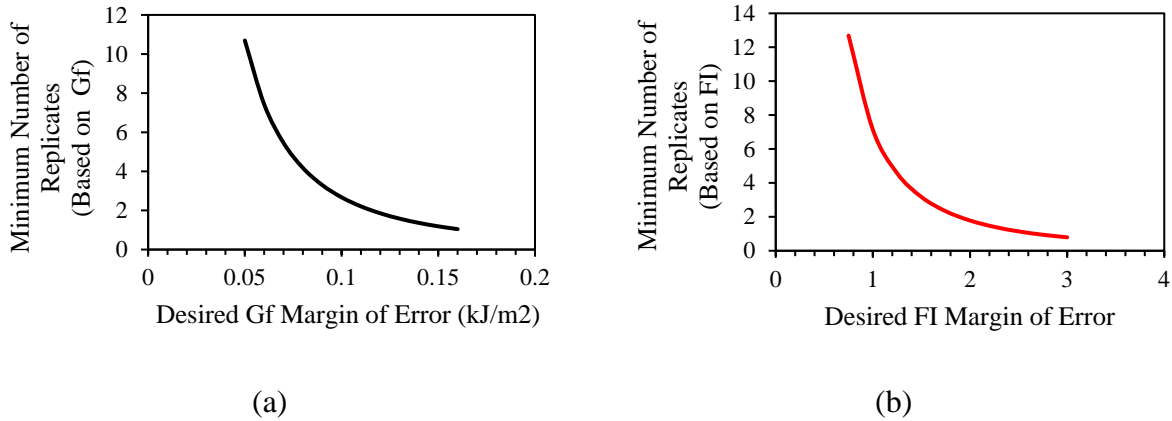
Figure 23. The minimum number of replicates versus the desired margin of error: (a) based on fracture energy, Gf, and (b) based on the flexibility index, FI.

As a result, test fracture energy of the 18 specimens was taken to be of a normal distribution which allowed the use of the equation (3.4) to determine the recommended number of replicates. Figure 23 shows the different recommended minimum numbers of replicates per the margin of errors of both G_f (Figure 23(a)) and FI (Figure 23(b)). The probability level α was 5% which corresponded to $Z_{\alpha/2} = 1.96$. The average and the standard deviation for G_f calculated were 0.7 kJ/m² and 0.0834 kJ/m², respectively. To determine the recommended n, a margin of error (E) equal to 0.07 kJ/m², which is 10% of the average G_f, was selected as a threshold to calculated the minimum recommended number of replicates $n \approx 5.34$. Therefore, a minimum of five to six replicates is recommended when conducting the SCB test.

3.6.1.2. Thickness

Based on previous studies that have highlighted that the thickness of the specimen affects the fracture response this study investigated four practical thicknesses 30, 40, 50, and 60 mm were investigated. Six specimens per each thickness were prepared are recommended from the

previous section. Other testing variables were reasonably selected based on literature reviews as such notch length = 15 mm (Li and Marasteanu 2009, European Committee for Standardization 2010), loading rate = 1 mm/min. (Biligiri, Said et al. 2012, Im, Kim et al. 2013), and temperature = 21°C (Kim and Aragão 2013, Im, Ban et al. 2014). Figure 24 shows the SCB test results at the different thicknesses in which the maximum load increased with thicknesses.
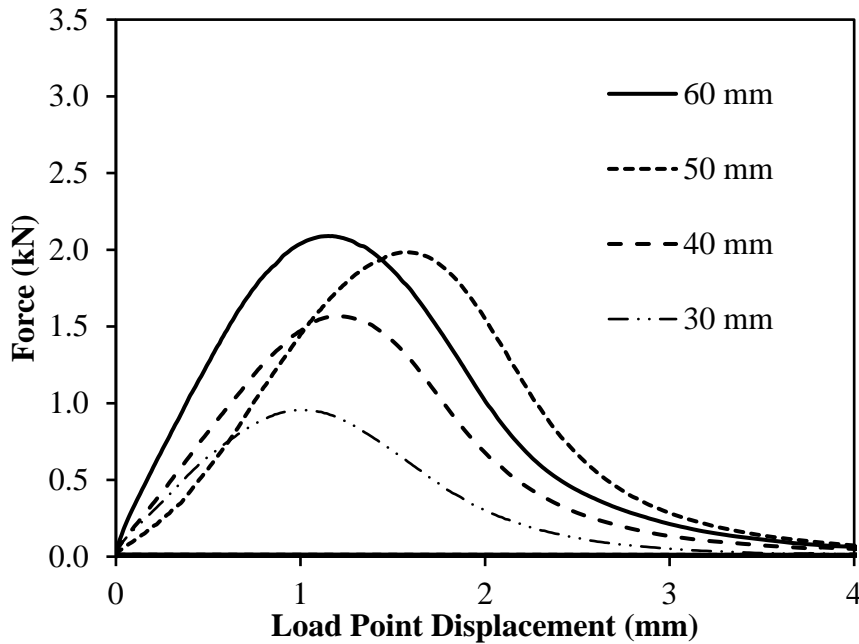
Figure 24. SCB test results at different thicknesses.

Analysis of the results in Figure 24 is shown in Figure 25 where the fracture energy and the flexibility index were calculated along with their corresponding COVs (coefficient of variation). It noteworthy that COV is the standard deviation normalized to mean (Dowdy, Wearden et al. 2011). The analysis results showed that G_f initially increased with thickness up until 50 mm beyond which it reduced (Figure 25(a)). In addition, COV results show that increasing thickness benefitted repeatability. However, beyond 40 mm thickness, the improvement in repeatability was minimal.
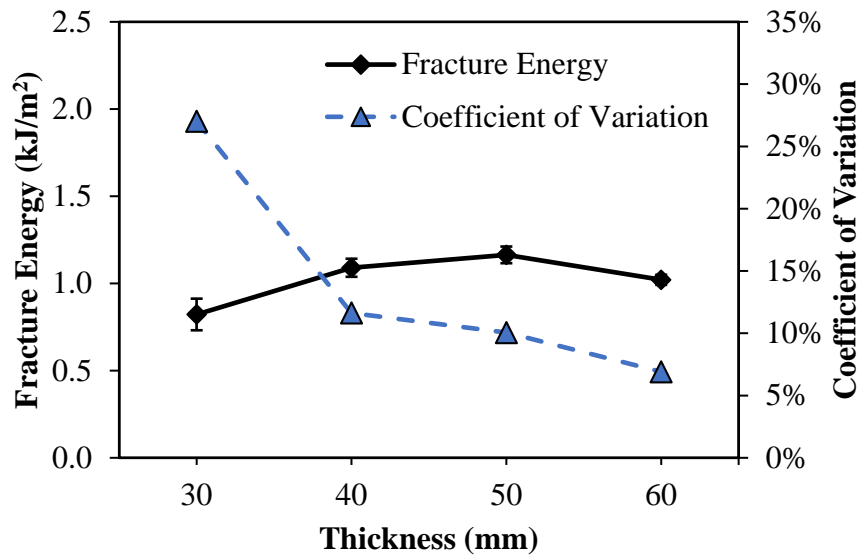
(a)
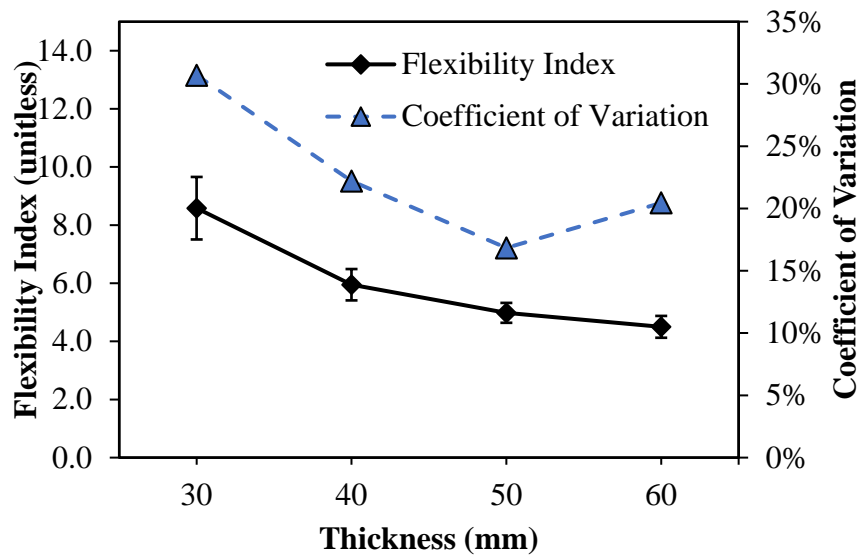
(b)

Figure 25. Effect of specimen thickness on test results and their repeatability: (a) fracture energy and (b) flexibility index.

The analysis also indicates that FI values are reduced with increasing thickness until 50 mm (Figure 25(a)). Beyond 50 mm, the FI continued to decrease, however, its COV increased.

This indicates that a thickness of 50 mm provides the optimal repeatability of both G_f and FI when conducting the SCB test. Therefore, a thickness of 50 mm was recommended and selected for the next steps based on the overall low COV of both G_f and FI. The thickness of 50 mm agrees well with the previous studies by Brühwiler, Wang et al. (1990), Wittmann and Zhong (1996) indicating that the thickness of AC specimens should be at least four times larger (i.e., 12.5 mm ×4 = 50 mm) than NMAS size (12.5 mm in this study).

3.6.1.3. Notch Length

As stated before, the purpose of a notch in SCB is to allow for controlled crack initiation which then propagates during testing. To investigate the effect of notch lengths on the SCB test results, specimens were prepared using four different notch lengths of 5, 15, 25, 40 mm, and one notch-less case (i.e. 0 mm). The testing variables used included the already determined n = 6 and t = 50 mm. The remaining variables were selected based on the literature review as such the loading rate = 1 mm/min. (Biligiri, Said et al. 2012, Im, Kim et al. 2013), and temperature = 21°C (Kim and Aragão 2013, Im, Ban et al. 2014). Figure 26 shows the average (from six replicates) load-displacement results from all the notch length cases investigates. It is observed that the maximum load (P_{max}) increased with reducing notch length which is reasonable since a smaller notch allows for more ligament area thus more load-resisting materials resulting in increased force at a given LPD. The results curves also show that the displacement at which the maximum load occurs increased (i.e., shifted to the right) with reducing notch length.
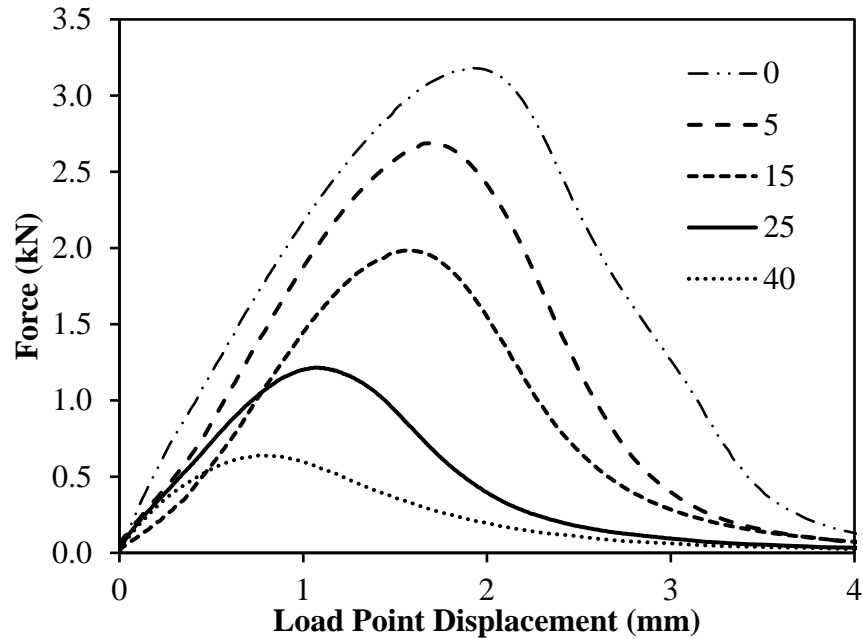
Figure 26. Effect of notch length on test results and their repeatability: (a) fracture energy and (b) flexibility index.

Figure 27 shows the analysis of test results (from Figure 26) at varying notch lengths. The results show that the fracture energy (G_f) generally decreased with increasing notch length with the sharpest drop happening for notches longer than 15 mm. An interesting observation is that the notch length of 5 and 15 mm produced virtually similar G_f values. However, the COV results show that the 5 mm notch had the lowest value of approximately 10%, while the remaining notches had similar values of approximately 15% (Figure 27(a)).
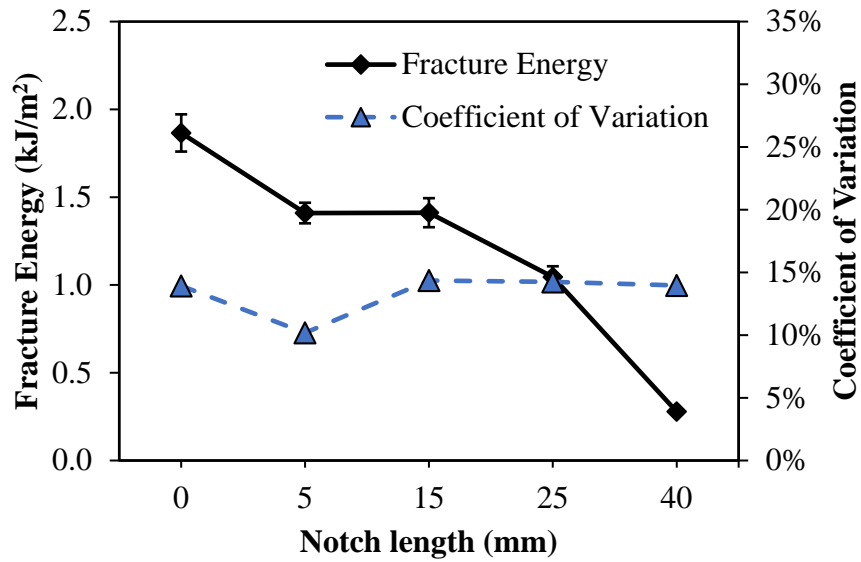
(a)
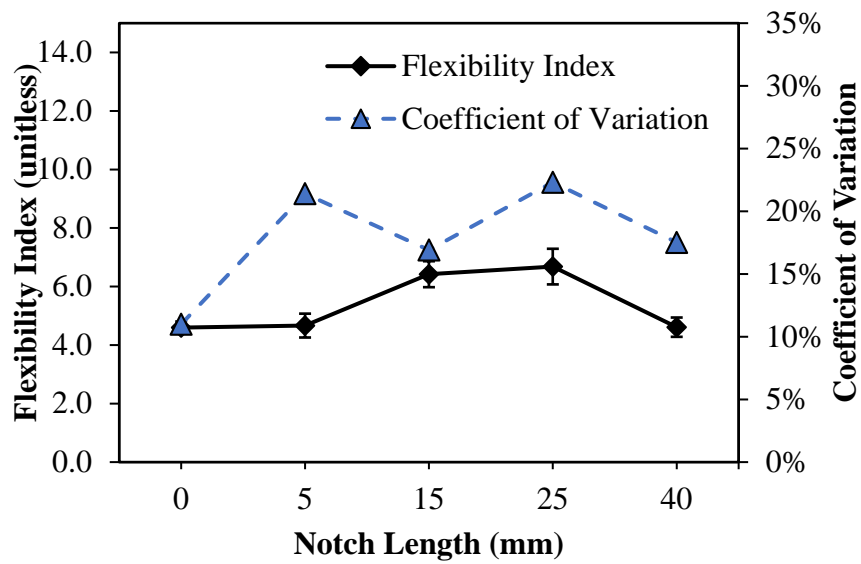
(b)

Figure 27.Effect of notch length on test results and their repeatability: (a) fracture energy and (b) flexibility index.

The effects of notch length on the FI results and their repeatability in terms of COV are shown in Figure 27(b). Unlike for G_f, the FI results remained relatively similar at the different notch lengths, suggesting reduced sensitivity of FI to the notch variation when compared to G_f.

Therefore, in the case where notch length manufacturing is an issue, FI would yield more consistent results. However, as seen in the same figure, the COV of FI at the notch lengths generally higher than for COV of G_f. The lowest COV of FI can be found on notch-less (i.e., 0 mm) specimens while the highest is found on 25 mm long notches. Notch-less specimens are undesired since they produce off-centered cracks that are not consistent with the mode-I fracture (Figure 28). With consideration of the respective repeatabilities of both G_f and FI, the notch length of 15 mm was selected for the next steps.

Figure 28. Off-center crack initiation for notch-less SCB specimens.

3.6.1.4. Loading Rate

The loading rate has fundamental effects on the fracture behavior of asphalt concrete mixtures because of viscoelastic deformation characteristics of asphaltic materials as demonstrated by many studies. (Kim and Aragão 2013, Im, Ban et al. 2014). Four loading rates of 0.1, 0.5, 1, 5, and 10 mm were investigated. The testing parameters included the determined number of replicates, $n=6$, specimen thickness, $t=50$ mm, and notch length, $nl=15$ mm. The testing temperature, T, was selected as 21°C based on the literature (Kim and Aragão 2013, Im, Ban et

al. 2014). Figure 29 shows test results at the different loading rates in which faster rates produced

higher load from the SCB specimens. Since AC mixtures are considered to be viscoelastic

(Monismith and Secor 1962, Park, Kim et al. 1996, Kim, Lee et al. 1997, Song, Paulino et al.

2006), an increase in the rate of loading thus strain rate resulted in higher stress response in

mixtures due to viscosity (Wineman and Rajagopal 2000). The higher stress in the specimen then

translated into higher reaction maximum forces (P_{max}) with increasing loading rate as reflected in

Figure 29.
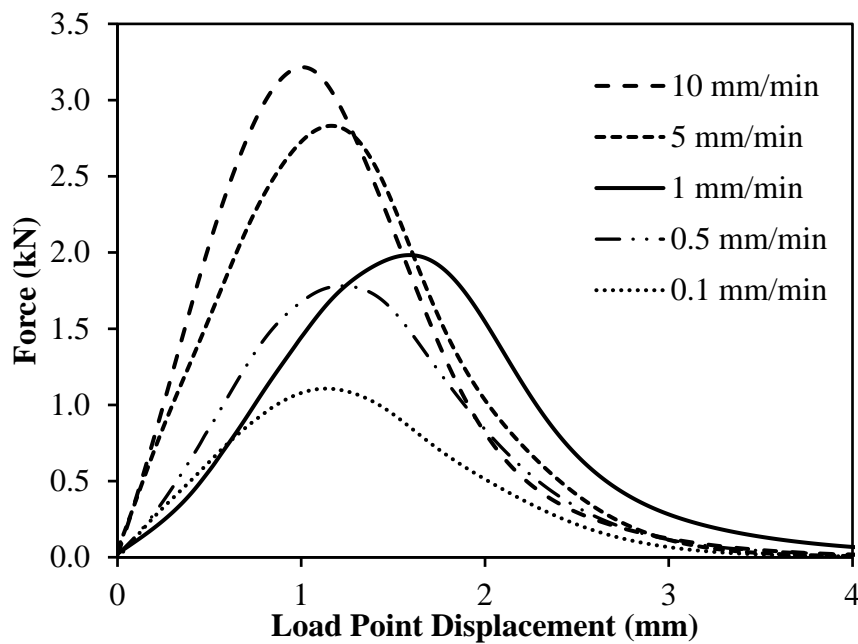
Figure 29. SCB test results at different loading rates.

Analysis of the results at different loading rates is shown in Figure 30. Figure 30 (a)

indicates that G_f continually increased with increasing loading rate which is reasonable since

the load-displacement curves presented in Figure 29 show that the area underneath the curve

(i.e., fracture work) increased with the loading rate. Since all specimens were prepared with the

59

same notch length and thus the same ligament area, G_f followed the same trend as the fracture work. The repeatability results of G_f show initial low COVs at the slower loading rates (i.e., 0.1 and 0.5 mm/min) followed by an increase at higher rates (i.e., 1, 5, and 10 mm/min) to saturate at the loading rate of 5mm/min.

Figure 30(b) shows the results of FI and its repeatability at different loading rates. The FI results were minimally affected by the loading rates up until 5 mm/min rate, beyond which the FI dropped by almost 50% (halved). The reduced sensitivity of the FI over the wide range (i.e., 0.1 to 5 mm/min) suggests that FI results from this range can directly be compared with each other. The suggestion warrants further investigation, which is out of the scope of this study. COV of FI varied with loading rate with the rates of 0.1 and 5 mm/min having the lowest values. It should be noted that beyond 5 mm/min, FI COV seemed to start increasing and would likely keep increasing. As aforementioned, with increasing loading rate asphalt mixtures become stiffer and therefore more brittle. Brittle specimens break suddenly and make it difficult to obtain the post-peak slope (m_2) needed to calculate FI and thus increase in variability (i.e., COV).

The SCB loading rate has minimal effect on FI results and linearly increase with G_f. The COV of FI is more sensitive to varying loading rates compared to COV of G_f. Although a slow loading rate (e.g., 0.1 mm/min) yields repeatable results, it significantly reduces practicality due to the considerable increase in testing time. As a result, loading rates between 1-5 mm/min are recommended mainly because within the range, COV of G_f and FI varied only within 10% to 15%. A COV of G_f lower than 25% is considered indicative of satisfactory repeatability (Li and Marasteanu 2010).
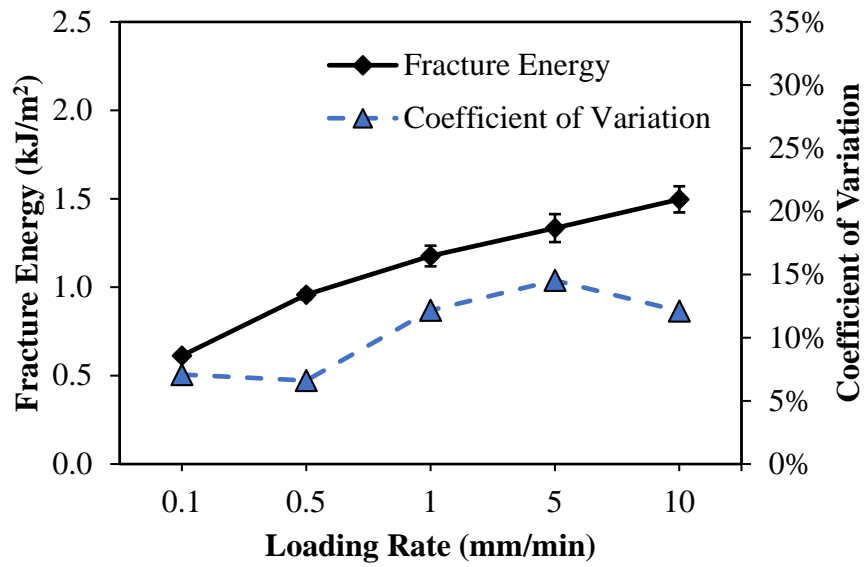
(a)
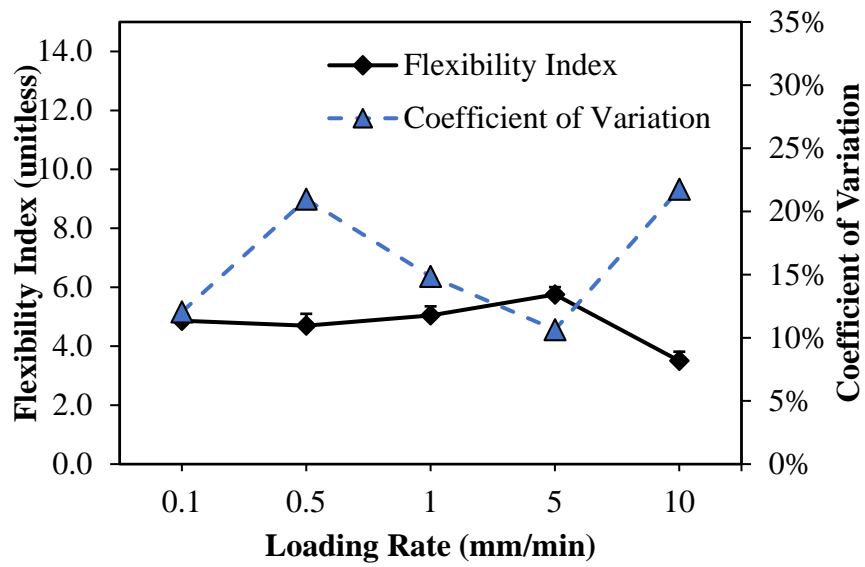
(b)

Figure 30. Effect of loading rate on test results and their repeatability: (a) fracture energy and (b) flexibility index.

3.6.1.5. Temperature

It is widely documented that AC is highly temperature-dependent due to the viscoelastic nature of the asphalt binder (Marasteanu, Li et al. 2004, Im, Kim et al. 2013). Following, the next effort was to characterize the temperature effect on the repeatability of the test results, particularly for characterizing the fatigue-type cracking potential of mixtures. Three different temperatures such as 15, 21, and 40°C were attempted to investigate their effect on the fracture energy, G_f, and flexibility index FI. Beyond the temperatures, other testing variables were selected to match already determined recommended values. Specifically, the number of replicates, $n = 6$, the thickness of the specimens, $t = 50$ mm, the notch length, $nl = 15$ mm, and the loading rate, $lr = 5$ mm/min.

Figure 31 shows the SCB test results of the different temperature where the maximum load (P_{max}) increased with decreasing temperature. As aforementioned, AC mixtures are viscoelastic, and as such, they are time and temperature-dependent. The low temperature resulted in stiffer mixtures manifested as a higher P_{max} and pre-peak slope (m_1). Conversely, increased temperature resulted in soft, more compliant mixtures which reduced the m_1 and m_1. Comparing Figure 29 and Figure 31, it becomes apparent that increasing temperature has a similar effect as lowering the loading rate. This is a core characteristic of viscoelastic materials that allow time-temperature superposition depending on the rheological classification (e.g., simple or complex) of the material (Wineman and Rajagopal 2000).
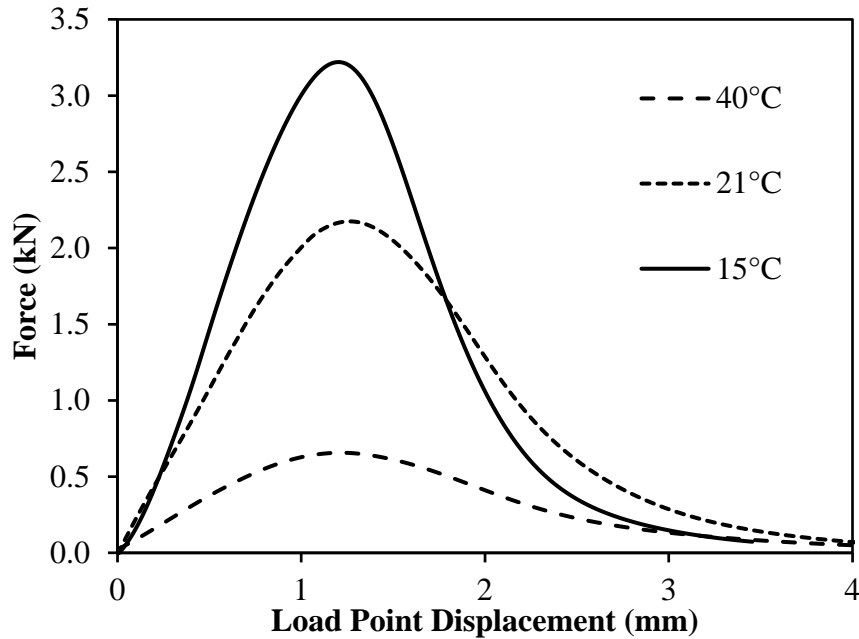
Figure 31. SCB test results at different temperatures.

Results analysis is shown in Figure 32 for the three temperatures cases. Generally, fracture energy-reduced with increasing temperature which is reasonable since the area underneath the curve (Figure 31) decreased with temperature (T) increase. However, the decrease of G_f with increasing T was less pronounced between 15°C and 21°C compared to between 21°C and 40°C. Continually increasing temperature would eventually result in a too soft mixture that would collapse at the slightest application of force and thus untestable. As a result, rutting (permanent deformation) is the main type of failure of interest at high temperatures. For the fracture testing in AC mixtures, high temperatures are usually avoided due to the increased compliance which dilutes results.

Repeatability of G_f in terms of COV (Figure 32(a)) shows an initial increase until 21°C followed by saturation. As the higher temperature increased, the compliance of mixtures also

increased resulted in higher variability (i.e., COV) of G_f. Higher temperatures increase the possibility of that the main failure phenomenon is in from of deformation rather than fracture. However, it is noteworthy that within the temperature range tested COV of G_f remained significantly lower than 25% considered to be a threshold of good repeatability in SCB G_f results (Li and Marasteanu 2010).

The effect of temperature on FI is presented in (Figure 32 (b)) where the FI increased with increasing temperature. This is reasonable since FI is obtained by dividing the G_f to the post-peak slope. As can be seen in Figure 28, higher temperature SCB test results produce more compliant post-peak slope (m_2). Apparently, although G_f reduces with increasing temperature, the post-peak effect is dominant in the calculation of FI.
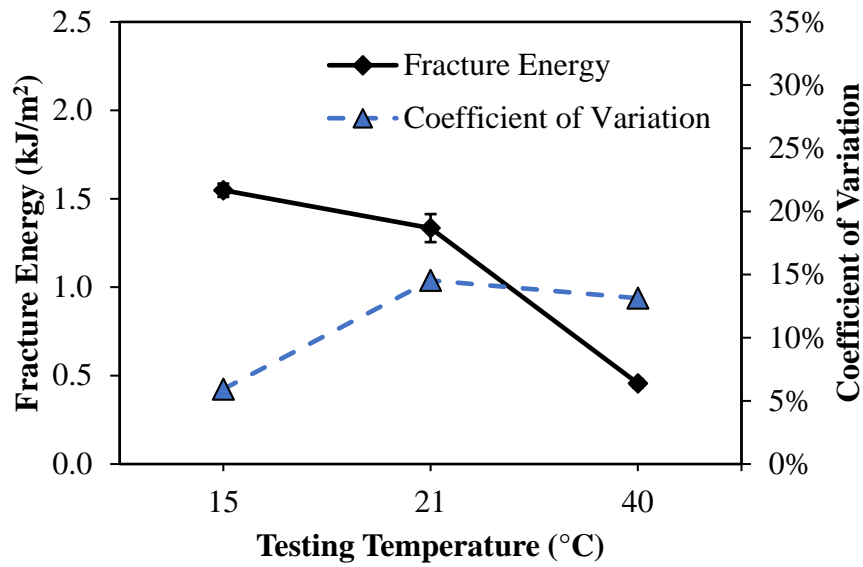
(a)
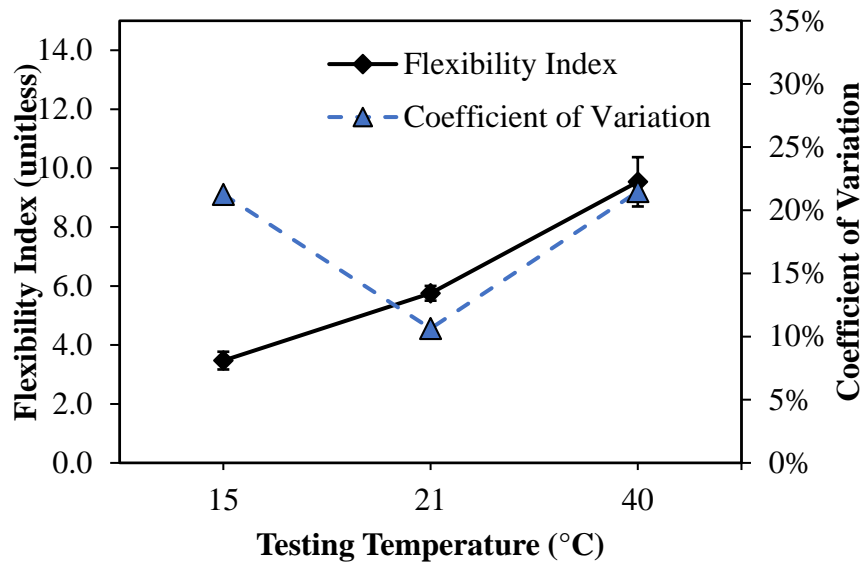
(b)

Figure 32. Effect of testing temperature on test results and their repeatability: (a) fracture energy and (b) flexibility index.

COV of *FI* show an initial decrease between the temperature range of 15°C to 21°C, after which the COV value sharply increased. It is as though the low temperature increases the variability of *FI* due to the aforementioned brittleness behavior that complicates the calculation

of post-peak slope (m_2). Similarly, the higher temperature seems to have increased the variability of FI since the mixture became more compliant and thus more likely to vary. Ultimately, considering the results and repeatability of G_f and FI, a temperature of 21°C is recommended for SCB testing. The 21°C temperature has an added advantage of being the typical room temperature and thus, eliminates the need for an expensive environmental chamber and therefore increasing the practicality of the SCB test method.

3.6.2. Testing Fixtures

Based on the recommendations from the previous section, the test variables were selected as such: thickness (t) = 50 mm, notch length (nl) = 15 mm, loading rate (lr) = 3 mm/min, and temperature (T) 23 ± 0.5°C. Eight SCB replicates per fixture were tested, which was more than the minimum number of replicates (six) recommended, which was based on the observed variability from one testing fixture. However, since the scope of this effort involves multiple fixtures, which may bring a greater level of variability, the sample size was conservatively increased to eight. SCB test results from all fixtures are shown in Figure 33 for the eight replicates. From the results, it is apparent that fixtures with a jig (i.e., S-C-J and S-C-J) tended to produce curves within a relatively narrower band compared to other fixtures. Another observation is that combination of spring rollers and jig considerably narrowed the band of curves in the pre-peak region for the S-C-J fixture suggesting the existence of constrain on SCB specimen when the fixture is used. The jig effect was especially apparent by comparing test results from S-C-NJ and S-C-J where the jig indeed did narrow the band of results curves.

F-Fa-NJ

S-Fa-NJ

F-C-J

S-C-J

S-C-NJ
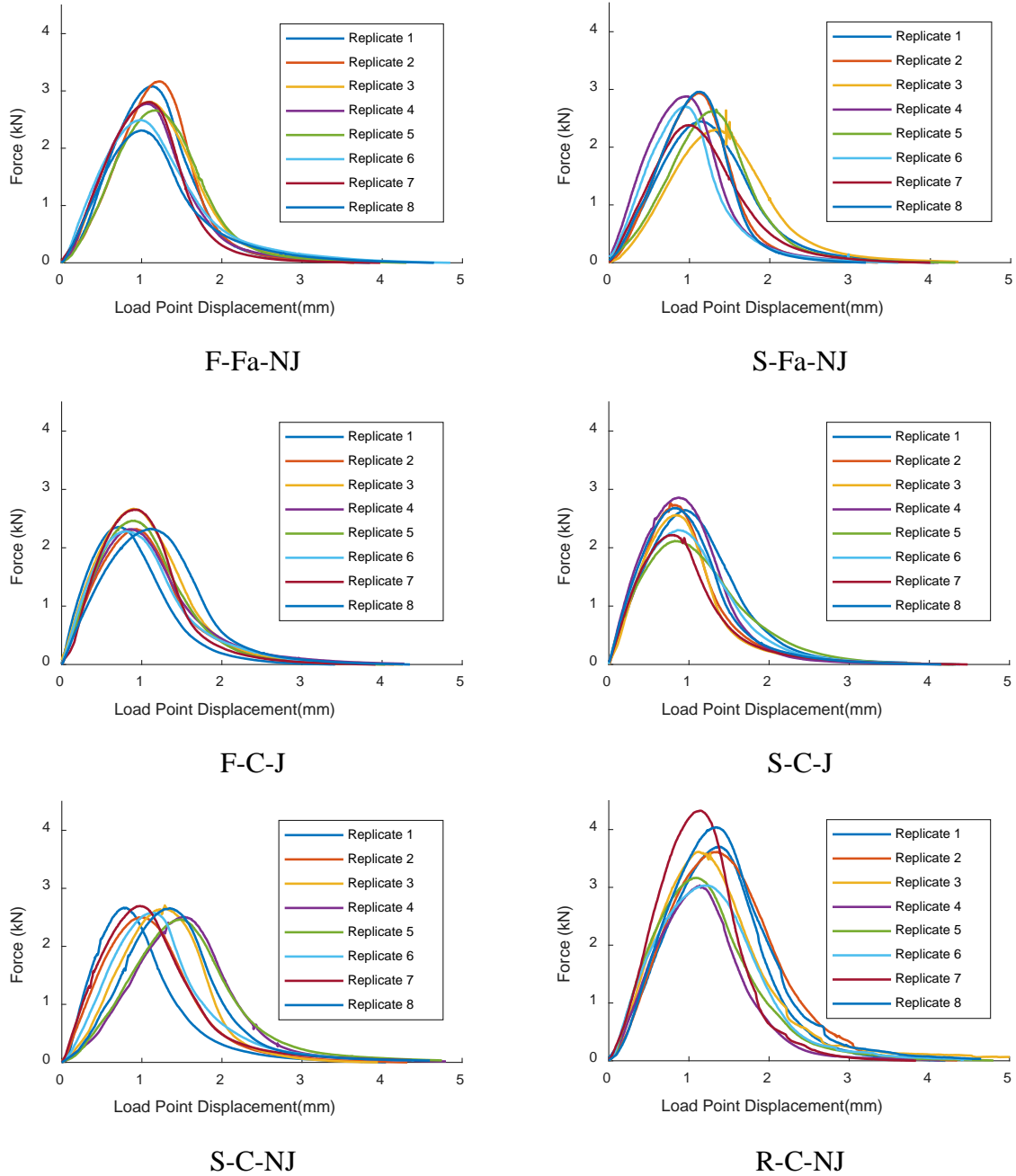
R-C-NJ

Figure 33. SCB test results (load vs. LPD) of each fixture cases from eight replicates.

When the free horizontal rolling was restricted as is the case for R-C-NJ, the maximum

load was highest among all fixtures investigated. The high P_{max} of R-C-NJ can be attributed to

restriction and high contact area at support which generated friction between the rollers and the

rolling surface. The friction was then transmitted as a resistance force to SCB specimens and manifests itself as increased overall P_{max} in the results. It is noteworthy that visually, roller springs minimally affected how much the test results (i.e., curves) were condensed or spread apart (i.e., the band of curves). Additionally, all test results ended nearly at approximately the same LPD of 3.5 mm.

Figure 34 shows the averaged force-LPD curve of each fixture case. As aforementioned, the maximum (peak) force of all fixtures appears to be similar except for R-C-NJ which was higher. The average results confirm that roller springs only minimally affected results (force vs. LPD) for both rolling surface shapes (i.e., flat vs. curved) as seen by comparing: F-Fa-NJ vs. S-Fa-NJ and S-C-J vs. F-C-J. For both rolling surfaces, cases without roller springs exhibited a slightly higher peak force. This result implies that the springs reduced the friction at roller supports which is reasonable since the role of springs is to reduce lateral sliding during rolling. It should be noted that increasing the spring constant (i.e., from 0.12 N/mm to higher) on a flat rolling surface would results similar to R-C-NJ. Similarly, decreasing the spring constant would effectively increase the rolling freedom at support result in F-Fa-NJ-like behavior.
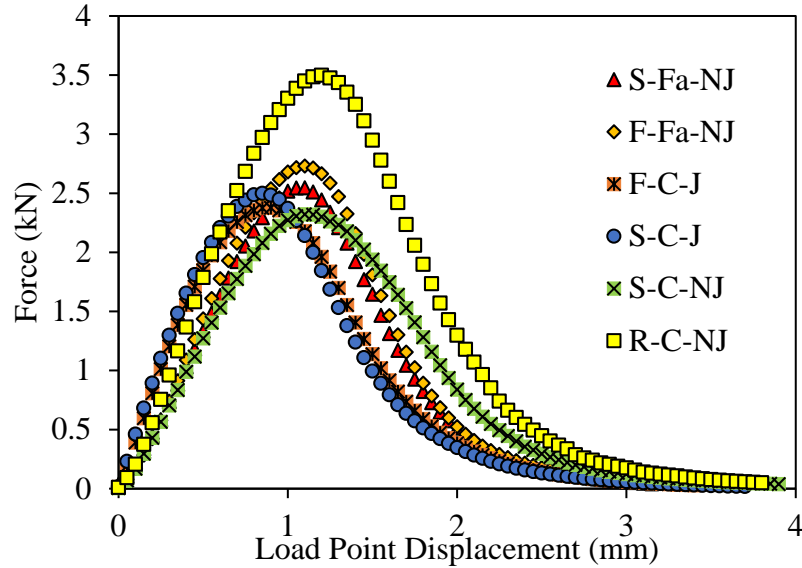
Figure 34. Average per fixture of SCB test results (load vs. LPD).

3.6.2.1. Fracture Energy

Figure 35 presents fracture energy (G_f) results along with associated COV from all the test

fixtures. Fracture energy results from the different load-support fixtures are generally similar

(based on error bars), except for R-C-NJ, which produced the highest G_f among other fixtures.

The higher fracture energy can be explained by the increased friction at the roller support that

generated resistance at the loading point and thus generated higher apparent work (i.e., area

underneath the curve) as observed in Figure 34. The jig effect is seen by comparing S-C-J and S-

C-NJ. The jig reduced G_f while simultaneously increasing its variability (i.e., COV). As such,

the presence of a jig on an SCB fixture may be detrimental to the repeatability of G_f and thus in

case the fracture energy is of interest use of jig is not recommended.
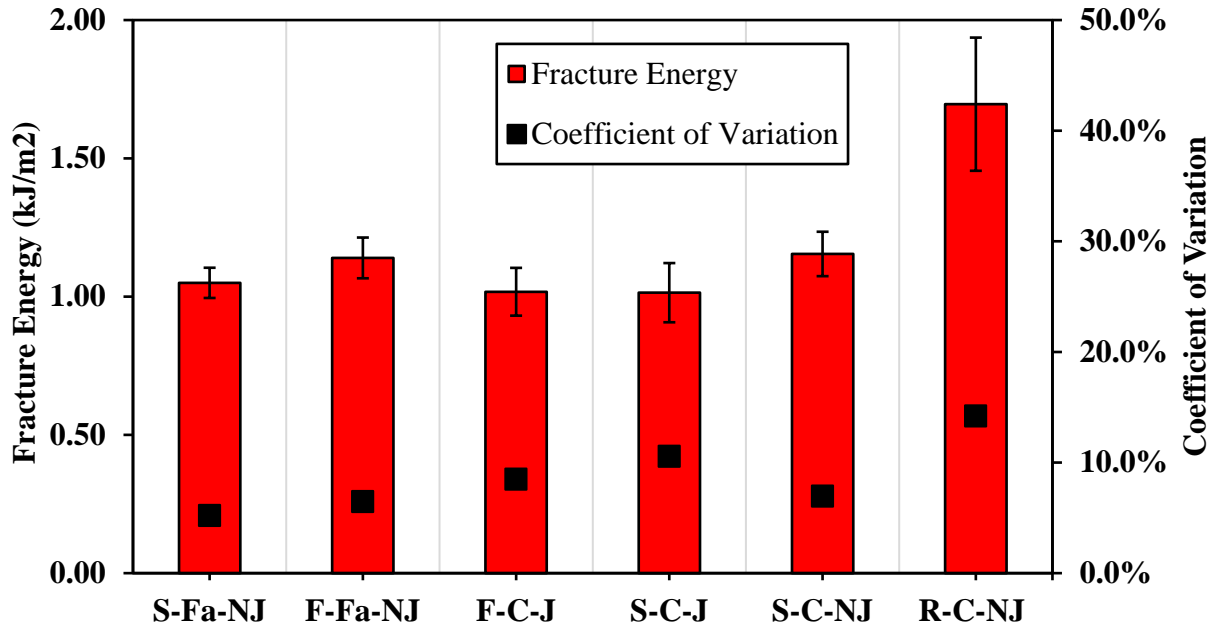
Figure 35. Effect of testing fixtures of fracture energy results and repeatability.

The shape of the rolling surface can be gauged by comparing S-Fa-NJ and S-C-NJ which shows that a curved surface increased both G_f and its COV. The effect of roller springs was contrasting for flat and curved rolling surface shapes. On a flat surface, the use of springs improved the repeatability of G_f while for curved surfaces, the same springs reduced repeatability (i.e., increased COV) of G_f. However, it is noteworthy that the springs minimally affected G_f results on both rolling surface shapes. Therefore, the overall recommendation when testing for G_f is to avoid the mid-span jig and use roller springs only on flat rolling surfaces (and avoid them on curved surfaces).

3.6.2.2. Flexibility Index

FI results along with associated COV are shown in Figure 36 and were calculated using the

equation (3.2) from test results of eight replicates per fixtures shown in Figure 33. From the

results, the highest FI was obtained from R-C-NJ fixture which is the fixture with a restricted

curved rolling surface without a mid-span jig. The higher G_f translated to higher FI even after

normalization of the fracture energy with the post-peak slope (m_2). From the results, it is seen

that the presence of the jig (S-C-NJ vs. S-C-J) slightly reduced FI while dramatically increasing

COV from 20% to 40%. The jig increases repeatability of FI only when it is used without roller

springs (F-C-J vs, S-C-J). Therefore, when FI is of interest, the mid-span jig should only be used

without roller springs on a curved surface to improve the repeatability of results.
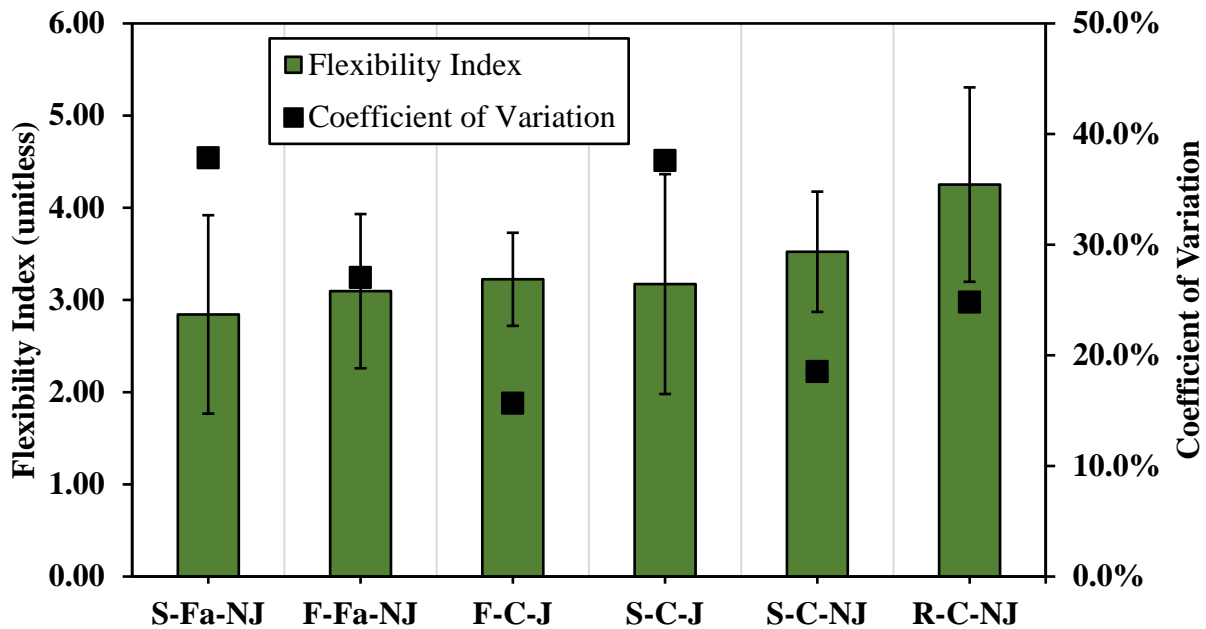
Figure 36. Effect of testing fixtures on flexibility index results and repeatability.

In general, roller springs significantly increased COV of FI regardless of the rolling surface shape. In fact, for curved surfaces, COV more than doubled when roller springs were added (F-C-J vs. S-C-J). For the flat surfaces, COV increased by about 50% with the addition of roller springs. Comparing S-Fa-NJ and S-C-NJ, it is noticeable that curved rolling surface improved repeatability of FI (i.e., lowered COV). In sum, while roller springs minimally affected the values of FI, they greatly contributed to an increase in COV. Also, the mid-span jig is only beneficial to the repeatability of FI only when is used without springs and on a curved rolling surface.

3.6.2.3. Maximum Load

The maximum load results shown in Figure 37 show that P_{max} results were similar for all fixtures except for the R-C-NJ, where the horizontal rolling was restricted. As aforementioned, the rolling restriction at support present in R-C-NJ increased the friction, which was then reflected as higher P_{max} in the test results. The COVs of P_{max} were also similarly low, about 10%, indicating higher repeatability of P_{max} when compared to other indicators such as FI. It is noteworthy that the lowest COV was obtained on S-C-NJ suggesting that the curved rolling surface increased the repeatability of P_{max}.
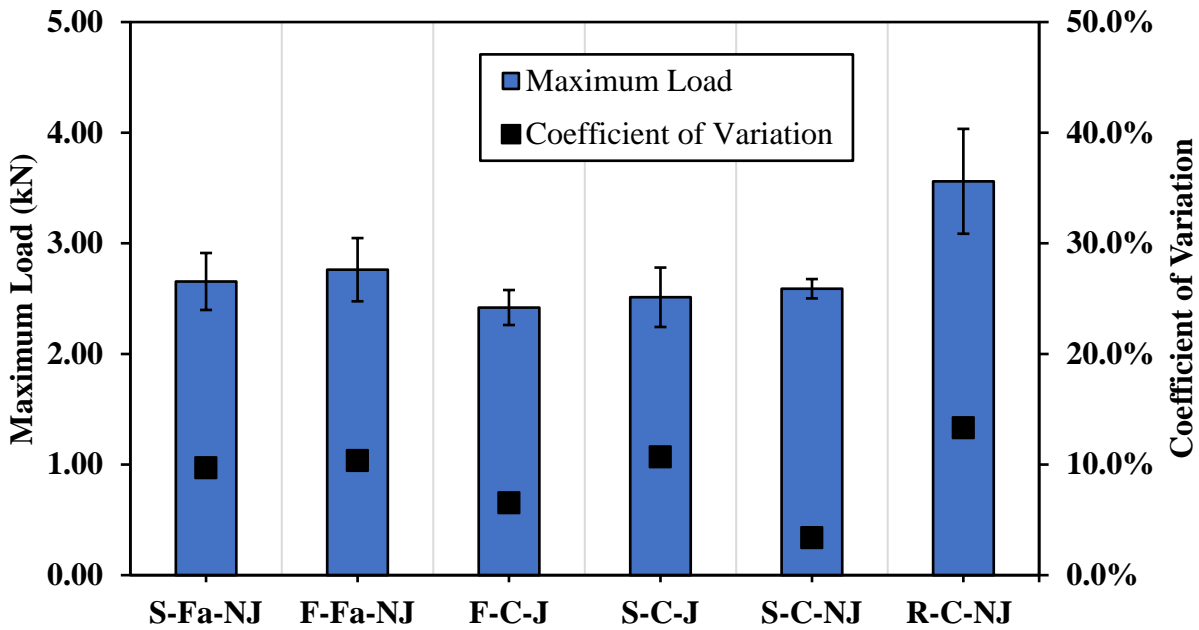
Figure 37. Effect of testing fixtures on maximum load results and repeatability.

3.6.2.4. Cracking Resistance Index

Figure 38 presents the *CRI* results calculated from Figure 33 using the equation (3.3). Considering the error bars, *CRI* results from all fixtures were generally similar which indicate fixture independence of *CRI* . In addition, the COV results from all fixtures were generally low, around 10%, suggesting high repeatability of the *CRI* indicator regardless of testing fixture used. The fixture-independence and low COV make *CRI* an attractive indicator when comparing results from different testing fixtures. However, the lack of sensitivity to the fixtures component may also be indicative of a lack of power to properly detect an existing difference in mixtures. Thus, more studies on *CRI* sensitivity in AC mixtures are mandated.
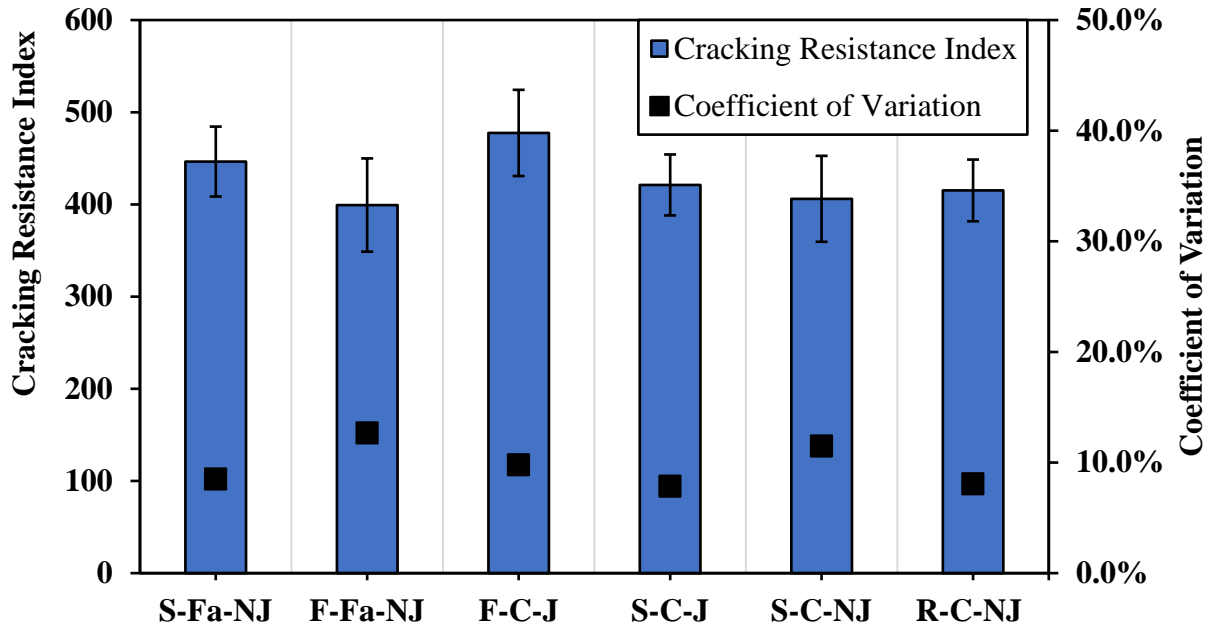
Figure 38. Effect of testing fixtures on cracking resistance index results and repeatability.

3.6.2.5. Pre- and Post-peak Slopes

More effect of the fixtures on test results can be achieved by examining the characteristics of slopes of the SCB test results curves. Figure 39 shows the slopes of curves as pre-peak (m_1) and post-peak (m_2) in addition to their ratios $\left|{m_1}/{m_2}\right|$. The pre-peak slope m_1 can be related to the apparent stiffness of the SCB specimen. Meaning, the higher the m_1 the stiffer is the SCB specimens appear. Figure 39(a) shows that fixtures with the mid-span jig (F-C-J and S-C-J) had the highest m_1 similar to the fixture with restricted rolling at the support (R-C-NJ). The remaining fixtures had similar m_1 values. COV results indicate that the mid-span jig increased the repeatability of m_1 when used with on a curved rolling surface. In addition, roller springs reduced COV on the curved surface (F-C-J vs. S-C-J) while, increasing it on a flat surface.

The post-peak slope m_2 is related to the speed at which fracture is happening in SCB specimens (Nsengiyumva, Haghshenas et al. 2020). Results of m_2 are shown in Figure 39(b) where curved rolling surfaces had lower m_2 values compared to flat surfaces with exception of the fixture with restricted rolling (R-C-NJ). The lower m_2 is indicative of reduced crack propagation speed in SCB specimen when curved rolling surfaces are used. COV results of m_2 show elevated values which are on average that are double that of m_2. The increased COV of m_2 has been identified in studies as the main source of the COV of FI results as well (Haghshenas, Nsengiyumva et al. 2019, Nsengiyumva and Kim 2019). Repeatability of m_2 can be improved by totally avoiding a mid-span jig or using the jig on a curved rolling surface.
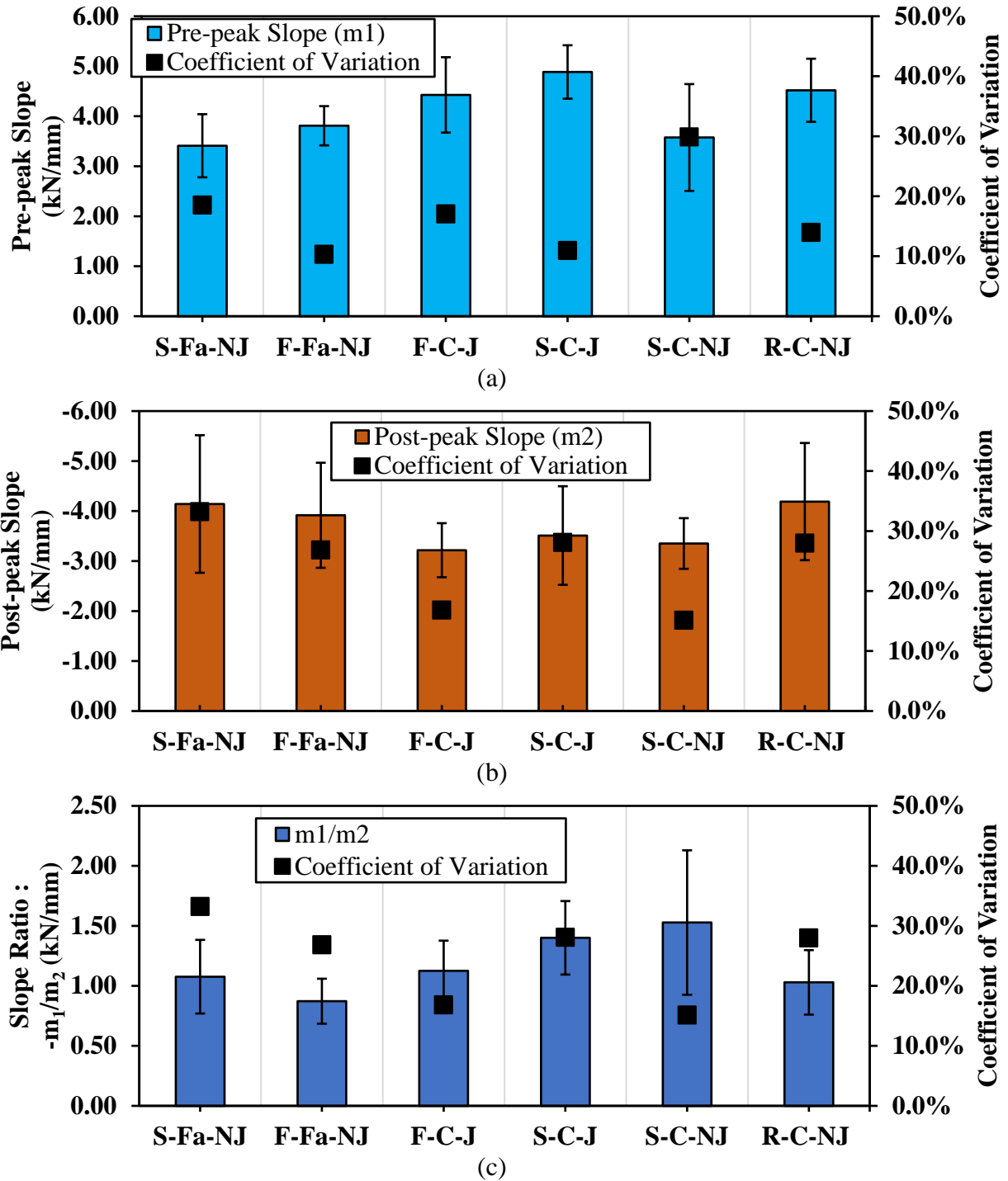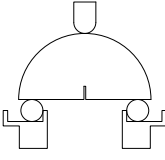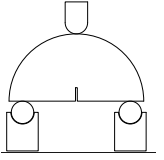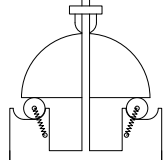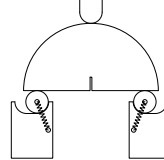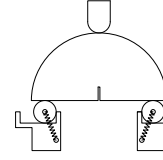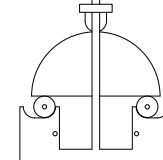
Figure 39. Effect of testing fixtures on slope properties: (a) pre-peak slope, (b) post-peak slope, and (c) slope ratios.

Finally, the slope ratios $\left|\frac{m_1}{m_2}\right|$ are compared and the results are shown in Figure 39(c). This

ratio indicates how fixtures affect the symmetry of the curve of the SCB test results. If the slope

ratio $\left|\frac{m_1}{m_2}\right|$ is larger than one, as is the case for both S-C-J and S-C-NJ, then m_1 is higher than m_2

and vice versa. A ratio larger than one portrays a brittle-like behavior during the fracture of an

SCB specimen. At intermediate test temperature and the loading rate used, the AC mixture is

considered compliant and thus not brittle. Therefore, a slope ratio $\left|\frac{m_1}{m_2}\right|$ of less than one is

expected from all the SCB results tested here-in. Remarkably, only the two fixtures with springs

and on curved rolling surfaces (i.e., S-C-J and S-C-NJ) had a slope ratio higher than one. To this

point, it is unclear whether a slope ratio higher or lower than one is beneficial to the SCB test

results which warrant more investigation that is outside the scope of this study.

The COVs of all four indicators (i.e., FI, G_f, P_{max}, and CRI) obtained from all cases are

summarized in Table 2. By simply averaging and comparing the COVs, the overall repeatability

per fixture can be assessed. S-C-NJ had the lowest overall COV and therefore is considered to be

the most consistent fixture. However, for a flat rolling surface, F-Fa-NJ (without springs) was

more repeatable than S-Fa-NJ (with springs). As previously mentioned, roller springs had a

detrimental effect on testing repeatability with both flat and curved rolling surfaces. This

detrimental effect of roller springs is still observed in comparisons of overall repeatability (e.g.,

comparison of F-Fa-NJ and F-C-J to S-Fa-NJ and S-C-J). The mid-span jig (S-C-J vs. S-C-NJ)

and rolling friction (R-C-NJ vs. F-Fa-NJ) at the support increased COV.
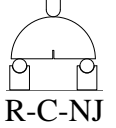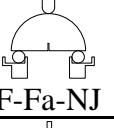
Table 2. COV of Fracture-Related Indicators from Different Fixtures

COV of:	F-Fa-NJ	R-C-NJ	S-C-J	S-C-NJ	S-Fa-NJ	F-C-J
FI	27.0%	24.8%	37.6%	18.5%	37.8%	15.7%
G_f	6.5%	14.2%	10.6%	7.0%	5.2%	8.5%
P_{max}	10.3%	13.3%	10.7%	3.4%	9.7%	6.5%
CRI	8.1%	9.8%	11.5%	8.5%	12.7%	7.9%
Average	13.0%	15.5%	17.6%	9.3%	16.4%	9.6%

3.6.2.6. Statistical Analysis of the Results

A pairwise comparison study was conducted to determine the effect of each load-support fixture component on individual indicators. As shown in Table 5 the lack of free rolling at the support increased all fracture indicators and their COVs. Roller springs minimally affected fracture-related indicators but increased their COVs, regardless of the rolling surface shape. In addition, the removal of the mid-span jig generally increased the magnitude of indicators and also beneficial to their repeatability. The flat rolling surface reduced indicators and their COVs except for the COV of FI, which was increased two-fold.

Table 5 Summary of Effect of Each Load-Support Fixture Component

Support Fixtures		Outcomes				Effect of:
F-Fa-NJ → R-C-NJ		$G_f \uparrow$ [COV↑]	$FI \uparrow$ [COV ↓]	$P_{max} \uparrow$ [COV ↑]	$CRI \uparrow$ [COV ↑]	Lack of free rolling at support
F-Fa-NJ → S-Fa-NJ		$G_f \approx$ [COV ↓]	$FI \approx$ [COV ↑]	$P_{max} \approx$ [COV ≈]	$CRI \approx$ [COV ↑]	Roller springs on a flat surface
S-C-J → S-C-NJ		$G_f \uparrow$ [COV ↓]	$FI \uparrow$ [COV ↓↓]	$P_{max} \approx$ [COV ↓↓]	$CRI \uparrow$ [COV ↓]	Removing the mid-span jig
F-C-J → S-C-J		$G_f \approx$ [COV ↑]	$FI \approx$ [COV ↑↑]	$P_{max} \approx$ [COV ↑]	$CRI \approx$ [COV ↑]	Roller springs on a curved surface
S-C-NJ → S-Fa-NJ		$G_f \downarrow$ [COV ↓]	$FI \downarrow$ [COV ↑↑]	$P_{max} \downarrow$ [COV ↓]	$CRI \approx$ [COV ≈]	Rolling surface shape

Note: ↑: increase, ↓: decrease, ↑↑, ↓↓: increase and decrease two-fold, respectively
↑↑↑, ↓↓↓: increase and decrease three-fold, respectively
≈: minimal change, →: switching between fixtures

To identify if there are significantly different pairs of fixtures, the Duncan's New Multiple Range Test (Dowdy, Wearden et al. 2011), which is a multiple-comparison procedure, was used. Duncan's New Multiple Range Test can perform a pairwise comparison as opposed to the overall group comparison of the analysis of variance (ANOVA) test. Duncan's test is useful even when no overall difference was detected in a data set by ANOVA. Results of the Duncan's New Multiple Range Test are shown in Figure 40, in which mean values are arranged in increasing order from left to right. Mean values not underlined by the same line segment are significantly different at a 95% confidence level (i.e., significance level or $\alpha =5\%$). Pairwise comparison of fracture indicators per case revealed a similarity between them except for G_f and

P_{max} from R-C-NJ. Additionally, S-C-NJ was the only case in which *FI* and *CRI* were not significantly different from R-C-NJ. This similarity between S-C-NJ and R-C-NJ is unsurprising since S-C-NJ is essentially identical to R-C-NJ but with increased rolling freedom at the support. Finally, the multiple-comparison test confirmed that the addition of springs did not significantly change indicators (F-Fa-NJ vs. S-Fa-NJ and F-C-J vs. S-C-J).

FI (unitless)

S-Fa-NJ	F-Fa-NJ	S-C-J	F-C-J	S-C-NJ	R-C-NJ
2.84	3.10	3.17	3.22	3.52	4.25

P_{max} (kN)

F-C-J	S-C-J	S-C-NJ	S-Fa-NJ	F-Fa-NJ	R-C-NJ
2.42	2.51	2.59	2.65	2.76	3.56

G_f (kJ/m^2)

S-C-J	F-C-J	S-Fa-NJ	F-Fa-NJ	S-C-NJ	R-C-NJ
1.01	1.02	1.05	1.14	1.15	1.70

CRI (unitless)

S-Fa-NJ	S-C-J	F-Fa-NJ	F-C-J	S-C-NJ	R-C-NJ
399.3	406.1	415.2	421.1	446.5	477.6

Figure 40. Results of Duncan's Test for (a) FI, (b) Pmax, (c) G_f, and (d) CRI. Note: Test results underlined by the same line segment are statistically similar using α = 5%.

3.7. **Summary**

In this chapter, the SCB test method was developed by first investigating critical testing variables

such as the recommended minimum number of replicates (n), the thickness of specimens(t),

notch length (nl), loading rate(lr), and the testing temperature (T). After the determination of the

SCB testing variables based on repeatability and practicality, this chapter also investigated the

effects of SCB testing variables on the test results and their repeatability. In total six different

and prominent testing fixtures were investigated. Table 6 presents the recommended SCB testing

variables determined in this chapter.

Table 6. Recommended Values for SCB Testing Variables

Critical Testing Variable	Recommended Value
Number of Replicates	≈6
Thickness of Specimen	≈ 50 mm
Notch length	≈15 mm
Loading Rate	≈ 3 mm/min
Testing temperature	≈21°C

The SCB testing fixture investigation revealed that:

1. Fixtures affected test results, fracture-related indicators, and their associated repeatability

2. When testing for G_f is to avoid the mid-span jig and use roller springs only on flat rolling

   surfaces (and avoid them on curved surfaces).

3. In general, the mid-span jig should be avoided to improve the repeatability of from SCB

   test results.

4. While roller springs minimally affected the values of FI, they greatly contributed to the increase of its COV. In addition, the mid-span jig is only beneficial to the repeatability of FI when used without springs and on a curved rolling surface.

5. The fixture-independence and low COV make *CRI* an attractive indicator for comparing results from different fixtures.

CHAPTER IV

DEVELOPMENT OF GYRATORY STABILITY RUTTING TEST

This chapter presents the effort of the development of a novel simple and practical rutting test

called G-Stability. Table 7 shows the arrangement of phases involved in the G-Stability test

development and parameters contained in this chapter. The first part of the chapter focuses on

identifying critical testing parameters for the test that are the testing temperature, loading rate,

specimen geometry, and the number of replicates. Subsequently, the second part establishes a

relationship by correlating the developed test and the existing FN (flow number) rutting test.

Table 7. Phases of G-Stability Test Development with Parameters Investigated in This Chapter

Phase of SCB test development	Parameter investigated
G-Stability testing variables	Testing temperature
	Testing loading rate
	Specimen thickness
	Number of replicates
	Temperature
The sensitivity of the G-Stability test	
Correlation between G-Stability and flow number test results	

4.1. **Introduction**

Although there are several existing rutting tests, they are usually complicated and require

complex equipment to conduct. As aforementioned, among the rutting tests, the FN (flow

number) test has demonstrated a good correlation with field rutting performance (Biligiri,

Kaloush et al. 2007, Dongré, D'Angelo et al. 2009). The FN is a cyclic test on a cylindrical specimen of 100 mm diameter and 150 mm in height (Figure 41(a)). The specimen is prepared by cutting and coring the SGC tall sample (150 mm diameter and 170 mm height). The cyclic load is applied with 0.1 seconds load and 0.9 seconds of unloading periods to make the entire cycle lasts one second. The test requires the determination of testing parameters such as the testing temperature, contact stress, and the deviatoric stress to ensure that the flow occurs within 10,000 cycles (i.e., 2 hours 48 minutes). Choosing these testing parameters is time-consuming and destructive to the specimen. It is noteworthy that the test automatically terminates at 50,000 microstrains.

The test results and data analysis are shown in Figure 41(b) where the flow number is obtained by finding the minimum of numerical differentiation of accumulated microstrains with respect to the loading cycles (by first fitting a function to the curve). It is apparent that despite the advantages of FN such as good correlation with field performance, both complex testing, and data analysis impedes the test be readily and widely implemented for performance-based purposes. Thus, there is a need for a more practical, simpler, and easy to implement rutting test.
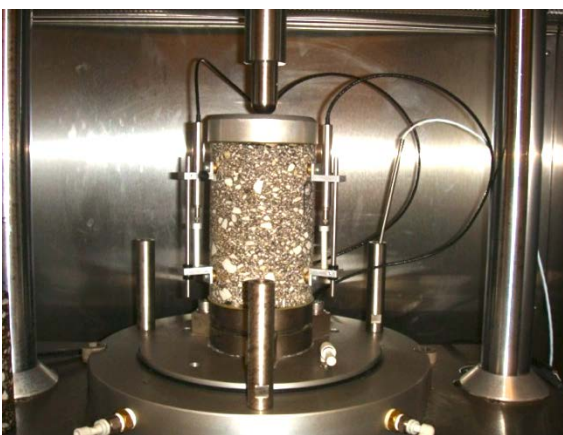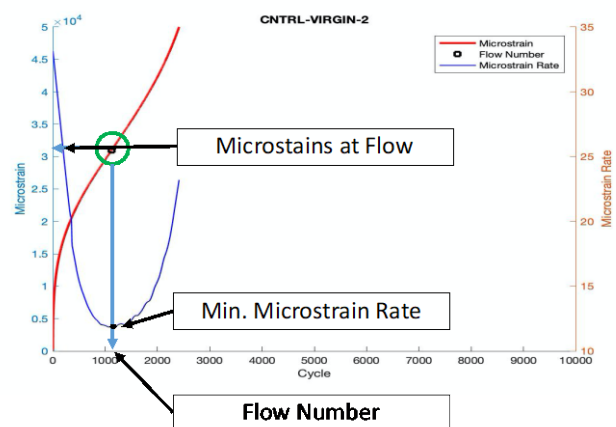
(a)   (b)

Figure 41. Flow number test: (a) set-up and (b) data analysis.

4.2. **Objectives and Research Methodology**

The need to accelerate performance-based AC design and lack of practical rutting test motivated this study with the following specific objectives:

1) To develop a practical and simple rutting testing of AC,

2) To explore the sensitivity of the new rutting test to the difference in mixtures, and

3) To validate the developed test method by correlating it to established rutting test (i.e., FN).

To achieve the objectives the methodology shown in Figure 42 was adopted. The effort to develop G-Stability was subdivided into two phases: 1) development of the G-Stability test method and 2) the correlation of the G-Stability to the FN test. In the first phase, critical testing parameters: temperature (T), loading rate (lr), specimen thickness (t), and the number of replicates (n), are determined based on sensitivity, practicality, and repeatability. In the second phase, the developed G-Stability test method is correlated to the FN method using test results from one typical mixture. The correlation investigates the compatibility of the ranking order between the two test methods. Finally, an interconversion study is conducted on the test results of G-Stability and FN from the same AC mixture.
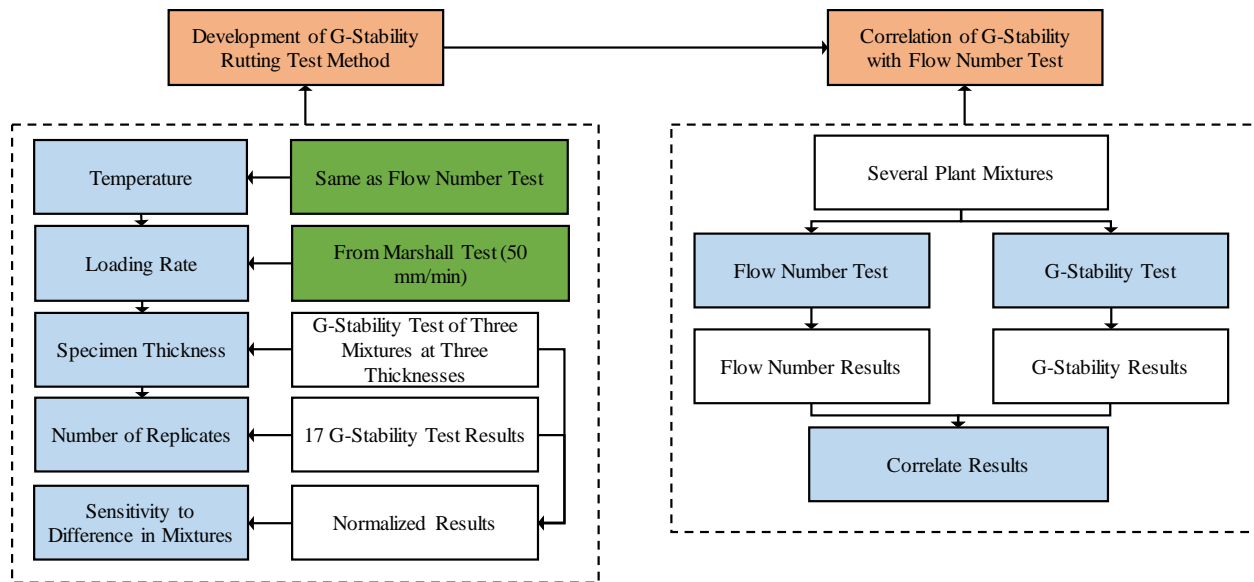
Figure 42. Research methodology for G-Stability showing phases of development and correlation with FN.

4.3. **Materials**

Three AC mixtures were collected over the State of Nebraska and brought to the laboratory in sealed containers to avoid aging by oxidation. The selection of mixtures was made to represent typical mixtures and their usage across Nebraska. The first mixture (SPS) is considered a low-quality mixture and mainly used on road shoulders or low-traffic roads. The SPS mixture used here-in contained 50% RAP which is considered as a high amount of RAP (Nsengiyumva, Haghshenas et al. 2020). It is noteworthy the RAP in SPS is typically sourced from low-quality batches such as those from shoulder pavement as opposed to batched from interstate RAP. Finally, SPS contained the lowest quality binder among the rests (i.e., PG 52-34) and the binder content was the lowest of all mixtures (i.e., 5.2%) as shown in Table 8.

The second is SPR which is an intermediate mixture in Nebraska that is mainly on the surface of medium- to high-traffic roads. The RAP used in SPR was 45% per weight of the

whole mixture and was sourced from a better-quality batch than that of SPS. Furthermore, the

SPR used had a 5.3% content binder of PG 64-34. Therefore, SPR contained a higher amount of

better-quality binder than the SPS. Aggregates gradation of SPR and had NMAS (nominal

maximum aggregate size) of 12.5 mm.

Table 8 Key Characteristics of Mixtures Used

Mixture Name	Usage	RAP	Binder Type and Content (%)
SPS	Shoulder	50%	PG 52-34 (5.2%)
SPR	Highway	45%	PG 64-34 (5.3%)
SLX	Interstate	25%	PG 64-34 (5.4%)

The third mixture was a high-quality mixture called SLX and was engineered by the

Nebraska DoT (department of transportation) to be durable when used as a thin-lift wearing

course (Im, You et al. 2018) on high-traffic roads such as the interstate. The SLX had a binder

content of 5.4%, which was more than the SPR although the quality (performance grade, PG) of

the binder (i.e., PG 64-34) was the same for both mixtures (i.e., SLX and SPR). The RAP

contained in SLX of 25% was less than that in SPR and was from a better source compared.

Since the main application of SLX is for thin-lift, it had finer aggregates compared to the rest of

the mixtures with the NMAS (nominal maximum aggregate size) of 4.75mm. Table 8 presents

the important characteristics of each mixture selected for G-Stability test development. Figure 43

compared the aggregate gradations of the mixtures used in G-Stability test development. It can

be seen the key difference between SLX and the rest of the mixtures is the higher content of finer

aggregates. The figure also shows that the gradations of SPR and SPS were similar.
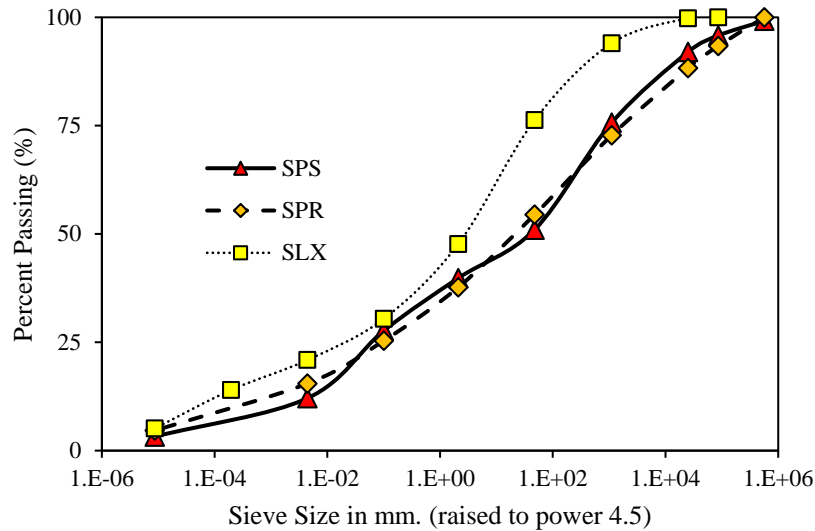
Figure 43. Aggregate gradation of mixtures used in G-Stability development.

4.4. **G-Stability Sample Fabrication**

The sample fabrication process for the G-Stability test begins with the collection of a mixture from a plant and then transported in sealed containers to the testing laboratory at UNL (University of Nebraska-Lincoln). The mixture is compacted at recommended compaction temperature using the SGC into tall samples of 150 mm diameter and 170 mm height as shown in Figure 44(a). Subsequently, the tall samples are sliced into discs at the desired thickness. The sample fabrication of G-Stability is considerably simpler than FN since only cutting is needed after compaction. As a result, after compaction only one cutting equipment is needed to complete sample fabrication of G-Stability thus eliminating a need for coring as done for FN specimens. It must be noted that laboratory prepared mixtures can also be used to prepare G-Stability specimens. In this study, the already mixed AC brought from the plant to help expedite the sample fabrication process.

Figure 44. SCB sample preparation: (a) compaction by SGC and (b) slicing.

The simplicity of G-Stability presents some possible limitations such as being empirical and lack of field-level verification data. To overcome both limitations, test results from G-Stability can be correlated with FN results on the same AC mixture. In addition to being a fundamental test, FN is an established rutting test that has shown a good correlation with field rutting performance (Biligiri, Kaloush et al. 2007, Dongré, D'Angelo et al. 2009).

4.5. **G-Stability Test Set-up and Data Analysis**

The new rutting test was named after Gyratory Stability as G-Stability. The test set-up for the G-Stability test is shown in Figure 45(a) and is composed of a disc-shaped AC specimen of 150 mm in diameter loaded using the Marshall stability test fixture. The loading is applied in a displacement-controlled mode from top-down. Test results recorded as force and displacement are shown in Figure 45(b). From the result, data analysis is straight forward to determine rutting-related indicators. For example, the maximum load is the G-Stability (gyratory stability) measure while the displacement corresponding to the G-stability is the G-Flow (gyratory flow).

The G-Stability has the advantage of having a simple monotonic displacement-controlled loading which can be performed in most AC mixtures laboratories without complicated

equipment. In addition, the testing fixture is widely available the AC laboratories as a Marshall stability fixture. Finally, G-Stability data analysis is simple and can easily be performed visually without complex calculations, unlike the FN test.

(a)	(b)
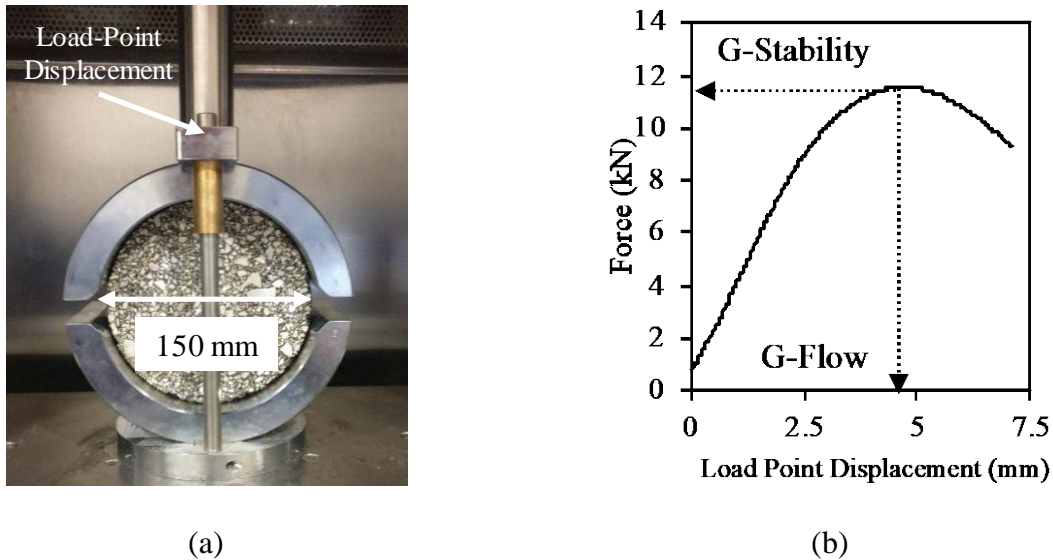
Figure 45. Gyratory stability test: (a) set-up and (b) results and data analysis.

4.6. **Results and Discussions**

4.6.1. Testing Temperature

Rutting usually occurs at high temperatures where AC mixtures have reduced stiffness. As a result, most of the rutting tests are conducted at high temperatures, which are typically above 40°C (West, Rodezno et al. 2018). Therefore, for the G-Stability as well a high (i.e., ≥ 40°C) testing temperature sought. For simplicity and since the FN is an established test, its testing temperature could be applied to the G-Stability test method as well. It is noteworthy that the purpose of G-Stability was to replace the FN with a simpler and easy to conduct a rutting test method. The main complexity of the FN rose from the complicated sample fabrication and testing protocol. Therefore, the temperature was not the main source of concern, thus could be

adopted for G-Stability as well. Furthermore, the approach of using established rutting to infer temperature for G-Stability ensured future compatibility between the tests and minimized uncertainties from temperature mismatches.

A preliminary study was conducted to investigate a proper testing temperature of the FN test according to the recommendation by the AASHTO T 378. First, a combination of temperature, contact stress, and cyclic stress was determined to ensure flow within 10,000 cycles (Haghshenas, Nsengiyumva et al. 2019). After multiples trials and errors, the temperature of 54°C achieved the flow using 600 kPa cyclic load and 32 kPa contact stress. As a result, the temperature of 54°C was adopted for the G-Stability rutting test method.

4.6.2. Testing Loading Rate

To ensure simplicity and practicality of G-Stability, it is critical to the loading rate be readily and easily achievable in most laboratories without expensive equipment. Towards that, a common loading rate of 50 mm/min corresponding to the widely available Marshall stability test equipment was adopted for the G-Stability test method. The typical loading facilitates the implementation of the G-stability test by repurposing existing equipment without modification. With the loading rate of 50 mm/min the duration of a G-Stability test is around 6 seconds and therefore remarkably short. The short testing time minimizes the temperature drop during testing in case the G-Stability is conducted without an expensive environmental chamber attached to the test equipment, which can hinder the practicality of the G-Stability test. Temperature conditioning of G-Stability specimens can easily be achieved by simply using an oven that is available in most AC mixture laboratories and therefore facilitating the adoption of the G-Stability test. It is noteworthy that with the duration of just 6 seconds, G-Stability dramatically

reduces testing time and increases practicality compared to the FN, which typicaly lasts for more than two hours to complete.

4.6.3. Specimens Thickness

Several studies have demonstrated that test results from AC mixtures are thickness-dependent up until a saturation point beyond which addition thickness minimally affects the accuracy of the test results (Kim, Lutif et al. 2009, Kim, Lee et al. 2010). The saturation thickness is related to the RVE (representative volumetric element), which is typically four times the NMAS (nominal maximum aggregate size). Using the predetermined temperature of 54°C and the loading rate of 50 mm/min, the SPS and SPR mixtures were tested at different thicknesses (Figure 45) to determine a practical thickness.

The results in Figure 46 reasonably show that G-Stability (i.e., maximum load) generally increased with thickness and that the higher quality SPR (used on highways) was stiffer than SPS(used on shoulders). The 50 mm thick of SPS resulted in comparable G-Stability as that of 75 mm of SPR.

Given the simplicity of both SCB and G-Stability, it is attractive from the practicality perspective to use one equipment to conduct both tests. The capacity of the load-cell is typically the constrain in choosing such equipment capable of both SCB and G-Stability testing. Typical loading frames present in AC mixtures laboratories have a maximum capacity of 20 kN or less. Therefore, for the practical reasons the G-Stability thickness should be selected to ensure that the maximum load remains the typical load-cell ranges. The purpose of investigating multiple thicknesses and mixtures was to gauge the expected G-Stability (i.e., maximum load) for common Nebraska mixtures and select a thickness that satisfied practicality (i.e., load-cell constrains) and the RVE requirements. As a result, the expected G-Stability for the thickness of

interest should not exceed 20 kN to ensure compatibility with the existing testing frames at most state DoTs and industry laboratories (e.g., AutoSCB™). Based on the results shown in Figure 45, a thickness of 50 mm was chosen since the maximum loads from both high- and low-performing mixtures were below the 15 kN threshold.
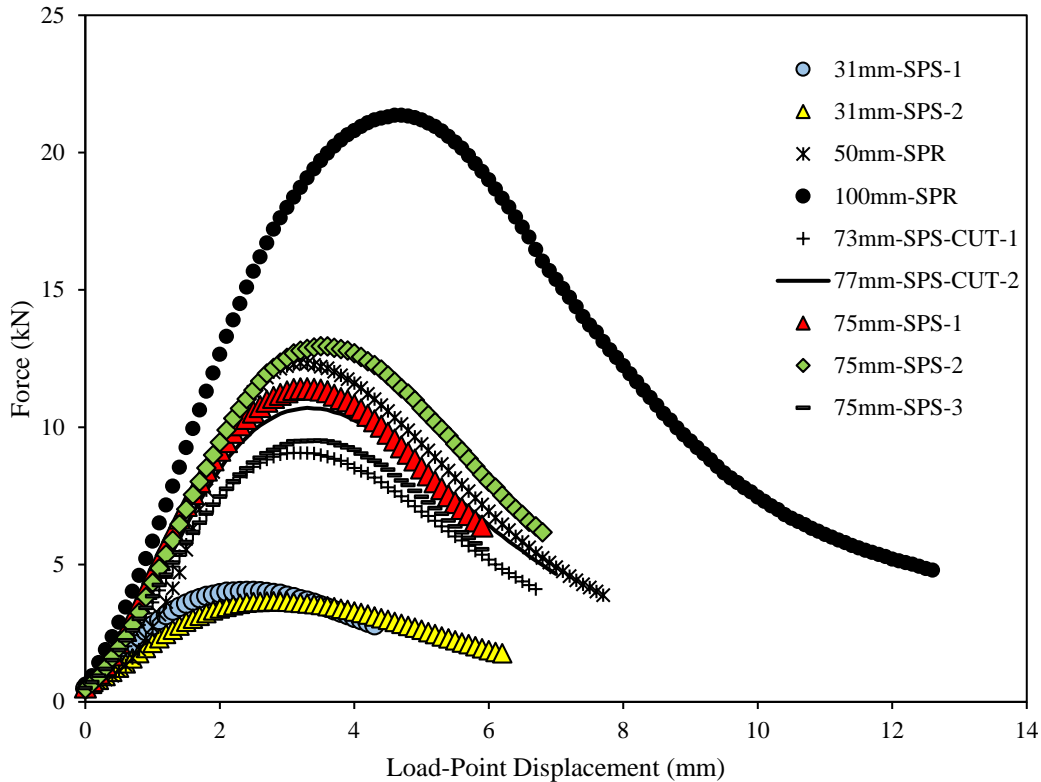
Figure 46. G-Stability testing results at different specimen thickness and mixture.

4.6.4. Recommended Minimum Number of Specimens

A total of 17 specimens were prepared from the SLX mixture at the determined thickness of 50 mm. Next, the specimens were tested using the determined parameters: temperature = 54°C and loading rate = 50mm/min. Statistical analysis (in 3.6.1.1) of the test results was used to determine the recommended minimum number of specimens/replicates (Nsengiyumva 2015,

Nsengiyumva, You et al. 2017). The sufficiently large sample size of 17 specimens (Figure 47(a)) was used to approximate the true standard deviation of the population.
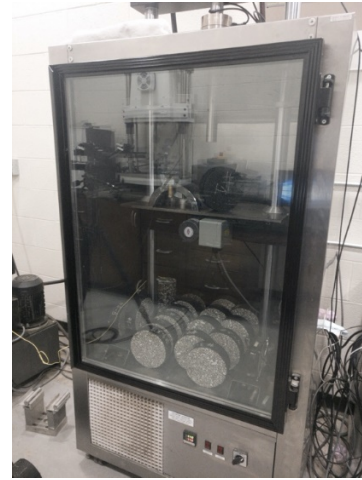
(a)   (b)

Figure 47. Determination of the number of replicates: (a) sample fabrication and (b) environmental conditioning prior testing.

After the temperature conditioning of the test sample (Figure 47(b)), the G-Stability testing was conducted at the aforementioned testing parameters(lr =50 mm/min, t = 50 mm, and T = 54°C). The testing was conducted on the same day and within the same hour to minimize any temperature-related variability. The test results for all the 17 specimens are shown in Figure 48 and show good repeatability as the spread of the maximum G-Stability and the minimum was only 3kN. The average G-Stability results was10.8 kN with the COV of 7.7% which indicates high repeatability associated with the G-Stability test.
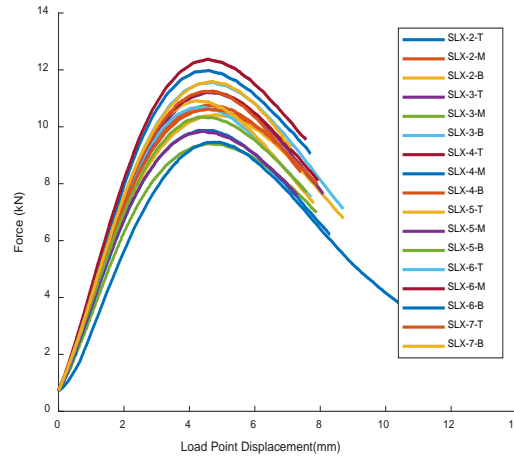
Figure 48. G-Stability test results to determine the minimum number of replicates.

After testing the equation (3.4) was then used to statistically calculate the recommended number of replicates necessary to estimate the mean of the population given a margin of error and a statistical significance (α value). Figure 49 presents the relationship between the margin of error and the minimum number of specimens. It is noteworthy that the curve in Figure 49 was simply calculated using the equation (3.4) with a standard deviation of 0.82 kN from the 17 specimens. The standard normal deviate Z value was 1.96, which corresponds to $\alpha/2 = 2.5\%$. As the figure shows, smaller margins of error require more replicates than larger margins of error.

The figure shows a plot with "Minimum Number of Replicates" on the y-axis (0 to 10) and "Desired Margin of Error (kN)" on the x-axis (0 to 2). A curve decreases from top-left to bottom-right. The equation shown is:

$$n = \left[\frac{Z_{\alpha/_2} \times \sigma}{E}\right]^2$$

A green box labeled "≈ 3" with red arrows indicating that a margin of error of 1.0 corresponds to approximately 3 replicates.
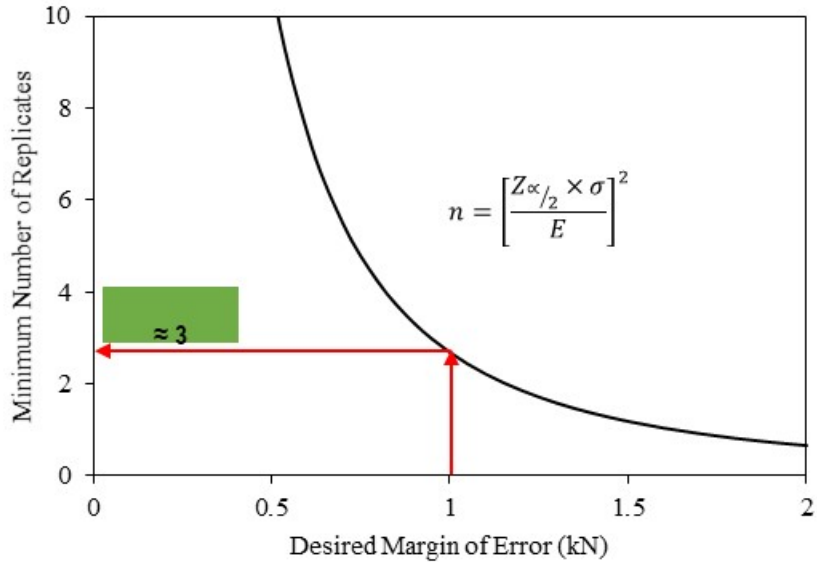
Figure 49. Relationship between the margin of error and the minimum number of G-Stability replicates.

A margin of error of 1.0 kN corresponds to three replicates as shown in Figure 49. The three replicates for G-Stability are particularly attractive as only one tall SGC sample would suffice to obtain them. Minimizing the number of SGC samples required also minimizes the time and effort to prepare G-Stability specimens and highlights the simplicity of the test. Furthermore, both the SCB and G-Stability test specimen would require only two SGC tall samples which can encourage their adoption thus BMD implementation. Therefore, the minimum number of specimens for G-Stability was determined to be three based on repeatability and practicality.

4.6.5. Sensitivity of G-Stability

The G-Stability test needs to have the capability to detect an existing difference in mixtures as a potential QA/QC tool. Therefore, a sensitivity study was conducted on the three mixtures using G-Stability. The sensitivity was checked by comparing test results normalized to thickness (Figure 50). The normalized results showed a difference between the AC mixtures tested. The

lowest quality mixture (i.e., SPS) had the lowest G-Stability while the others (i.e., SPR and SLX) which were better quality, had equally higher results. It is noteworthy that although SPR and SLX had similar G-Stability, G-Flow values were different. SLX which is the highest quality mixture had a higher G-Flow at higher displacement than the SPR. Although more investigation is warranted, the difference in displacement at G-flow between the two mixtures is assumed to be related to increased resiliency of SLX compared to SPR. Meaning that under identical conditions, SLX most likely experiences rutting later than SPR. Given both distinction of mixtures in G-Stability and G-Flow values, the developed rutting test has demonstrated acceptable sensitivity to the existing difference in mixtures.
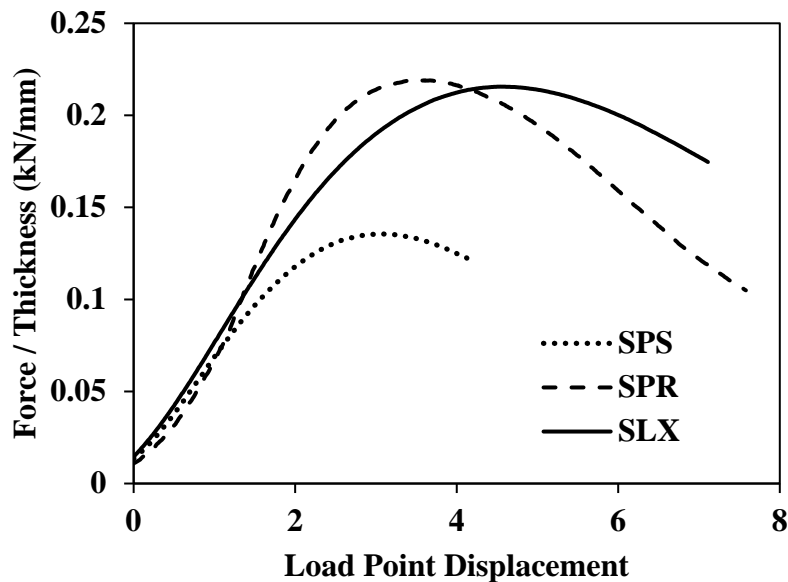
Figure 50. The sensitivity of the G-Stability test method.

4.6.6. Correlation of G-Stability to Flow Number Test

A correlation effort was conducted to establish compatibility between the developed G-Stability and the existing rutting test (e.g., FN). Towards that, six different plant-produced mixtures were

97

collected across the state of Nebraska and tested using the G-Stability and the FN. The test results as shown in Figure 51(a)) had a good correlation between the ratio of G-Stability to G-Flow and the ratio of flow number to flow time (Figure 51(b)). The correlation measure of R^2 (coefficient of determination) was 92% indicating a strong correlation between the two test methods.

Since the objective of the correlation effort was to gauge interchangeability and compatibility between FN and G-Stability test results, material properties and mixture design of the tested mixtures were not of interest. However, the one important material property was the quality of RAP used. Mixtures that end with 15 had good quality RAP, while mixtures ending in 23 had poor quality RAP. As stated before, SLX mixtures are characterized by having finer aggregates, more binder content, better quality binder, and less percentage of RAP. As a result, SLX is typically used on high traffic roads. SPR is an intermediate mixture used on medium to high traffic roads as a surface course while the SRM is typically a base mixture.
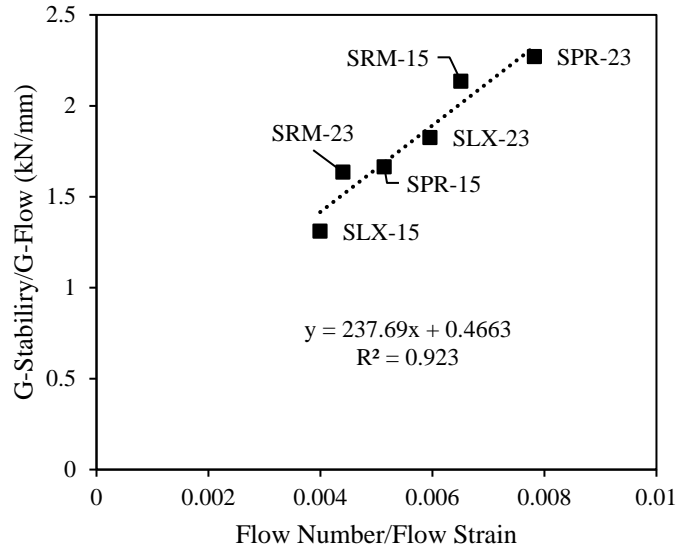
(a)
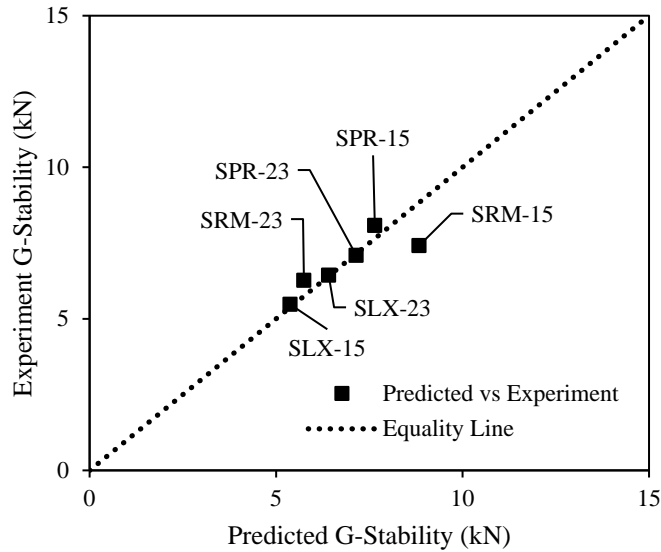
(b)

Figure 51. Correlation between G-Stability vs. FN test results: (a) with the outlier and (b) without the outlier

After confirming a good correlation between FN and G-Stability, a comparison study was conducted between the actual experimental results and predicted values. The equation of the linear relationship between the two tests shown in Figure 51(b) was used to predict G-Stability from FN results as such:

$$\frac{G_{Stability}}{G_{Flow}} = 237.69 \frac{F_{Number}}{F_{Strain}} + 0.4663 \qquad (4.1)$$

Where $G_{Stability}$, G_{Flow}, F_{Number} and F_{Strain} are the G-Stability, G-Flow, flow number, and flow strain, respectively. By taking G-Flow of 3.92 mm which is the average from all G-Stability test here-in, the equation (4.1) then becomes:

$$G_{Stability} = 902.77 \frac{F_{Number}}{F_{Strain}} + 1.77 \qquad (4.2)$$

Using the equation (4.2), G-Stability was then predicted and the results are shown in Figure 52 which is an equality graph. The predicted and actual experimental results of G-Stability were reasonably close to the equality line implying that the developed G-Stability and FN test results are interconvertible.
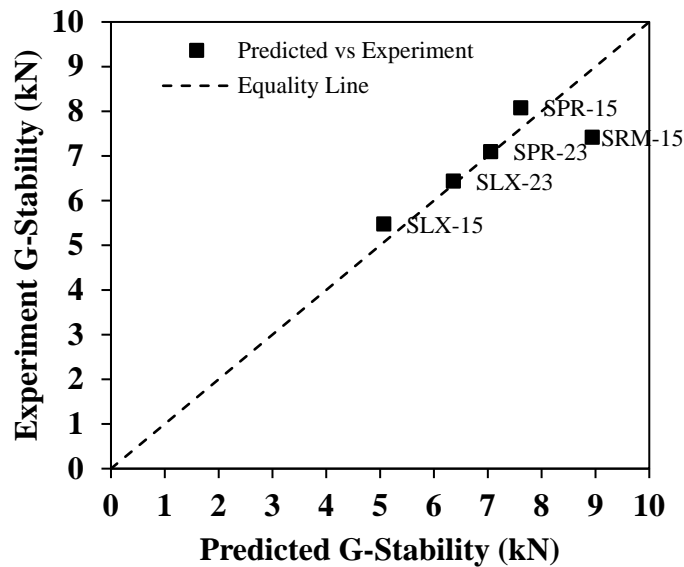
Figure 52. G-Stability predicted from FN vs. experimental results.

100

4.7. **Summary**

In this chapter, the G-Stability test which simple, practical, and easily implementable rutting test was developed and correlated to the existing and established flow number test. Critical testing parameters for the G-Stability test were determined based on repeatability and practicality. The test parameters were temperature, loading rate, specimen thickness, and the recommended minimum number of replicates. In addition, sensitivity analysis of the G-Stability test to the existing difference in mixtures was investigated by testing different mixtures and comparing the outcomes. Finally, the correlation study was conducted so several Nebraska mixtures from different locations to gauge the interconvertibility of the G-Stability with FN results.

The G-Stability test is simpler, fast; it requires less effort, logistics, and time to conduct. The recommended testing parameters for G-Stability are summarized in Table 9. The developed test showed good correlation and interconvertibility with the FN (flow number) test.

Table 9. Recommended Values for G-Stability Testing Variables

Critical Testing Variable	Recommended Value
Number of replicates	≈3
Thickness of specimen	≈ 50 mm
Notch length	≈15 mm
Loading rate	50 mm/min
Testing temperature	≈54°C

CHAPTER V

PERFORMANCE-BASED MIXTURE DESIGN OF HIGH-RAP MIXTURES WITH

REJUVENATORS*

Proper use of rejuvenators can improve properties and performance of aged asphalt mixtures; however, there is currently a lack of understanding of how rejuvenator treatment details such as type-dosage of rejuvenators and blending-curing of rejuvenation affect material properties and performance characteristics. This study thus aims to investigate the effects of type, dosage, and treating methods of rejuvenators when they are added in aged bituminous materials. To meet the goal, three rejuvenators were selected categorized by their production technology to improve a high-recycled asphalt pavement (RAP) mixture by conducting various binder-level and mixture-level tests. For the binder-level testing, the performance grading (PG) method was used to primarily determine proper dosages targeting desired binder grades. The selected dosage levels from the binder testing were then applied to mixture-level performance evaluation by conducting two tests: flow number for rutting and semicircular bending fracture for cracking. Test-analysis results indicated that PG binder testing, although it can successfully determine the proper dosage range of rejuvenators, it is limited to only assess the effects of rejuvenators in rheological properties, which can be better aided by integrating chemical characterization that provides a more in-depth material-specific rejuvenation process. In addition, it appears that rejuvenation methods (e.g., blending and/or curing) can alter the performance of aged mixtures.

Therefore, the selection of rejuvenators and their implementation into practice should be carried out by considering multiple aspects not only by its PG recovery.

5.1. **Introduction**

The use of reclaimed asphalt pavement (RAP) materials in producing asphalt mixtures offer great benefits by reducing costs for producers and highway agencies as well as reducing the environmental impact associated with the extraction, transportation, and processing of virgin materials. Currently, most states allow up to 40–50% of RAP for primary types of asphalt mixtures. Maximum use of RAP materials into asphalt mixtures has been desired; however, it is not a simple task because of undesired inherent characteristics of RAP such as aged (stiff) asphalt binder and inconsistent aggregate properties. To overcome the inherent concerns of RAP materials, many researchers have made significant efforts in various ways.

Since RAP has been severely aged, it is much stiffer and brittle relative to a new asphalt mixture. As results, RAP can transfer its stiffness and brittleness to the final mixture and causing durability issues if mixed with virgin mixture without treatment (Tam, Joseph et al. 1991, McDaniel, Shah et al. 2007, Daniel, Pochily et al. 2010, West 2010, Al-Qadi, Aurangzeb et al. 2012, Khosla, Nair et al. 2012, West, Willis et al. 2013). Several strategies have thus been employed to address the durability issues associated with the use of RAP, and among the various options, using rejuvenators has been a quite conventional practice for the last decade because of their effectiveness to immediately alter the mechanical properties of mixtures even with high-RAP content (more than 50%).

The effects of rejuvenation to reduce stiffness/brittleness of aged materials have been well documented in many studies. Im and Zhou (2014) examined the stiffness of recycled mixtures treated with three types of rejuvenators, namely: triglycerides & fatty acid, an aromatic

extract type, and tall oil. The first two rejuvenators were introduced to the virgin binder at a rate of 0.6 and 1.5% of the total weight of asphalt binder, while the third one was directly introduced into the recycled materials at a dose of 2% by weight of the recycled materials. The results showed that rejuvenators minimally affected mixture stiffness at lower temperatures (i.e., 4 °C and 20 °C) relative to its unrejuvenated mixture, while rejuvenators could significantly reduce stiffness at the higher temperature (e.g., 40 °C). Another study by Kaseer, Yin et al. (2017) observed stiffness reduction of high-RAP mixtures due to the addition of rejuvenators in several types of mixtures, binders, aggregates, and recycled material. A similar observation was made in the case of bio-rejuvenators (Oldham, Hung et al. 2018).

When optimally using rejuvenators, fracture resistance of 100% recycled mixtures can even be greater than that of virgin mixtures(Zaumanis, Mallick et al. 2014). The optimality of a rejuvenator dose is typically determined using the performance grading (PG) system which compares the grade of proportionally mixed rejuvenated binder (mix of the virgin, aged binder, and rejuvenator) to that of a target PG binder grade (Tam, Joseph et al. 1991, Al-Qadi, Aurangzeb et al. 2012, Kaseer, Cucalon et al. 2018, Garcia Cucalon, Kaseer et al. 2019). Kaseer, Yin et al. (2017) showed that a continuous increase of rejuvenator dosage can result in mixtures that fail the rutting criterion. Although several studies have reported improved rutting resistance after the addition of rejuvenators into the mixture (Tran, Taylor et al. 2012, Mogawer, Austerman et al. 2013, Zaumanis, Mallick et al. 2013), other studies have reported reduced stiffness of rejuvenated mixtures which render them more prone to rutting (Jia, Huang et al. 2015, Im, Karki et al. 2016, Arámbula-Mercado, Kaseer et al. 2018).

Recently, many studies have investigated how mixtures/materials perform due to different treatments and dosages of rejuvenators so that an optimum rejuvenation practice can be

achieved. For instance, Tran, Taylor et al. (2012) employed the Superpave performance grade (PG) to find the amount of rejuvenator required to recover the performance properties of the recycled binders. Zaumanis, Mallick et al. (2014) evaluated the effect of different dosages of six rejuvenators on rheological and physical properties of extracted binders from RAP. They reported that the high and low PG temperatures have a linear correlation with the dose of rejuvenators while the penetration changes exponentially. They concluded that the Superpave PG requirements can be pursued for the optimization purpose of rejuvenators. More recently, Arámbula-Mercado, Kaseer et al. (2018) evaluated three different methods including (1) rejuvenating low-temperature PG and verifying high-temperature PG, (2) achieving $\Delta T_c = -5C$ after 20-hour pressure aging vessel (PAV) aging, and (3) rejuvenating high-temperature PG to explore the optimum dosage of rejuvenators. They claimed that the method to recover high-temperature PG is a reliable approach to determine the optimum dosage of rejuvenators.

It is well documented that proper use of rejuvenators can improve properties and performance of aged asphalt mixtures; however, there is currently a lack of understanding of how rejuvenator treatment details such as type-dosage of rejuvenator and blending-curing of rejuvenation affect terminal material properties and long-term performance characteristics. The rejuvenator penetration/blending process is critical to the resulting performance of the mixture especially towards the broad implementation of rejuvenated mixtures(Mogawer, Booshehrian et al. 2013, Kriz, Grant et al. 2014, Ma, Huang et al. 2015). Based on outcomes from other relevant studies, it is hypothesized that the effects of type, dosage, and treating methods of rejuvenators in recycled asphaltic materials can be reasonably pursued by investigating the two core aspects; chemical and mechanical properties.

5.2. **Objectives and Research Methodology**

This study thus aims to investigate the effects of type, dosage, and treating methods of rejuvenators by conducting laboratory evaluation at both binder-level and mixture-level. To meet the goal, this study selected three rejuvenators categorized by their production technology.

The specific objectives of this effort are:

1) To evaluate the effects of rejuvenator type and dosage on rheological (mostly based on the Superpave PG method) characteristics of binder that is blended with different rejuvenators, and

2) To evaluate the effects of treating (e.g., blending and curing) methods of rejuvenators on fracture and rutting performance of high-RAP mixtures.

Figure 53 presents the experimental program designed for binder and mixture-level testing. For each rejuvenator, varying dosages per total weight of VBR (65% VB and 35% RAB) were investigated. The effects of the rejuvenators were then examined using Superpave performance grading (mechanical recovery). Subsequently, each rejuvenator with its proper dose determined by the Superpave PG method (Figure 53(a)) was applied to mixture level testing for further investigation as shown in Figure 53(b). In addition to the types of rejuvenators, attention was also paid to the mixing-curing methods on the mixture-level. The R2 rejuvenator was shear mixed into the virgin binder in addition to direct mixing into RAP, and the curing for 5 minutes was considered for the mixture with R2 to be compared with the case without curing. R3 was further incorporated with an antistripping agent to investigate the integrated effect of rejuvenator and antistripping agents against moisture susceptibility in high-RAP asphalt mixtures. The mixtures were tested using the flow number test whose results were later converted (using equation (4.2)) to G-Stability results for PSD analysis.

106
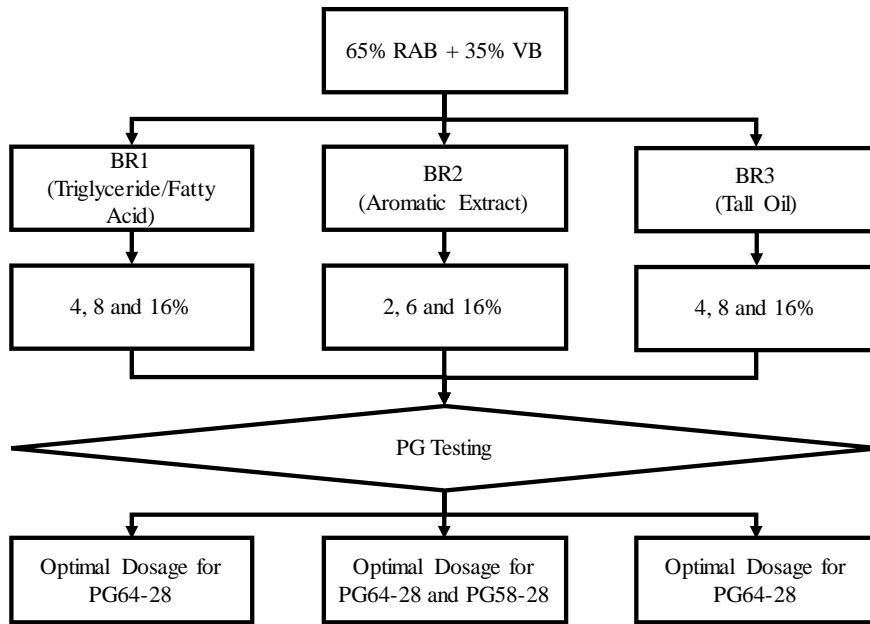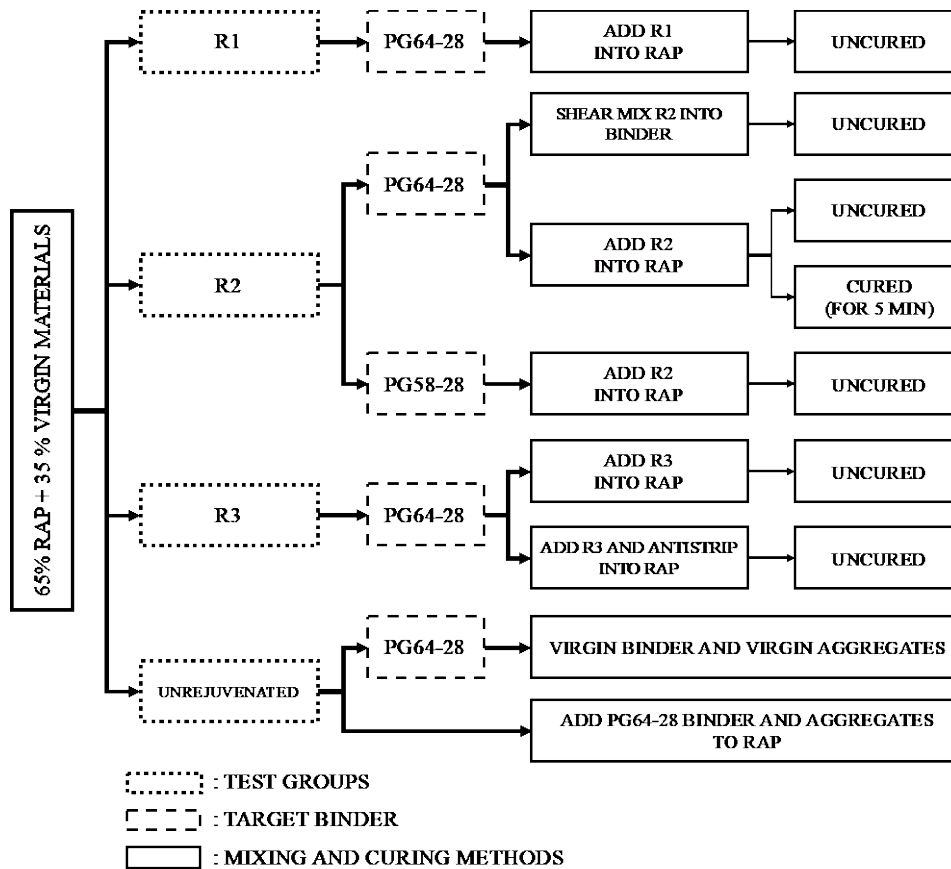
Figure 53. Research methodology used for: (a) binder testing; (b) mixture testing.

5.3. **Materials**

5.3.1. Rejuvenators and Asphalt Binder

Three types of rejuvenators were selected and categorized by their production technology: triglycerides & fatty acids (R1) rejuvenator which was derived from vegetable oils; an aromatic extract type (R2) rejuvenator which originated from refined crude oil products with polar aromatic components and; a tall oil (R3) rejuvenator which was a paper industry byproduct is classified in the same chemical family as liquid anti-stripping agents and emulsifiers. Table 10 lists the rejuvenator and anti-stripping additives used.

Table 10. Rejuvenators and Anti-Stripping Additive

Additives	Type	ID
Triglyceride/Fatty Acid	Agriculture Technology	R1
Aromatic Extract	Petroleum Technology	R2
Tall Oil	Green Technology	R3
Anti-Stripping	Liquid	AS

5.3.2. Asphalt Concrete Mixture

RAP materials and aggregates used here-in were collected from a conveyor belt of an asphalt plant before mixing and then transported to the testing laboratory in sampling sacks. The target gradation of all AC mixtures prepared was that of a typical mixture used in Nebraska on medium trafficked road sections called SPR. It should be noted that since the gradation of SPR originally

contained 45% of RAP, the final gradation was adjusted to meet the target 65% RAP by simply

adjusting the proportion of virgin aggregates added to the total blend.

With the aggregate gradations determined, AC mixtures were prepared by adding a virgin

binder, rejuvenators, and antistripping agent where applicable according to the experimental

design. The required amount of VB (virgin binder) content in percentage of the total weight was

calculated as follows:

$$VB = \left(\frac{100}{100 + \mathrm{R}_{dosage}} \right) P_b - RAB \qquad (5.1)$$

where R_{dosage} is the percent rejuvenator content, P_b is the percent total binder content, and

RAB is the percent RAP content.

Equation (5.1) accounts for the effect of pre-existing binder in RAB, rejuvenator dosage,

and the total binder was used in this study. A previous study by the authors found that tall-oil-

based rejuvenator (e.g., R3) was relatively more susceptible to moisture damage compared to

others type of rejuvenators (i.e., R1 and R2)(Tran, Taylor et al. 2012, Haghshenas, Nabizadeh et

al. 2016). As a result, in this study, 0.7% of the total binder (RAB + VB) was used for the

antistripping agent that is included in the mixture with R3. The target total binder and additive

(i.e., rejuvenator for R1 and R3 and, antistripping in addition to rejuvenator for R3) content was

5.2% per total weight of the mixture.

5.4. **Sample Fabrication and Test Set-Up**

5.4.1. Rejuvenators and Asphalt Binder

The old (i.e., aged) asphalt binder denoted as RAB (recycled asphalt binder) was separated from

RAP by using a solvent (e.g., toluene) and subsequently standard methods: ASTM D2172

(Standard Test Methods for Quantitative Extraction of Asphalt Binder from Asphalt Mixtures)

and ASTM D7906 (Standard Practice for Recovery of Asphalt from Solution Using Toluene and

the Rotary Evaporator) were used to retrieve the RAB from the solvent mix. In addition to the

RAB, a virgin binder (VB) with the Superpave performance grading of PG 58-34 was used as a

control binder. As shown in Table 11, for each rejuvenator (i.e., R1, R2, and R3), three different

dosages based on the total weight of binder were used into VBR (virgin binder mixed and RAB).

Table 11. Information on Binders Used

Binder Description	Binder ID
Control Binder: Virgin Binder (PG 58-34)	VB
Extracted Binder from RAP	RAB
Virgin Binder (35%) + RAB (65%)	VBR
VBR + R1 (4, 8, 16%)*	BR1 (4, 8, 16)
VBR + R2 (2, 6, 16%)*	BR2 (2, 6, 16)
VBR + R3 (4, 8, 16%)*	BR3 (4, 8, 16)

*dosages of each rejuvenator (by the total weight of binder)

5.4.2. Asphalt Concrete Mixture

For AC fabrication, virgin aggregates were heated overnight at SPR mixing temperature of

160°C for 12 hours to remove moisture while VB and RAP were heated for only two hours in the

oven at the mixing temperature. Rejuvenators were not heated before mixing due to their very

volatile nature thus, they were added to RAP right before mixing. After mixing, a short-term aging period was allowed at the compaction temperature of 138°C. The Superpave gyratory compactor (SGC) was used to fabricate two different testing specimens. For the rutting performance evaluation, FN (flow number) testing specimens (150 mm tall and 100 mm diameter cylindrical specimens) were fabricated by cutting and coring of SGC cylindrical samples of 170 mm tall and 150 mm diameter at target air voids of 4% ± 0.5. For cracking performance evaluation, SCB (semicircular bending) specimens were fabricated. After room temperature conditioning for 24 hours, SGC cylinders compacted at target air voids of 7% ± 0.5 were sliced into 50 mm thick disks, and the disks were halved into two semicircular shaped samples, followed by the introduction of a 15 mm long and 2 mm wide notch in the mid-bottom (Nsengiyumva 2015, Nsengiyumva and Kim 2019). For the moisture conditioning group, AASHTO T-283 method was used.

5.5. **Results and Discussions**

5.5.1. *Rejuvenators and Asphalt Binder Results*

Dynamic shear rheometer tests were conducted on 25 mm diameter binder samples to obtain the temperatures at which the permanent deformation (rutting) parameter (i.e., $G^*/\sin\delta$) of original and short-term (RTFO) aged binders meet the performance grade (PG) criteria. Bending beam rheometer (BBR) tests were also performed on binder samples aged through RTFO plus PAV procedures to determine the temperatures at which relaxation constant (m-value) and flexural creep stiffness (S) at 60 s of loading were equal to 0.3 and 300 kPa, respectively. Then, the obtained high and low temperatures were used to determine the continuous performance grades of each binder blend.

The high and low-temperature performance grades of VBR (blend of extracted binder from the RAP and virgin binder) and each rejuvenated asphalt binder are shown in Figure 54. The results show that the addition of rejuvenators decreased both high and low temperatures grades of VBR. This observation confirms that the rejuvenators soften the aged asphalt binder as several studies showed (Haghshenas, Nabizadeh et al. 2016, Nabizadeh, Haghshenas et al. 2017, Elkashef, Williams et al. 2018, Haghshenas, Nsengiyumva et al. 2019). Figure 54(a) demonstrates that the high-temperature PG controls the maximum allowable dosage of rejuvenator, while the low-temperature PG limits the minimum required dosage (Figure 54(b)). In addition, the range of dosage for each rejuvenator can be determined using the data presented in Figure 54 by targeting the PG of VBR binder to the desired PG such as 64-28 or 58-28. Test results indicate that the VBR binder requires a lower amount of R1 and R3 compared to R2 to meet the target PG. It should be noted the dosages determined using the PG method need to be defined and verified on the mixture-level to ensure acceptable performance at intermediate temperature.
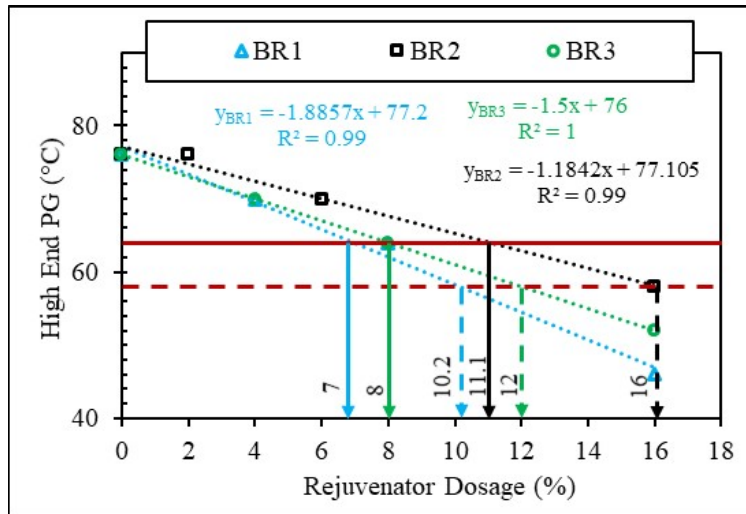
(a)
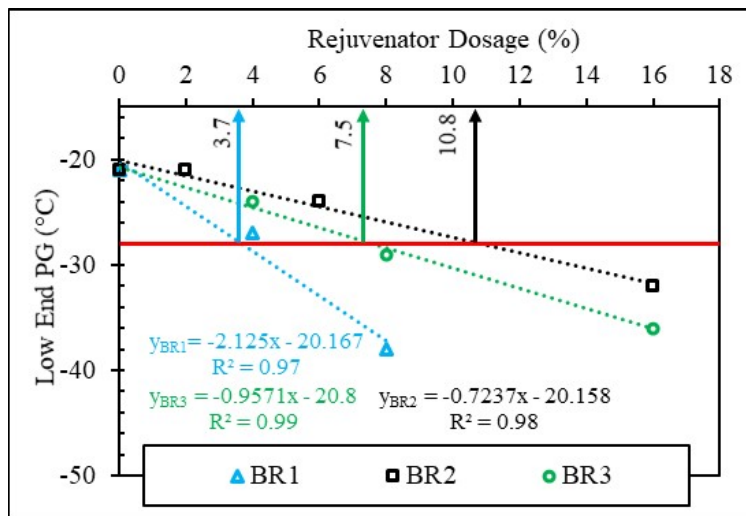
(b)

Figure 54. Test results of rejuvenated binders: (a) high end; (b) low end.

Table 12 summarizes the resulting minimum and maximum dosage range of each

rejuvenator to meet the target PG: either 64-28 or 58-28. The results of the Superpave

performance grade (PG) tests showed that all rejuvenators soften (measured by G* and δ, DSR

tests) binders which increases the rutting susceptibility (measured by G*/sinδ, DSR tests) and

improves the low temperature cracking resistance (measured by S(t) and m-value, BBR tests) of

the blend of extracted binder from the RAP and virgin binder. These trends intensified when the

amount of rejuvenator increased. Furthermore, the results of PG tests showed that there is a specific dosage range for each rejuvenator (so-called optimum/selected range) that can change the PG of the resultant blend (i.e., VBR) into its target binder which is PG 64-28/PG 58-34. The optimum range of each rejuvenator was then used to conduct mixture-level performance evaluation (i.e., flow number testing for rutting and semicircular bending fracture testing for cracking).

Table 12. Rejuvenator Dosage Range Selected from Binder PG Testing

Rejuvenator	Minimum Dosage (%)	Maximum Dosage (%)
	Target PG: 64-28	
R1	3.7	7
R2	10.8	11.1
R3	7.5	8
	Target PG: 58-28	
R1	3.7	10.2
R2	10.8	16.1
R3	7.5	12

5.5.2. Asphalt Concrete Mixture Results

The mixture-level testing program adopted in this study is shown in Table 13. The testing program was designed to investigate the effect of the rejuvenators selected, dosage, mixing, and curing method on mixture performance. To target PG 64-28, dosages of 7%, 11%, and 8% were selected for R1, R2, and R3, respectively. In addition, R2 was used to target PG 58-28 by using a dosage of 14%. It should be noted that for R3 mixtures, the selected dosage (i.e., 8%) was incorporated with an anti-stripping agent to check if the addition of an anti-stripping agent can improve the moisture susceptibility of mixtures treated by R3. For each mixture, three Superpave

gyratory compacted (SGC) tall samples were prepared to conduct the flow number testing with

two replicates and SCB testing with three replicates in both dry and wet conditions.

Table 13. Final Mixture-Level Testing Program

TEST GROUP	DOSAGE	MIXING AND CURING METHODS		MIXTURE ID
R1	7%	ADD R1 INTO RAP	UNCURED	R1-7-UNCURED
	11%	SHEAR MIX R2 INTO BINDER	UNCURED	R2-11-VBR2
R2	11%	ADD R2 INTO RAP	UNCURED	R2-11-UNCURED
	11%	ADD R2 INTO RAP	CURED	R2-11-CURED
	14%	ADD R2 INTO RAP	UNCURED	R2-14-UNCURED
R3	8%	ADD R3 INTO RAP	UNCURED	R3-8-UNCURED
	8%	ADD R3 AND ANTISTRIPPING INTO RAP	UNCURED	R3-8-AS-UNCURED
UNREJUVENATED	N/A	VIRGIN BINDER AND VIRGIN AGGREGATES		CONTROL-VIRGIN
	N/A	ADD PG64-28 BINDER AND AGGREGATES TO RAP		CONTROL-RAP

Flow number testing was conducted at 54.0°C which required specimens to be

temperature conditioned for at least 24 hours inside the environmental chamber. The temperature

of specimens was cross-checked using a dummy specimen possessing a thermocouple in its core.

Loading was applied axially in a cyclic fashion at deviatoric stress of 600 kPa and contact stress

of 32 kPa. The testing stresses and temperature were determined following the recommendation

(Witczak, Pellinen et al. 2002, Haghshenas, Nsengiyumva et al. 2019). It is noted that the flow

number test involves purse loading of the deviatoric stress for 0.1 seconds and a rest period (at

the contact stress) for 0.9 seconds. The accumulated strain due to specimen deformation was

recorded after each loading cycle. It should be noted that the flow number results were converted

(using equation (4.2) to G-Stability results for PSD analysis in the subsequent section.

As mentioned, two FN replicates were tested per mixture to assess the rutting performance of the mixtures. The test stopped when the accumulated strain reached 5% (i.e., 50,000 $\mu\varepsilon$) or when the number of loading cycles reached 10,000. During testing, the rate of strain accumulation was being calculated in real-time. Figure 55(a) presents the results of the flow number test as accumulated strains vs. loading cycles. The test results between the two replicates were generally repeatable. Figure 55(b) presents averages of the two replicates of each mixture and it shows that all rejuvenator-treated mixtures were softer compared to untreated control mixture (i.e., CONTROL-RAP).

For a more quantitative evaluation of the effect of rejuvenators on AC mixtures, the flow number was found by taking a numerical derivative of results to capture the number of loading cycles at which the minimum strain rate was achieved. The minimum strain rate occurs onset of the tertiary flow that is well correlated with field rutting of mixtures (Witczak, Pellinen et al. 2002). Figure 55(c) shows the resulting flow number of each mixture. As shown, the control mixture with RAP (i.e., CONTROL-RAP) and the mixture with 14% of R2 (i.e., R2-14-UNCURED) presented the highest and lowest flow numbers, respectively. The highest flow number from the CONTROL-RAP mixture was expected due to aging. In general, rejuvenator treated mixtures effectively softened the high-RAP mixture and tried to reach the virgin mixture, CONTROL-VIRGIN, which demonstrates that the rejuvenator dosages were found from the binder-level testing program are appropriate for mixture-level deformation characteristics.

Among the rejuvenated mixtures, three R2 rejuvenated mixtures (i.e., R2-11-CURED, R2-11-UNCURED, and R2-14-UNCURED) presented lower flow numbers (i.e., faster deformation gain) than the control virgin mixture (CONTROL-VIRGIN), whereas when R2 was shear-mixed with the aged binder, the mixture was stiffer than the control virgin mixture. This

116

indicates, although it is limited to make any definite conclusions at this stage, that the blending

of rejuvenators may affect the mechanical behavior of RAP mixtures. The effect of curing after

adding rejuvenator can be assessed by comparing two R2 mixtures: R2-11-CURED to R2-11-

UNCURED. Curing for 5 min after adding rejuvenator reduced the flow number value by 33.5 %

(i.e., from 800 to 532) which implies that curing may help rejuvenators to soften further AC

mixtures. However, for practical purposes, curing may not be necessary since the mixture

without curing is by itself softer than the virgin mixture. An increase in rejuvenator dosage (i.e.,

from 11% to 14%) resulted in a softer mixture (R2-11-UNCURED vs. R2-14-UNCURED).

Regarding mixtures with R3, the flow number was higher than R2 mixtures and somewhat

further different from the target CONTROL-VIRGIN. It is also noted that the R3 mixture with an

antistripping agent (i.e., R3-8-AS-UNCURED) was softer than its counterpart (i.e., R3-8-

UNCURED), which implies that the antistripping agent may help additional softening of high-

RAP mixtures.
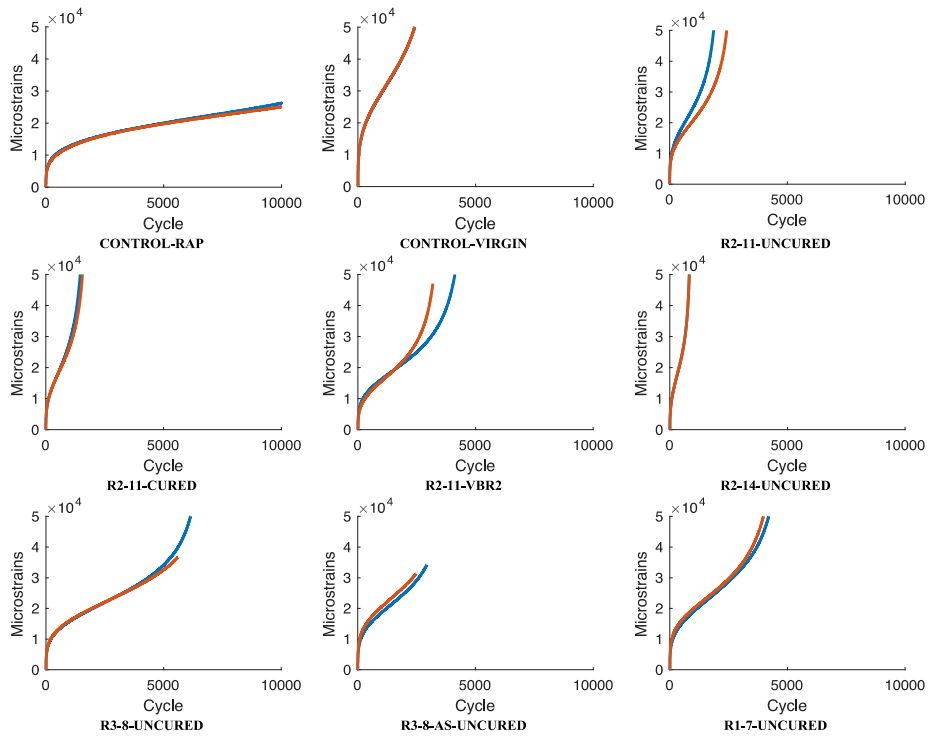
(a)
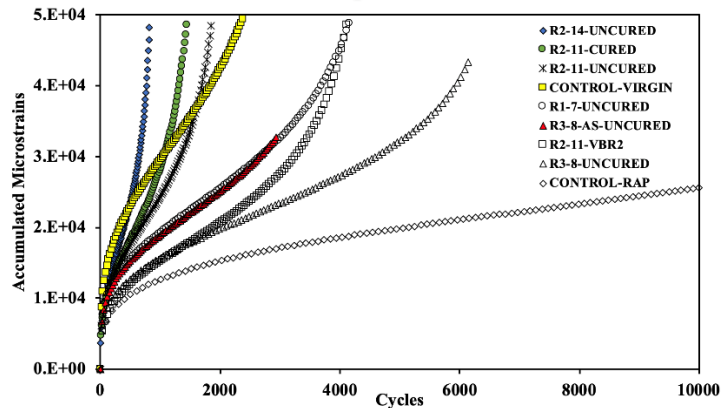
(b)
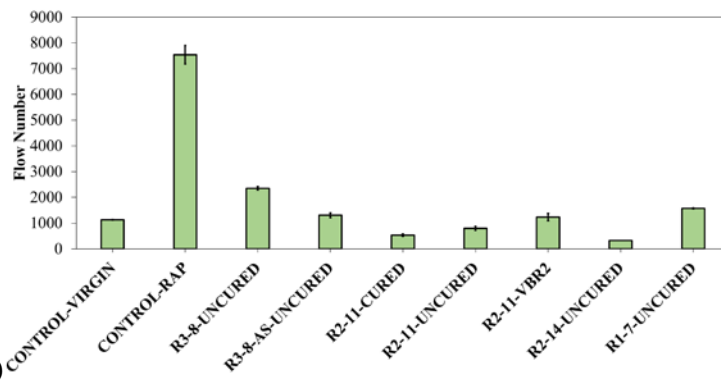
(c)

Figure 55. Flow number test results: (a) two replicates of each mixture; (b) averages of all mixtures; (c) comparison of flow numbers of all mixtures.

To perform a full performance-based mixture design, they need to be a fracture test. The SCB test was conducted in a displacement-controlled mode at a rate of 3 mm/min (Nsengiyumva 2015, Nsengiyumva and Kim 2019). Averaged (i.e., of three replicates) SCB results of all mixtures in both dry and wet conditions are presented in Figure 56(a). Overall, due to higher stiffness introduced by RAP, CONTROL-RAP showed the highest peak loads for both dry and wet conditions which were then noticeably reduced once rejuvenators were introduced. In addition, moisture conditioned specimens were in general more compliant than their dry counterparts in all test cases. The increased compliance in wet SCB specimens was especially apparent in the post-peak regions of the test results. At this point, it is uncertain as to why wet specimens had increased compliance compared to dry specimens. By comparing results of R3 with and without the antistripping agent, it is obvious that the agent improved moisture resistance of R3 mixtures by minimizing the difference of results obtained from the wet and dry conditions.

For a better comparison between the mixtures, all averaged SCB curves were plotted together in Figure 56(b) and Figure 56(c) for dry and wet conditions, respectively. Clearly, the two control mixtures (i.e., CONTROL-RAP and CONTROL-VIRGIN) showed the highest and lowest peak load regardless of moisture conditioning. In general, rejuvenator treated mixtures effectively improved fracture resistance of the CONTROL-RAP and reached the virgin mixture, CONTROL-VIRGIN. This demonstrates that the rejuvenator dosages found from the binder-level PG testing are effective for the mixture-level fracture resistance.

From the force-displacement curves presented in Figure 56 (b) and Figure 56 (c), the flexibility index (FI), which is considered a fracture resistance indicator of asphaltic mixtures, was obtained, and the results are shown in Figure 56 (d). Overall, all mixtures showed higher FIs

from moisture-conditioned samples compared to dry samples with an exception of R3 mixture added with an antistripping agent. Currently, it is not clear why moisture conditioned mixtures presented higher FI values than dry mixtures. Rejuvenator-treated mixtures increased FI of CONTROL-RAP and became closer to the FI of target CONTROL-VIRGIN. R2 mixtures in dry conditions performed similarly with a minimal effect of curing and blending method. The increased content of the rejuvenator improved crack resistance. The antistripping agent in the R3 mixture increased FI in dry case, however less effective when the mixture was moisture conditioned. Despite the improvement in fracture resistance due to rejuvenators, rejuvenated mixtures could not reach the level of fracture resistance of the target virgin mixture. The implication is that mixture-level rejuvenation is only partial even with optimal rejuvenation in binder-level.
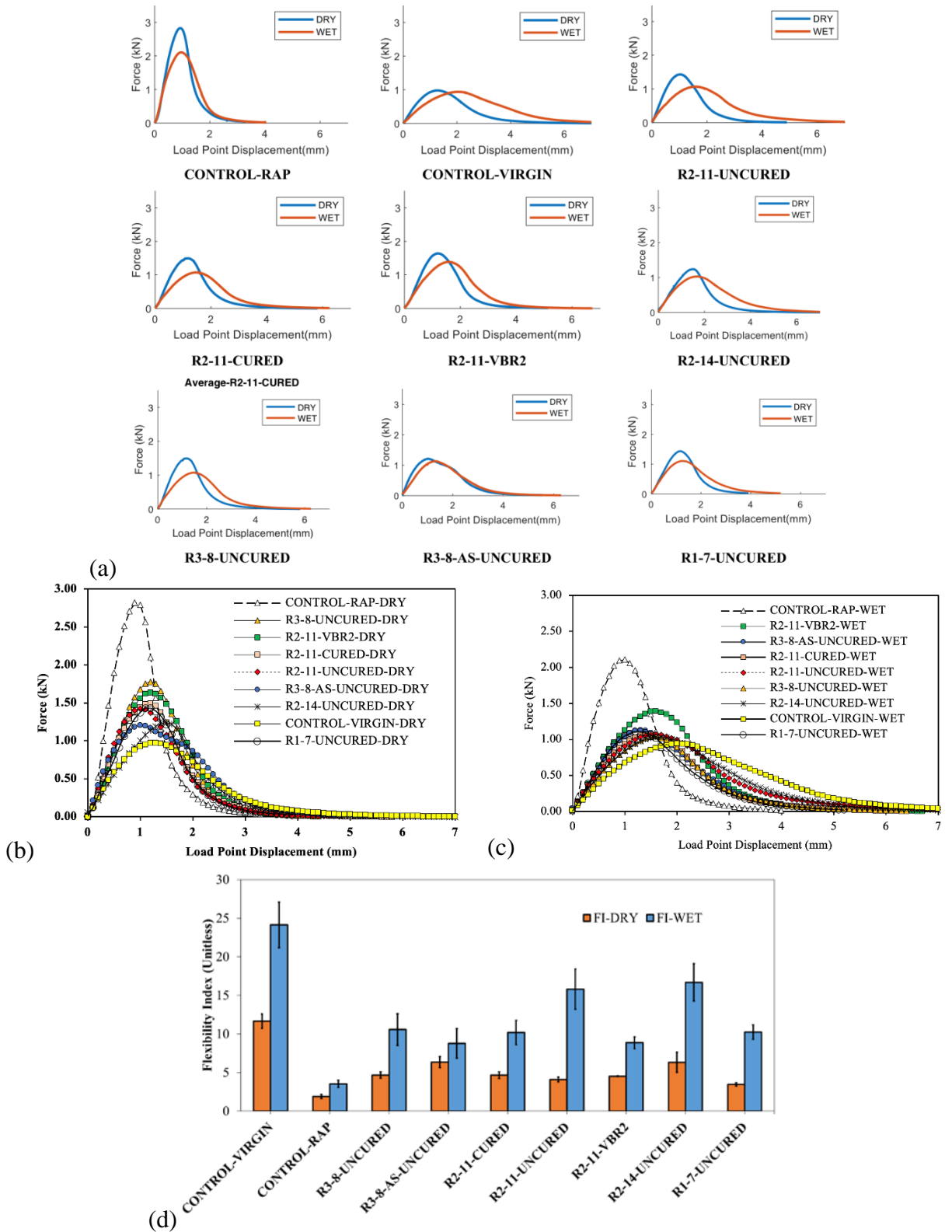
Figure 56. SCB test results: (a) dry and wet conditions for each case; (b) combined plots of dry condition; (c) combined plots of wet condition; (d) FI of each mixture.

121

For a more objective comparison of mixtures under moisture, the *WFR* (work of fracture ratio) was initially proposed by Kim, Zhang et al. (2012) and is calculated as a ratio of fracture energy under wet condition (G_{f_WET}) to fracture energy under dry condition (G_{f_DRY}) as follows:

$$WFR = \frac{G_{f\_WET}}{G_{f\_DRY}} \qquad (5.2)$$

WFR results in Figure 57 show that the virgin mixture (CONTROL-VIRGIN) and the R3 mixture without AS (R3-8-UNCURED) had the highest and lowest value of WFR, respectively. Interestingly, the CONTROL-RAP mixture performed better than the R3 without the antistripping agent indicating that if used alone, R3 rejuvenators can produce highly moisture susceptible mixtures. This observation agrees with a previous study (Haghshenas, Kim et al. 2018). The results also show that although the addition of AS to R3 mixture (R3-8-AS-UNCURED) helped increase *WFR*, the improvement was slight and the final *WFR* was comparable to that of the unrejuvenated mixture (CONTROL-RAP). The result implies the limited capacity of the antistripping to improve the moisture resistance of mixtures rejuvenated with R3.

Figure 57 shows that curing the rejuvenated mixture (R2-11-CURED vs. R2-11-UNCURED), negatively impacted the moisture damage resistance by reducing *WFR*. Even though shear mixing R2 into VB (R2-11-VBR2) reduced the *WFR*, which remained higher than one. It should be noted that, in this study, a mixture with a *WFR* larger than one is considered to be moisture resistant. *WFR* results also show that increasing dosage of rejuvenator (i.e., R2-11-UNCURED vs. R2-14-UNCURED) minimally affected mixture performance under moisture.

With these limited results, it can be implied that rejuvenator type and curing-blending methods affect the performance of mixtures under moisture conditions.
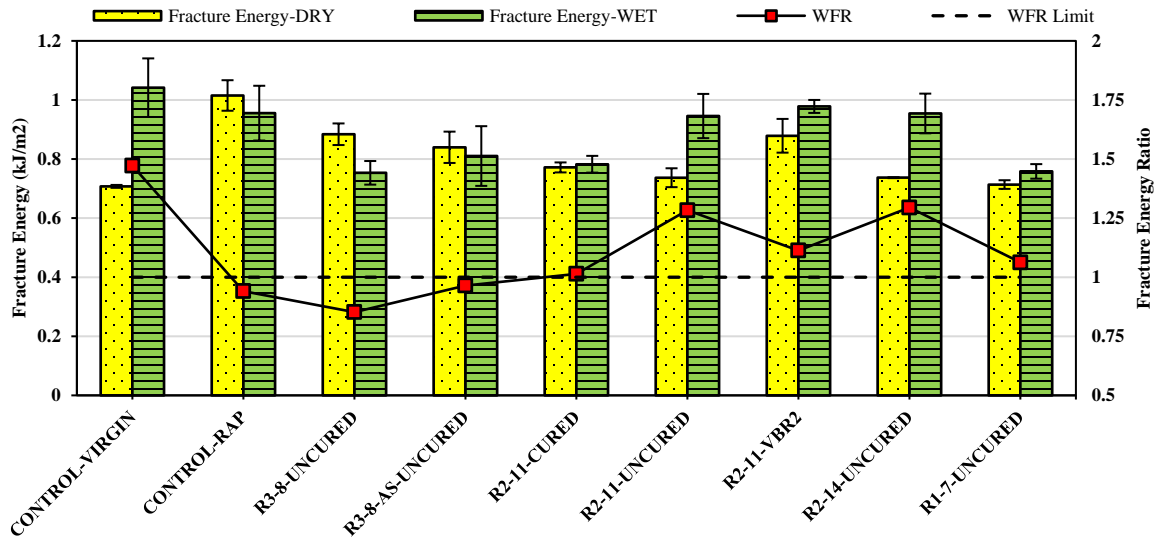
Figure 57. Work of fracture energy.

5.5.2.1. Performance Space Diagram

PSD (performance space diagram) is an important tool for the implementation of performance-based mixture design as it allows for graphically representing mixtures according to their fracture and rutting performances. The graph is a two-dimensional representation of the performance of a mixture to help engineers gauge the mixture's overall performance spectrum. A common practice for PSD is to plot the fracture- and rutting related indicators on the y-axis (vertical) and x-axis (horizontal), respectively. Test results of the mixture for both rutting and fracture are then used as coordinates on the graph.
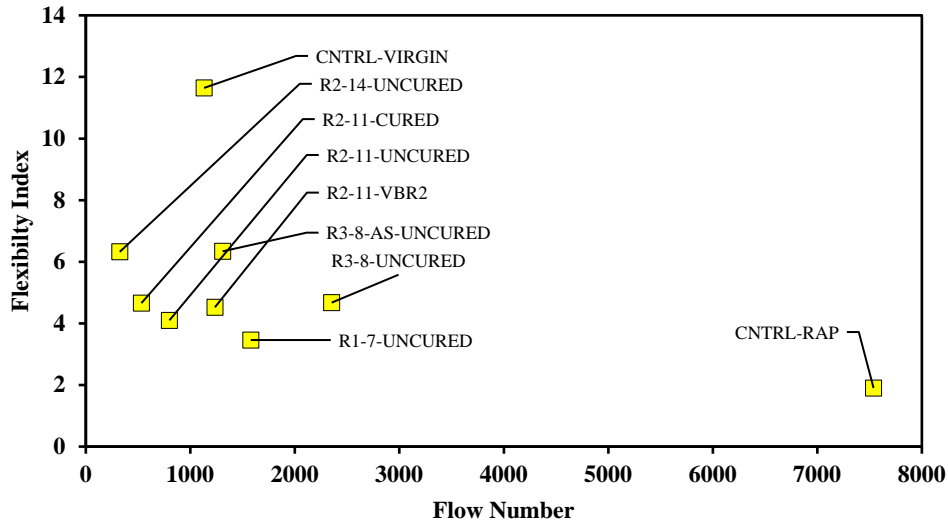
Figure 58. PSD of high-RAP mixtures tested in the dry condition: FI vs. FN.

Using the two AC performance measurements (FN and FI), a performance space diagram (PSD) can be developed as shown in Figure 58. A stiff mixture is preferable to minimize rutting while a soft and more compliant mixture is usually well suited for crack prevention in AC. Figure 58 demonstrates the contribution of rejuvenation by R2 and R3. The two rejuvenators softened mixtures (i.e., from FN of around 7,000 to FN less than 3,000), while increased FI more than twice. It can be noted that mixtures with higher FN and FI are desired for better performance of both rutting and fracture. It is also seen that the curing of R2 mixtures resulted in a reduced FN while marginally improving FI. In contrast, shear mixing of R2 into virgin binder increased FN by more than 50% (from 800 to 1,200), while minimally affecting FI. This implies that shear mixing of R2 into binder could be an attractive way if the mixing process (i.e., mixing R2 with the virgin binder, and then mixed with RAP and virgin aggregates) can be permitted without significant modification to the existing plant facility. PSD also shows that the antistripping agent improved fracture resistance of the R3 mixture, while rutting resistance was somewhat reduced. The increase of FI indicates an additional benefit of the antistripping agent

124

other than moisture damage mitigation. It is noted that a more realistic and long-term PSD can be

obtained by considering SCB testing on aged AC mixture as aging negatively affects fracture

resistance of the mixture in the long-term.
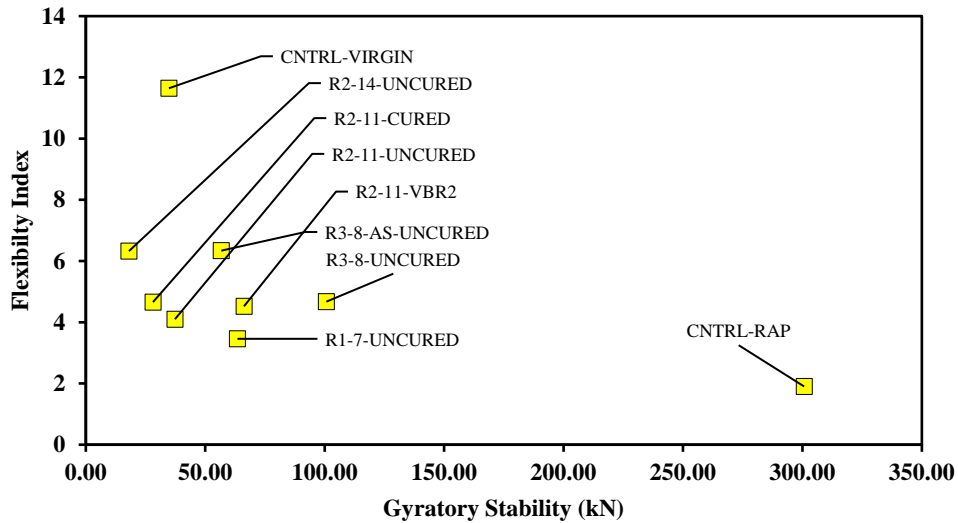
Figure 59. PSD of high-RAP mixtures tested in the dry condition: FI vs. G-Stability.

Figure 59 shows a PSD obtained by interconverting the FN results in Figure 58 into G-

Stability results using the equation (4.2). As can be seen in Figure 59, the PSD from the

converted G-Stability results agrees well with the experimental FN results (in Figure 58)

suggesting the validity of the interconversion relationship even on high-RAP mixtures. Another

observation is that the G-Stability results of the high-RAP mixtures are significantly higher than

that of typical mixtures such as SLX (Figure 48). The average G-Stability result of SLX, which

is a high-quality mixture, was around 10 kN on 50 mm thick specimens. On the high-RAP

mixtures, the minimum G-Stability was 18 kN (R2-14-UNCURED) and the maximum was 300

kN (CNTRL-RAP). The large difference in rutting performance (in terms of G-Stability) can be

attributed to the difference in RAP content. For typical mixtures such as SLX, the RAP content is

normally between 25-40%, while for the high-RAP mixtures, the RAP content was 65%. Even

with the added rejuvenators, the stiffness of the high-RAP mixtures remained higher than of a

typical AC mixture suggesting a possibility that the rejuvenation process of the high-RAP

mixtures was only partial.

A chemical investigation was conducted using the FT-IR (Fourier infrared) spectroscopy

into the interaction between aged binder (RAB) and rejuvenators at different dosages

(Nsengiyumva, Haghshenas et al. 2020). The results of FT-IR are shown in Figure 60 and are

presented in terms of the sum of the polar indexes of carbonyl index ($I_{C=O}$) and sulfoxide index

($I_{S=O}$). Both indexes have been used as potential indicators of the aging process by (Lamontagne,

Dumas et al. 2001, Feng, Yu et al. 2012). The results revealed that the rejuvenation process was

indeed partial regardless of the dosage and type. Rejuvenated binders can be artificially aged in

the laboratory using RTFOT (rolling thin-film oven test) and PAV (pressure aging vessel) for

short and long-term aging respectively. As expected, laboratory aging of the rejuvenated binders

increased their polar index ($I_{C=O} + I_{S=O}$) and was rejuvenator type dependent.
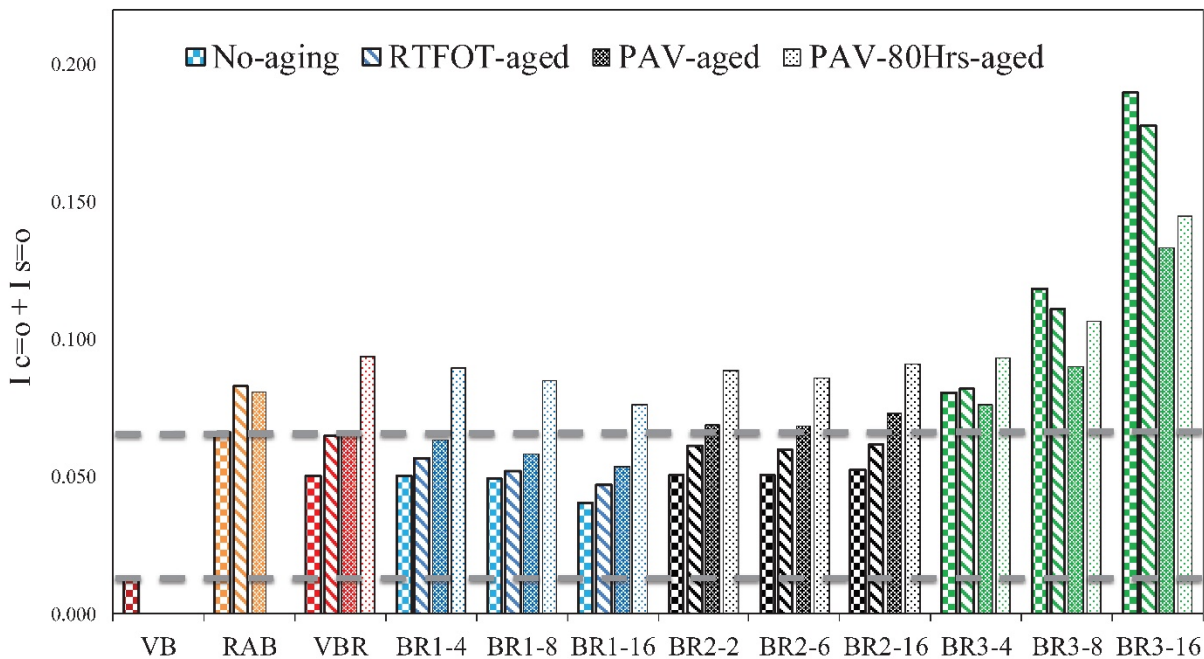
Figure 60. Polar index of binders under different aging-rejuvenation conditions(Nsengiyumva, Haghshenas et al. 2020).

In sum, PG binder testing was successfully used to determine the proper dosage range of each rejuvenator. However, the testing is limited to assessing the effects of rejuvenators on rheological properties (stiffness-oriented) only. It appears that chemical restoration is quite limited and rejuvenator dependent, which has been demonstrated by the FT-IR test results.

5.5.2.2. Short-time Performance Criteria

As aforementioned, key components of the performance-based mixture design method are the performance tests and performance criteria. Both fracture and rutting need to have criteria, which serve as thresholds to determine whether the performance of a mixture against the distresses is acceptable. The normal method to determine the criteria is to deploy the mixtures in the field and monitor their performance during service. Subsequently, the performance of mixtures in the field

is measured using traditional methods such as IRI (international roughness index), visual ranking, and automatic ranking (Rami and Kim 2015). The pavement engineer determines which mixtures and corresponding performance-related results that are acceptable (Kim, Mohammad et al. 2015).

Since G-Stability is a newly developed test, there is a lack of field performance data to determine appropriate performance criteria. However, for the FN test, NCHRP Report 673 by Jenks, Jencks et al. (2011) recommended traffic level-dependent rutting performance criteria based on field validation data. As the FN results are interconvertible into G-Stability results using the equation (4.2), it possible to infer rutting performance criteria of AC mixtures based on G-Stability results. It should be noted that this is a short-term solution to conducting field performance monitoring, which would require a significant amount of time to complete and out of the scope of this study. Nonetheless, field performance monitoring is underway on several pavement sections in Nebraska to establish the long-term performance criteria of the AC mixtures. Table 8 shows the FN rutting performance criteria per traffic level recommended by the NCHRP report 673 (Jenks, Jencks et al. 2011). The FN criteria were then converted into G-Stability to establish performance criteria in terms of G-Stability.

Table 14 Performance Criteria for Rutting in FN and G-Stability

Traffic Level (ESALs in Million)	Minimum Flow Number Requirement*	G-Stability (kN)**
<3	---	---
3 to <10	53	5.55
10 to <30	190	17.24
≥ 30	740	64.17

* recommended criteria from NCHRP report 673, page 142 (AAT, 2011)
** converted from the FN results using the equation (4.2)

The other criterion that needs to be determined is for the cracking performance in terms of FI. Similar to the G-Stability rutting criterion, long-term pavement performance monitoring data is needed to practically determine the cracking criterion. However, as the field data require a significant amount of time and cost, this study used the literature where SCB cracking criteria were investigated. Using the literature serves to establish a starting point (i.e., preliminary) while waiting for input from the pavement performance. It is of utmost importance to mention that different AC mixtures require different performance criteria. It is necessary to ultimately establish the performance criteria considering unique mixtures' characteristics, local conditions, and applications. For the FI, a threshold range of five to six is commonly accepted to distinguish poor to acceptable performance of mixtures (Ozer, Al-Qadi et al. 2016, Batioja-Alvarez, Lee et al. 2019) with exception of the Illinois DoT which uses a threshold of eight (Ali, Al-Qadi et al. 2020). In this study, the preliminary fracture performance criteria in terms of FI was selected as six.
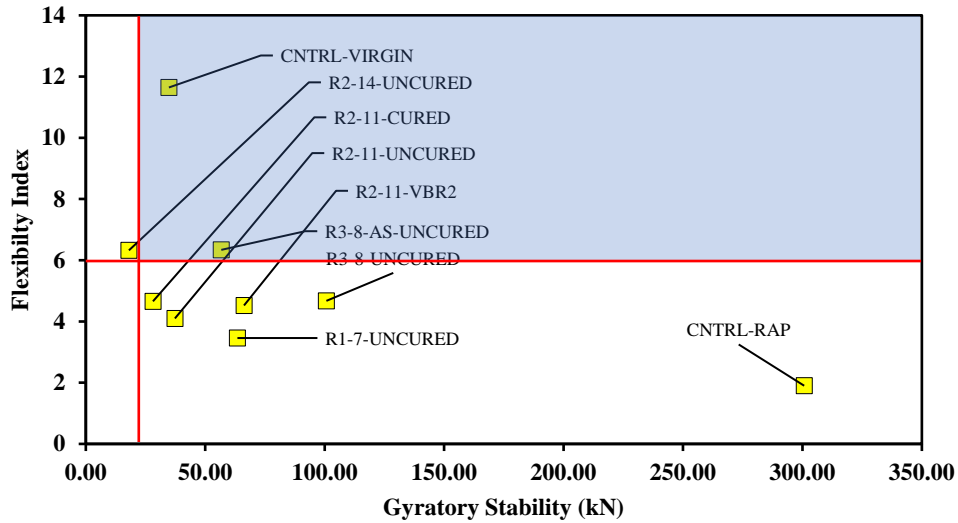
Figure 61. PSD of high-RAP mixtures with performance criteria.

Figure 61 shows the performance space diagram with performance criteria. For the rutting, a criterion of 17.24 kN G-Stability was selected to correspond to the traffic level of 10 to 30 million ESALs. Similarly, other levels of traffic can be selected for SPD from Table 8. The fracture criteria as FI was six. As the PSD shows, according to the performance criteria and the traffic level used, only one high-RAP mixture (R3-AS-UNCURED) along with the virgin mixture (CNTRL-VIRGIN) satisfied the threshold. This highlights the importance of a performance-based mixture design in high-RAP mixtures to show the effectiveness of rejuvenators and other additives. It should be noted that the R3-AS-UNCURED mixture contained was a tall oil rejuvenator with an added anti-stripping agent. Although the performance criteria need adjustment pending field monitoring results, the preliminary criteria can provide help designers improve their mixtures by targeting the blue-shaded corner in Figure 61 that represents an improvement in both rutting and cracking resistance.

130

5.6. **Summary**

This chapter presented efforts of performance-based mixture design on mixtures containing a high amount of RAP (i.e., 65% RAP) and treated with rejuvenators. Binder PG testing on extracted binder treated with rejuvenator was used to determine optimum rejuvenator dosages. Determined dosages were then used in AC mixtures to investigate the effects of type, dosage, and treating methods of rejuvenators on chemical-mechanical characteristics of high-RAP (i.e., 65% RAP) mixtures. Three popular types of rejuvenators: a triglyceride & fatty acid (R1), an aromatic extract type (R2) and, a tall oil (R3) were selected and used for various laboratory tests in the binder-level and mixture-level. Based on the test-analysis results, the following conclusions can be drawn.

- PG binder testing was successfully used to determine the proper dosage range of each rejuvenator. However, it is limited to assess the effects of rejuvenators in rheological properties (stiffness-oriented) only. It appears that chemical restoration is quite limited and rejuvenator-dependent, which has been demonstrated by the FT-IR test results.

- AC mixtures treated with rejuvenators at the dosage levels selected from the binder PG testing showed improved fracture resistance compared to unrejuvenated mixtures.

- Rejuvenation methods (e.g., blending and/or curing) can alter the performance of mixtures. For example, in this study, R2 softened mixtures more than enough when it was directly mixed into RAP, while its addition to binder (through shear mixing) improved both performances in a more balanced manner.

- The PSD showed that curing of R2 mixtures reduced rutting resistance (i.e., FN) while, shear mixing of R2 into virgin binder significantly increased FN. Fracture resistance (i.e., FI) was minimally affected by either curing or blending. Although post-aging fracture

131

testing is necessary for more long-term performance evaluation of rejuvenated mixtures, PSD results show that mixing R2 with the virgin binder and then mix with RAP and virgin aggregates could be an attractive way toward optimal rejuvenator practice.

- More studies that can evaluate the longer-term performance and economics of rejuvenated materials are necessary. Toward that end, using more realistic aging methods that can account for the combined effects of ultraviolet light, moisture, and vehicular stresses is recommended.

CHAPTER VI

INVERSE METHOD USING DIGITAL IMAGE CORRELATION AND FINITE ELEMENT

MODELING (DIC-FEM) TO IDENTIFY LINEAR MATERIAL PROPERTIES

This chapter presents the method to inversely compute the material properties via non-linear

optimization of DIC measurements and FEM simulation results. This chapter introduces several

components including the experimental set-up (i.e., DIC and mechanical testing machine),

numerical computation package, data analysis, and optimization software. The DIC-FEM inverse

method was applied to an example linear elastic material of PEEK (Polyetheretherketone) since

its elastic properties are well known. The accuracy of the DIC-FEM inverse method was

assessed by comparing the resulting elastic modulus from the optimization process to the known

property of PEEK. Subsequently, the DIC-FEM inverse method was used to identify linear

viscoelastic (LVE) material properties. As an example, FAM (fine aggregate matrix) of AC

(asphalt concrete) was selected. The analytical solution was used to assess the accuracy of the

inverse method on the LVE properties.

6.1. **Introduction**

Even with improved performance tests, identification of mixture components, and their

interactions that collectively contribute to mixture-level performance is still limited. As a result,

the performance-based mixture design is accomplished through recursive mixture testing in the

form of trial-and-error. This is both cumbersome and inefficient. To alleviate this, a linkage

between component properties and mixture performance via computational micromechanics

modeling is advantageous. However, directly obtaining component-level properties from AC

mixture testing presents challenges due to heterogeneity, anisotropy, nonlinear inelasticity, and damage growth in multiple forms. With advances in digital image correlation (DIC) and computation modeling, it is possible to experimentally measure and numerically model complex failure and deformation phenomena in heterogeneous materials. Subsequently, optimization of the results from numerical modeling (e.g., FEM) and DIC is used to inversely solve for unknown material properties.

6.1.1. Digital Image Correlation

DIC is a method of choice for measuring surface deformation through digital cameras and correlation algorithms. The DIC was pioneered by (Sutton, Wolters et al. 1983) in South Carolina and uses successively acquired images to deduce deformations of a measured target. The deformation information is extracted from each image by correlating the current image to the previous in the series.

The underlining principle of DIC involves taking successive images in time of a specimen under loading and deducing field deformations data by correlating (i.e., back-calculate) deformation gradients of several sections of the image (i.e., subsets). The success of DIC is highly dependent on ensuring the uniqueness of the subsets which translate to the convergence of the correlation. The uniqueness of subsets can be achieved by applying random contrasting speckles on the surface of the specimen (Figure 62). It should be noted that the correlation function is based on kinematics and assumes continuity between consecutive images. Despite being a contactless technique, DIC yields highly accurate results that can achieve sub-micron (sub-pixel) resolution (Vendroux and Knauss 1998).

134

Figure 62 Random contrasting speckle pattern applied to a specimen for DIC purpose.

Assuming a random, isotropic, and non-repetitive speckle pattern, DIC determines deformations by comparing the original to the current image through a subset matching technique. The matching technique involves calculating a correlation objective function to be minimized utilizing methods such as the Newton-Raphson.

Suppose a subset of pixels is subjected to a two-dimensional deformation. Let (x, y) be the points in the reference image and $(\tilde{x}, \tilde{y})$ be their corresponding points in the deformed image. The mapping function between the two points is:

$$\begin{aligned} \tilde{x} &= x + u \\ \tilde{y} &= y + v \end{aligned}$$

(6.1)

where u and y are the displacement components which can be approximated at different orders using the Taylor series expansion method. The second-order expansion around a point (x_0, y_0) leads to the following mapping functions:

$$\begin{aligned} \tilde{x} &= x_o + u_o + u_x \Delta x + u_y \Delta y + \frac{1}{2} u_{xx} \Delta x^2 + \frac{1}{2} u_{yy} \Delta y^2 + u_{xy} \Delta x \Delta y \\ \tilde{y} &= y_o + v_o + v_y \Delta y + v_x \Delta x + \frac{1}{2} v_{yy} \Delta y^2 + \frac{1}{2} v_{xx} \Delta x^2 + v_{xy} \Delta x \Delta y \end{aligned}$$

(6.2)

135

where $\Delta x = (x - x_o)$ and $\Delta y = (y - y_o)$.

Parameters of the mapping function presented in equation (6.2) are twelve:

u_o and v_o are displacement components at (x_o, y_o)

u_x, v_x, u_y, v_y are the components of the first-order gradient

u_{xx}, v_{xx}, u_{yy}, v_{yy}, u_{xy}, v_{xy} are the components of the second-order gradient.

A higher order of approximation yields a more accurate representation of the deformation in the subset.

The deformation equations shown in equation (6.2) are for a group of pixels called a subset which limits the possible resolution to the pixel-level and thus points onto which correlation can be accomplished. To address the limitation, interpolation is used to increase the resolution of DIC, achieve sub-pixel resolution, and allow correlated points to be placed anywhere within the measured area after deformation. A bicubic spline is the function of choice often used for the interpolation. The function ensures C^2 continuous gradients of the topographic in-plane gray-scale values and for the reference image the function is defined by Vendroux and Knauss (1998) as:

$$f(x, y) = \sum_{m=0}^{3} \sum_{n=0}^{3} \alpha_{nm} x^n y^m$$

(6.3)

where α_{nm} are the fitting coefficients.

After deformation the interpolating spline is expressed as:

$$g(\tilde{x}, \tilde{y}) = \sum_{m=0}^{3} \sum_{n=0}^{3} \beta_{nm} \tilde{x}^n \tilde{y}^m$$

(6.4)

where β_{nm} are the fitting coefficients.

During image acquisition, there is a possibility of light intensity change, which can offset the gray-scale values of images taken. To account for the offset, an additional parameter ω is introduced to the spline function for offset in the gray-scale value between consecutive images:

$$\tilde{g}(\tilde{x}, \tilde{y}) = g(\tilde{x}, \tilde{y}) + \omega \tag{6.5}$$

Now, let S_p represents any single point inside S, a subset (i.e., group) of points (e.g., pixels), the mapping functions become:

$$f(S_p) = f(x, y)$$
$$\tilde{g}(S_p, \boldsymbol{P}) = g(\tilde{x}, \tilde{y}) + \omega \tag{6.6}$$

where $\boldsymbol{P} = \{u_o, v_o, u_x, v_x, u_y, v_y, u_{xx}, v_{xx}, u_{yy}, v_{yy}, u_{xy}, v_{xy}, \omega\}$ represents the 13 parameters in the mapping function (12 from equation (6.2) and ω). The total number of mapping parameters are then determined by a least-square correlation coefficient

$$C = \frac{\sum\limits_{S_p \in S} \left\{ f(S_p) - \tilde{g}(S_p, \boldsymbol{P}) \right\}^2}{\sum\limits_{S_p \in S} f^2(S_p)} \tag{6.7}$$

The equation (6.7) can be solved by the Newton-Raphson method under consideration that at the solution the gradient $\nabla C = 0$ or

$$\nabla C = \left(\frac{\partial C}{\partial P_i} \right)_{i=1,13} = \frac{-2}{\sum\limits_{S_p \in S} f^2(S_p)} \left\{ \sum\limits_{S_p \in S} \left(f(S_p) - \tilde{g}(S_p, \boldsymbol{P}) \right) \frac{\partial \tilde{g}(S_p, \boldsymbol{P})}{\partial P_i} \right\}_{i=1,13} = 0 \tag{6.8}$$

The problem then becomes an iterative loop in the form of:

$$\left[\nabla\nabla C(\boldsymbol{P}_o)(\boldsymbol{P}-\boldsymbol{P}_o)\right]=-\left[\nabla C(\boldsymbol{P}_o)\right] \tag{6.9}$$

where $\boldsymbol{P}_o$ is the initial guess and $\boldsymbol{P}$ is the next iterative approximate solution. $\nabla\nabla C$ is the Hessian matrix, which is calculated as follows (Lu and Cary 2000):

$$\nabla\nabla C=\left(\frac{\partial^2 C}{\partial P_i \partial P_j}\right)_{\substack{i=1,13\\j=1,13}}=\left\{\frac{-2}{\sum\limits_{S_p\in S} f^2\left(S_p\right)}\sum\limits_{S_p\in S}\left[f\left(S_p\right)-\tilde{g}\left(S_p,\boldsymbol{P}\right)\right]\frac{\partial^2\tilde{g}\left(S_p,\boldsymbol{P}\right)}{\partial P_i \partial P_j}\right.$$

$$\left.+\frac{2}{\sum\limits_{S_p\in S} f^2\left(S_p\right)}\sum\limits_{S_p\in S}\frac{\partial\tilde{g}\left(S_p,\boldsymbol{P}\right)}{\partial P_i}\frac{\partial\tilde{g}\left(S_p,\boldsymbol{P}\right)}{\partial P_j}\right\}_{\substack{i=1,13\\j=1,13}} \tag{6.10}$$

Since the calculation of the Hessian matrix (equation (6.10)) is computationally expensive, it is approximated by assuming a very small difference between $f(S_p)$ and $\tilde{g}(S_p,\boldsymbol{P})$. That is by taking $f(S_p)\approx\tilde{g}(S_p,\boldsymbol{P})$ and results in

$$\sum\limits_{S_p\in S}\left[f\left(S_p\right)-\tilde{g}\left(S_p,\boldsymbol{P}\right)\right]\frac{\partial^2\tilde{g}\left(S_p,\boldsymbol{P}\right)}{\partial P_i \partial P_j}\approx 0 \tag{6.11}$$

The approximate Hessian matrix becomes:

$$\nabla\nabla C=\left(\frac{\partial^2 C}{\partial P_i \partial P_j}\right)_{\substack{i=1,13\\j=1,13}}=\left[\frac{2}{\sum\limits_{S_p\in S} f^2\left(S_p\right)}\sum\limits_{S_p\in S}\frac{\partial\tilde{g}\left(S_p,\boldsymbol{P}\right)}{\partial P_i}\frac{\partial\tilde{g}\left(S_p,\boldsymbol{P}\right)}{\partial P_j}\right]_{\substack{i=1,13\\j=1,13}} \tag{6.12}$$

It should be noted that now equation (6.2) can be expressed as:

$$\tilde{x} = x_o + P_1 + P_3 \Delta x + P_5 \Delta y + \frac{1}{2} P_7 \Delta x^2 + \frac{1}{2} P_9 \Delta y^2 + P_{11} \Delta x \Delta y$$

$$\tilde{y} = y_o + P_2 + P_4 \Delta y + P_6 \Delta x + \frac{1}{2} P_8 \Delta y^2 + \frac{1}{2} P_{10} \Delta x^2 + P_{12} \Delta x \Delta y$$

(6.13)

The remaining first-order derivatives in equation (6.12) can be calculated by the chain rule as such:

$$\frac{\partial \tilde{g}(S_p, P)}{\partial P_i} = \frac{\partial \tilde{g}(\tilde{x}, \tilde{y}, P)}{\partial \tilde{x}} \cdot \frac{\partial \tilde{x}(S_p)}{\partial P_i} + \frac{\partial \tilde{g}(\tilde{x}, \tilde{y}, P)}{\partial \tilde{y}} \cdot \frac{\partial \tilde{y}(S_p)}{\partial P_i} + \frac{\partial \tilde{g}(\tilde{x}, \tilde{y}, P)}{\partial P_i}$$

(6.14)

The above derivative leads to the following 13 terms:

$$\frac{\partial \tilde{g}(S_p, P)}{\partial P_1} = \frac{\partial \tilde{g}(S_p, P)}{\partial \tilde{x}} \qquad\qquad \frac{\partial \tilde{g}(S_p, P)}{\partial P_2} = \frac{\partial \tilde{g}(S_p, P)}{\partial \tilde{y}}$$

$$\frac{\partial \tilde{g}(S_p, P)}{\partial P_3} = \frac{\partial \tilde{g}(S_p, P)}{\partial \tilde{x}} \Delta x \qquad\qquad \frac{\partial \tilde{g}(S_p, P)}{\partial P_4} = \frac{\partial \tilde{g}(S_p, P)}{\partial \tilde{y}} \Delta y$$

$$\frac{\partial \tilde{g}(S_p, P)}{\partial P_5} = \frac{\partial \tilde{g}(S_p, P)}{\partial \tilde{x}} \Delta y \qquad\qquad \frac{\partial \tilde{g}(S_p, P)}{\partial P_6} = \frac{\partial \tilde{g}(S_p, P)}{\partial \tilde{y}} \Delta x$$

$$\frac{\partial \tilde{g}(S_p, P)}{\partial P_7} = \frac{1}{2} \cdot \frac{\partial \tilde{g}(S_p, P)}{\partial \tilde{x}} \Delta x^2 \qquad\qquad \frac{\partial \tilde{g}(S_p, P)}{\partial P_8} = \frac{1}{2} \cdot \frac{\partial \tilde{g}(S_p, P)}{\partial \tilde{y}} \Delta y^2$$

$$\frac{\partial \tilde{g}(S_p, P)}{\partial P_9} = \frac{1}{2} \cdot \frac{\partial \tilde{g}(S_p, P)}{\partial \tilde{x}} \Delta y^2 \qquad\qquad \frac{\partial \tilde{g}(S_p, P)}{\partial P_{10}} = \frac{1}{2} \cdot \frac{\partial \tilde{g}(S_p, P)}{\partial \tilde{y}} \Delta x^2$$

$$\frac{\partial \tilde{g}(S_p, P)}{\partial P_{11}} = \frac{1}{2} \cdot \frac{\partial \tilde{g}(S_p, P)}{\partial \tilde{x}} \Delta x \Delta y \qquad\qquad \frac{\partial \tilde{g}(S_p, P)}{\partial P_{12}} = \frac{1}{2} \cdot \frac{\partial \tilde{g}(S_p, P)}{\partial \tilde{y}} \Delta x \Delta y$$

$$\frac{\partial \tilde{g}(S_p, P)}{\partial P_{13}} = \frac{\partial \tilde{g}(S_p, P)}{\partial \omega} = 1$$

(6.15)

The derivative terms in equation (6.15) are calculated from the bicubic spline interpolating polynomial from the current image as follows (Lu and Cary 2000):

$$
\begin{aligned}
\frac{\partial \tilde{g}\left(S_p, \boldsymbol{P}\right)}{\partial \tilde{x}} =\ & \beta_{01} + 2\beta_{02}\tilde{x} + 3\beta_{03}\tilde{x}^2 \\
& + \beta_{11}\tilde{y} + 2\beta_{12}\tilde{x}\tilde{y} + 3\beta_{13}\tilde{x}^2\tilde{y} \\
& + \beta_{21}\tilde{y}^2 + 2\beta_{22}\tilde{x}\tilde{y}^2 + 3\beta_{23}\tilde{x}^2\tilde{y}^2 \\
& + \beta_{31}\tilde{y}^3 + 2\beta_{32}\tilde{x}\tilde{y}^3 + 3\beta_{33}\tilde{x}^2\tilde{y}^3 \\
\frac{\partial \tilde{g}\left(S_p, \boldsymbol{P}\right)}{\partial \tilde{y}} =\ & \beta_{01} + 2\beta_{02}\tilde{y} + 3\beta_{03}\tilde{y}^2 \\
& + \beta_{11}\tilde{x} + 2\beta_{12}\tilde{x}\tilde{y} + 3\beta_{13}\tilde{x}\tilde{y}^2 \\
& + \beta_{21}\tilde{x}^2 + 2\beta_{22}\tilde{x}^2\tilde{y} + 3\beta_{23}\tilde{x}^2\tilde{y}^2 \\
& + \beta_{31}\tilde{x}^3 + 2\beta_{32}\tilde{x}^3\tilde{y} + 3\beta_{33}\tilde{x}^3\tilde{y}^2
\end{aligned}
\tag{6.16}
$$

The subset DIC can now be implemented with the above equations. However, as the subsets selected are discrete groups of pixels, it is possible to have undesired discontinuities at the subset boundaries (Figure 63(a)). To mitigate the issue, a step between adjacent subsets is often used to ensure overlap of subsets at their boundary (Figure 63(b)). As a result, the step pixels provide an overlap between two adjacent subsets and reduce errors by ensuring compatibility between calculated displacement fields.

<div align="center">(a)   (b)</div>
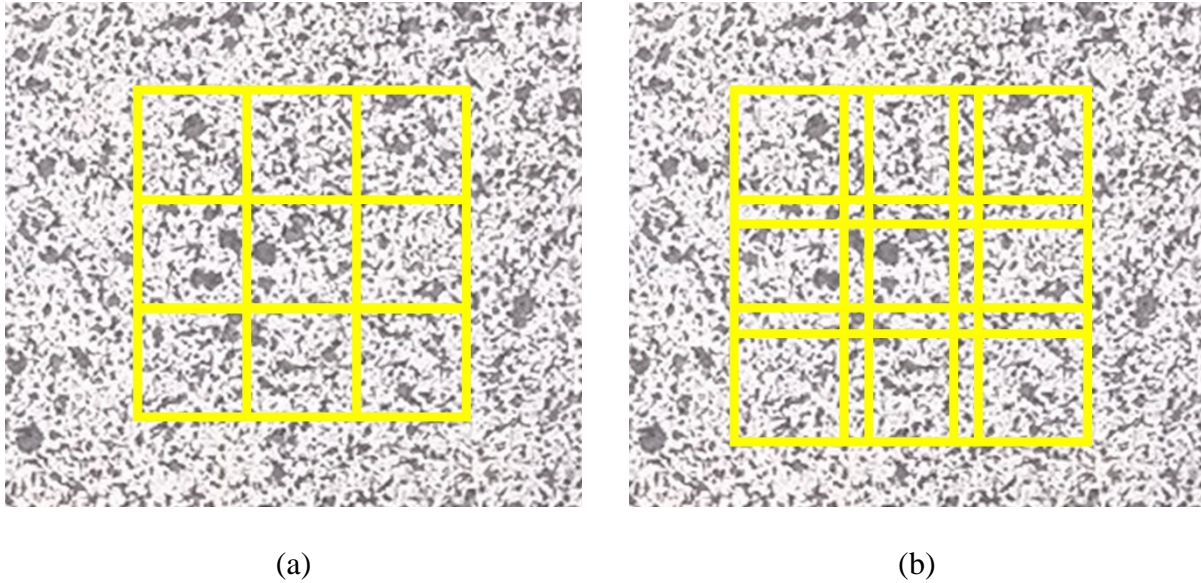
Figure 63. DIC subsets: (a) without a step, (b) with a step.

The subset DIC method has been used to obtain measurement resolutions of 4.8 nm and 1.5 nm for in-plane and out-of-plane measurements, respectively (Vendroux and Knauss 1998). Another study by (Lu and Cary 2000) obtained an accuracy of $\pm\ 10^{-4}$ per pixel.

A full-field DIC is an alternative technique that correlates the entire measured area (i.e., the region of interest (ROI)) instead of subsets. The technique involves placing multiple tracking points in the reference image and representing their corresponding displacement by a bicubic function. The overall displacement of ROI is then obtained by a linear combination of the individual tracking points. The full-field DIC has an advantage over subset DIC in that calculated displacements are compatible and continuous instead of using the discrete subsets. However, full-field DIC requires an additional regularization term to ensure C^2 continuity of displacements gradients due to their higher sensitivity compared to calculated displacements.

Shen (2009) compared subset and full-field DIC algorithms and showed that the full-field DIC was relatively more accurate around the edge of the ROI (measured region of interest).

Beyond the edges, the accuracy of subset DIC was significantly improved with comparable noise

levels compared to the full-field DIC. The cited study used discrete subsets of 21x21 pixels. It

can be noted that the accuracy of a subset DIC can be improved by increasing the size of the

subset (e.g., 31x31 pixels) and using step pixels (e.g., 7 pixels). Further, the edge problem of

subset DIC can be overcome by using an offset such as a half subset from the edge of ROI

(Figure 64). With the above considerations, the shortcomings of subset DIC are circumvented

resulting in more accurate and less noisy displacement fields. In this study, the DIC algorithm

called VIC-3D based on the subset method was used.
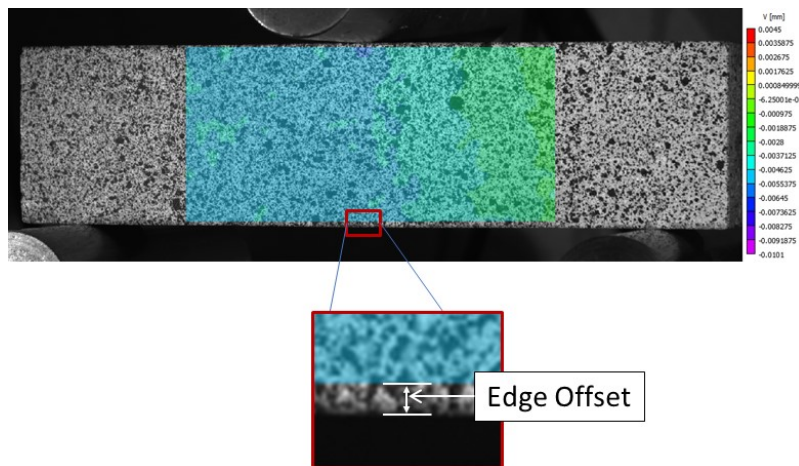
Figure 64. Example edge offset in subset DIC to reduce edge noise.

6.1.2. DIC-FEM Inverse Method

6.1.2.1. Formulation of the Objective Function

The measured deformation by DIC can be used to infer material properties by either direct or

inverse method. The direct method incorporates measured deformations into an analytical

solution to deduce material properties. In contrast, the inverse method calculates material

properties by minimizing the error between DIC and numerical simulation results. Although the inverse method avoids analytical solutions, by utilizing the computational modeling (e.g., FEM), complicated properties and geometries (e.g., fracture) can be accommodated. Four primary components of the DIC-FEM inverse method are the experimental set-up, DIC deformation measurement, finite element modeling, and optimization. When FEM is used for numerical simulation, the inverse problem becomes a DIC-FEM minimization of displacement difference as shown in equation (6.17):

$$\underset{\boldsymbol{\chi} \in \mathbb{R}^N}{\arg \min} \, \Psi_u(\boldsymbol{\chi}) = \left\| \mathbf{u}_{DIC} - \mathbf{u}_{FEM}(\boldsymbol{\chi}) \right\|_2 \tag{6.17}$$

where $\Psi_u(\boldsymbol{\chi})$ is the objective function, $\boldsymbol{\chi}$ is a vector of size N material properties, $\mathbf{u}_{DIC}$ is experimental displacements from DIC, $\mathbf{u}_{FEM}(\boldsymbol{\chi})$ is the computational displacements from FEM at $\boldsymbol{\chi}$ and, $\left\| \bullet \right\|_2$ is the Euclidian norm.

6.1.2.2. Nelder-Mead Optimization Algorithm

Although conventional methods such as the Newton-Raphson can be used to solve the equation (6.17), Nelder-Mead (N-M) solver is preferred due to its robustness, derivative-free nature, ease to incorporate constrain functions as part of the objective function (Lagarias, Reeds et al. 1998). The N-M method is a simplex-based solver that systematically replaces the point with the highest function value within the simplex by either reflecting, contracting or expanding.

For example, given an initial guess point $\boldsymbol{\chi} \in \mathbb{R}^2$ then, N-M composes a simplex with vertices: $\boldsymbol{\chi}_1$, $\boldsymbol{\chi}_2 = \boldsymbol{\chi}_1 + (\alpha, 0)^T$ and $\boldsymbol{\chi}_3 = \boldsymbol{\chi}_1 + (0, \alpha)^T$ where the coefficient α controls the step

size of the algorithm. Subsequently, the vertex with the highest function value (e.g., χ_1) undergoes a replacement process following the Algorithm 1 (see the Appendix A) that implements the iteration process graphically shown in Figure 65 for a two-dimensional vector (i.e., $\chi \in \mathbb{R}^2$). A solving step is complete with Algorithm 1 and continues until a stopping criterion, for example, a set function value decrease between two iterations, the maximum number of iterations, or a sufficiently small function value $\Psi_u(\chi)$.
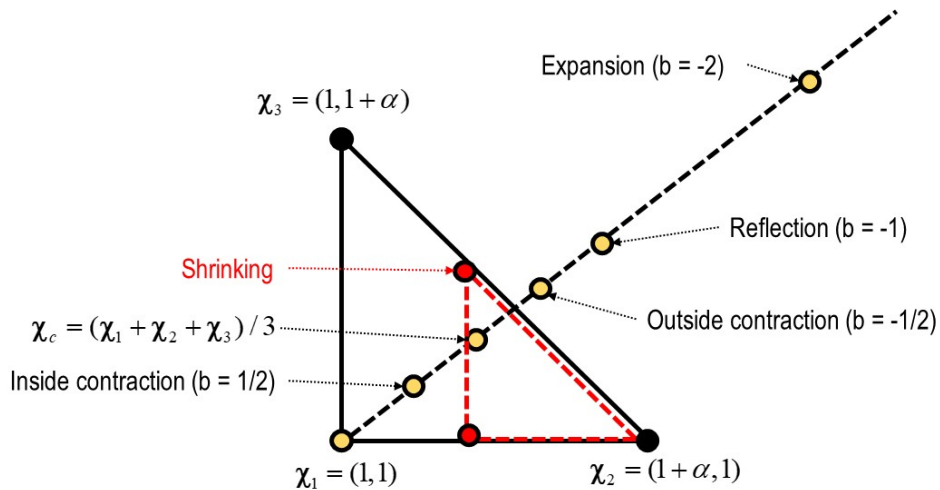
Figure 65. Nelder-Mead simplex algorithm for $\chi \in \mathbb{R}^2$.

Figure 66 presents a general N-M solver. As aforementioned, the solver is very robust in that it can accommodate several dimensions and does not require the calculation of derivatives. As shown in Figure 65 and Figure 66, the main concept of N-M is to take an initial guess of the solution $\chi \in \mathbb{R}^N$ and create vertices of $N+1$ using the concept shown in Figure 65, calculate objective functions at each vertex and replace the vertices with the largest objective function value. The replacement process (shown in Figure 66) is conducted very fast as only simple calculations are needed. The N-M solver has been used by (Shen and Paulino 2011) to identify

144

the cohesive zone model (CZM) and elastic parameters of fiber-reinforced cementitious composites.

The inverse method is attractive to identify complex material properties in both homogenous as well as in heterogeneous materials since it inherits the advantages of both computation modeling and DIC. However, in AC mixtures, the DIC-computation method has been limited to mainly the elasticity-dominant regime (i.e., low temperatures) even though significant inelastic deformation and fatigue cracking occur at intermediate temperatures during the AC pavement lifecycle. Therefore, there is a lack of a robust DIC-computation inverse method capable of characterizing properties of bituminous mixture components and their interactions in the presence of significant viscoelastic effects and fracture. The inverse method can then save time and cost to obtain properties of component materials and mixtures that are necessary for pavement design.

The combination of DIC and FEM to identify material properties is a very attractive method when dealing with complex materials. For example, the DIC can measure surface deformation of homogenous and heterogenous materials even under damage. Similarly, FEM is robust to model complex material behavior under loading and failure. Thus, using both DIC and FEM allows the characterization of a wide range of materials that are heterogeneous and multiphase and undergoing different deformation and failure phenomena.
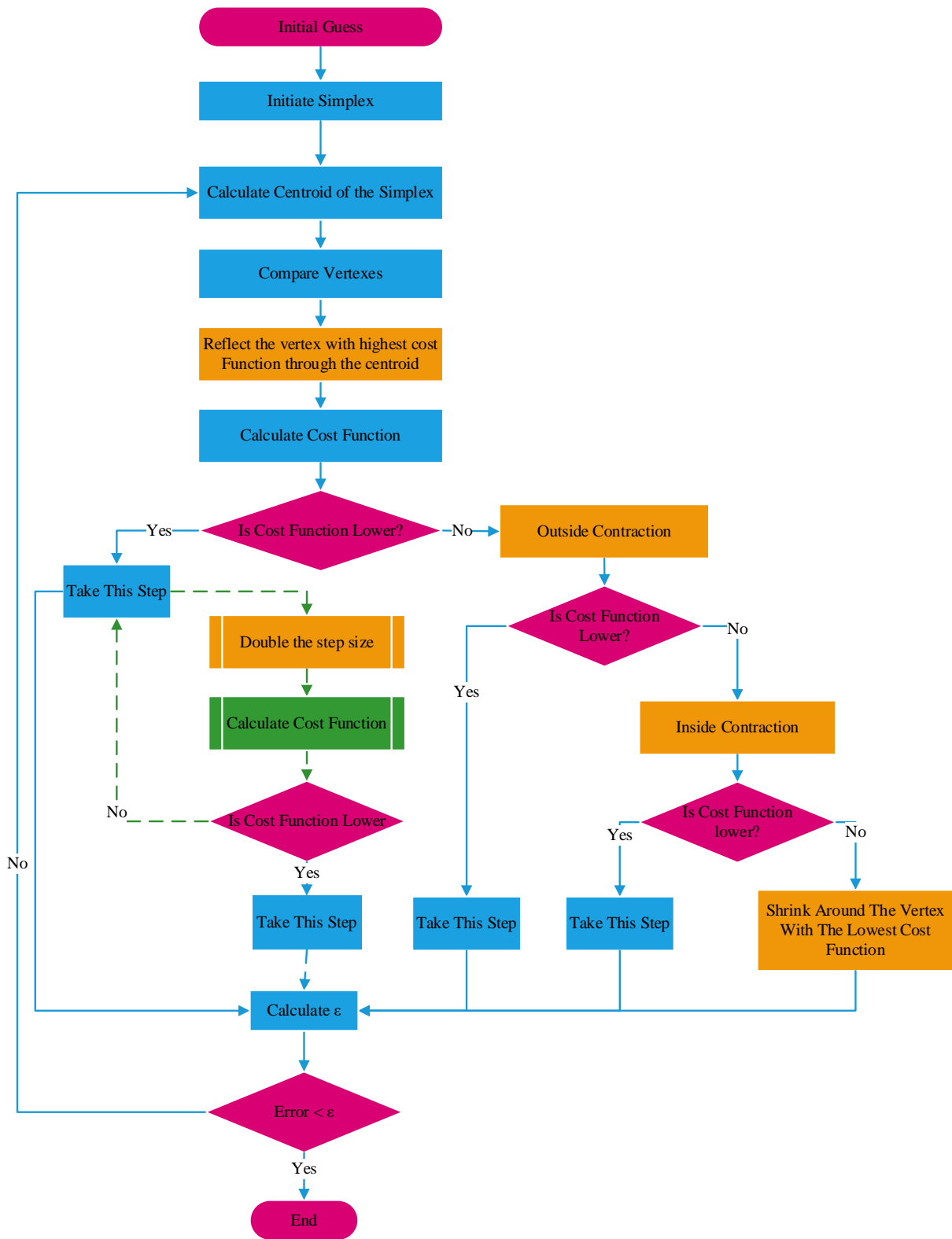
Figure 66. Nelder-Mead solver.

6.2. **Objectives and Research Methodology**

The objective of this chapter is to implement a DIC-FEM inverse method that is capable of identifying constitutive elastic and viscoelastic properties of materials solely through the optimization of field displacement data. The developed method improves fundamental understanding of inelastic deformation and fracture of homogeneous materials and even highly heterogeneous mixtures.

For computational modeling, the commercial FE package, ABAQUS (Abaqus 2014) was used. The modeling replicated testing set-up and loading condition including the assumed constitutive behavior (e.g., elastic), boundary conditions, and specimen geometry. For each case, a mesh convergence study was conducted to ensure the selection of optimal mesh size. Material properties in the input file (i.e., .inp file) were iteratively identified until they reach optimum values by minimizing differences from DIC results through the DIC-FEM inverse method. The overall methodology for the DIC-FEM inverse method framework is presented in Figure 67.
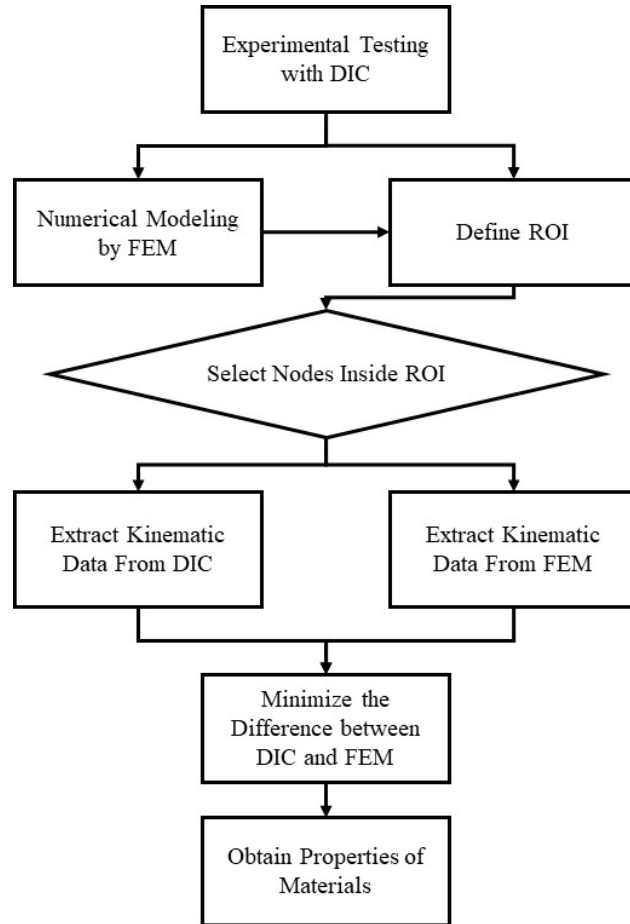
Figure 67. Framework for the DIC-FEM inverse method implemented in this study.

6.3. **Materials and Constitutive Relationship**

6.3.1. Elastic Investigation

PEEK (Polyetheretherketone) is the example material chosen. PEEK is a thermoplastic semi-crystalline polymer (El-Qoubaa and Othman 2015). It has a high strength-to-weight ratio, a good resistance to wear, and excellent biocompatibility (Rivard, Rhalmi et al. 2002).

The general constitutive relationship between stress σ and strain ε for time-independent elastic materials is:

$$\sigma_{ij} = C^E_{ijkl}\varepsilon_{kl} \tag{6.18}$$

where C^E_{ijkl} is the fourth-order elastic modulus tensor.

For isotropic and linearly elastic materials in isothermal conditions, the elastic modulus, E, and the Poisson's ratio, v, are the only two necessary independent constants to establish the stress-strain relationship such as:

$$\sigma_{ij} = \frac{Ev}{(1+v)(1-2v)}\delta_{ij}\varepsilon_{kk} + \frac{E}{(1+v)}\varepsilon_{ij} \tag{6.19}$$

where δ_{ij} is the Kronecker delta.

6.3.2. Viscoelastic Investigation

FAM (fine aggregate matrix) was selected as an example of viscoelastic material, while it is a primary component of typical AC (asphalt concrete) mixtures (Aragão and Kim 2012). FAM contains aggregates smaller than 1.19 mm and asphalt cement (Im, Ban et al. 2014). Understanding FAM is critical since most of the deformations (e.g., rutting) and damage (e.g., fracture/cracks) originate from this media which after accounting for large aggregates, the overall behavior of corresponding AC can be deduced. In fact, (Underwood and Kim 2013) and (You, Masad et al. 2014) showed that LVE properties from FAM and AC are interrelated by a vertical shift.
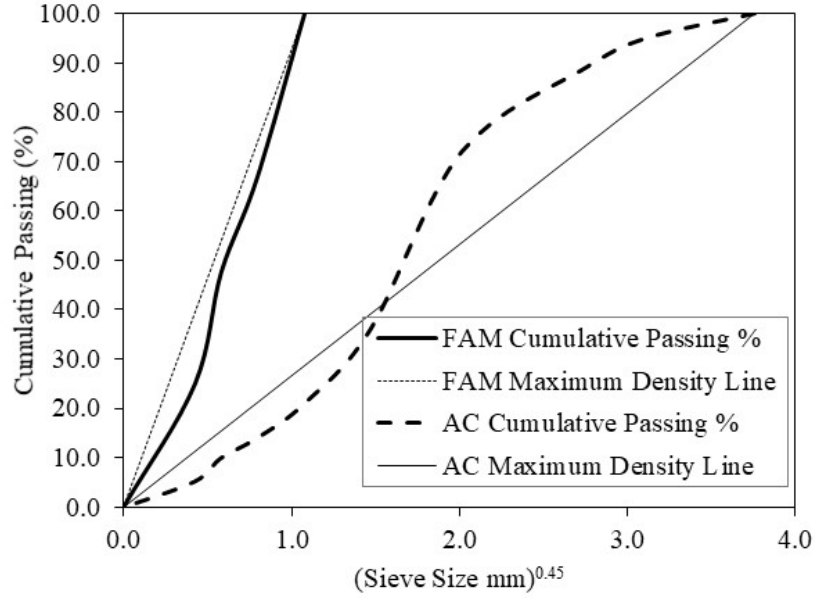
Figure 68. Aggregate gradations of FAM compared to AC.

As Figure 68 shows, the key differentiator between aggregate gradation of the FAM and AC mixture is the content of large aggregates. FAM has a much smaller maximum aggregate size of 1.19 mm (passing No. 30 sieve) compared to its AC mixture.

The general thermomechanical constitutive relationship of time-dependent, isotropic, linearly viscoelastic material is expressed as follows:

$$\sigma_{ij}(t) = \int_0^t E_{ijkl}(t-\tau)\frac{\partial \varepsilon_{kl}(\tau)}{\partial \tau}d\tau - \int_0^t \beta_{ij}(t-\tau)\frac{\partial \Delta T(\tau)}{\partial \tau}d\tau \tag{6.20}$$

where E_{ijkl}, β_{ij} and ε_{kl} are the linear viscoelastic relaxation modulus, thermal relaxation tensor, and the strain tensor, respectively, and t, τ are the time of interest and integration variable, respectively. The isotropic uniaxial relaxation modulus, $E(t)$, in the isothermal condition can be expressed in Prony series terms as:

$$E(t) = E_\infty + \sum_{i=1}^{m} E_i e^{\frac{-t}{\rho_i}} \qquad (6.21)$$

where E_∞ and E_i are the Prony terms, ρ_i is the relaxation time, t is the time of interest.

Similarly, the creep compliance can also be expressed in Prony series terms as:

$$D(t) = D_g + \sum_{j=1}^{n} D_j \left(1 - e^{\frac{-t}{\tau_j}} \right) \qquad (6.22)$$

The $E(t)$ and $D(t)$ expressed in the Prony series are interconvertible using the following relationship (Park and Schapery 1999):

$$\sum_{i=1}^{m} \left[D_g e^{\frac{-t}{\rho_i}} + \sum_{j=1}^{n} \frac{D_j \rho_i}{\tau_j - \rho_i} \left(e^{\frac{-t}{\tau_j}} - e^{\frac{-t}{\rho_i}} \right) \right] E_i = 1 - E_\infty \left[D_g + \sum_{j=1}^{n} D_j \left(1 - e^{\frac{-t}{\tau_j}} \right) \right] \qquad if \ \rho_i \neq \tau_j$$

$$\sum_{i=1}^{m} \left[D_g e^{\frac{-t}{\rho_i}} + \sum_{j=1}^{n} \frac{t D_j}{\tau_j} e^{\frac{-t}{\rho_i}} \right] E_i = 1 - E_\infty \left[D_g + \sum_{j=1}^{n} D_j \left(1 - e^{\frac{-t}{\tau_j}} \right) \right] \qquad if \ \rho_i = \tau_j \quad (6.23)$$

$$E_\infty = \frac{1}{D_g} - \sum_{i=1}^{m} E_i$$

6.4. **Sample Fabrication**

While specimens for PEEK were machined to the specification by machines shop, to form FAM, the aggregates were mixed with eight percent binder at the mixing temperature of 160°C. The mixed materials were placed in an oven at a compaction temperature of 149°C for two hours to induce short-term aging before being compacted by a Superpave gyratory compactor to make tall cylindrical samples of 170 mm in height and 150 mm in diameter. Beam FAM specimens were then prepared from the cylindrical samples by cutting as shown in Figure 69. In total, one tall sample can produce 10 beam specimens (150 × 35 × 25 mm in length × height × width).
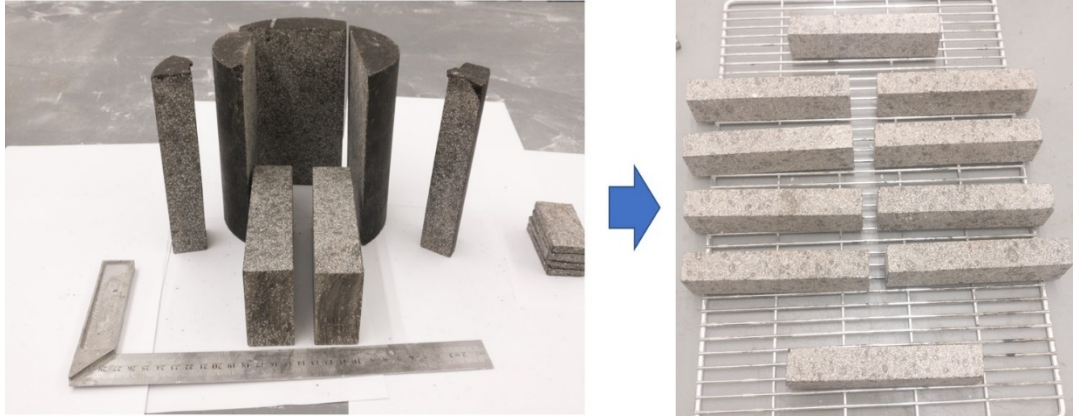
Figure 69. FAM sample fabrication.

Before any experimental testing with DIC, the surface of target specimens were prepared

by applying a speckle pattern. First, the surface was smoothened to remove imperfections

(Figure 70(a)) before a white base paint was applied by spraying to cover the whole surface.

Next, a speckle of black dots was applied by spraying on the top of the white layer (Figure

70(b)). Several spraying techniques were attempted to select the optimal speckle preparation

method. The condition of the speckle was to be isotropic, random, homogenous, non-repetitive,

and with high contrast. All the conditions were satisfied by simply spraying black dots on a

painted white surface (Figure 70(b)). It should be noted that depending on the size of the

specimens, the sizes of the dots were adjusted so to maintain high contrast of the speckle.

(a)

(b)

Figure 70. Example of DIC sample preparation (PEEK): (a) before and (b) after speckle pattern application.

6.5. **Test Set-Up and Data Analysis**

Figure 71 shows the complete DIC testing set-up used in this study. The set-up is comprised of the mechanical testing machine and the digital image correlation hardware. The DIC hardware includes a desktop computer to store acquired images, two stereo cameras, two light sources, and a DAQs (data acquisition system) (Figure 71(a)). The mechanical testing station includes a desktop computer, a load-frame, a loadcell of 3kN capacity, and a testing fixture (Figure 71(b)).

Since the loading machine and DIC are two completely different systems, both systems were synchronized through their respective DAQs via BNC cables for load and trigger information communication. As a result, the DIC image acquisition could be initiated as soon as a threshold load was achieved. It is important to link both systems to associate every image in DIC with a known load stage, otherwise, deformation data would be decoupled from actual loading information.
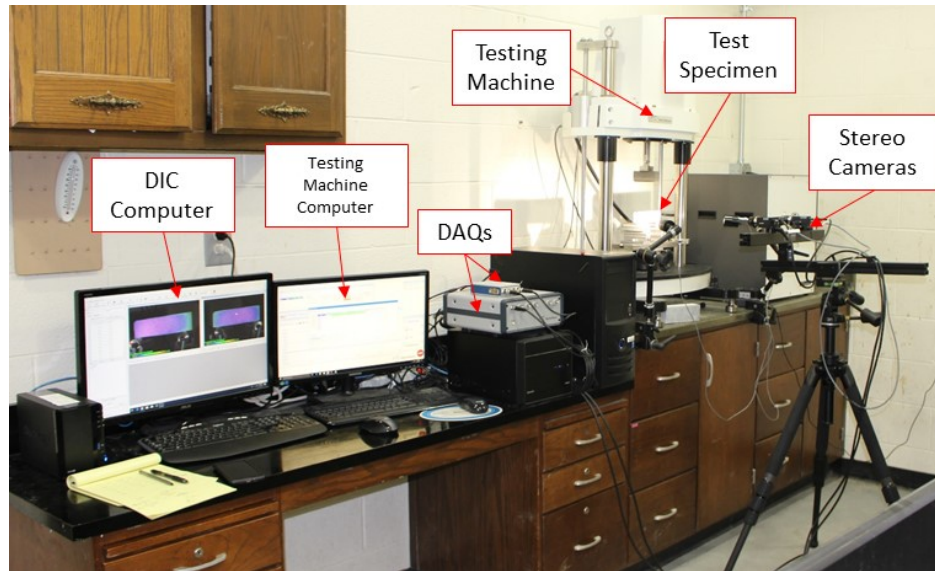
(a)
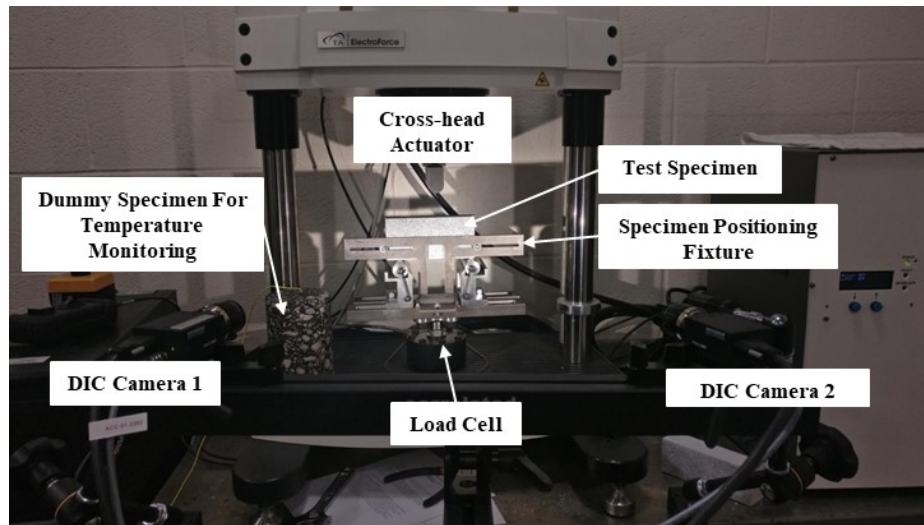
(b)

Figure 71. Experimental set-up used: (a) the entire set-up showing DIC and mechanical loading machine, and (b) detailed close-up of the set-up. (note DAQs: Data Acquisition System).

The DIC system used in this study was supplied by Correlated Solutions and included software for image acquisition and image processing via VIC-3D. The mechanical loading system was electrically activated Electroforce supplied by TA Instrument. The machine was

capable of dynamic mechanical analysis (DMA); however, testing in this study was conducted only in quasistatic mode. For more consistent test results, a special fixture for accurate specimen positioning was developed, and temperature monitoring was conducted through a dummy specimen with a thermocouple embedded inside.

6.5.1. Linear Elastic Properties of PEEK

The test set-up for constitutive properties is shown in Figure 72. PEEK specimen was a beam with a geometry of 75 mm, 10 mm, and 4 mm for length, height, and thickness, respectively (Figure 72(a)). The specimen was loaded from top center after being positioned on a bending fixture with a span length of 60 mm. The testing was conducted at 23°C in a displacement-controlled mode with a monotonic loading of 10 mm/min. The test terminated at the load of 350 N that corresponded to a maximum tensile stress of 14 MPa at the bottom of the beam, which is well below of PEEK's yield stress of around 120 MPa (El-Qoubaa and Othman 2015, Chen, Gatea et al. 2016, Chen, Ou et al. 2016).
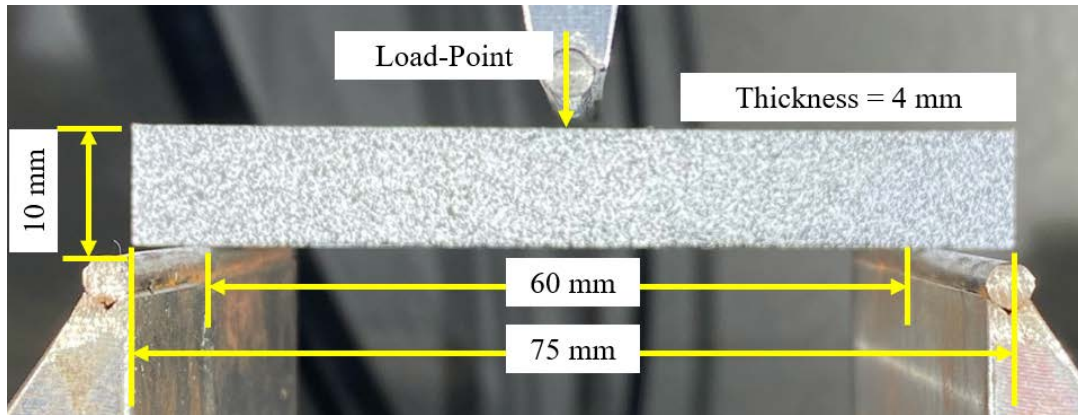
(a)
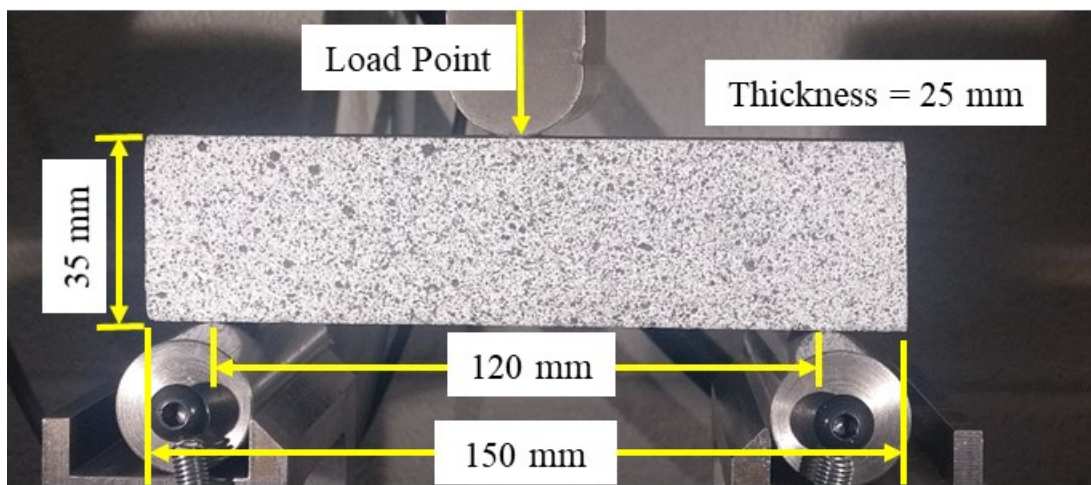
(b)

Figure 72. Test set-up for constitutive properties of: (a) PEEK, and (b) FAM.

6.5.2. Linear Viscoelastic Properties of FAM

For linear viscoelastic properties, each beam FAM specimen was subjected to creep testing

(Figure 72(b)). A preliminary study was conducted to ensure linear viscoelastic behavior during

testing of FAM. First, an analytical solution was used to relate the deflection of the beam to its

linear viscoelastic properties. The elastic solution for the Timoshenko beam theory was

converted into a viscoelastic solution using the elastic-viscoelastic correspondence principle and

obtain the deflection as a function of the creep compliance as follows:

$$u^T(t) = \left(\frac{P_o L^3}{48I} + \frac{2M_o(1+v)}{AKs} \right) D(t) \qquad (6.24)$$

where $u^T(t)$, P_o and M_o are the deflection at the middle center of the beam, creep load, and

creep moment. The moment can be obtained as $M_o = PL/4$, which results in the deflection

equation as follows:

$$u^T(t) = P_o B(t)$$
$$B(t) = \left(\frac{L^3}{48I} + \frac{2L(1+v)}{4AKs} \right) D(t) \qquad (6.25)$$

Therefore, within the LVE condition, the middle-center deflection is directly and linearly

proportional to the applied creep load. The LVE condition reasonably assumes that the specimen

geometry (e.g., A, L, l), and material properties (i.e., v and $D(t)$) remain constant during

loading. Given the above equation, the LVE creep load was investigated by conducting creep

tests at increasing loading levels. The LVE creep load was then determined by taking a level of

load that violates LVE conditions such as homogeneity and superposition.

DIC was used to measure the deflection in the middle center ($u^T(t)$) of the specimen.

Measurement of deformation besides the load-point displacement highlights the capability and

advantages of using DIC as opposed to the traditional methods. Figure 73 shows the creep

compliance ($D(t)$) calculated from creep loads of 2.5 N, 5 N, and 10 N. It should be noted that

except for the creep loads, all testing conditions were identical during testing for all load levels.

The LVE limit was examined based on the homogeneity concept (i.e, linear scaling), where the

creep compliance ($D(t)$) remains constant as long as the material is under LVE condition. Figure

73 shows creep compliances calculated when the level of loads increased. As can be seen, the

157

creep compliance was similar between the two loads: 2.5 N and 5.0 N. However, beyond 5.0 N, the creep compliance deviated which infers onset of nonlinear viscoelastic response in the FAM beam specimen. As a result, 5.0 N was selected as the limit of LVE creep load, and the smaller load (i.e., 2.5 N) was used for later tests as it guarantees LVE condition.
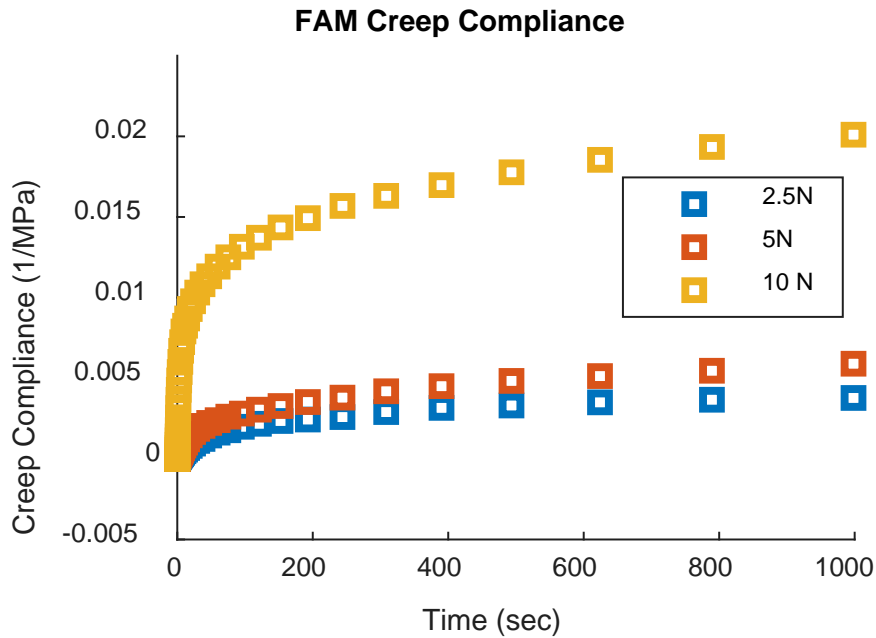
Figure 73. Determination of LVE: creep compliance calculated at different load levels.

It should be noted that the tests were conducted on a single specimen loaded for 1,000 seconds and unloaded for 24 hours. During the unloading, the specimens were removed from the testing fixture to avoid any additional creep loading due to gravity. The temperature during testing was carefully controlled and monitored via the dummy sample with a thermocouple embedded.

6.5.3. Data Analysis and Optimization

The inverse method was based on displacement results from DIC and FEM. As a result, the location to extract the displacement data needs to be spatially matched between DIC and FEM. To address this, an algorithm was used to extract nodal locations as coordinates from FEM modeling (Figure 74(a)) that were then imported in DIC software to extract the corresponding kinematic data (Figure 74(b)). This ensured use of matching locations inside the selected ROI when calculating the objective function.

(a)

(b)
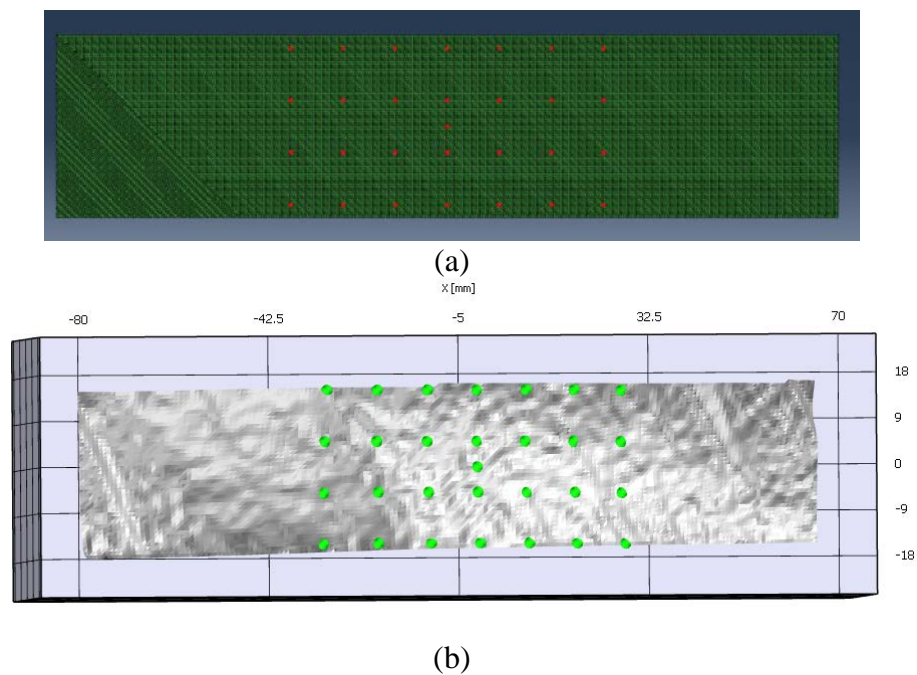
Figure 74. Matching location of deformation data: (a) FEM and (b)DIC.

FEM simulation was performed via a script written in Python language to interface with ABAQUS FEA software (Abaqus 2014). The Python script had specific subsequent features to specify the input file, run FEM simulation per the input file, wait until the FEM simulation is completed, extract simulation results at specified nodes (i.e., ROI nodes) in a form of text files. DIC deformation data were obtained via a commercial DIC analysis software called VIC-3D

provided by the Correlated Solutions. The DIC data was processed to remove measurement noise

by data smoothing and signal processing tools implemented in MATLAB™. An exemplified

denoising is shown in Figure 75.
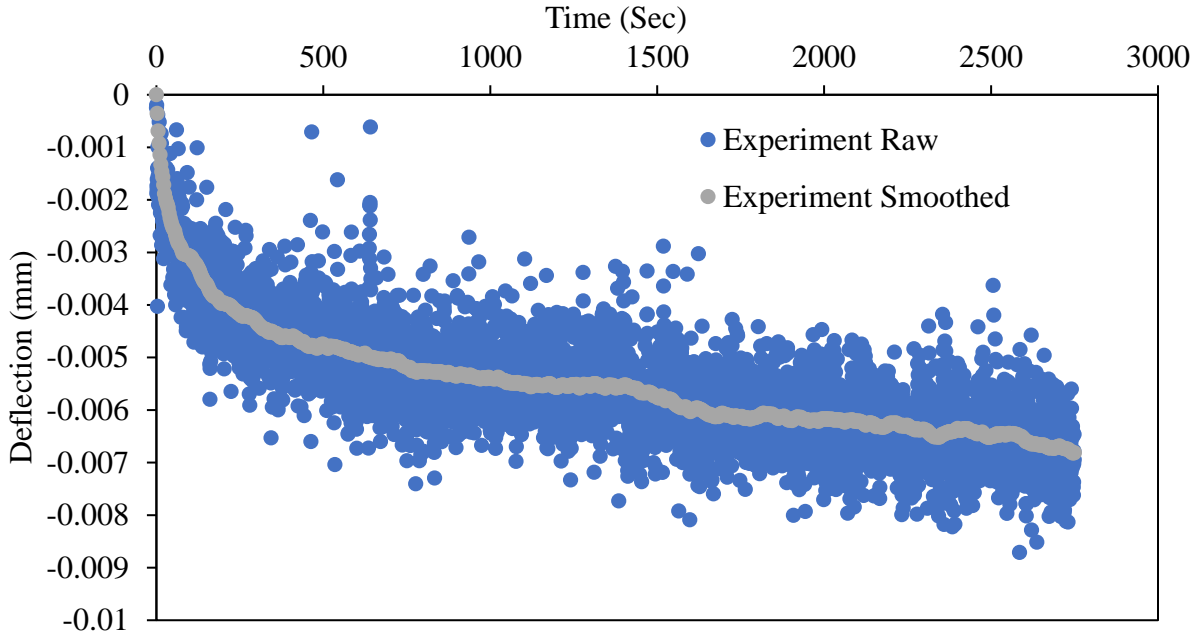
Figure 75. DIC data denoising.

After data denoising, the calculation of the function value was then performed by

MATLAB™ by comparing displacements in both horizontal and vertical from both DIC and

FEM. Subsequently, the N-M solver (Figure 65) implemented in MATLAB™ was used to

update the next step in ABAQUS input file. Since N-M solver is a constraint-free method, the

constraints were externally applied by the penalty method that assigned a large number to the

function value if the χ was outside the boundary domain Ω_χ. An example of a reasonable

constraint is that the elastic modulus is always positive (i.e., $E \geq 0$). The final objective function

is shown in equation (6.26).

$$\min_{\chi \in \mathbb{R}^N} \Psi_u(\chi) = \begin{cases} \left\| \mathbf{u}_{DIC} - \mathbf{u}_{FEM}(\chi) \right\|_2 & \textit{if } \chi \in \Omega_\chi \\ 10^{20} & \textit{for } \chi \notin \Omega_\chi \end{cases} \tag{6.26}$$

6.6. **Results and Discussions**

6.6.1. Linear Elastic Properties of PEEK

DIC data were analyzed using a subset size of 25x25 pixels and a step size of 8 pixels.

Concurrently, the FE model simulation was conducted using a 0.5 mm mesh of 3-node linear

elements (CPS3). The mesh size was selected after a mesh convergence study. Figure 76 shows

horizontal strain distributions from the DIC (Figure 76(a)) and FEM (Figure 76(b)).
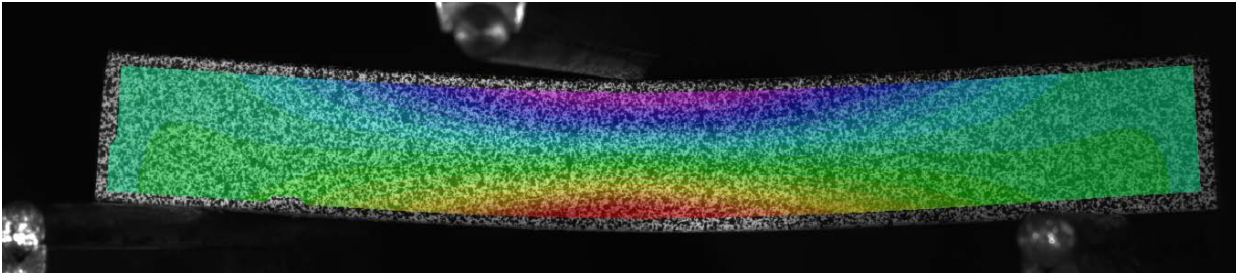
(a)

(b)
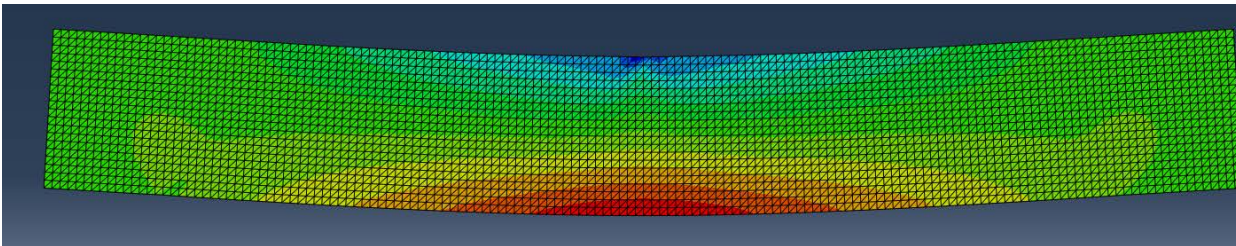
Figure 76. Strain (ε_{xx}) profile of DIC and FEM results.

As aforementioned, the objective function (expressed in the equation (7.1)) was

constructed by comparing displacements inside the ROI (region of interest). For the PEEK

elastic properties, a total of 697 points were used to calculate the objective function at each iteration (Figure 77).

(a)

(b)
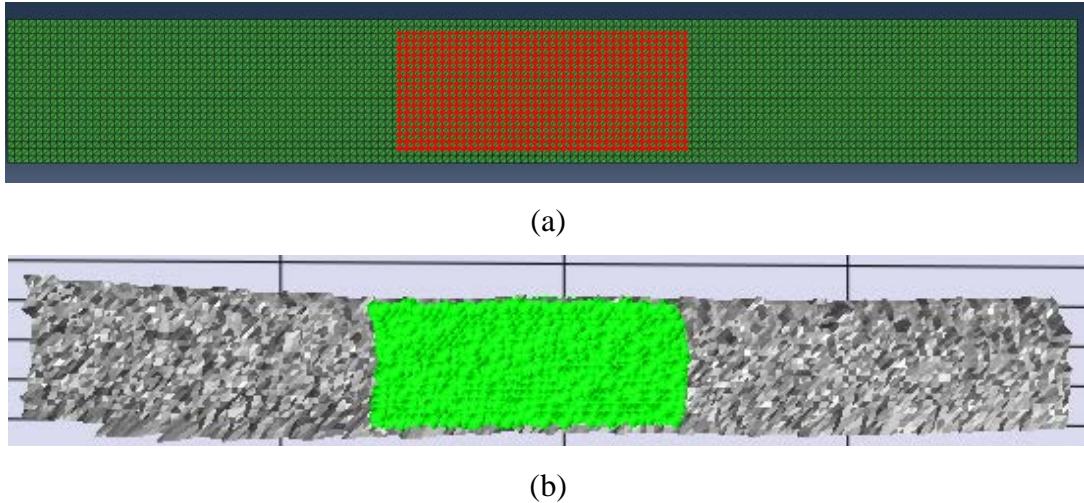
Figure 77. Selecting points inside a region of interest (ROI) to construct an objective function (number of points = 697) for (a) FEM, and (b) DIC.

Using Timoshenko beam theory for elasticity the deflection at the neutral axis in the middle of the beam can be calculated as follows:

$$u^T = \frac{PL^3}{48EI} + \frac{M}{GAK_S} \tag{6.27}$$

where u^T, P, L, E, I, M, A, G and K_S are the deflection at the neutral axis in the mid-span, applied load, the support span length, modulus of elasticity, second moment of inertia of the cross-section about the y-axis, bending moment, cross-sectional area, shear modulus, and the Timoshenko's shear coefficient, respectively. For a simply-supported beam problem, the K_S is calculated as (Cowper 1966):

$$K_s = \frac{10(1+v)}{12+11v} \qquad (6.28)$$

6.6.1.1. Effect of Poisson's Ratio

Equations (6.27) and (6.28) implies the effects of Poisson's ratio on the mid-span deflection.

However, as Figure 78 shows, the Poisson's ratio has a minimal effect on the deflection of the

PEEK beam within the elastic region. As a consequence, the Poisson's ratio was assumed to be a

constant of 0.35 (Sobieraj, Kurtz et al. 2009). This simplification requires identifying only

Young's modulus of the PEEK from the DIC-FEM inverse process.
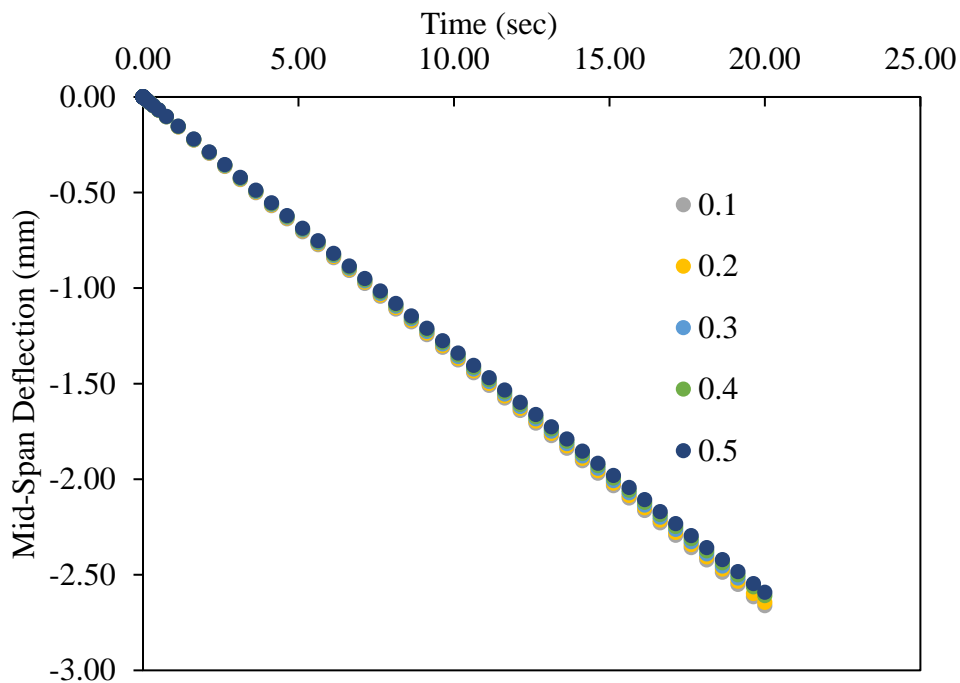
Figure 78. Effect of Poisson's ratio on the deflection of PEEK via analytical solution.

6.6.1.2. Results of DIC-FEM Inverse Process

The results of the inverse method to calculate E are shown in Figure 79(a), where the optimal elastic modulus E for PEEK was calculated to be 3951.8 MPa. The modulus value is in good agreement with published results on PEEK (Jaekel, MacDonald et al. 2011, Chen, Gatea et al. 2016, Lesiuk, Sawicka et al. 2017, Kurtz 2019). Along with the elastic modulus identified, Figure 79(a) also shows the variation of function value over the iteration. As can be seen, the solution converged fast and was saturated at approximately 20 iterations. Figure 79(b) presents the resulting displacements at the optimized elastic modulus. Five different locations were arbitrarily selected to demonstrate the agreement between DIC experimental results and FEM computational simulations. Generally, the displacements were in good agreement which implies the validity of the DIC-FEM inverse process in identifying unknown material properties such as Young's modulus in this particular example.
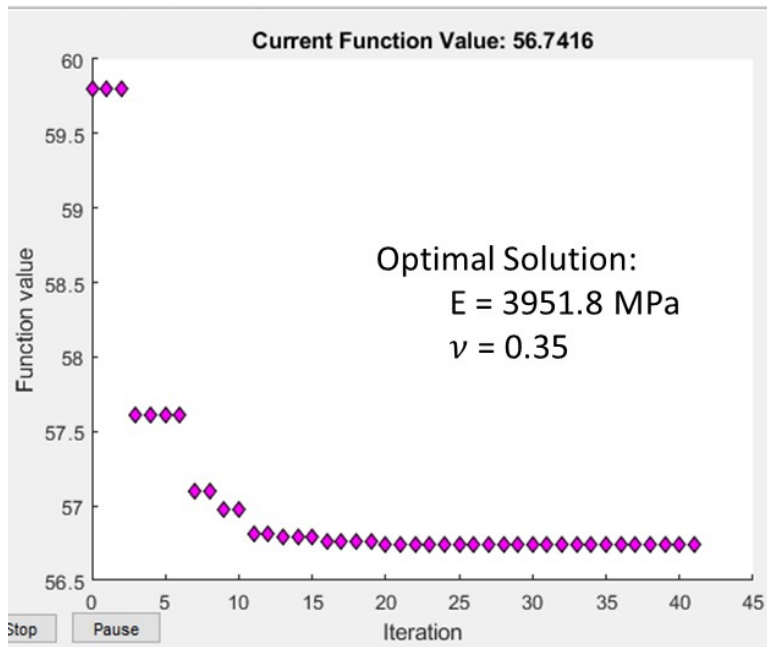
(a)
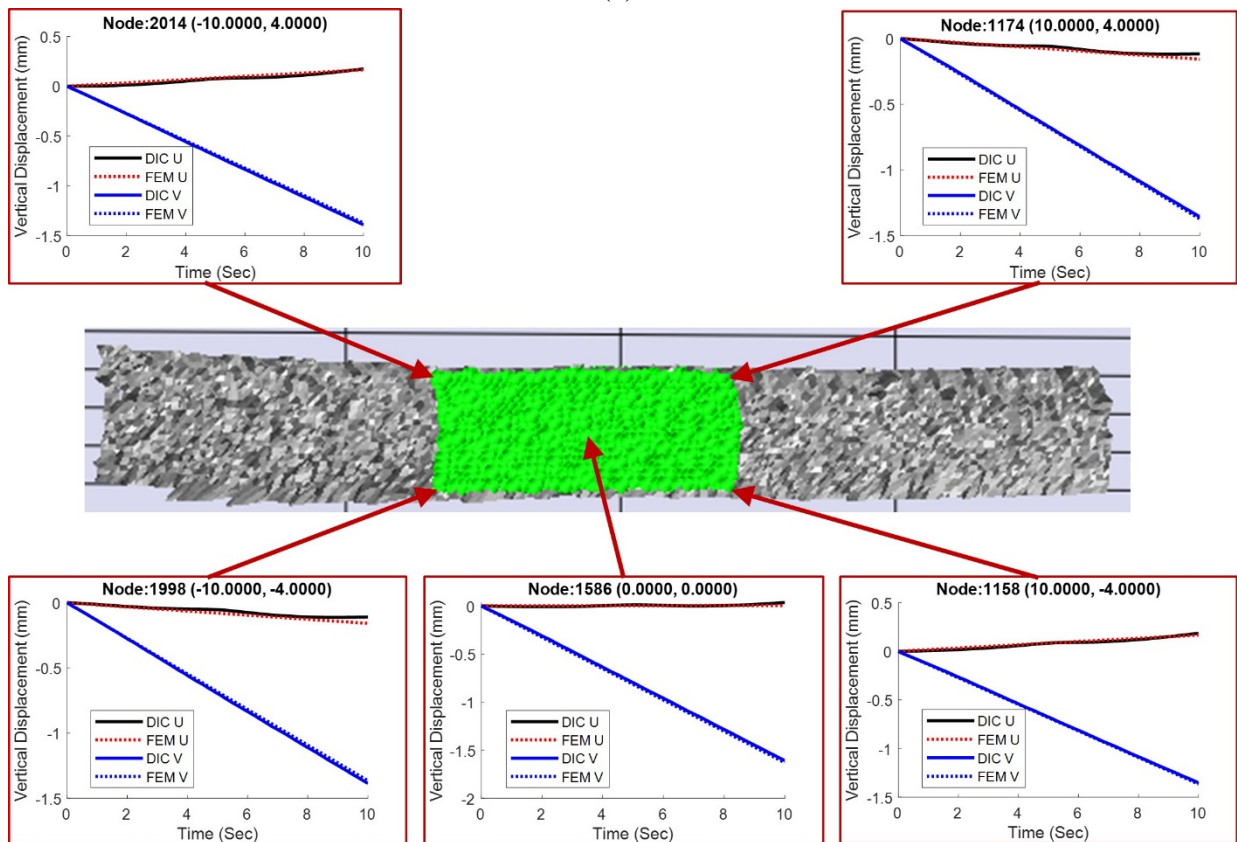
(b)

Figure 79. LE results from the DIC-FEM inverse method: (a) optimal LE properties of PEEK and evolution of objective function and (b) displacements at the solution.

6.6.2. Linear Viscoelastic Properties of FAM

6.6.2.1. Effect of Poisson's Ratio

Figure 80 shows the effect of Poisson's ratio on the deflection of a viscoelastic specimen. In the figure, typical creep compliance of FAM was used to plot the graph at different Poisson's ratios. As can be seen, Poisson's ratio had minimal effects on the deflection, which is advantageous for the DIC-FEM optimization process due to the reduced unknowns, while it is limited to fully characterize the LVE properties using the beam geometry. The relative maximum difference in deflection between the smallest (i.e., 0.1) and the largest (i.e., 0.5) Poisson's ratio attempted was approximately five percent. As a result, the Poisson's ratio of FAM was assumed to be constant and equal to 0.35 based on other studies (Aragão and Kim 2012, Im, Kim et al. 2013). With the constant Poisson's ratio, the time-dependent relaxation modulus $E(t)$ was identified via the DIC-FEM inverse process.
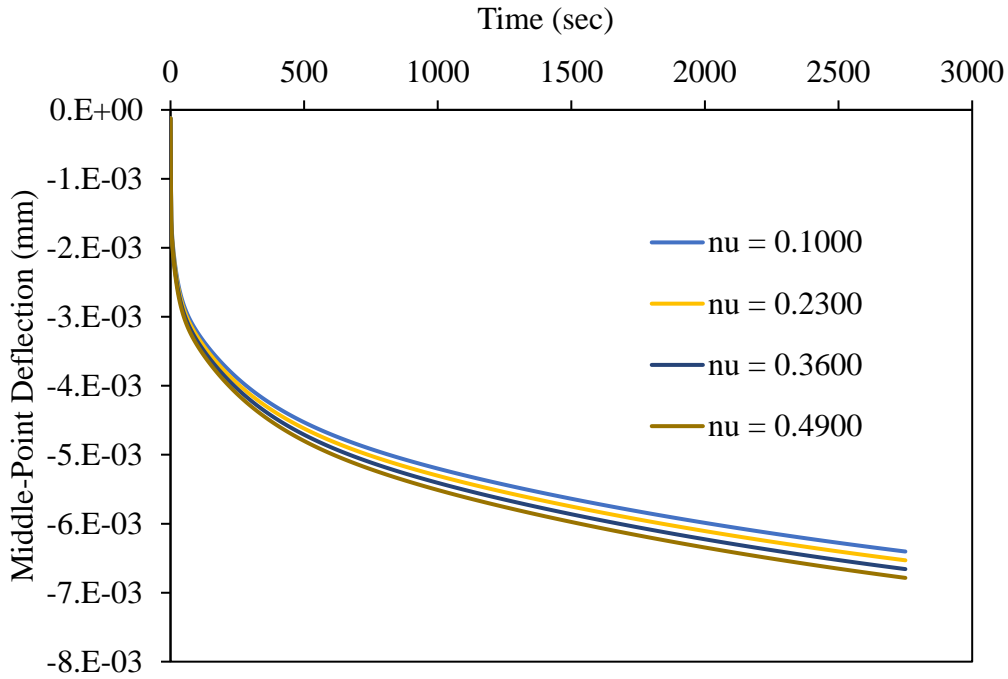
Figure 80. Effect of Poisson's ratio on the analytical deflection of viscoelastic beam specimens.

6.6.2.2. Results of DIC-FEM Inverse Process

The main complexity of determining LVE properties using the FEM-DIC inverse method arises from the many Prony series terms required to represent a certain relaxation function. To address this, the relaxation function was first assumed as a power function during DIC-FEM optimization then was converted into Prony series terms during the FEM simulation which improved efficiency and reduced the computational cost of the DIC-FEM inverse process.

(a)

(b)
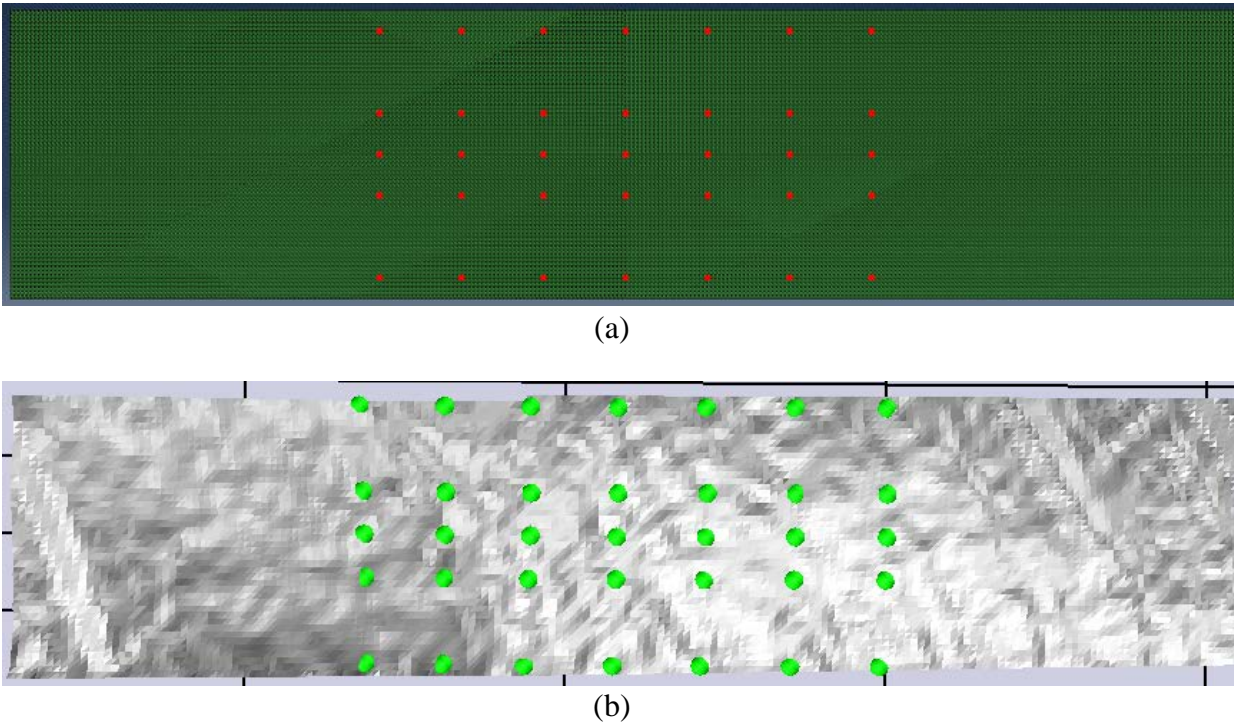
Figure 81. Selecting points inside ROI of FAM testing to construct an objective function (number of points = 35) for (a) FEM, and (b) DIC.

The construction of the objective function was conducted by extracting displacement data from both FEM simulation and DIC measurement at the same nodal locations as shown in Figure 81. As an example, a total of 35 points were extracted in the figure, although the number of nodal points can be controlled by the user.

With the LVE creep load of 2.5 N, each creep testing was conducted for 2,750 seconds. DIC data were analyzed using a subset size of 25 x 25 pixels and a step size of 8 pixels. Concurrently, the FE model simulation was conducted using a 0.5 mm mesh of 3-node linear elements (CPS3). The mesh size was selected after a mesh convergence study. Figure 82 shows the distribution of the vertical displacements from the DIC (Figure 82 (a)) and FEM (Figure 82(b)).

(a)

(b)
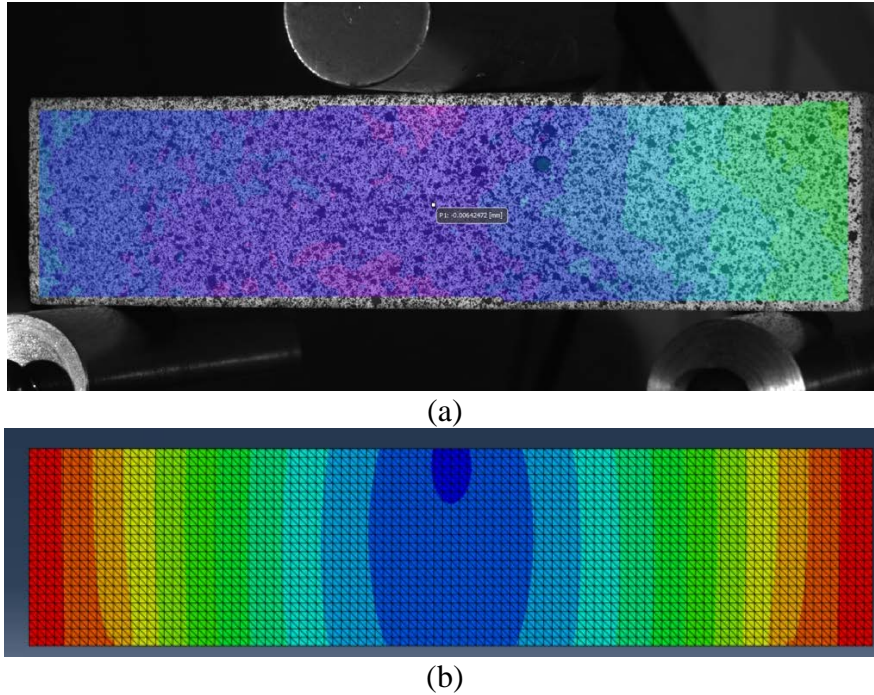
Figure 82. Linear viscoelastic properties characterization: (a) DIC and, (b) FEM.

Figure 83(a) shows the resulting relaxation modulus from the DIC-FEM inverse method along with the variation of the objective function. As the figure shows, the inverse method rapidly converged at around 20 iterations, and the objective function has been quite saturated at 100 iterations. The relaxation modulus determined in terms of Prony series parameters is shown in Figure 83(a), where $E(t)$ is represented with a total of ten Prony series terms. Figure 83(b) presents the resulting displacements at the optimized LVE property. Five different locations were arbitrarily selected to demonstrate the agreement between DIC experimental results and FEM computational simulations. Generally, the time-dependent displacements were in good agreement, which implies the validity of the DIC-FEM inverse process in identifying unknown LVE material properties such as relaxation modulus.
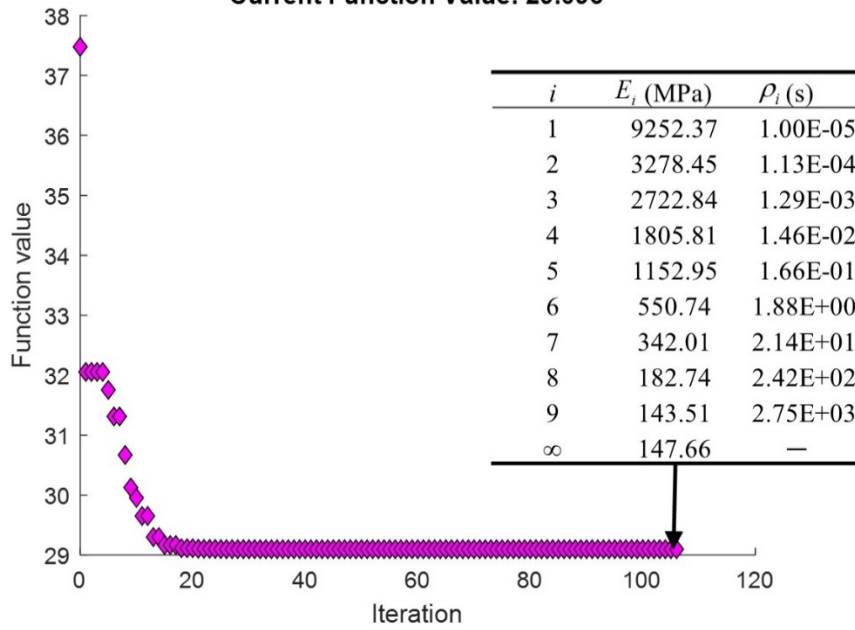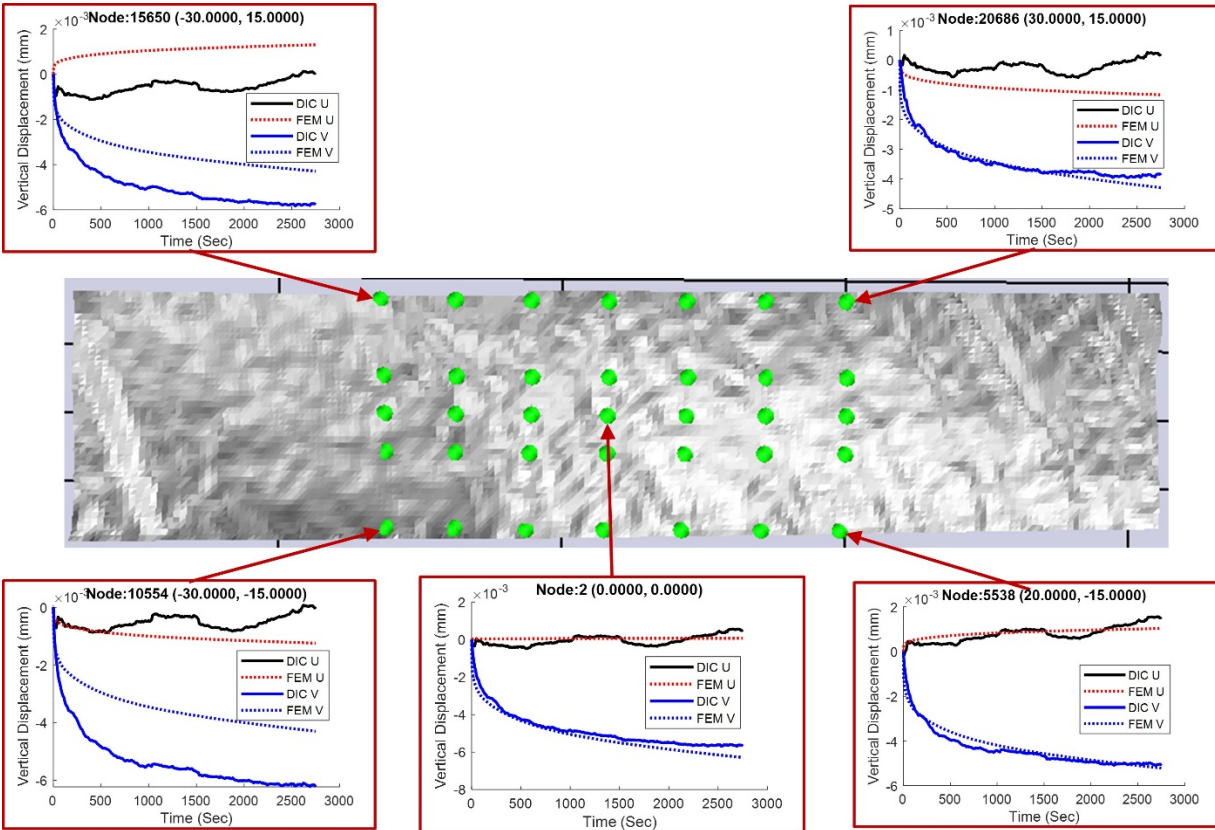
Figure 83. LVE results from the DIC-FEM inverse method: (a) optimal LVE properties of FAM and evolution of objective function and (b) displacements at the solution.
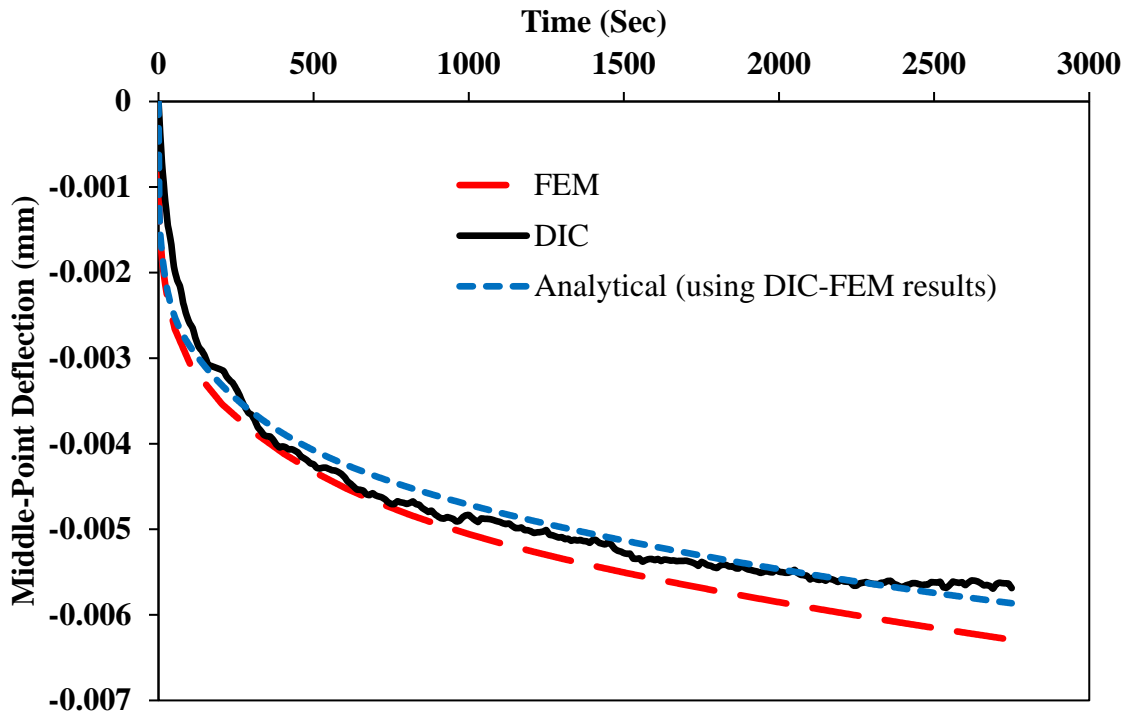
Figure 84. Comparison of deflection results from the FEM, the experiment (i.e., DIC), and analytical solution calculated using results from the DIC-FEM inverse method.

Using the results from the DIC-FEM inverse method (Figure 83(a)) the analytical solution to the deformation at the center of the FAM beam specimen was calculated using the equation (9.5). Figure 84 shows the results from the analytical solution compared to FEM and DIC results. It can be seen that both the analytical and FEM deflections using LVE properties obtained from the inverse method were in good agreement with experimental DIC results. The good agreement between the deflection results implies that the DIC-FEM inverse method implemented in this study is valid for the characterization of linear viscoelastic properties of materials.

6.7. **Summary**

This chapter presented the DIC-FEM inverse method for characterizing the constitutive properties of linear elastic and viscoelastic materials. The inverse method was implemented by performing experimental testing aided with DIC and by conducting FEM simulation. The DIC analysis was accomplished by a commercial software called VIC-3D, while the FEM simulation was done through ABAQUS. A python script was written to communicate with ABAQUS to retrieve simulation results at each iteration. MATLAB numerical software was used as a hub for optimization, which used the Nelder-Mead solver.

Two example materials selected were PEEK and FAM for elastic and viscoelastic investigation, respectively. The selected testing set-up for both investigations was the three-point bending. For PEEK, the load was monotonically increased in displacement-controlled mode using a 350 N. For FAM, a creep testing at 2.5 N for 2750 seconds was conducted after a preliminary study to determine the linear viscoelastic region. In both cases, DIC was used to monitor field displacement. The inversely obtained material properties for PEEK agreed well with the literature, and FAM results were in good agreement with the analytical solution.

CHAPTER VII

DIC-FEM INVERSE METHOD TO CHARACTERIZE FRACTURE PROPERTIES

This chapter presents the DIC-FEM inverse method to further characterize fracture properties of linear elastic and linear viscoelastic materials whose constitutive materials properties have been identified in the previous chapter (i.e., PEEK and FAM). The test set-up, test results, and DIC-FEM results are presented. The calculated fracture properties were compared to those found in the open literature.

7.1. **Introduction**

Fracture is a critical mechanism in engineering materials that can cause the failure of engineered structures such as asphalt concrete pavements. Without identification and characterization of fracture properties, proper material design, and ultimately, structural design of pavements are not appropriately accomplished. In this chapter, the developed DIC-FEM inverse method was deployed to characterize fracture properties of elastic and viscoelastic materials. The inverse method has several advantages over the traditional methods by using local deformation results. Since fracture is a local phenomenon, the DIC-FEM inverse method is uniquely positioned to improve fracture characterization towards more accurate material models and performance prediction.

One of the well-known and widely used methods to model fracture using the FEM framework is by the CZM (cohesive zone model). The cohesive zone is a fictitious crack at the onset of the crack path that relates tractions to crack opening displacement. The CZM has been

used to model fracture of various kinds of materials including elastic (Shen and Paulino 2011) and viscoelastic (Im, Ban et al. 2014, Rodrigues, Teixeira et al. 2019).
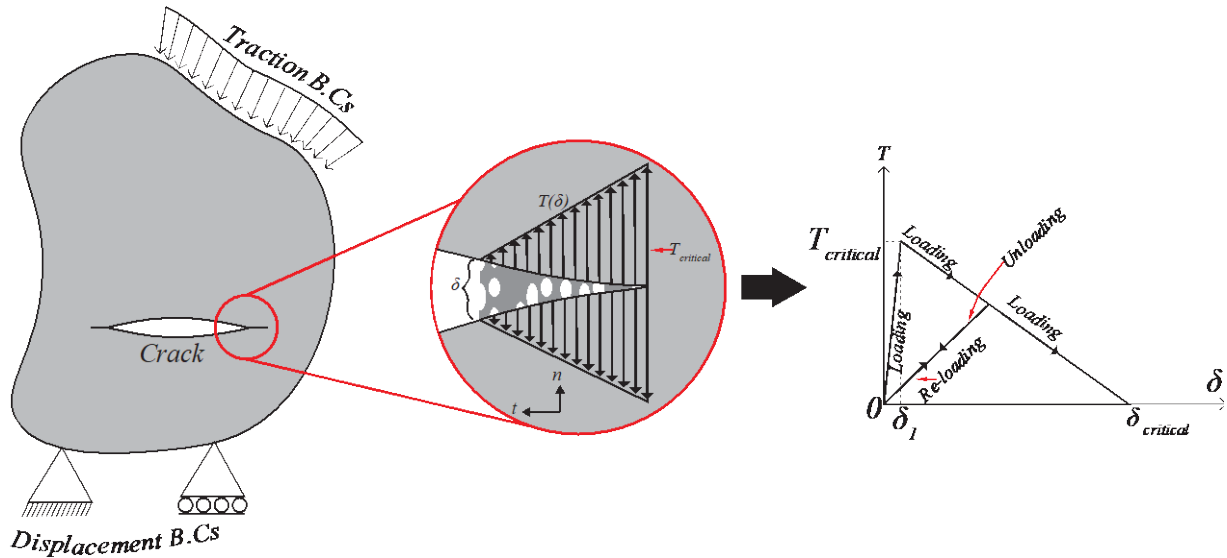
Figure 85. Modeling fracture using a CZM.

Figure 85 shows a continuum body undergoing fracture where microcracks continually coalesce into a macrocrack. During the crack opening and coalescence of microcracks into macrocracks, traction is exerted on the two opposing crack surfaces. The CZM then provides a relation between crack opening displacement (δ) and the traction (T) at the tip of the crack surface. The relationship assumes critical traction $T_{critical}$ beyond which a cohesive zone is initiated. Subsequently, the traction continually decays until a critical crack opening displacement ($\delta_{critical}$), where cohesive traction becomes zero, which infers a physical separation of the cohesive zone.

Depending on the shape of the traction-separation curve, there are several types of CZMs such as linear, bi-linear (as shown in Figure 85), exponential (Xu and Needleman 1993), cubic

174

polynomial (Song, Paulino et al. 2006), Park and Paulino (2011). More CZMs have been proposed for rate-, temperature-, and time-dependent viscoelastic materials. Yoon and Allen (1999) and Allen and Searcy (2001) used Helmholtz free energy and micromechanics to develop a nonlinear viscoelastic CZM. The rate-dependent CZM was used to model cracking of bituminous materials and pavements (Kim 2003, Kim, Allen et al. 2007, Lutif, Souza et al. 2010, Aragão, Kim et al. 2011).

Rate-independent CZMs (e.g., bi-linear) have also been used with limited success to modeling fracture in rate-dependent materials such as bituminous (Aragão and Kim 2012, Im, Kim et al. 2013, Aragão, Hartmann et al. 2014, Im, Ban et al. 2014, Rodrigues, Teixeira et al. 2019). In the cited studies, CZM parameters were determined through the process of calibration in which CZM properties are continually adjusted until a good agreement is obtained between FEM and global experimental test results (Aragão, Kim et al. 2010, Aragão and Kim 2012, Im, Kim et al. 2013). As aforementioned, using global results to identify properties of materials may overlook the true material characteristics, in particular when local issues such as cracking and heterogeneities are significant to affect the overall material behavior (e.g., asphalt mixtures).

This chapter aims at expanding the developed FEM-DIC inverse method to include the characterization of fracture properties for both elastic and viscoelastic materials.

7.2. **Experimental Test Set-Up**

Figure 86 shows the experimental set-up for the characterization of fracture properties of PEEK and FAM. The set-up was essentially identical to the testing (in Chapter VI) for constitutive properties with exception of the notch. For PEEK, the notch was triangular with a rounded crack-tip as shown in Figure 86(a). The notch length for the PEEK specimen was V-shaped and machined to have dimensions of 2.54 mm, 2.36 mm, 0.36 mm, and 0.25 mm for the initial crack-

mouth width, notch length, crack-tip width, and radius of the crack-tip, respectively (Figure 86(a)). For FAM, a rectangular notch was inserted in the specimen with dimensions of 5 mm in height and 2 mm in width(Figure 86(b)). Both fracture tests for PEEK and FAM were loaded in a displacement-controlled mode from the load point located at the top center of the specimen. The loading rates were 5 mm/min and 0.5 mm/min for PEEK and FAM fracture tests, respectively.
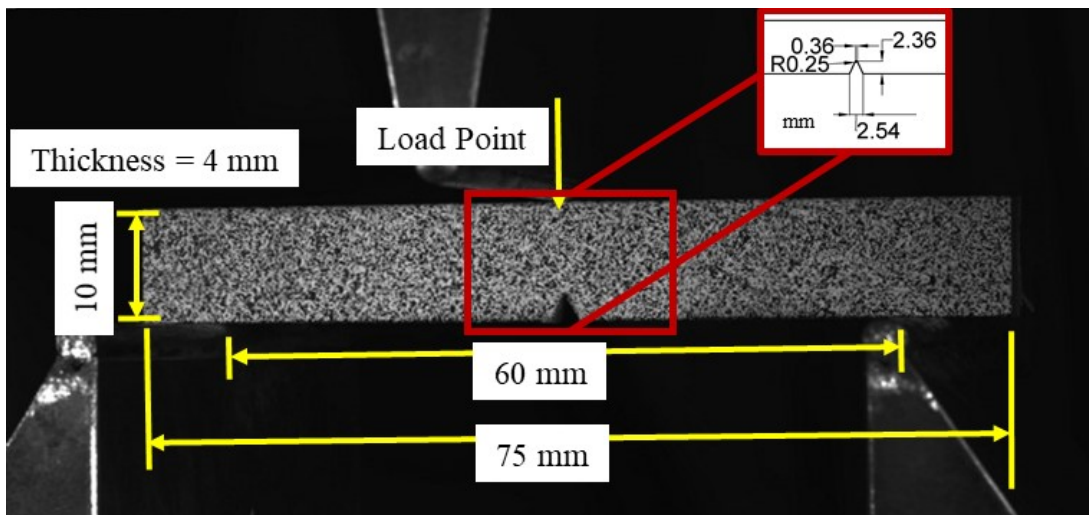
(a)
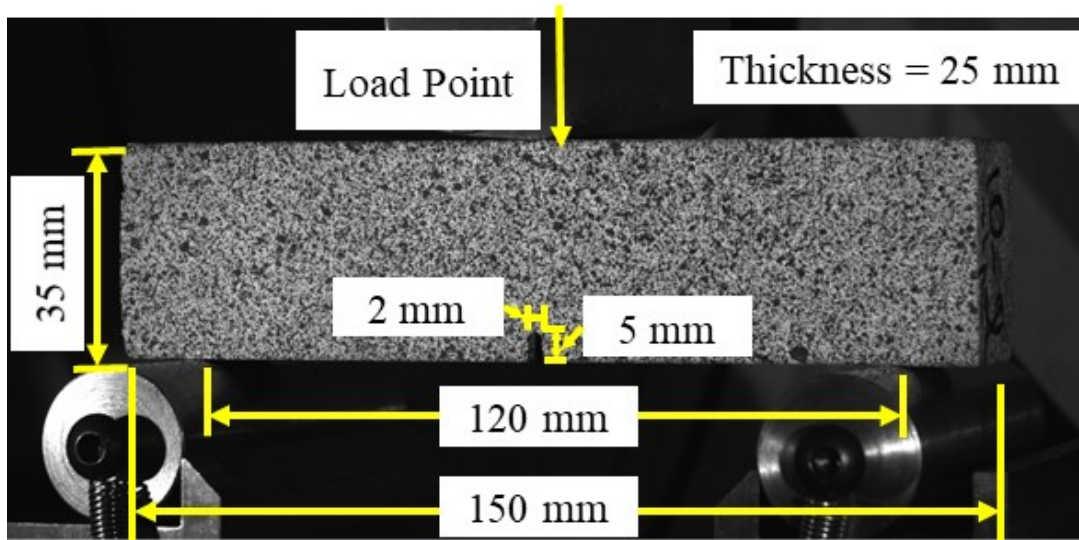
(b)

Figure 86 Test set-up for fracture properties of (a) PEEK, and (b) FAM.

7.3. **Results of DIC-FEM Inverse Process**

DIC data were analyzed using a subset size of 25 x 25 pixels and a step size of 8 pixels. Concurrently, the FE model simulation was conducted using a 0.5 mm mesh of 3-node linear elements (CPS3). The final mesh size was selected after a mesh convergence study. To accommodate fracture initiation and propagation, cohesive elements (COH2D4) of zero thickness were embedded in the center vertical line of the FE model. Figure 87 shows the boundary conditions used in the FEM for PEEK (Figure 87(a)) and FAM (Figure 87(b)). In both cases, a graded mesh was used so that region with fracture can be modeled with a sufficient number of cohesive zone elements, while other areas are with coarser meshes to reduce computational costs without compromising model simulation accuracy.

(a)

(b)
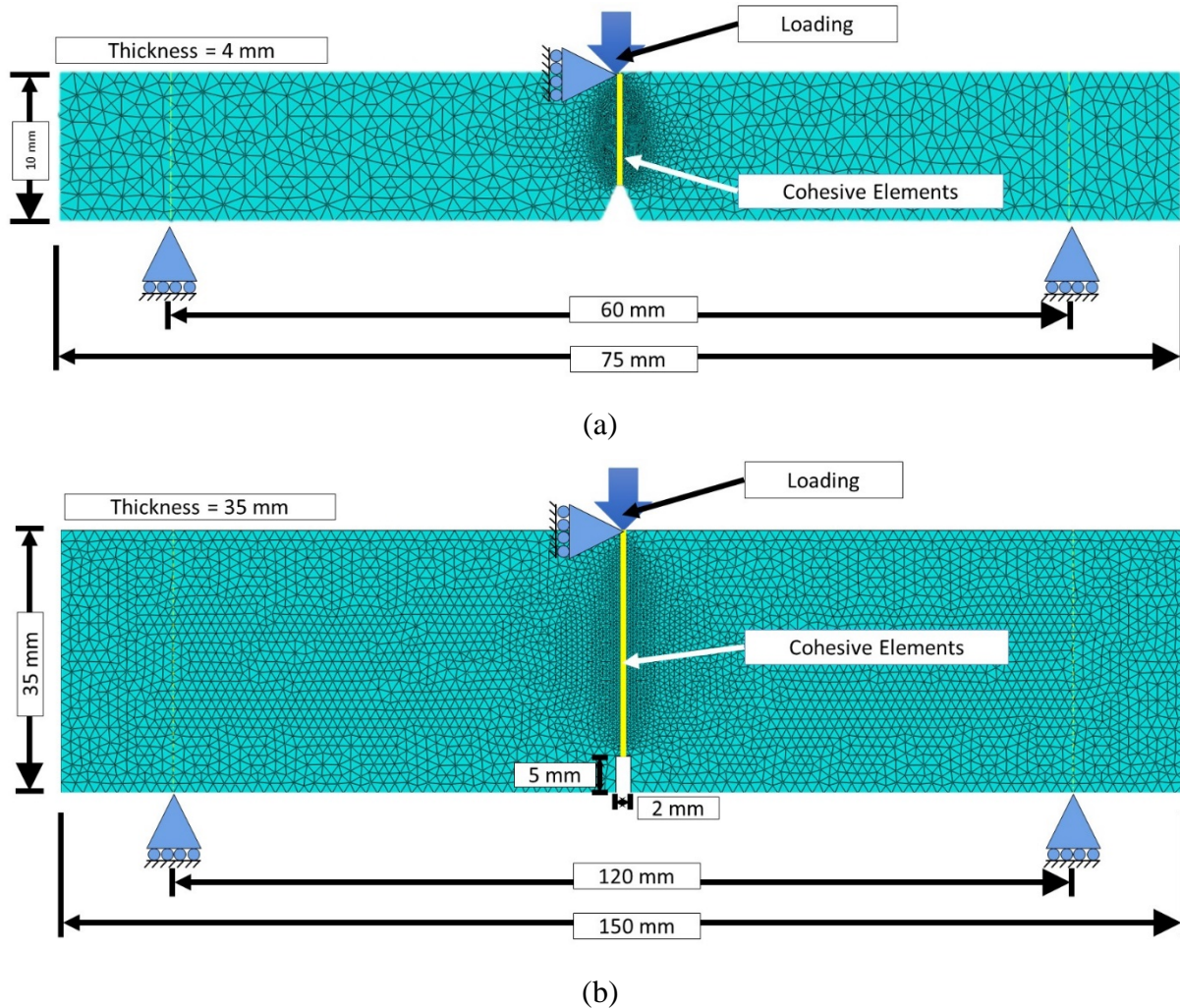
Figure 87. FEM modeling for fracture properties characterization.

The beam fracture testing of PEEK was performed using the loading rate of 5 mm/min. The reaction at LP (load point) was recorded by the data acquisition (DAQ) system of the mechanical testing station, while the surface deformations were captured by two cameras for DIC analysis. As aforementioned, both testing systems (i.e., mechanical testing station and DIC) were synchronized. Figure 88 shows fracture propagation in PEEK simulated by FEM (Figure 88(a)) and DIC (Figure 88(b)).
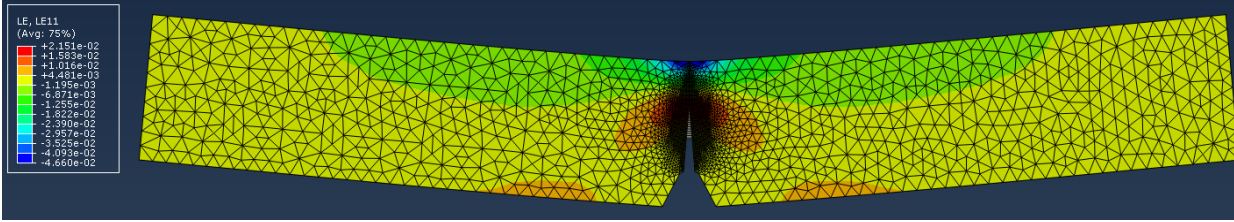
(a)
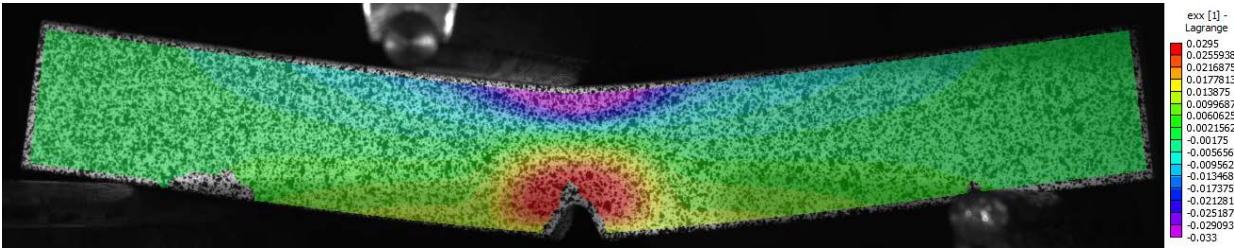
(b)

Figure 88. Fracture modeling and experiment of PEEK showing the distribution of ε_{xx} (i.e., ε_{11}) (a) FEM, and (b) DIC.

Due to the brittle nature of PEEK, the specimen experienced a sudden fracture. It should be noted that the testing set-up (cameras) used in this study was limited to effectively capture the rapid fracture. The frame rate used for DIC of PEEK testing was 100 frames per second, which was insufficient to capture the dramatic fracture of PEEK. As a result, only the experimental results prior to the abrupt fracture were recorded and used in the DIC-FEM inverse method for fracture characterization of PEEK. It is important to note that brittle fracture often lacks post-peak (i.e., post maximum load) load and displacement measurements as evidenced in the ASTM D5045−14. In the standard, a method is presented to determine fracture toughness (i.e., critical stress intensity factor, K_{IC}) of polymeric material based on pre-peak global data (i.e., force vs. crack opening displacement) (Chu and Schultz 1990, Lesiuk, Sawicka et al. 2017). Therefore, although the DIC was limited to fully capture the rapid fracture and post-peak behavior, the displacement at the onset of fracture was captured and used in the DIC-FEM inverse method.

It is noteworthy that high-speed DIC systems have been used to detect crack propagation in brittle materials including polymeric materials (Kirugulige, Tippur et al. 2007) and granite (Gao, Huang et al. 2015) using frame rates per second of 225,000 and 180,000, respectively. In contrast, the DIC system used in this study had a maximum frame rate per second of 163.

Figure 89 shows the points (nodes) selected to perform the DIC-FEM inverse method. As the figure shows, several points were selected, and the majority of points were located along the center of the specimen around the cohesive zone elements.

(a)

(b)
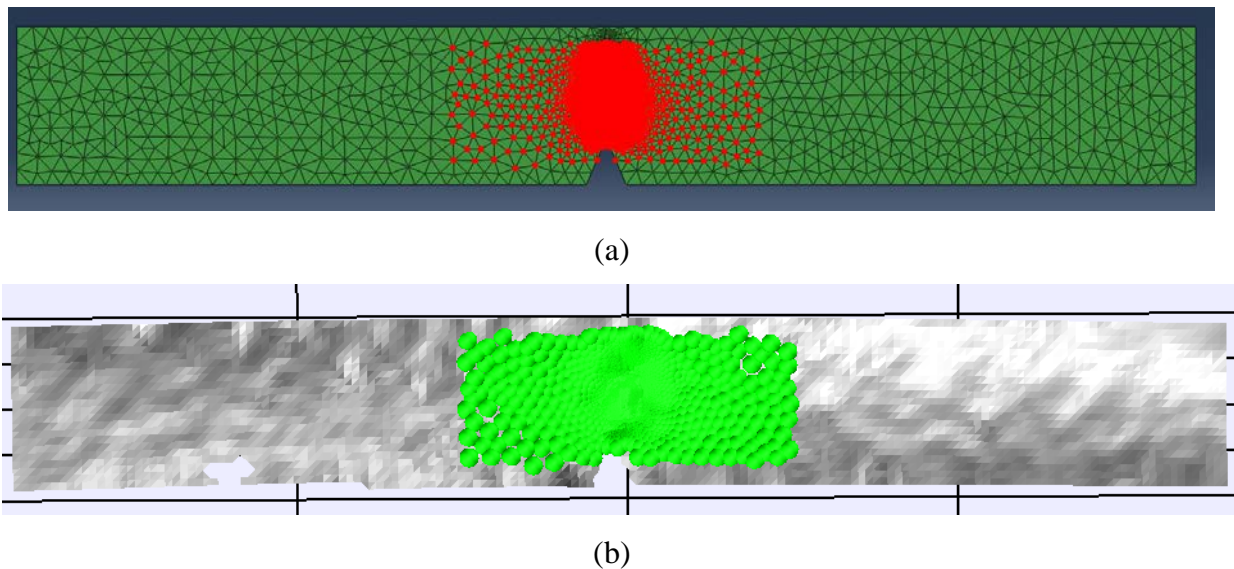
Figure 89. Selection of ROI for fracture characterization of PEEK: (a) FEM, and (b) DIC.

The results of the DIC-FEM inverse method on PEEK fracture properties are presented in Figure 90, where the optimal results for CZM were found to be 126.226 MPa and 67.449 kJ/m^2 for the $T_{critical}$ and Gf_{CZM} (cohesive fracture energy), respectively. It should be noted that the CZM in this study was an intrinsic bilinear model with a cohesive stiffness of 5×10^8 MPa. The steep ramping to the peak traction can efficiently reduce the artificial compliance issue in the intrinsic CZM such as the bilinear model.

Assuming plane stress conditions, the fracture toughness (K_{IC}) is related to the cohesive

fracture energy (Gf_{CZM}) as follows (Karger-Kocsis and Friedrich 1986, Broek 2012):

$$\frac{K_{IC}^2}{Gf_{CZM}} = E \tag{7.1}$$

where, E is the elastic modulus of PEEK (determined in Chapter VI). Substituting the elastic

modulus and cohesive energy values into the equation (6.29) gives the fracture toughness (K_{IC})

of 16.33 $\text{MPa}\sqrt{\text{m}}$. Given that the published K_{IC} of PEEK ranges from 2 to 10 $\text{MPa}\sqrt{\text{m}}$ (Karger-

Kocsis and Friedrich 1986, Chivers and Moore 1994, Lesiuk, Sawicka et al. 2017), the DIC-

FEM inverse method overestimated the fracture toughness of the materials. This might be due to

the limited capability of capturing the full fracture process of the PEEK using the DIC system

used in this study. A follow-up examination is recommended as a further study.
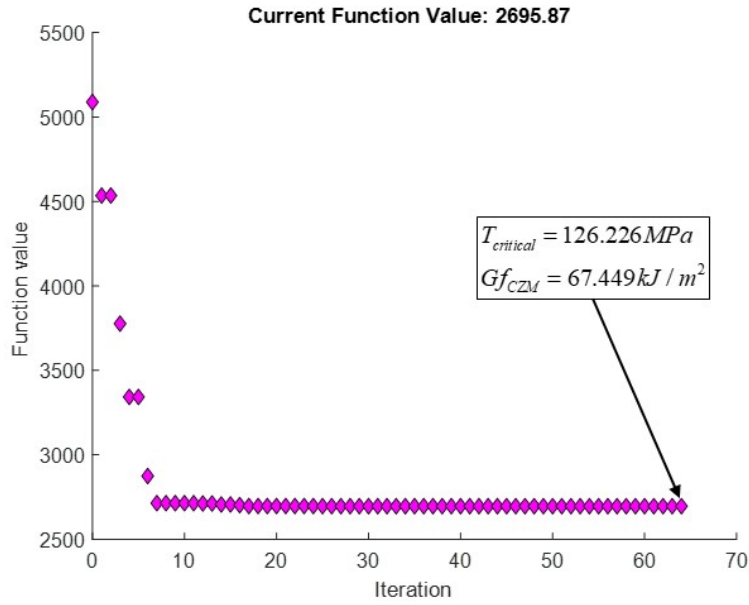
(a)
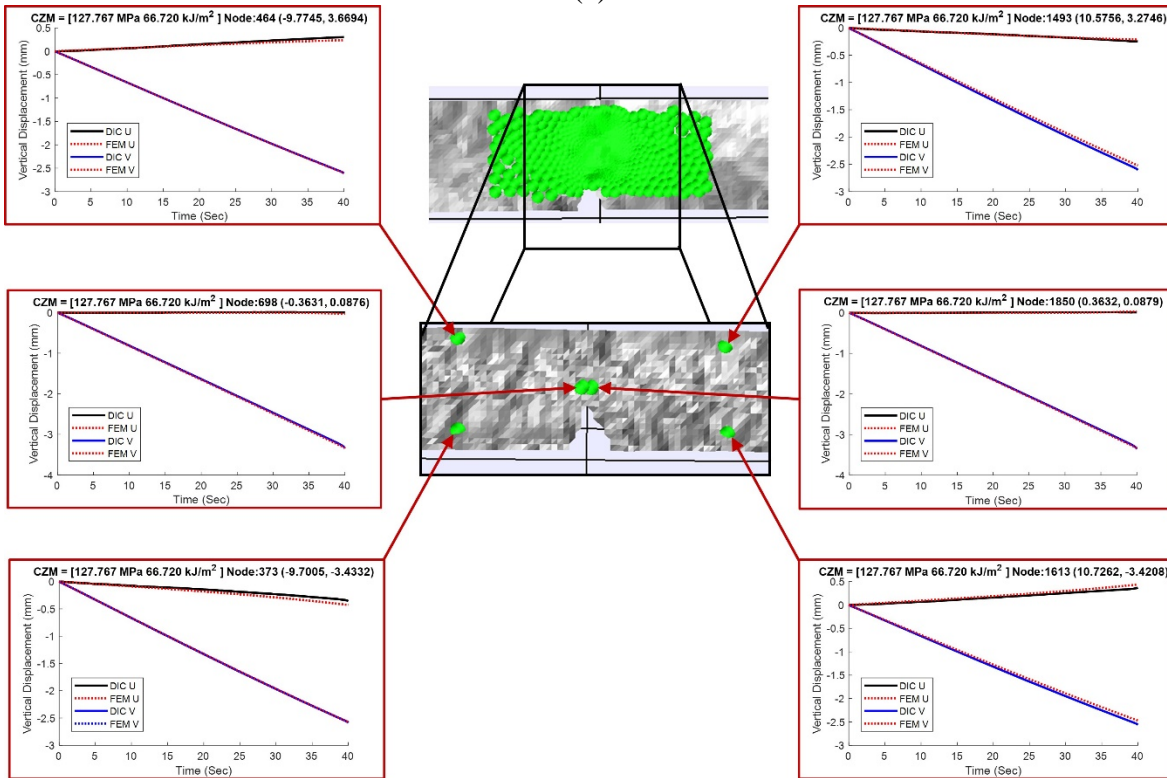
(b)

Figure 90. Evolution of the objective function for DIC-FEM inverse characterization of PEEK fracture properties.

Similar to the PEEK, the fracture properties of FAM were also characterized using the DIC-FEM inverse method based on the bilinear CZM. Figure 91 shows the fracture process from DIC imaging (Figure 91(a)) and FE simulation (Figure 91(b)). The load was applied in a displacement-controlled mode at a rate of 0.5 mm/min.

(a)

(b)
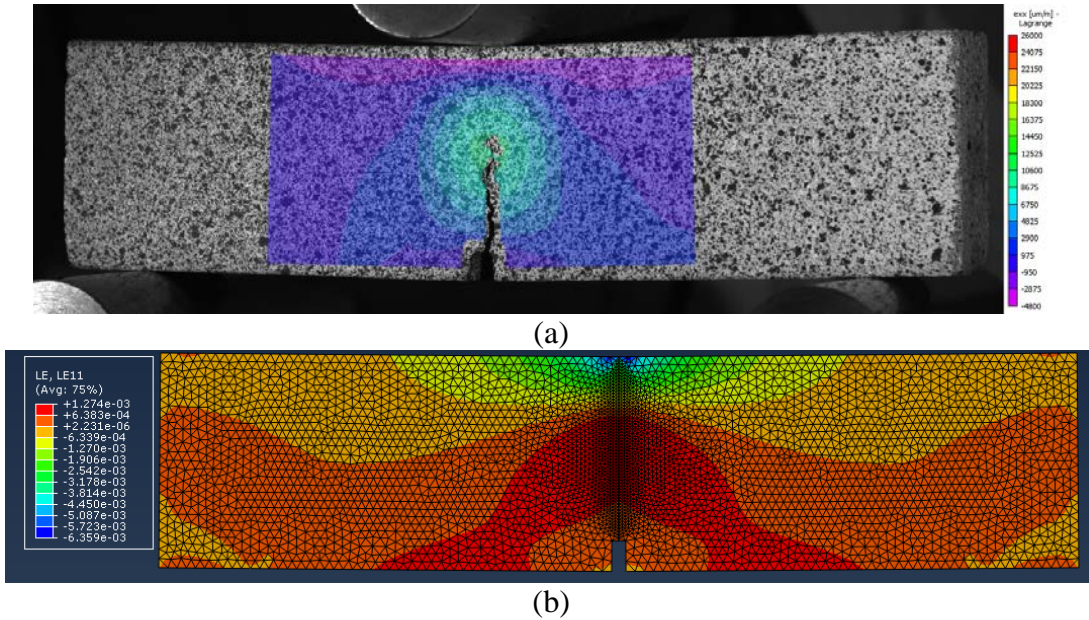
Figure 91. Fracture profile of FAM: (a) experiment and (b) FEM.

To construct the objective function, the ROI was selected as shown in Figure 92 from FEM(a) and DIC(b). The points used in the objective function were concentrated around the cohesive region to better capture fracture-related displacements. As can be seen in Figure 91(a), the experimental fracture ligament closely followed Mode-I fracture with some minor deviations. However, in the FEM modeling shown in Figure 91 (b), the fracture was pure Mode-I due to the vertically-inserted cohesive elements. Similar to the precedent cases, the DIC-FEM inverse method was conducted by selecting points (i.e., nodes) inside the cohesive region that were used to construct the objective function. Figure 92 shows the process of selection of the points from DIC (Figure 92 (a)) and FEM (Figure 92 (b)).

(a)

(b)
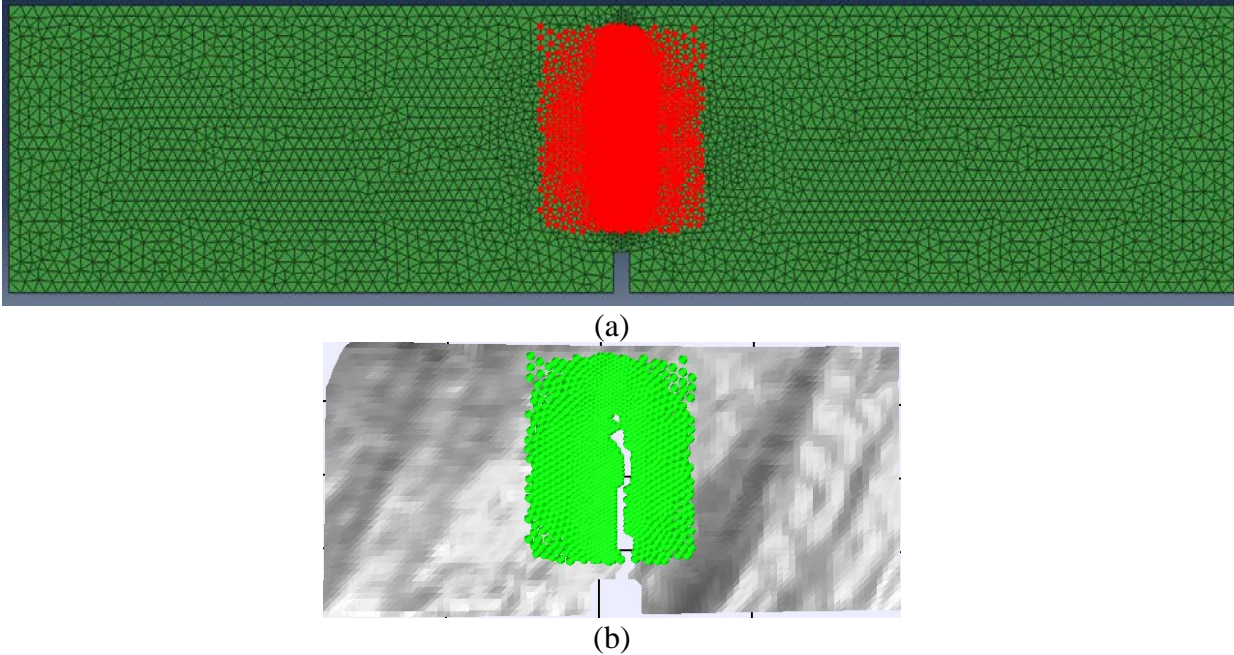
Figure 92. Selection of ROI for fracture characterization of FAM: (a) FEM, and (b) DIC.

Figure 93 shows the CZM parameters identified by the DIC-FEM inverse method. The function evolution plot over the number of iterations (Figure 93(a)) shows a rapid initial convergence followed by a saturation of the function value at only 25 iterations. The optimal CZM for FAM was identified as 1.093 MPa and 0.234 kJ/m^2 for the $T_{critical}$, and Gf_{CZM} , respectively. The CZM values of FAM were compared to the results obtained by (Aragão and Kim 2012) on the identical FAM used in this study. (Aragão and Kim 2012) investigated Mode-I fracture CZM at different loading rates. The CZM value from the DIC-FEM inverse method is considered reasonable as it is well suited to the results from the literature at the loading rate (i.e., 0.5 mm/min) and testing temperature (i.e., 23C) given. Figure 93(b) shows the matching of vertical and horizontal displacements between FEM and DIC. As seen from the figure, with the properties identified, the displacements from each data set were in good agreement for both vertical (V) and horizontal (U) displacements.

184

(a)

(b)
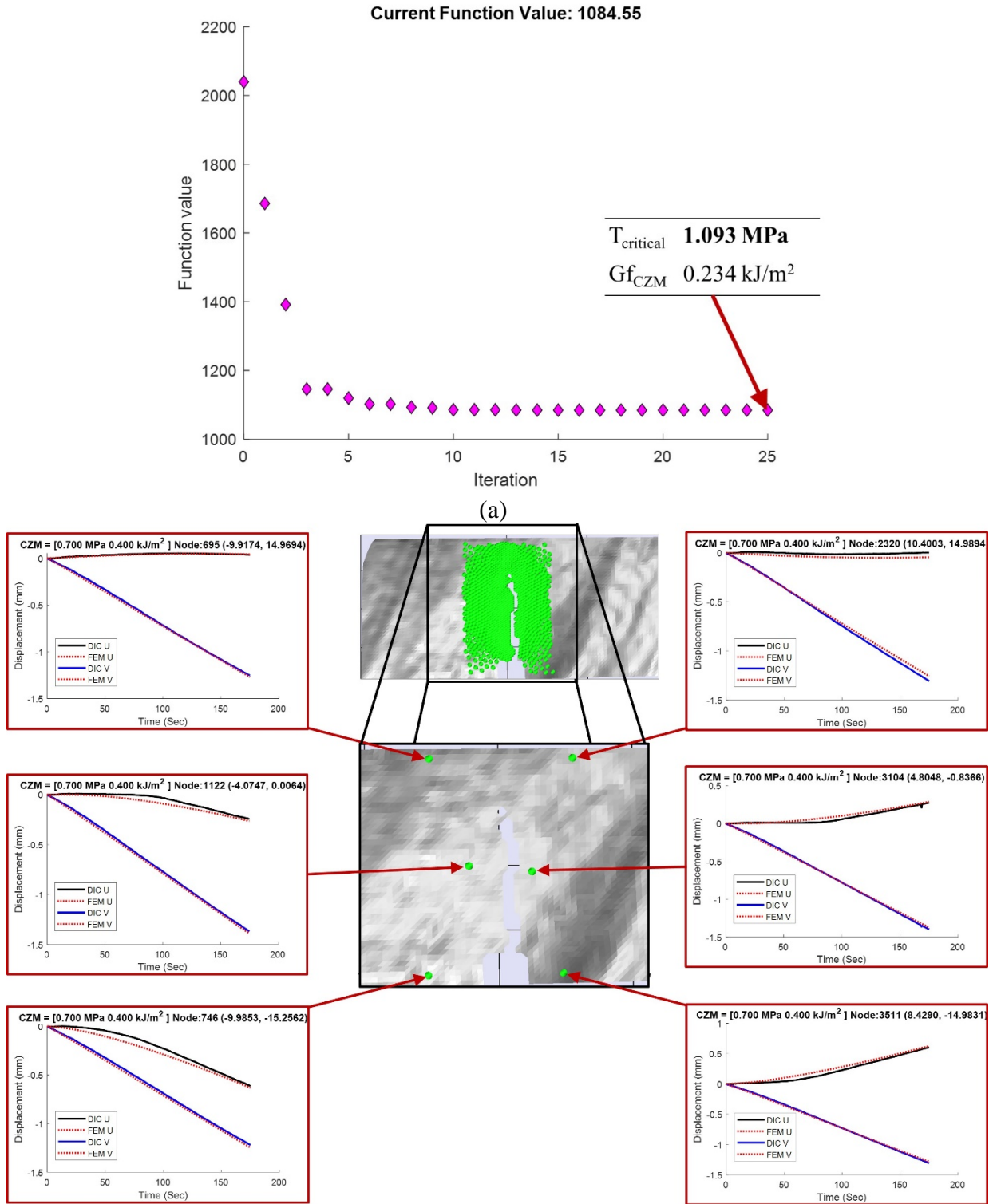
Figure 93 DIC-FEM results for FAM fracture: (a) evolution of the objective function with optimal CZM parameters, and (b) displacements at the solution.

7.4. **Summary**

This chapter expanded the previously implemented DIC-FEM inverse method to include fracture characterization. The basic testing set-up remained constant as for constitutive properties with exception of the notch. The loading rate to investigate fracture in PEEK was 5 mm/min, while the loading rate was 0.5 mm/min for FAM. The bilinear cohesive zone model was used to simulate fracture in the specimens using FEM. The cohesive zone model parameters were identified using the DIC-FEM inverse optimization method.

The inversely obtained results for PEEK were overpredicted when compared to the values found in existing literature, while the fracture properties of FAM looked reasonable. This might be due to the limited capability of capturing the full fracture process of the PEEK using the DIC system used in this study.

CHAPTER VIII

CONCLUSIONS

This study was to improve the performance test methods of bituminous mixtures for their practical implementation and to explore a method to help fundamental understanding of inelastic deformation and fracture in materials including bituminous mixtures. An experimental-statistical approach was used to improve practical performance testing of bituminous mixtures, while a DIC-FEM optimization method was used to characterize properties of materials. Based on the results and findings, the following conclusions can be drawn:

- The SCB investigation resulted in recommended values of testing conditions that can improve the repeatability of test results without hindering the practicality.

- The G-stability testing developed in this study can estimate the rutting performance of bituminous mixtures. The G-Stability test method used disc-shaped specimens of 150 mm in diameter that are loaded quasi-statically in displacement-controlled mode along the diameter. The G-Stability investigation resulted in recommended values of testing conditions that can provide repeatable and sensitive results.

- The SCB and G-Stability test methods were successfully applied to a performance space diagram (PSD) where high-RAP mixtures with rejuvenators were used.

- The SCB and G-Stability test methods applied to the performance-based mixture design need to be further validated by field data. In addition, the two test methods should consider durability issues such as aging and moisture damage.

- The two test methods explored in this study have both immediate and emerging impacts on the design, material selection, and performance prediction of asphalt concrete

mixtures. To fulfill the method, only two tall, gyratory compacted specimens are necessary using a single mechanical testing station with about 15 kN loading capacity.

- The DIC-FEM inverse method was utilized to determine the constitutive and fracture properties of PEEK and FAM. The inverse optimization method produced reasonable elastic modulus of PEEK, viscoelastic relaxation modulus of FAM, and cohesive zone fracture characteristics of FAM, while fracture toughness of PEEK requires further examination as PEEK showed a brittle fracture and was not fully characterized by the DIC used in this study.

- The DIC-FEM method can be expanded to asphalt concrete mixtures to characterize properties of components and their interactions towards more mechanistic mixture design as the method can capture important local phenomena within the mixture. This enhanced understanding can help develop the mixture performance tests in a more accurate and efficient manner.

REFERENCES

Abaqus, V. (2014). 6.14 Documentation. <u>Dassault Systemes Simulia Corporation</u>. **651:** 6.2.

Abdi, H. and P. Molin (2007). "Lilliefors/Van Soest's test of normality." <u>Encyclopedia of measurement and statistics</u>: 540-544.

Al-Qadi, I. L., Q. Aurangzeb, S. H. Carpenter, W. J. Pine and J. Trepanier (2012). "Impact of high RAP contents on structural and performance properties of asphalt mixtures." <u>FHWA-ICT-12-002</u>.

Al-Qadi, I. L., H. Ozer, J. Lambros, A. El Khatib, P. Singhvi, T. Khan, J. Rivera-Perez and B. Doll (2015). Testing protocols to ensure performance of high asphalt binder replacement mixes using RAP and RAS, Illinois Center for Transportation/Illinois Department of Transportation.

Ali, U. M., I. L. Al-Qadi and H. Ozer (2020). "Flexibility Index Threshold Optimization for Various Asphalt Concrete Mixes and Climatic Conditions." <u>Transportation Research Record</u> **2674**(1): 104-112.

Allen, D. H., D. N. Little, R. F. Soares and C. Berthelot (2017). "Multi-scale computational model for design of flexible pavement–part I: expanding multi-scaling." <u>International Journal of Pavement Engineering</u> **18**(4): 309-320.

Allen, D. H., J. E. S. Lutif and Y.-R. Kim (2009). "Determining Representative Volume Elements of Asphalt Concrete Mixtures Without Damage." <u>Transportation Research Record: Journal of the Transportation Research Board</u> **2127**(-1): 52-59.

Allen, D. H. and C. R. Searcy (2001). "A micromechanical model for a viscoelastic cohesive zone." <u>International Journal of Fracture</u> **107**(2): 159-176.

Amelian, S., Y.-R. Kim, P. Osmari, F. T. S. Aragão, D. Braz and L. P. Nogueira (2019). Development of a Volumetric Mix Design Approach for Fine Aggregate Matrix (FAM) and Validation with Micro-CT Method.

Anderson, T. L. (2017). <u>Fracture mechanics: fundamentals and applications</u>, CRC press.

Apeagyei, A. K. (2011). "Laboratory evaluation of antioxidants for asphalt binders." <u>Construction and Building Materials</u> **25**(1): 47-53.

Aragão, F. and Y.-R. Kim (2012). "Mode I fracture characterization of bituminous paving mixtures at intermediate service temperatures." <u>Experimental mechanics</u> **52**(9): 1423-1434.

Aragão, F. T. S., D. A. Hartmann, Y.-R. Kim, L. M. G. Da Motta and M. Haft-Javaherian (2014). "Numerical–experimental approach to characterize fracture properties of asphalt mixtures at low temperatures." <u>Transportation Research Record</u> **2447**(1): 42-50.

Aragão, F. T. S., Y.-R. Kim, J. Lee and D. H. Allen (2010). "Micromechanical model for heterogeneous asphalt concrete mixtures subjected to fracture failure." Journal of Materials in Civil Engineering **23**(1): 30-38.

Aragão, F. T. S., Y.-R. Kim, J. Lee and D. H. Allen (2011). "Micromechanical model for heterogeneous asphalt concrete mixtures subjected to fracture failure." Journal of Materials in Civil Engineering **23**(1): 30-38.

Aragão, F. T. S. and Y. R. Kim (2012). "Mode I Fracture Characterization of Bituminous Paving Mixtures at Intermediate Service Temperatures." Experimental mechanics **52**(9): 1423-1434.

Arámbula-Mercado, E., F. Kaseer, A. E. Martin, F. Yin and L. G. Cucalon (2018). "Evaluation of recycling agent dosage selection and incorporation methods for asphalt mixtures with high RAP and RAS contents." Construction and Building Materials **158**: 432-442.

Artamendi, I. and H. A. Khalid (2006). "A comparison between beam and semi-circular bending fracture tests for asphalt." Road Materials and Pavement Design **7**(sup1): 163-180.

Aschenbrener, T. (1995). "Evaluation of Hamburg wheel-tracking device to predict moisture damage in hot-mix asphalt." Transportation Research Record **1492**: 193.

Bahia, H., P. Teymourpour, D. Swiertz, C. Ling, R. Varma, T. Mandal, P. Chaturabong, E. Lyngdal and A. Hanz (2016). Analysis and feasibility of asphalt pavement performance-based specifications for WisDOT, Wisconsin. Dept. of Transportation.

Ban, H., P. Karki and Y.-R. Kim (2014). "Nanoindentation test integrated with numerical simulation to characterize mechanical properties of rock materials." Journal of Testing and Evaluation **42**(3): 787-796.

Barros, L., V. M. Garcia, J. Garibay, I. Abdallah and S. Nazarian (2019). "Implications of Including Reclaimed Asphalt Pavement Materials to Performance of Balanced Asphalt Concrete Mixes." Transportation Research Record **2673**(12): 670-678.

Batioja-Alvarez, D., J. Lee and J. E. Haddock (2019). "Understanding the Illinois Flexibility Index Test (I-FIT) using Indiana Asphalt Mixtures." Transportation Research Record **2673**(6): 337-346.

Biligiri, K. P., K. E. Kaloush, M. S. Mamlouk and M. W. Witczak (2007). "Rational modeling of tertiary flow for asphalt mixtures." Transportation Research Record **2001**(1): 63-72.

Biligiri, K. P., S. Said and H. Hakim (2012). "Asphalt Mixtures' Crack Propagation Assessment using Semi-Circular Bending Tests." International Journal of Pavement Research and Technology **5**(4): 209.

Boulkeraa, T., A. Ghenaiet, S. Mendez and B. Mohammadi (2014). "A numerical optimization chain combining computational fluid dynamics and surrogate analysis for the aerodynamic design

of airfoils." Proceedings of the Institution of Mechanical Engineers, Part G: Journal of Aerospace Engineering **228**(11): 1964-1981.

Broek, D. (2012). Elementary engineering fracture mechanics, Springer Science & Business Media.

Brühwiler, E., J. Wang and F. H. Wittmann (1990). "Fracture of AAC as influenced by specimen dimension and moisture." Journal of Materials in Civil Engineering **2**(3): 136-146.

Buttlar, B. "Disk-Shaped Compact Tension Test." Retrieved 3/16, 2020, from http://www.dot.state.mn.us/mnroad/projects/Low%20Temperature%20Cracking/PDF%27s%20 &%20Images/Task%20Reports/SCB%20vs%20DCT%20Fracture%20Test.pdf.

Buttlar, W. G., B. C. Hill, H. Wang and W. Mogawer (2017). "Performance space diagram for the evaluation of high-and low-temperature asphalt mixture performance." Road Materials and Pavement Design **18**(sup1): 336-358.

Chehab, G. R. (2002). Characterization of asphalt concrete in tension using a viscoelastoplastic model. DEPARTMENT OF CIVIL ENGINEERING. Raleigh, North Carolina, North Carolina State University. **Doctor of Philosophy:** 327.

Chen, F., S. Gatea, H. Ou, B. Lu and H. Long (2016). "Fracture characteristics of PEEK at various stress triaxialities." journal of the mechanical behavior of biomedical materials **64**: 173-186.

Chen, F., H. Ou, B. Lu and H. Long (2016). "A constitutive model of polyether-ether-ketone (PEEK)." journal of the mechanical behavior of biomedical materials **53**: 427-433.

Chivers, R. and D. Moore (1994). "The effect of molecular weight and crystallinity on the mechanical properties of injection moulded poly (aryl-ether-ether-ketone) resin." Polymer **35**(1): 110-116.

Choi, S. and S. P. Shah (1997). "Measurement of deformations on concrete subjected to compression using image correlation." Experimental mechanics **37**(3): 307-313.

Chong, K. and M. Kuruppu (1984). "New specimen for fracture toughness determination for rock and other materials." International Journal of Fracture **26**(2): R59-R62.

Chu, J.-N. and J. M. Schultz (1990). "The influence of microstructure on the failure behaviour of PEEK." Journal of materials science **25**(8): 3746-3752.

Cominsky, R. J., G. A. Huber, T. W. Kennedy and M. Anderson (1994). The superpave mix design manual for new construction and overlays, Strategic Highway Research Program Washington, DC.

Cooper III, S. B., L. N. Mohammad, S. Kabir and W. King Jr (2014). "Balanced asphalt mixture design through specification modification: Louisiana's experience." Transportation Research Record **2447**(1): 92-100.

Cowper, G. R. (1966). "The Shear Coefficient in Timoshenko's Beam Theory." Journal of Applied Mechanics **33**(2): 335-340.

Dai, Q. and Z. You (2007). "Prediction of creep stiffness of asphalt mixture with micromechanical finite-element and discrete-element models." Journal of Engineering Mechanics **133**(2): 163-173.

Daniel, J., J. Pochily and D. Boisvert (2010). "Can more reclaimed asphalt pavement be added? Study of extracted binder properties from plant-produced mixtures with up to 25% reclaimed asphalt pavement." Transportation Research Record: Journal of the Transportation Research Board(2180): 19-29.

Daniel, J. S. and A. Lachance (2005). "Mechanistic and Volumetric Properties of Asphalt Mixtures with Recycled Asphalt Pavement." Transportation Research Record **1929**(1): 28-36.

Doll, B., H. Ozer, J. J. Rivera-Perez, I. L. Al-Qadi and J. Lambros (2017). "Investigation of viscoelastic fracture fields in asphalt mixtures using digital image correlation." International Journal of Fracture **205**(1): 37-56.

Dongré, R., J. D'Angelo and A. Copeland (2009). "Refinement of flow number as determined by asphalt mixture performance tester: Use in routine quality control–quality assurance practice." Transportation Research Record **2127**(1): 127-136.

Dowdy, S., S. Wearden and D. Chilko (2011). Statistics for research, John Wiley & Sons.

Duan, K., X.-Z. Hu and F. H. Wittmann (2003). "Thickness effect on fracture energy of cementitious materials." Cement and concrete research **33**(4): 499-507.

El-Qoubaa, Z. and R. Othman (2015). "Characterization and modeling of the strain rate sensitivity of polyetheretherketone's compressive yield stress." Materials & Design (1980-2015) **66**: 336-345.

Elkashef, M., R. C. Williams and E. Cochran (2018). "Investigation of fatigue and thermal cracking behavior of rejuvenated reclaimed asphalt pavement binders and mixtures." International Journal of Fatigue **108**: 90-95.

European Committee for Standardization, B., Belgium. (2010). "Bituminous mixtures—Test methods for hot mix asphalt—Part 44: Crack propagation by semi-circular bending test." (EN 12697-44: 2010).

Fakhri, M. and A. Ahmadi (2017). "Evaluation of fracture resistance of asphalt mixes involving steel slag and RAP: Susceptibility to aging level and freeze and thaw cycles." Construction and Building Materials **157**: 748-756.

Faruk, A. N., X. Hu, Y. Lopez and L. F. Walubita (2014). "Using the Fracture Energy Index Concept to Characterize the HMA Cracking Resistance Potential under Monotonic Crack Testing." International Journal of Pavement Research and Technology **7**(1): 40.

Feng, Z., J. Yu and Y. Liang (2012). "The relationship between colloidal chemistry and ageing properties of bitumen." Petroleum science and technology **30**(14): 1453-1460.

Fujie Zhou, B. C., Jun Zhang, Sheng Hu, Jon Epps, and Lijun and Sun (2020). "Development and Validation of an Ideal Shear Rutting Test for Asphalt Mix Design and QC/QA." Journal of the Association of Asphalt Paving Technologists.

Gao, G., S. Huang, K. Xia and Z. Li (2015). "Application of digital image correlation (DIC) in dynamic notched semi-circular bend (NSCB) tests." Experimental mechanics **55**(1): 95-104.

Garcia Cucalon, L., F. Kaseer, E. Arámbula-Mercado, A. Epps Martin, N. Morian, S. Pournoman and E. Hajj (2019). "The crossover temperature: significance and application towards engineering balanced recycled binder blends." Road Materials and Pavement Design **20**(6): 1391-1412.

Garcia, V. M., A. Miramontes, J. Garibay, I. Abdallah and S. Nazarian (2018). "Assessing crack susceptibility of asphalt concrete mixtures with overlay tester." Journal of Testing and Evaluation **46**(3): 924-933.

Garcia, V. M., M. Valenzuela, A. Torres, I. Abdallah and S. Nazarian (2019). Performance Characterization of Asphalt Concrete Mixtures Modified with a Latex Additive. Airfield and Highway Pavements 2019: Testing and Characterization of Pavement Materials, American Society of Civil Engineers Reston, VA**:** 88-99.

Goodrich, J. L. (1988). Asphalt and polymer modified Asphalt properties related to the performance of Asphalt concrete mixes (with discussion). Association of Asphalt Paving Technologists Proc.

Haghshenas, H., H. Nabizadeh, Y.-R. Kim and K. Santosh (2016). Research on high-rap asphalt mixtures with rejuvenators and WMA additives. Lincoln, NE, USA, Nebraska Transportation Center.

Haghshenas, H., G. Nsengiyumva, Y.-R. Kim, K. Santosh and S. Amelian (2019). Research on High-RAP Asphalt Mixtures with Rejuvenators-Phase II. Lincoln, NE, USA, Nebraska Transportation Center.

Haghshenas, H. F., Y.-R. Kim, M. D. Morton, T. Smith, M. Khedmati and D. F. Haghshenas (2018). "Effect of softening additives on the moisture susceptibility of recycled bituminous materials using chemical-mechanical-imaging methods." Journal of Materials in Civil Engineering **30**(9): 04018207.

He, Y., A. Makeev and B. Shonkwiler (2012). "Characterization of nonlinear shear properties for composite materials using digital image correlation and finite element analysis." Composites Science and Technology **73**: 64-71.

Hill, B. C., O. Giraldo-Londoño, G. H. Paulino and W. G. Buttlar (2017). "Inverse Estimation of Cohesive Fracture Properties of Asphalt Mixtures Using an Optimization Approach." Experimental mechanics **57**(4): 637-648.

Huang, B., X. Shu and G. Zuo (2013). "Using notched semi circular bending fatigue test to characterize fracture resistance of asphalt mixtures." Engineering Fracture Mechanics **109**: 78-88.

Im, S., H. Ban and Y.-R. Kim (2014). "Characterization of mode-I and mode-II fracture properties of fine aggregate matrix using a semicircular specimen geometry." Construction and Building Materials **52**: 413-421.

Im, S., H. Ban and Y.-R. Kim (2014). "Mode-Dependent Fracture Behavior of Asphalt Mixtures with Semicircular Bend Test." Transportation Research Record: Journal of the Transportation Research Board(2447): 23-31.

Im, S., P. Karki and F. Zhou (2016). "Development of new mix design method for asphalt mixtures containing RAP and rejuvenators." Construction and Building Materials **115**: 727-734.

Im, S., Y.-R. Kim and H. Ban (2013). "Rate-and Temperature-Dependent Fracture Characteristics of Asphaltic Paving Mixtures." Journal of Testing and Evaluation **41**(2): 257-268.

Im, S., T. You, Y.-R. Kim, G. Nsengiyumva, R. Rea and H. Haghshenas (2018). "Evaluation of Thin-Lift Overlay Pavement Preservation Practice: Mixture Testing, Pavement Performance, and Lifecycle Cost Analysis." Journal of Transportation Engineering, Part B: Pavements **144**(3): 04018037.

Im, S. and F. Zhou (2014). "Field Performance of RAS Test Sections and Laboratory Investigation of Impact of Rejuvenators on Engineering Properties of RAP/RAS Mixes." Texas A&M Transportation Institute, FHWA/TX-14/0-6614-3.

Jaekel, D. J., D. W. MacDonald and S. M. Kurtz (2011). "Characterization of PEEK biomaterials using the small punch test." journal of the mechanical behavior of biomedical materials **4**(7): 1275-1282.

Jahangiri, B., H. Majidifard, J. Meister and W. G. Buttlar (2019). "Performance evaluation of asphalt mixtures with reclaimed asphalt pavement and recycled asphalt shingles in Missouri." Transportation Research Record **2673**(2): 392-403.

Jenks, C., C. Jencks, E. Harrigan, M. Adcock, E. Delaney and H. Freer (2011). "NCHRP Report 673: A manual for design of hot mix asphalt with commentary." Transportation Research Board, Washington, DC.

Jia, X., B. Huang, J. A. Moore and S. Zhao (2015). "Influence of waste engine oil on asphalt mixtures containing reclaimed asphalt pavement." Journal of Materials in Civil Engineering **27**(12): 04015042.

Karger-Kocsis, J. and K. Friedrich (1986). "Temperature and strain-rate effects on the fracture toughness of poly(ether ether ketone) and its short glass-fibre reinforced composite." Polymer **27**(11): 1753-1760.

Kaseer, F., L. G. Cucalon, E. Arámbula-Mercado, A. E. Martin and J. Epps (2018). "Practical tools for optimizing recycled materials content and recycling agent dosage for improved short-and long-term performance of rejuvenated binder blends and mixtures." Journal of the Association of Asphalt Paving Technologists **87**: 513-550.

Kaseer, F., F. Yin, E. Arámbula-Mercado and A. Epps Martin (2017). "Stiffness Characterization of Asphalt Mixtures with High Recycled Material Content and Recycling Agents." Transportation Research Record: Journal of the Transportation Research Board(2633): 58-68.

Kaseer, F., F. Yin, E. Arámbula-Mercado, A. E. Martin, J. S. Daniel and S. Salari (2018). "Development of an index to evaluate the cracking potential of asphalt mixtures using the semi-circular bending test." Construction and Building Materials **167**: 286-298.

Khosla, N. P., H. Nair, B. Visintine and G. Malpass (2012). "Effect of reclaimed asphalt and virgin binder on rheological properties of binder blends." International Journal of Pavement Research and Technology **5**(5): 317.

Kim, M., L. N. Mohammad, H. Challa and M. A. Elseifi (2015). "A simplified performance-based specification for asphalt pavements." Road Materials and Pavement Design **16**(sup2): 168-196.

Kim, M., L. N. Mohammad and M. A. Elseifi (2012). "Characterization of fracture properties of asphalt mixtures as measured by semicircular bend test and indirect tension test." Transportation Research Record **2296**(1): 115-124.

Kim, Y.-R. (2003). Mechanistic fatigue characterization and damage modeling of asphalt mixtures. Civil Engineering. College Station, Texas, USA, Texas A & M University. **DOCTOR OF PHILOSOPHY**.

Kim, Y.-R., D. Allen and D. Little (2005). "Damage-induced modeling of asphalt mixtures through computational micromechanics and cohesive zone fracture." Journal of Materials in Civil Engineering **17**(5): 477-484.

Kim, Y.-R., D. Allen and D. Little (2007). "Computational constitutive model for predicting nonlinear viscoelastic damage and fracture failure of asphalt concrete mixtures." International Journal of Geomechanics **7**(2): 102-110.

Kim, Y.-R. and F. T. S. Aragão (2013). "Microstructure modeling of rate-dependent fracture behavior in bituminous paving mixtures." Finite Elements in Analysis and Design **63**: 23-32.

Kim, Y.-R., J. E. S. Lutif and D. H. Allen (2009). "Determining representative volume elements of asphalt concrete mixtures without damage." Transportation Research Record **2127**(1): 52-59.

Kim, Y.-R., J. Zhang and H. Ban (2012). "Moisture damage characterization of warm-mix asphalt mixtures based on laboratory-field evaluation." Construction and Building Materials **31**: 204-211.

Kim, Y., J. Lee and J. E. Lutif (2010). "Geometrical evaluation and experimental verification to determine representative volume elements of heterogeneous asphalt mixtures." Journal of Testing and Evaluation **38**(6): 660-666.

Kim, Y. R., H.-J. Lee and D. N. Little (1997). "Fatigue characterization of asphalt concrete using viscoelasticity and continuum damage theory (with discussion)." Journal of the Association of Asphalt Paving Technologists **66**.

Kirugulige, M. S., H. V. Tippur and T. S. Denney (2007). "Measurement of transient deformations using digital image correlation method and high-speed photography: application to dynamic fracture." Applied optics **46**(22): 5083-5096.

Kollmann, J., P. Liu, G. Lu, D. Wang, M. Oeser and S. Leischner (2019). "Investigation of the microstructural fracture behaviour of asphalt mixtures using the finite element method." Construction and Building Materials **227**: 117078.

Kriz, P., D. L. Grant, B. A. Veloza, M. J. Gale, A. G. Blahey, J. H. Brownie, R. D. Shirts and S. Maccarrone (2014). "Blending and diffusion of reclaimed asphalt pavement and virgin asphalt binders." Road Materials and Pavement Design **15**(sup1): 78-112.

Kurtz, S. M. (2019). PEEK biomaterials handbook, William Andrew.

Lagarias, J. C., J. A. Reeds, M. H. Wright and P. E. Wright (1998). "Convergence properties of the Nelder--Mead simplex method in low dimensions." SIAM Journal on optimization **9**(1): 112-147.

Lamontagne, J., P. Dumas, V. Mouillet and J. Kister (2001). "Comparison by Fourier transform infrared (FTIR) spectroscopy of different ageing techniques: application to road bitumens." Fuel **80**(4): 483-488.

Lesiuk, G., A. Sawicka, J. Correia and R. Frątczak (2017). "Fracture resistance analysis of PEEK-polymer." Engineering Structures and Technologies **9**(4): 207-213.

Li, X.-J. and M. Marasteanu (2010). "Using semi circular bending test to evaluate low temperature fracture resistance for asphalt concrete." Experimental mechanics **50**(7): 867-876.

Li, X. J. and M. O. Marasteanu (2009). "Using Semi Circular Bending Test to Evaluate Low Temperature Fracture Resistance for Asphalt Concrete." Experimental mechanics **50**(7): 867-876.

Little, D. N., D. H. Allen and A. Bhasin Modeling and design of flexible pavements and materials, Springer.

Liu, J. H. (2011). <u>Fatigue life evaluation of asphalt rubber mixtures using semi-circular bending test</u>. Advanced Materials Research, Trans Tech Publ.

Liu, P., D. Wang, F. Otto, J. Hu and M. Oeser (2018). "Application of semi-analytical finite element method to evaluate asphalt pavement bearing capacity." <u>International Journal of Pavement Engineering</u> **19**(6): 479-488.

Lu, H. and P. Cary (2000). "Deformation measurements by digital image correlation: implementation of a second-order displacement gradient." <u>Experimental mechanics</u> **40**(4): 393-400.

Lutif, J. E., F. V. Souza, Y. Kim, J. B. Soares and D. H. Allen (2010). "Multiscale modeling to predict mechanical behavior of asphalt mixtures." <u>Transportation Research Record</u> **2181**(1): 28-35.

Ma, T., X. Huang, Y. Zhao and Y. Zhang (2015). "Evaluation of the diffusion and distribution of the rejuvenator for hot asphalt recycling." <u>Construction and Building Materials</u> **98**: 530-536.

Machiwal, D. and M. K. Jha (2012). <u>Hydrologic time series analysis: Theory and practice</u>, Springer Science & Business Media.

Mahmoud, E., S. Saadeh, H. Hakimelahi and J. Harvey (2014). "Extended finite-element modelling of asphalt mixtures fracture properties using the semi-circular bending test." <u>Road Materials and Pavement Design</u> **15**(1): 153-166.

Marasteanu, M. O., X. Li, T. R. Clyne, V. Voller, D. H. Timm and D. Newcomb (2004). "Low Temperature Cracking of Asphalt Concrete Pavement."

McDaniel, R. S., A. Shah, G. A. Huber and V. Gallivan (2007). "Investigation of properties of plant-produced RAP mixtures." <u>Transportation Research Record: Journal of the Transportation Research Board</u>(1998): 103-111.

McDonald, D. B., W. J. Grantham, W. L. Tabor and M. J. Murphy (2007). "Global and local optimization using radial basis function response surface models." <u>Applied Mathematical Modelling</u> **31**(10): 2095-2110.

Miramontes, A., J. L. Garibay, I. Abdallah, S. Nazarian and V. Garcia (2017). Improved overlay tester for fatigue cracking resistance of asphalt mixtures, University of Texas at El Paso. Center for Transportation Infrastructure ….

Mogawer, W., A. Austerman, L. Mohammad and M. E. Kutay (2013). "Evaluation of high RAP-WMA asphalt rubber mixtures." <u>Road Materials and Pavement Design</u> **14**(sup2): 129-147.

Mogawer, W. S., A. Booshehrian, S. Vahidi and A. J. Austerman (2013). "Evaluating the effect of rejuvenators on the degree of blending and performance of high RAP, RAS, and RAP/RAS mixtures." <u>Road Materials and Pavement Design</u> **14**(sup2): 193-213.

Mokhtari, M., A. Hayatdavoudi, R. Nizamutdinov, H. Rizvi and F. Nath (2017). Characterization of Complex Fracture Propagation in Naturally Fractured Formations Using Digital Image Correlation Technique. SPE Hydraulic Fracturing Technology Conference and Exhibition. The Woodlands, Texas, USA, Society of Petroleum Engineers: 11.

Monismith, C. L. and K. E. Secor (1962). Viscoelastic behavior of asphalt concrete pavements. International Conference on the Structural Design of Asphalt PavementsUniversity of Michigan, Ann Arbor.

Nabizadeh, H., H. F. Haghshenas, Y.-R. Kim and F. T. S. Aragão (2017). "Effects of rejuvenators on high-RAP mixtures based on laboratory tests of asphalt concrete (AC) mixtures and fine aggregate matrix (FAM) mixtures." Construction and Building Materials **152**: 65-73.

Newcomb, D. and F. Zhou (2018). Balanced Design of Asphalt Mixtures. Minnesota. Dept. of Transportation. Research Services & Library, Minnesota. Dept. of Transportation. Research Services & Library.

Nsengiyumva, G. (2015). Development of Semi-Circular Bending (SCB) Fracture Test for Bituminous Mixtures. Civil Engineering. December 2015, University of Nebraska-Lincoln. **Master of Science**.

Nsengiyumva, G., H. F. Haghshenas, Y.-R. Kim and S. R. Kommidi (2020). "Mechanical-Chemical Characterization of the Effects of Type, Dosage, and Treatment Methods of Rejuvenators in Aged Bituminous Materials." Transportation Research Record **0**(0): 0361198120909110.

Nsengiyumva, G. and Y.-R. Kim (2019). "Effect of Testing Configuration in Semi-Circular Bending Fracture of Asphalt Mixtures: Experiments and Statistical Analyses." Transportation Research Record **2673**(5): 320-328.

Nsengiyumva, G., T. You and Y.-R. Kim (2017). "Experimental-statistical investigation of testing variables of a semicircular bending (SCB) fracture test repeatability for bituminous mixtures." Journal of Testing and Evaluation **45**(5): 1691-1701.

Nsengiyumva, G. M., K. Santosh, Y.-R. Kim, H. Xu and Y. Yang (2018). New Mixture Additives for Sustainable Bituminous Pavements. Lincoln, NE, USA, Nebraska Transportation Center.

Oldham, D., A. Hung, M. M. Parast and E. H. Fini (2018). "Investigating bitumen rejuvenation mechanisms using a coupled rheometry-morphology characterization approach." Construction and Building Materials **159**: 37-45.

Osmari, P. H., R. F. da Costa, F. T. S. Aragão, D. Braz, R. C. R. Barroso, L. P. Nogueira and A. K. Y. Ng (2020). "Determination of Volumetric Characteristics of FAM Mixtures using X-Ray Micro-Computed Tomography and Their Effects on the Rheological Behavior of the Material." Transportation Research Record: 0361198120914607.

Ozer, H., I. L. Al-Qadi, E. Barber, E. Okte, Z. Zhu and S. Wu (2017). Evaluation of I-FIT Results and Machine Variability using MnRoad Test Track Mixtures, Illinois Center for Transportation/Illinois Department of Transportation.

Ozer, H., I. L. Al-Qadi, P. Singhvi, T. Khan, J. Rivera-Perez and A. El-Khatib (2016). "Fracture characterization of asphalt mixtures with high recycled content using Illinois semicircular bending test method and flexibility index." Transportation Research Record **2575**(1): 130-137.

Park, K. and G. H. Paulino (2011). "Cohesive zone models: a critical review of traction-separation relationships across fracture surfaces." Applied Mechanics Reviews **64**(6): 060802.

Park, S. and R. Schapery (1999). "Methods of interconversion between linear viscoelastic material functions. Part I—A numerical method based on Prony series." International journal of solids and structures **36**(11): 1653-1675.

Park, S. W., Y. R. Kim and R. A. Schapery (1996). "A viscoelastic continuum damage model and its application to uniaxial behavior of asphalt concrete." Mechanics of materials **24**(4): 241-255.

Passieux, J. C., F. Bugarin, C. David, J. N. Périé and L. Robert (2015). "Multiscale Displacement Field Measurement Using Digital Image Correlation: Application to the Identification of Elastic Properties." Experimental mechanics **55**(1): 121-137.

Rami, K. Z. and Y.-R. Kim (2015). Nebraska data collection. Lincoln, NE, USA, Nebraska Transportation Center.

Rami, K. Z., Y.-R. Kim, M. Khedmati, G. Nsengiyumva and H. Alanazi (2018). "Two-way linked multiscale method integrated with nanomechanical tests and cohesive zone fracture to model highly heterogeneous binding materials." Journal of Engineering Mechanics **144**(10): 04018095.

Razali, N. M. and Y. B. Wah (2011). "Power comparisons of shapiro-wilk, kolmogorov-smirnov, lilliefors and anderson-darling tests." Journal of Statistical Modeling and Analytics **2**(1): 21-33.

Rivard, C. H., S. Rhalmi and C. Coillard (2002). "In vivo biocompatibility testing of peek polymer for a spinal implant system: a study in rabbits." Journal of Biomedical Materials Research: An Official Journal of The Society for Biomaterials, The Japanese Society for Biomaterials, and The Australian Society for Biomaterials and the Korean Society for Biomaterials **62**(4): 488-498.

Roberts, F. L., P. S. Kandhal, E. R. Brown, D.-Y. Lee and T. W. Kennedy (1991). Hot mix asphalt materials, mixture design and construction. 5100 Forbes Boulevard, Lanham, MD United States 20706-4413, National Asphalt Pavement Association Research and Education Foundation.

Rodezno, M. C., R. West and A. Taylor (2015). "Flow number test and assessment of AASHTO TP 79-13 rutting criteria: Comparison of rutting performance of hot-mix and warm-mix asphalt mixtures." Transportation Research Record **2507**(1): 100-107.

Rodrigues, J. A., J. E. S. L. Teixeira, Y.-R. Kim, D. N. Little and F. V. Souza (2019). "Crack modeling of bituminous materials using extrinsic nonlinear viscoelastic cohesive zone (NVCZ) model." Construction and Building Materials **204**: 520-529.

Saadeh, S., H. Hakimelahi and J. Harvey (2014). Correlation of Semi-circular Bending and Beam Fatigue Fracture Properties of Asphalt Concrete Using Non-Contact Camera and Crosshead Movement. T&DI Congress 2014: Planes, Trains, and Automobiles, ASCE.

Shanbara, H. K., F. Ruddock and W. Atherton (2018). "Predicting the rutting behaviour of natural fibre-reinforced cold mix asphalt using the finite element method." Construction and Building Materials **167**: 907-917.

Shen, B. (2009). Functionally graded fiber-reinforced cementitious composites—Manufacturing and extraction of cohesive fracture properties using finite elements and digital image correlation. Civil Engineering. Urbana, Illinois, University of Illinois at Urbana-Champaign. **Doctor of Philosophy**.

Shen, B. and G. Paulino (2011). "Direct extraction of cohesive fracture properties from digital image correlation: a hybrid inverse technique." Experimental mechanics **51**(2): 143-163.

Shen, B. and G. H. Paulino (2011). "Identification of cohesive zone model and elastic parameters of fiber-reinforced cementitious composites using digital image correlation and a hybrid inverse technique." Cement and Concrete Composites **33**(5): 572-585.

Shu, X., B. Huang and D. Vukosavljevic (2010). "Evaluation of cracking resistance of recycled asphalt mixture using semi-circular bending test." Paving materials and pavement analysis (GSP 203): 58-65.

Sobieraj, M. C., S. M. Kurtz and C. M. Rimnac (2009). "Notch sensitivity of PEEK in monotonic tension." Biomaterials **30**(33): 6485-6494.

Song, S. H., G. H. Paulino and W. G. Buttlar (2006). "A bilinear cohesive zone model tailored for fracture of asphalt concrete considering viscoelastic bulk material." Engineering Fracture Mechanics **73**(18): 2829-2848.

Sutton, M., W. Wolters, W. Peters, W. Ranson and S. McNeill (1983). "Determination of displacements using an improved digital correlation method." Image and vision computing **1**(3): 133-139.

Sutton, M. A., J. J. Orteu and H. Schreier (2009). Image correlation for shape, motion and deformation measurements: basic concepts, theory and applications, Springer Science & Business Media.

Tam, K., P. E. Joseph and D. Lynch (1991). Five year experience on low temperature performance of recycled hot mix, Ontario Ministry of Transportation, Engineering Materials Office.

Tran, N. H., A. Taylor and R. Willis (2012). "Effect of rejuvenator on performance properties of HMA mixtures with high RAP and RAS contents." NCAT Report 12-05, National Center for Asphalt Technology, Auburn, AL.

Underwood, B. S. and Y. R. Kim (2013). "Effect of volumetric factors on the mechanical behavior of asphalt fine aggregate matrix and the relationship to asphalt mixture properties." Construction and Building Materials **49**: 672-681.

Vendroux, G. and W. Knauss (1998). "Submicron deformation field measurements: Part 2. Improved digital image correlation." Experimental mechanics **38**(2): 86-92.

Wagnoner, M., W. G. Buttlar and G. Paulino (2005). "Disk-shaped compact tension test for asphalt concrete fracture." Experimental mechanics **45**(3): 270-277.

Wagoner, M. P., W. G. Buttlar and G. H. Paulino (2005). "Development of a single-edge notched beam test for asphalt concrete mixtures." Journal of Testing and Evaluation **33**(6): 452-460.

Walubita, L. F., A. N. Faruk, G. Das, H. A. Tanvir, J. Zhang and T. Scullion (2012). The overlay tester: a sensitivity study to improve repeatability and minimize variability in the test results, Texas Transportation Institute.

West, R. (2010). "Reclaimed asphalt pavement management: best practices." Auburn, AL: National Center for Asphalt Technology, NCAT Draft Report.

West, R., C. Rodezno, F. Leiva and F. Yin (2018). "Development of a Framework for Balanced Mix Design. Project NCHRP 20-07/Task 406." Transportation Research Board, Washington, DC.

West, R. C., J. R. Willis and M. O. Marasteanu (2013). "Improved mix design, evaluation, and materials management practices for hot mix asphalt with high reclaimed asphalt pavement content." Transportation Research Board, Washington, DC **752**.

Wineman, A. S. and K. R. Rajagopal (2000). Mechanical response of polymers: an introduction, Cambridge university press.

Witczak, M., T. Pellinen and M. El-Basyouny (2002). "Pursuit of the simple performance test for asphalt concrete fracture/cracking." Journal of the Association of Asphalt Paving Technologists **71**.

Wittmann, X. and H. Zhong (1996). On some experiments to study the influence of size on strength and fracture energy of concrete, Aedificatio Verlag.

Wu, S., W. Zhang, S. Shen, B. Muhunthan and L. N. Mohammad (2017). "Short-Term Performance and Evolution of Material Properties of Warm-and Hot-Mix Asphalt Pavements: Case Studies." Transportation Research Record **2631**(1): 39-54.

Wu, Z., L. N. Mohammad, L. Wang and M. A. Mull (2005). "Fracture resistance characterization of superpave mixtures using the semi-circular bending test." Journal of ASTM International **2**(3): 1-15.

Xu, X.-P. and A. Needleman (1993). "Void nucleation by inclusion debonding in a crystal matrix." Modelling and Simulation in Materials Science and Engineering **1**(2): 111.

Yoon, C. and D. H. Allen (1999). "Damage dependent constitutive behavior and energy release rate for a cohesive zone in a thermoviscoelastic solid." International Journal of Fracture **96**(1): 55-74.

You, T., E. A. Masad, R. K. A. Al-Rub, E. Kassem and D. N. Little (2014). "Calibration and validation of a comprehensive constitutive model for asphalt mixtures." Transportation Research Record **2447**(1): 13-22.

Zaumanis, M., R. Mallick and R. Frank (2013). "Evaluation of Rejuvenator's Effectiveness with Conventional Mix Testing for 100% Reclaimed Asphalt Pavement Mixtures." Transportation Research Record: Journal of the Transportation Research Board(2370): 17-25.

Zaumanis, M., R. B. Mallick, L. Poulikakos and R. Frank (2014). "Influence of six rejuvenators on the performance properties of Reclaimed Asphalt Pavement (RAP) binder and 100% recycled asphalt mixtures." Construction and Building Materials **71**: 538-550.

Zegeye, E., J.-L. Le, M. Turos and M. Marasteanu (2012). "Investigation of size effect in asphalt mixture fracture testing at low temperature." Road Materials and Pavement Design **13**(sup1): 88-101.

Zhou, F. (2019). "Development of an IDEAL Cracking Test for Asphalt Mix Design, Quality Control and Quality Assurance." NCHRP-IDEA Program Project Final Report(195).

Zhou, F., S. Hu and T. Scullion (2006). Integrated asphalt (overlay) mixture design, balancing rutting and cracking requirements, Texas Transportation Institute, Texas A & M University System.

Zhou, F. and T. Scullion (2005). Overlay tester: A rapid performance related crack resistance test, Texas Transportation Institute, Texas A & M University System.

Algorithm 1 Vertex Replacement Process by N-M Method

```
% Calculate the centroid of the simplex%
```

$$\chi_c = (\chi_1 + \chi_2 + \chi_3)/3$$

```
%% Calculate a reflection χ(b) of the vertex with the highest function value
```

```
going through χc %%
```

$$\chi(b) = \chi_c + b(\chi_1 - \chi_c) \quad \text{% for the reflection } b = -1$$

```
if  Ψu(χ(-1)) < χ1
```
$$\text{if } \Psi_u(\chi(-1)) < \chi_1$$

```
        perform expansion by using  b = -2
        if  Ψu(χ(-2)) < Ψu(χ1)

                replace  χ1  with  χ(-2)
        return
        else

                replace  χ1  with  χ(-1)
        return
        end
else
        perform an outside contraction  b = -1/2
        if  Ψu(χ(-1/2)) < Ψu(χ1)

                replace  χ1  with  χ(-1/2)
        return
        else
                perform an inside contraction  b = 1/2
                if  Ψu(χ(1/2)) < Ψu(χ1)

                        replace  χ1  with  χ(1/2)
                else
                        shrink around the vertex with the lowest function value
                        return
                end
        end
end
```